UNIVERSIDAD DE
GUANAJUATO

Performance and Operational Aspects of High-Luminosity LHC Operational Scenarios

Thesis

submitted in partial fulfillment
of the requirements for the degree of

Doctor of Philosophy in Physics

by

Luis Eduardo Medina Medrano

Advisor: **Dr. Rogelio Tomás García** (CERN)
Co-advisor: **Dr. Mauro Napsuciale Mendívil** (UG-DCI)

October 30, 2019

Performance and Operational Aspects of High-Luminosity LHC Operational Scenarios

Thesis submitted in partial fulfilment of the requirements
for the degree of Doctor of Philosophy in Physics by

Luis Eduardo Medina Medrano

Advisor: **Dr. Rogelio Tomás García** (CERN)
Co-advisor: **Dr. Mauro Napsuciale Mendívil** (UG-DCI)

UNIVERSIDAD DE GUANAJUATO
División de Ciencias e Ingenierías

October 30, 2019

To my family

Acknowledgements

This work would not have been possible without the help of many people. First and foremost, I would like to thank my thesis supervisors both at the University of Guanajuato and at CERN: to Mauro Napsuciale for his trust, his constant support, and his endless efforts to push the development of the accelerator physics field in Mexico, efforts from which I feel honoured to have benefited from; and to Rogelio Tomás, for the opportunity to take part in his research projects at CERN, first as a Master's student, and later as a doctoral student, for sharing his knowledge and passion, and for his continuous guidance and encouragement throughout the full extent of my stay.

I would like to thank my colleagues in the BE department with whom I had the pleasure to work with, either briefly or extensively, in the different topics of my research: from the ABP group, to J. Barranco, X. Buffat, R. De Maria, S. Fartoukh, M. Giovannozzi, G. Iadarola, E. Métral, S. Papadopoulou, Y. Papaphilippou, G. Sterbini, T. Pieloni, and S. White; from the RF group, to P. Baudrenghien, R. Calaga, and E. Shaposhnikova. Thank you all for the invaluable input, explanations, discussions, and corrections, all of which helped me to better understand not only my research, but accelerator physics and the (HL)-LHC in general. I would also like to thank B. Petersen, P. Azzi, I. Efthymiopoulos, and the rest of the Experimental Data Quality group for the fruitful discussions that led to the introduction of the concept of effective pile-up density. A special acknowledgement to G. Arduini, leader of the ABP group, for the opportunities given and his support, and to O. Brüning and L. Rossi, leaders of the HL-LHC project, for all their comments on the many written works I prepared as part of this PhD.

To the members of the examining committee who kindly accepted to review this thesis, Dr. R. Castañeda Priego, Dr. A. Castilla Loeza, Dr. G. Herrera Corral, and Dr. H. Maury Cuna. their remarks, founded in their expertise, undoubtedly have improved the quality of this manuscript. This research was supported by the HL-LHC project, and my doctoral stay was possible thanks to the BEAM project sponsored by CONACYT and diligently coordinated by F. Zimmermann at CERN, to whom I also extend my most sincere gratitude.

To my friends Alex and Elena, Karim, Cristian, Marco and Daniela, Anders and Mario, and the many students I got to befriend, for all the good times throughout these years. To Rafa, *pela tua paciência e compreensão, pela tua*

ajuda, por me teres pressionado e encorajado: obrigado, muito obrigado.

A mi familia, por su apoyo incondicional, comprensión y fortaleza, a pesar de la distancia que la mayor parte del tiempo nos separa.

Finally, I would like to thank to all who I might not have mentioned by name, but who from one way or another, made this journey possible.

L. Medina
Geneva, September, 2019

Abstract

The High-Luminosity LHC (HL-LHC) is the upgrade of the Large Hadron Collider (LHC) at the European Organization for Nuclear Research (CERN) aiming at the full exploitation of the collider, with operations scheduled to start after 2025. Using the latest sets of parameters, the performance at the two main interaction points (IPs) of the HL-LHC baseline and main alternative operational scenarios is evaluated at both nominal and ultimate levelling (corresponding to levelled luminosities of $5 \times 10^{34}\,\mathrm{cm}^{-2}\,\mathrm{s}^{-1}$ and $7.5 \times 10^{34}\,\mathrm{cm}^{-2}\,\mathrm{s}^{-1}$, respectively). Realistic simulations of the evolution of the optimum fills are conducted with the purpose-developed LEVELLING program, which takes into account the effects of beam intensity burn-off, synchrotron radiation, intrabeam scattering, and crab cavity noise on emittance growth, in conjunction with a step-based luminosity levelling. Numerical computations of the luminosity can be implemented assuming a q-Gaussian bunch longitudinal profile –a realistic description based on observations in the LHC–, as well as with possible time offsets in the bunch position. Results provide an insight into the operational challenges of each scenario (e.g. the number of optics to be commissioned), and detailed characterisations of their corresponding luminous regions around the IPs –a valuable input for studies on the detector efficiency under a wide range of configurations. The latest estimates on the performance of the different HL-LHC operational scenarios in terms of yearly integrated luminosity and effective pile-up density comprise the central results of this work. The latter is a new and complementary figure-of-merit introduced in collaboration with the ATLAS and CMS experiments characterising the expected detector performance based on the integrated average distribution of events around the IPs. In the case of the baseline, it is shown that the goals of the HL-LHC project are met (yearly integrated luminosity above $250\,\mathrm{fb}^{-1}$ and $320\,\mathrm{fb}^{-1}$ at nominal and ultimate operation, respectively). The found effective pile-up densities of $0.80\,\mathrm{mm}^{-1}$ and $1.20\,\mathrm{mm}^{-1}$, respectively, constitute the references for comparisons with the alternative scenarios. In order to understand the effect of each parameter and to guide possible future optimisations, an extensive series of sensitivity studies is conducted for the baseline. Operation at the ultimate energy of 7.5 TeV and several scenarios for a high-luminosity LHCb experiment are also explored. Lastly, a correction scheme of the long-range beam-beam effects –which might limit the machine performance– using local corrector magnets is also proposed.

Resumen

El *High-Luminosity LHC* (HL-LHC) es el proyecto de mejora del *Large Hadron Collider* (LHC) en la Organización Europea para la Investigación Nuclear (CERN) que tiene por objetivo la explotación de forma completa de las capacidades del colisionador, y cuya entrada en operación está prevista para después del año 2025. Usando los parámetros más actuales, el desempeño en los dos principales puntos de interacción (IPs) del diseño base del HL-LHC y de sus principales escenarios operacionales alternativos es evaluado con nivelado nominal y *último* (correspondientes a luminosidades niveladas de $5 \times 10^{34}\,\mathrm{cm}^{-2}\,\mathrm{s}^{-1}$ y $7.5 \times 10^{34}\,\mathrm{cm}^{-2}\,\mathrm{s}^{-1}$, respectivamente). Simulaciones realistas de la evolución de los ciclos de llenado y operación (*fill*) óptimos de la máquina son llevadas a cabo con el programa Levelling. Desarrollado para este propósito, el programa toma en consideración los efectos de la reducción de la intensidad de los haces de partículas, radiación sincrotrón, dispersión interna del haz y ruido de las *crab cavities* en el crecimiento de la emitancia, en conjunto con el proceso de nivelado por pasos de la luminosidad. Los cálculos numéricos de la luminosidad pueden ser implementados asumiendo una densidad q-Gaussiana para la distribución longitudinal de cada paquete (*bunch*) de protones –una descripción realista basada en observaciones en el LHC–, así como desplazamientos temporales de la posición de los paquetes en el haz. Los resultados obtenidos proveen una visión de los desafíos operacionales de cada escenario (por ejemplo, el número de ópticas a implementar), así como caracterizaciones detalladas de las regiones luminosas alrededor de los IPs correspondientes –parámetros de entrada valiosos para estudios de la eficiencia de los detectores bajo un amplio rango de configuraciones). Las estimaciones más recientes del desempeño de los diferentes escenarios operacionales del HL-LHC en términos de la luminosidad integrada anual y de la densidad de eventos efectiva constituyen los resultados centrales de este trabajo. Este último es una figura de mérito novedosa y complementaria introducida en colaboración con los experimentos ATLAS y CMS que caracteriza el desempeño esperado del detector, y está basada en la distribución promedio de eventos alrededor de los IPs integrada sobre la duración de los ciclos óptimos. En el caso del diseño base, se demuestra que los objectivos del proyecto HL-LHC son alcanzados (luminosidades integradas anuales superiores a $250\,\mathrm{fb}^{-1}$ y $320\,\mathrm{fb}^{-1}$ en su operación nominal y última). La densidades de eventos efectivas encontradas de $0.80\,\mathrm{mm}^{-1}$ and $1.20\,\mathrm{mm}^{-1}$ constituyen las

referencias contra las cuales los escenarios alternativos han de ser comparados. Con el objetivo de entender el efecto de cada parámetro y guiar posibles optimizaciones futuras, un conjunto extenso de estudios de la sensibilidad del diseño base con cada uno de ellos es llevado a cabo. La operación del HL-LHC a la energía *final* de 7.5 TeV y de varios escenarios para la operación del experimento LHCb a alta luminosidad también son exploradas. Finalmente, se propone un esquema de corrección de los efectos inducidos por la interacción electromagnética de largo alcance entre los haces –los cuales pudieran limitar el desempeño de la máquina– usando imanes correctores locales.

PhD publications

Thesis

L. Medina, *Performance and operational aspects of the High-Luminosity LHC operational scenarios*, PhD thesis, Universidad de Guanajuato (UGTO). Supervisors: Dr. R. Tomás (CERN) and Dr. M. Napsuciale (UGTO). León, Mexico, Oct. 2019, *this thesis*.

Articles

L. Medina, G. Arduini, R. Tomás, and M. Napsuciale. Assessment of the performance of High-Luminosity LHC operational scenarios: integrated luminosity and effective pile-up density, *Can. J. Phys.*, 97(5):498–508, 2019, `doi:10.1139/cjp-2018-0291`.

G. Arduini et al. High Luminosity LHC: challenges and plans, *J. Instr.*, 11(12):C12081, 2016, `doi:10.1088/1748-0221/11/12/c12081`.

Technical reports

I. Efthymiopoulos et al. LHCb Upgrades and operation at $10^{34}\,\mathrm{cm}^{-2}\,\mathrm{s}^{-1}$ luminosity - A first study. Technical Report CERN-ACC-NOTE-2018-0038, CERN, Geneva, Switzerland, May 2018. `https://cds.cern.ch/record/2319258`.

E. Metral et al. Update of the HL-LHC operational scenarios for proton operation. Technical Report CERN-ACC-NOTE-2018-0002, CERN, Geneva, Switzerland, Jan. 2018. `http://cds.cern.ch/record/2301292`.

L. Medina, G. Arduini and R. Tomás. Variants and options. In G. Apollinari et al., editors, *High-Luminosity Large Hadron Collider (HL-LHC): Technical Design Report V.0.1.* CERN Yellow Reports: Monographs, section 2.5, pages 69–76. CERN, Geneva, Switzerland, 2017. `http://cds.cern.ch/record/2284929`.

P. Gonçalves Jorge et al. MD 979: Beta-beating measurements on colliding beams. Technical Report CERN-ACC-NOTE-2017-0060, CERN, Geneva, Switzerland, Nov. 2017. `http://cds.cern.ch/record/2292102`.

F.S. Carlier et al. Optics measurements and correction challenges for the HL-LHC. Technical Report CERN-ACC-2017-0088, CERN, Geneva, Switzerland, Oct. 2017. `https://cds.cern.ch/record/2290899`.

Conference proceedings

G. Sterbini et al. First results of the compensation of the beam-beam effect with DC wires in the LHC. In *Proc. of 10th Int. Part. Accel. Conf. (IPAC'19)*, pages 2262–2265. JACoW Publishing, Jun. 2019. `doi:10.18429/JACoW-IPAC2019-WEYYPLM3`.

L. Medina et al. New High-Luminosity LHC baseline and performance at ultimate energy. In *Proc. of 9th Int. Part. Accel. Conf. (IPAC'18)*, pages 408–411. JACoW Publishing, Jun. 2018. `doi:10.18429/JACoW-IPAC2018-MOPML009`.

L. Medina, J. Barranco García, X. Buffat, T. Pieloni, and R. Tomás. Assessment of linear and non-linear optics errors due to beam-beam with multipoles for the High-Luminosity LHC. In *Proc. of 9th Int. Part. Accel. Conf. (IPAC'18)*, pages 3557–3560. JACoW Publishing, Jun. 2018. `doi:10.18429/JACoW-IPAC2018-THPAK135`.

L. Medina, G. Arduini, and R. Tomás. Studies on luminous region, pile-up and performance for HL-LHC scenarios. In *Proc. of 8th Int. Part. Accel. Conf. (IPAC'17)*,pages 1908–1911. JACoW Publishing, May 2017. `http://jacow.org/ipac2017/papers/tupik089.pdf`.

L. Medina, J. Barranco García, X. Buffat, Y. Papaphilippou, T. Pieloni, and R. Tomás. Correction of beta-beating due to beam-beam for the LHC and its impact on dynamic aperture. In *Proc. of 8th Int. Part. Accel. Conf. (IPAC'17)*, pages 2512–2515. JACoW Publishing, May 2017. `doi:10.18429/JACoW-IPAC2017-WEOAB2`.

P. Gonçalves Jorge et al. Measurement of beta-beating due to strong head-on beam-beam interactions in the LHC. In *Proc. of 8th Int. Part. Accel. Conf. (IPAC'17)*, pages 2121–2124. JACoW Publishing, May 2017. `doi:10.18429/JACoW-IPAC2017-TUPVA030`.

L. Medina and R. Tomás. Performance and operational aspects of HL-LHC scenarios. In *Proc. of 7th Int. Part. Accel. Conf. (IPAC'16)*, pages 1516–1519. JACoW Publishing, Jun. 2016 `doi:10.18429/JACoW-IPAC2016-TUPMW035`.

T. Pieloni et al. Dynamic beta and beta-beating effects in the presence of the beam-beam interactions. In *Proc. of ICFA Adv. Beam Dynam. Work. on High-Int. and High-Bright. Hadron Beams (HB'16)*, pages 136–139. JACoW Publishing, Aug. 2016. `doi:10.18429/JACoW-HB2016-MOPR027`.

Presentations

More than 20 internal presentations in the HL-LHC Working Package 2 (`https://indico.cern.ch/category/3664/`), the Experimental Data Quality (`https://indico.cern.ch/category/7932/`) and other working groups, as well as contributions to invited talks in the 2015 to 2018 annual HL-LHC Collaboration Meetings (`https://indico.cern.ch/category/4366/`)

Other related publications

Contributions to the lattice design and studies on dynamic aperture for the Future Circular Collider - ee (FCC-ee) project were also conducted as part this PhD. The following is a selection of publications associated with this work:

A. Abada et al. *Eur. Phys. J. Spec. Top.* (2019) 228:261. `doi:10.1140/epjst/e2019-900045-4`.

R. Tomás et al. *Nuc. Part. Phys. Proc. B*, 273–275 (2016) 149–155. `doi:10.1016/j.nuclphysbps.2015.09.018`.

L. Medina, In *Future Circular Collider Meeting*, invited talk. Rome, Italy, 2016. `https://indico.cern.ch/event/438866/contributions/1084987/attachments/1257982/1857896/2016-04-14_FCCWeekRome_LuisMedina.pdf`.

K. Oide et al. *Phys. Rev. Accel. Beams*, 19:111005, 2016. `doi:10.1103/PhysRevAccelBeams.19.111005`.

K. Oide et al. In *Proc. of 7th Int. Part. Accel. Conf. (IPAC'16)*, paper THPOR022, 2016. `doi:10.18429/JACoW-IPAC2016-THPOR022`.

L. Medina, R. Martin, R. Tomás and F. Zimmermann. In *Proc. of 6th Int. Part. Accel. Conf. (IPAC'15)*, paper MOPWA059, 2015. `doi:10.18429/JACoW-IPAC2015-MOPWA059`.

M. Koratzinos et al. In *Proc. of 6th Int. Part. Accel. Conf. (IPAC'15)*, paper TUPTY060, 2015. `doi:10.18429/JACoW-IPAC2015-TUPTY060`.

R. Martin, R. Tomás and L. Medina. In *Proc. of 55th ICFA Adv. Beam Dynam. Work. on High-Lum. Circ.* e^+e^- *Coll. - Higgs Fact.*, paper FRT2B2, 2014. `http://accelconf.web.cern.ch/AccelConf/HF2014/papers/frt2b2.pdf`.

F. Zimmermann et al. In *Proc. of 55th ICFA Adv. Beam Dynam. Work. on High-Lum. Circ.* e^+e^- *Coll. - Higgs Fact.*, paper THP3H1, 2014. `http://accelconf.web.cern.ch/AccelConf/HF2014/papers/thp3h1.pdf`.

Contents

List of Figures

List of Tables

Acronyms

ALICE	A Large Ion Collider Experiment
ATLAS	A Toroidal LHC Apparatus
BB, BBHO, BBLR	Beam-beam, head-on BB, long-range BB
BBCW	BB compensation wire
CERN	European Organization for Nuclear Research
CC	Crab cavity
CMS	Compact Muon Solenoid
CR, CK	Crab crossing, crab kissing
DA	Dynamic aperture
FWHM	Full width at half maximum
G, qG, SG	Gaussian, q-Gaussian, super-Gaussian
IBS	Intrabeam scattering
IP	Interaction point
IR	Interaction region
LHC, HL-LHC	Large Hadron Collider, High-Luminosity LHC
LHCb	LHC-beauty
LIU	LHC Injectors Upgrade
MAD-X	Methodical Accelerator Design
PU	Pile-up
RF	Radio-frequency
RMS	Root-mean-square
SR	Synchrotron radiation

Chapter 1

Introduction

1.1 The High-Luminosity LHC

To fully exploit the discovery potential of the Large Hadron Collider (LHC, see Fig. 1.1) at the European Organization for Nuclear Research (CERN) [1], the High-Luminosity LHC (HL-LHC) [2] upgrade aims at the increase of the original design performance –accounted by the integrated luminosity– by a factor of ten. A top priority of the European Strategy for Particle Physics, the first phase of the HL-LHC international collaboration began in 2011 and concluded with the publication of a technical design report [3], and the start of the civil engineering work in 2018, together with the development, prototyping and testing of new components. Operation of the HL-LHC is expected to start in the second half of the next decade.

Luminosity is a quantity proportional to the number of collisions per second: the higher the luminosity, the more data the experiments (such as ATLAS and CMS, the two general-purpose detectors of the LHC) can collect and analyse. With yearly integrated luminosities of $250\,\mathrm{fb}^{-1}$ to $320\,\mathrm{fb}^{-1}$ achieved via operation with levelled luminosities of $5.0 \times 10^{34}\,\mathrm{cm}^{-2}\,\mathrm{s}^{-1}$ (nominal) to $7.5 \times 10^{34}\,\mathrm{cm}^{-2}\,\mathrm{s}^{-1}$ (ultimate), the HL-LHC is expected to reach its goal of delivering an integrated luminosity of $3000\,\mathrm{fb}^{-1}$ to $4000\,\mathrm{fb}^{-1}$ after twelve years of operation [4].

In order to achieve its goals, machine and beam parameters have to be optimised, and new technologies have to be implemented [5, 6]. Increasing the luminosity is possible due to the foreseen operation at a larger bunch population (2.2×10^{11} protons per bunch or ppb), together with the addition of new cutting-edge 11 T niobium-tin magnets –which allow the reduction of the beam sizes at the interaction points (IPs)–, as well as the use of superconducting crab cavities –designed to rotate the bunches and increase their overlapping area around the IPs–. Larger luminosities, together with operation with levelling (first demonstrated at low intensity [7, 8] and then successfully tested during the 2018 LHC run [9, 10]), allow the increase of the present number of collisions at the ATLAS and CMS experiments, and to keep the

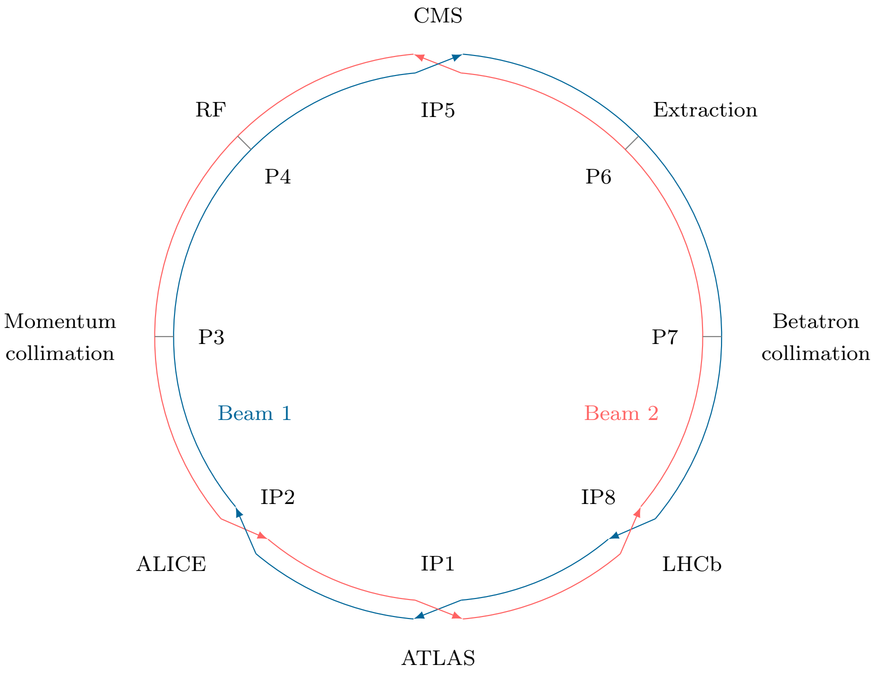

Figure 1.1. The LHC rings and interaction points.

number of collisions per bunch crossing at their IPs constant throughout the duration of the fill[1] (at 140 or 200 for nominal and ultimate operation, respectively). In terms of beam optics, the novel achromatic telescopic squeezing (ATS) scheme [11, 12] and new instrumentation to measure the beam parameters will also be implemented. Other key components of the HL-LHC project include new technology for beam collimation and reinforced machine protection, innovative high-temperature lossless superconducting transmission lines, the start of operation of Linac4 –which replaces the original proton injector– and the upgrade of the accelerator chain –the Proton Synchrotron Booster, the Proton Synchrotron, and the Super Proton Synchrotron– as part of the LHC Injectors Upgrade (LIU) [13], and two new 300-metre-long tunnels and shafts next to the ATLAS and CMS caverns to house sensitive existing and new equipment [14].

The high levels of pile-up (the average number of events per bunch crossing) expected in the HL-LHC, which translate in more complex collisions to record and analyse, have motivated major upgrade projects for the two main experiments [15–20]. These upgrades, designed to ensure and to improve the detector performance under such new and challenging conditions and, ultimately, the full exploitation of the detector potential, include better tracking performance, enhanced trigger capabilities, and computing infrastructure. Upgrade projects for the LHCb and ALICE detectors (experiments designed to focus on specific phenomena), are also currently ongoing [21–23].

---

[1] A *fill* is a period in the LHC in which beans have been injected into the machine, and are in circulation around the rings. A *physics* fill is a fill with stable beams, where the two beams are made to collide in the IPs and data is collected by the experiments.

The HL-LHC will allow to study known mechanisms in more detail, as well as to observe rare new phenomena. With the aim to identify the challenges and the physics landscape in proton-proton collisions at the HL-LHC, studies with the foreseen integrated luminosities of the HL-LHC have been conducted in the past [24], and work is currently being done to update them with the foreseen machine parameters, more realistic simulation tools, and the latest data from the LHC. The discovery of a Higgs boson at 125 GeV in the LHC define one of the primary goals of the HL-LHC: the large integrated luminosities in the HL-LHC will greatly extend the potential to study the properties of the decay final states of the Higgs boson, either improving the accuracy and precision of the measurements (at few percent levels) of the branching ratios and couplings corresponding to the many final states accessible in the collider (including rare process), or searching the rare decaying modes not yet observed, to test the boundaries of the Standard Model (SM) [25]. These studies are motivated by the fact that each of these decaying channels is sensitive, in a different way, to different effects of physics beyond the SM (BSM) [26]. Search of BSM physics –including supersymmetry and exotic models–, predicted by the theoretical work based on the SM but extended to explain phenomena such as dark matter, the baryon asymmetry, the neutrino masses, and the hierarchy problem, remains a key prospect of the physics programme in the HL-LHC [27]. The latest constraints (exclusion limits) placed by the LHC data are such that new physics might appear as rare phenomena even at 14 TeV, and therefore a detailed study of their properties demands very large integrated luminosities [26]. While some BSM models could be confirmed, many could be fully excluded. Additionally, the HL-LHC programme includes the continued exploration of the electroweak symmetry breaking, as well as the necessary measurements to improve the precision of theoretical predictions and reduce experimental and systematic errors, improving with it, the knowledge of the complete set of parameters of observables defining the SM, and motivating, as a whole, the upgrade project.

1.2 Motivation

The HL-LHC baseline operation has been designed to provide the experiments with maximal integrated luminosities and least impact on the detector performance or hardware degradation. Since the original proposal [28, 29], the HL-LHC machine parameters have constantly evolved. Simulations with the latest set of parameters not only allow to assess the accelerator performance in terms of the usual integrated luminosity, but to characterise in detail the corresponding event distributions from collisions at the the IPs. These updated descriptions are highly important for the experiments as they serve as input for realistic simulations of the expected detector efficiency on the reconstruction of recorded events under different configurations. In this context, the Experimental Data Quality working group was formed to evaluate the performance of the HL-LHC taking into account both the accelerator and experimental sides. From this synergy, and based on studies that have found that not only the pile-up has an impact on the detector efficiency but also its longitudinal distribution around the IP [30, 31], the effective pile-up density is proposed. This novel figure-of-merit, complementary to the integrated luminosity, allows to characterise the baseline and alternative scenarios in terms of the expected data quality at the detectors. Results can then be used to continuously refine the machine parameters, improving its overall performance and discovery capabilities.

1.3 Outline of the Thesis

The basic concepts of accelerator physics relevant for this work, such as beam motion around the synchrotron, bunch crabbing, and emittance evolution (including the effects of intrabeam scattering, synchrotron radiation, quantum equilibrium) are introduced in Chapter 2. The general definitions of luminosity and pile-up are then discussed, together with a model for beam intensity burn-off, a process that motivates the implementation of a levelling technique to maximise the integrated luminosity delivered by a machine fill. Other several useful parameters to describe the event distributions from collisions around an IP (luminous sizes and pile-up densities)are also included.

To perform realistic simulations for the wide range of settings of the different HL-LHC operational scenarios, new general formulae for the computation of luminosity and pile-up densities are derived in Chapter 3. In particular, formulae for q-Gaussian longitudinal distributions are motivated by the latest measurements of bunch profiles in the LHC [32, 33]. The effect of longitudinal beam offsets is also studied due to its direct impact on luminosity. Constituting the major theoretical contribution from this thesis, the novel concept of effective pile-up density –the newly-proposed figure of merit to asses the performance in terms of the expected detector efficiency–, is discussed in the same Chapter.

Chapter 4 extensively describes the Levelling program, a flexible simulation tool for the evolution of the optimum physics fill of the HL-LHC baseline and alternative scenarios. The main modules of Levelling are based on the theoretical background (known and new concepts) presented in the preceding chapters. Thanks to the inclusion of more refined formulae, machine performance can be better estimated with respect to previous works [29, 34].

Chapter 5 describes the major results of this work, a comprehensive characterisation of the HL-LHC baseline. The two first sections describe the latest general, beam, and optics parameters of the baseline operation with both the so-called standard and BCMS filling schemes [35, 36]. The evolution of each of these parameters, as well as other relevant quantities, is meticulously studied throughout their corresponding optimum fills. Results for both nominal and ultimate levelling operation are discussed in terms of the key figures of merit, the expected yearly integrated luminosity and effective pile-up density at the main IPs, and constitute the reference for comparisons with other operational scenarios. In order to provide an exhaustive characterisation of the HL-LHC baseline, results from a sensitivity study to each parameter are also reviewed. Additionally, two scenarios aiming at improving the current baseline performance via electromagnetic wires and adaptive crossing angle are simulated. The case of operation at an ultimate beam energy of 7.5 TeV is also explored as a potential upgrade of the HL-LHC project [37–39]. Prompted by the recent interest of the LHCb experiment [40], a series of operational scenarios for a high-luminosity operation of IP8 is investigated (including an assessment of their impact on the performance of the main IPs) in the last section.

The main alternative operational scenarios [29, 41, 42] aiming at improving the HL-LHC performance, reducing risks, or providing options for addressing possible limitations (such as electron-cloud formation) or changes of parameters, are examined in Chapter 6 under the same procedure than the baseline. The alternative scenarios treated in this work are a scenario with flat optics, with an 8b+4e filling scheme, with an additional 200 MHz RF system, without crab cavities, and with the so-called crab kissing. Special interest is given to the effect of the crabbing ratio, crab cavity noise, turn-around times, and cross-section for burn-off, for which similar sensitivity studies than the baseline are conducted for the alternative scenarios. The present results allow to better understand the capabilities and limitations of each alternative, and to optimise their parameters. For all scenarios considered in this work, characterisation of the luminous region for all scenarios is also conducted to serve as input for detector studies.

Increased bunch intensities, together with reduced beam-beam separation, yield to an increase of beam-beam effects. These effects, in turn, can directly impact on the machine performance or its protection system, deeming the implementation of correction schemes necessary. Different techniques have been proposed in the past, for example, the use of electron beam lenses [43–45] and current-carrying wires [46–49]; these approaches demand, however, new hardware in the interaction region (IR) around the IP, which might not be available. A new correction scheme acting simultaneously on both opposite-travelling beams using existing local common magnets in the IR is proposed in Chapter 7. A modified version of this procedure was used to derive a compensation of long-range beam-beam effects in the LHC, being successful tested in the machine measurements.

General conclusions derived from this Thesis are drawn in Chapter 8, together with particular conclusions for each analysed operational scenario (in view of the two key figures of merit, the yearly integrated luminosity and the newly-proposed effective pile-up density). The wide potential of the simulation tools developed for this work is also highlighted. Conclusions on the study of a new long-range beam-beam compensation technique are also presented.

Chapter 2

Theoretical background

In this Chapter, the basic concepts of beam dynamics relevant for this study are summarised, together with the definitions of the main beam and machine parameters. In particular, the geometry of bunch collisions and the concept of crab cavities are introduced. The formulae describing the emittance evolution with intrabeam scattering and synchrotron radiation are included. The general definitions of luminosity, pile-up, luminous region, and pile-up density, are also presented, as well as the notion of levelling and the considerations to estimate the integrated luminosity. These concepts, together with those in the following chapter, constitute the theoretical framework of the simulation tools described in Chapter 4.

2.1 Concepts of beam dynamics

2.1.1 Betatron motion

In order to describe the motion of a particle around a circular accelerator, let us assume the curvilinear coordinate system which follows the *design orbit* (Fig. 2.1) with origin at the *synchronous* particle. Due to the presence of bending dipoles (characterised by the local curvature radius ρ) and the strong focusing due to alternating gradient quadrupoles, particles perform *betatron* oscillations in the transverse coordinates x and y as they travel around the machine, described by [50]

$$u(s) = A_u \sqrt{\beta_u(s)} \cos[\mu_u(s) + \mu_{u_0}]\,, \qquad u = x, y, \tag{2.1}$$

where A_u and μ_{u_0} are integration constants, β_u is the betatron function, and μ_u is the phase advance in the coordinate u given by

$$\mu_u(s) = \int_{s_0}^{s_0+s} \frac{\mathrm{d}\tau}{\beta_u(\tau)}\,. \tag{2.2}$$

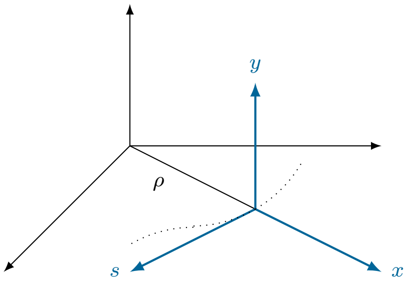

Figure 2.1. Coordinate reference system.

From the equation above, the number of oscillations per turn, known as the *tune*, can be computed as follows:

$$Q_u \equiv \frac{1}{2\pi}\mu_u(C) = \frac{1}{2\pi}\oint \frac{\mathrm{d}s}{\beta_u(s)}\,, \tag{2.3}$$

where C is the ring circumference.

In the absence of damping, particles describe ellipses in the phase space u–u' (where $u' = \mathrm{d}u\,/\,\mathrm{d}s$) as they move around the machine. The Courant-Snyder invariant A_u, related to area contained within the ellipse according to $A_u = \text{area}/\pi$, is a constant of motion according to Liouville's theorem [51, 52]. For an ensemble of particles, the *emittance* ϵ_u is defined as the average of the invariants of all single particles [3, 53]. In particular, for a bunch with a Gaussian transverse density profile the *beam size* and *beam divergence* are related with the transverse emittance by

$$\sigma_u \equiv \sqrt{\langle u^2\rangle} = \sqrt{\epsilon_u\beta_u} \qquad \text{and} \qquad \sigma_{u'} \equiv \sqrt{\langle u'^2\rangle} = \sqrt{\epsilon_u\gamma_{u'}}\,, \tag{2.4}$$

respectively, where $\gamma_u(s) \equiv [1+\alpha_u(s)^2]/\beta_u(s)$ and $\alpha_u(s) \equiv -\frac{1}{2}\beta'_u(x)$ for $u = x, y$. In reality, emittance is not constant due to several effects such as beam radiation, quantum excitation, intrabeam scattering, etc. (Section 2.2). During adiabatic acceleration, nevertheless, the *normalised* emittance remains an invariant,

$$\epsilon_{u_\mathrm{n}} \equiv \beta_r\gamma_r\epsilon_u\,, \tag{2.5}$$

with β_r and γ_r the Lorentz relativistic factors.

Smaller beam sizes, achieved by reducing the betatron functions at the IP (denoted by β^*_u), are desirable in colliders as they increase the likelihood of collisions between the particles of the two bunches (a parameter related with the *luminosity*, a concept explained in greater detail in Section 3.1). However, in a low-β region –such an IP–, the betatron functions change rapidly with s according to $\beta_u(s) = \beta^*_u\left[1+(s/\beta^*_u)^2\right]$ (for $u = x, y$), see Fig. 2.2. This yields to a modulation of the transverse beam size known as the *hour-glass effect* [54],

$$\sigma_u(s) = \sigma^*_u\sqrt{1+(s/\beta^*_u)^2}\,, \tag{2.6}$$

with σ^*_u the magnitude of the beam size at the IP, which in turn can lead to a reduction of the luminosity. The hour-glass effect becomes relevant for $\beta^*_u \lesssim \sigma_s$ where σ_s is the bunch length.

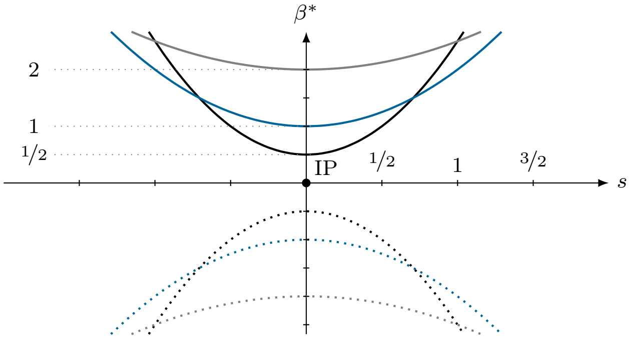

Figure 2.2. Hour-glass effect: Betatron functions around an IP (at $s = 0$) for $\beta^* = \frac{1}{2}$ (black), 1 (blue), and 2 (gray); their negative counterparts (dotted) are plotted to show the hour-glass shape. Bunch length: $\sigma_s = 1$.

A particle with a momentum deviation

$$\delta_p \equiv \frac{\Delta p}{p}\,, \tag{2.7}$$

with respect to the ideal momentum p of the design particle is bent differently by the dipole magnets of a planar ring, leading to a perturbation of the closed orbit in the horizontal coordinate. In this case, the trajectory is described by

$$x_{\delta_p}(s) = x(s) + D(s)\,\delta_p\,, \tag{2.8}$$

where $D(s)$ is the *dispersion* function and $x(s)$ the solution in Eq. (2.1). Thus, the length of the orbits of particles with different momenta after a full turn is different; this relative change is measured by the *momentum compaction factor* α_p, defined as

$$\frac{\Delta C}{C} \equiv \alpha_p \frac{\Delta p}{p}\,, \tag{2.9}$$

being C the ring circumference.

Regarding longitudinal motion, particles also describe oscillations around the ideal (synchronous) particle. In this case, however, oscillations are driven by the presence of a synchronised radio-frequency (RF) system for acceleration; the tune Q_s of the synchrotron oscillations, unlike the transverse tunes, is much smaller than the particle revolution frequency f_{rev} around the machine.

2.1.2 Crab cavities

In order to describe the collision of two bunches travelling in opposite directions at the IP, let us assume the 4-dimensional global reference system (x, y, s, ct) with origin at the point where the centroids of the bunches meet at $(x = 0, y = 0, s = 0, ct = 0)$.[1] In general, bunch pairs do not collide head-on, but with a crossing angle θ. The plane formed by the longitudinal coordinate s and the corresponding transverse coordinate where the crossing angle lays defines the *crossing* plane $\times$, while the remaining transverse coordinate defines, jointly with s, the *parallel separation* plane $\parallel$.

---

[1] The variable ct is used instead of the time t, as it simplifies the units of the four coordinates (x, y, s, and ct) to units of length.

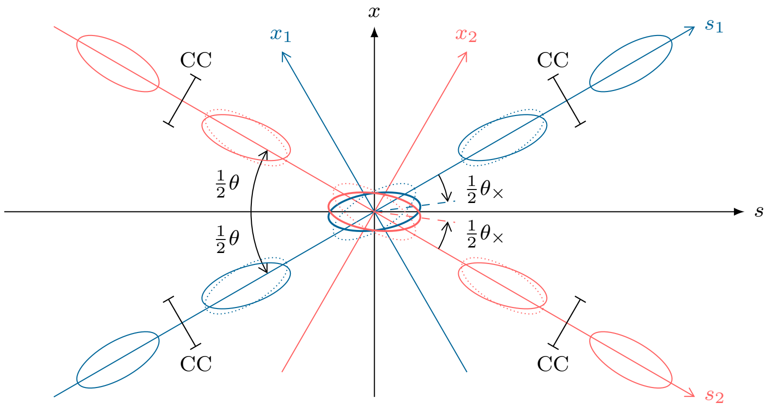

(a) Crab crossing in the crossing (horizontal) plane.

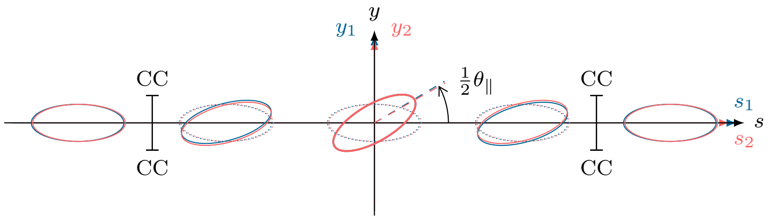

(b) Crab kissing in the parallel separation (vertical) plane.

Figure 2.3. Scheme of a bunch collision with simultaneous **(a)** crab crossing in the crossing plane (the horizontal plane, $\times = x$) and **(b)** crab kissing in the parallel separation plane (the vertical plane $\| = y$).

Let us assume the collision of a bunch pair at an IP with *horizontal crossing*, that is, the crossing and parallel separation planes are the x–s and y–s planes, respectively (see Fig. 2.3); in this case, $\beta_{\times,\|} = \beta_{x,y}$, and $\sigma_{\times,\|} = \sigma_{x,y}$. For *vertical crossing*, the inverse situation occurs. The presence of a crossing angle in the collision reduces the bunch overlapping, thus decreasing the luminosity. Crab cavities (CCs) are RF cavities that counteract the reduction of luminosity by exerting kicks in opposite directions to the particle bunches of each beam before the IP to compensate the crossing angle [55, 56]. The total RF voltage needed by a local CC of angular frequency ω_{CC} to rotate a bunch by an angle θ_{CC} in the crossing plane at the IP is [57]

$$V = \frac{cE\tan(\theta_{\mathrm{CC}}/2)}{q\omega_{\mathrm{CC}}\sqrt{\beta^*_\times \beta_{\mathrm{CC}}}\sin\mu_{\mathrm{CC}}}\,, \tag{2.10}$$

where E is the particle energy, q the particle charge, and μ_{CC} is the phase advance between the IP and the location of the CC (where the betatron function is β_{CC}). To minimise the voltage, crab cavities are usually located at positions with $\mu_{\mathrm{CC}} \approx \pi/2$. Depending on the available RF cavity voltage, the ideal head-on collision can be restored, that is, the *crab crossing angle* (or simply crabbing angle) θ_{CC} is equal to the crossing angle; $\theta_{\mathrm{CC}}/\theta$ is thus the *fraction* or *ratio* of compensated crossing angle. After the IP, a second set of CCs return the bunches of each beam to their original

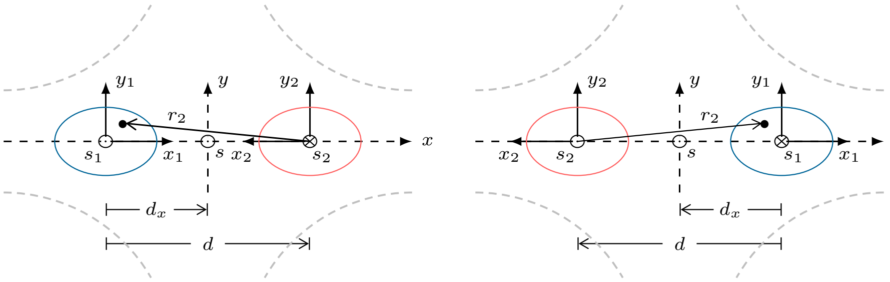

(a) Before (left of) the IP

(b) After (right of) the IP

Figure 2.4. Reference system for the beam-beam interactions: B1 (B2), in blue (red), travels clockwise (counterclockwise) around the machine –outwards (inwards) in the figure–, with the origin of the reference system x_1–y_1 (x_2–y_2) located at its centre. The dashed line represents an arbitrary magnet common to B1 and B2, centred at the origin of the x–y reference system. Both the situations **(a)** before and **(b)** after the IP are shown.

orientation, which then continue their travel around the ring. Rotation of the bunch in the parallel separation plane by means of crab cavity kicks is known as *crab kissing* (CK), and θ_{CK} is the crab kissing angle (see Fig. 2.3b).

2.1.3 Beam-beam effects

When the bunches of two beams of a particle collider come into proximity, they interact electromagnetically, giving rise to a series of *beam-beam* (BB) *effects* [58], such as tune shift and tune spread, β-beating, among others. Assuming equal Gaussian particle distributions in both transverse dimensions, the beam-beam kick experienced by a particle (charge q and mass m) of a bunch in beam 1 (B1) travelling in the opposite direction of a bunch in beam 2 (B2) –see Fig. 2.4– depends only on the radial distance r between the particle and the centre of the bunch. In the coordinate system of B2, the kick on the transverse momenta (or, equivalently, transverse angles) are given by [59]

$$\begin{Bmatrix} \Delta x_2' \\ \Delta y_2' \end{Bmatrix} = +\frac{2Nr_p}{\gamma_r}\frac{1}{r_2^2}\begin{Bmatrix} x_2 \\ y_2 \end{Bmatrix}\left[1-\exp\left(-\frac{r_2^2}{2\sigma^2}\right)\right] , \tag{2.11}$$

where $r_2^2 = x_2^2 + y_2^2$, N is the bunch population (assumed to be identical for both bunches), σ is the beam size (assumed to be identical in the horizontal and vertical coordinates for both round beams, as it is the case near/at the IP for the LHC and HL-LHC baseline), and r_p is the classical particle (proton) radius,

$$r_p = \frac{q^2}{4\pi\epsilon_0 mc^2} , \tag{2.12}$$

with c the speed of light and ϵ_0 the vacuum permittivity.

Beam-beam interactions can be *head-on* (BBHO) –those occurring at the IP–, or *long-range* (BBLR) –those taking place along the IR where the multi-bunch beams, travelling in opposite directions, share a common vacuum beam pipe. The crossing angle can be expressed in terms of the *beam-beam long-range separation* d_{BBLR} [60],

$$\theta = d_{\mathrm{BBLR}}\sigma_{\times'} , \tag{2.13}$$

with $\sigma_{\times',\parallel'}$ the beam divergence at the IP given by Eq. (2.4).

Depending on their magnitude, beam-beam effects can directly impact machine protection aspect or limit the machine performance due to the reduction of the beam lifetime [61]. In the case of the (HL-)LHC, for example, beam-beam effects can also yield to luminosity imbalance between the experiments, possibly making the implementation of a correction scheme mandatory. For small amplitudes, linearisation of Eq. (2.11) around the origin leads to the well-known definition of the *beam-beam parameter* [62]

$$\xi_{\times,\parallel} \equiv \frac{r_p N \beta_{\times,\parallel}}{2\pi\gamma_r \sigma_{\times,\parallel} g_{\times,\parallel}(\sigma_{\times,\parallel} g_{\times,\parallel} + \sigma_{\parallel,\times} g_{\parallel,\times})}\,, \tag{2.14}$$

where $g_{\times,\parallel}$ is a geometric factor (a function of the crossing and crabbing angles); it measures the induced deviation of the number of oscillations in the corresponding plane with respect to the unperturbed tune, Eq. (2.3), or *tune shift.* Assuming equal emittances ϵ_{n} in the crossing and parallel separation planes and round beams, the equation above reduces, in the case of a head-on collision, to $\xi = (r_p N)/(4\pi\epsilon_{\mathrm{n}})$ for both planes.

The β-beating measures the relative deviation of the betatron function $\beta_u(s)$ in a given transverse coordinate u with respect to the ideal $\beta_{u_0}(s)$. The β-beating due to a small quadrupole error at $s = s_i$ (such as a head-on collision at small amplitude) can be derived analytically and it is given by [63]

$$\begin{aligned} \frac{\Delta\beta_u}{\beta_{u_0}}(s) &\equiv \frac{\beta_u(s) - \beta_{u_0}(s)}{\beta_{u_0}(s)} \\ &= \frac{2\pi\xi_u}{\sin(2\pi\, Q_{u_0})} \cos\left[2\left|\mu_{u_0}(s) - \mu_{u_0}(s_i)\right| - \, 2\pi\, Q_{u_0}\right]\,, \quad u = x, y\,, \end{aligned} \tag{2.15}$$

with μ_{u_0} and Q_{u_0} the unperturbed phase advance and tune, respectively.

Beam-beam effects are studied in more detail in Chapter 7, where a scheme for the BBLR compensation in the HL-LHC using local corrector magnets is also proposed.

2.2 Emittance evolution

After being injected into a collider ring, particle beams typically circulate around the machine for several hours, during which they experience several effects that degrade their quality. The evolution of beam emittances is of special interest, in particular, due to their direct influence on luminosity via the beam sizes at the IPs. Synchrotron radiation (SR), quantum excitation, and *intrabeam scattering* (IBS) are the main drivers of the emittance evolution. In the following subsections, a brief description of each of these effects is given, as they are implemented in the simulations of the different HL-LHC operation scenarios presented in Chapters 5 and 6.

2.2.1 Synchrotron radiation and equilibrium emittances

Synchrotron radiation from accelerated charges has a large impact on particle motion in accelerators at ultra-relativistic energies. The non-conservative nature of the synchrotron radiation implies that the conditions of the Liouville's theorem are not met, yielding to reduction of 6-dimensional volume in phase space $(x, x', y', y', s, \delta_p)$ of the beam.

Table 2.1. Radiation integrals.

I_n	$D_x \neq 0,\, D_y = 0$	Iso-magnetic ring
I_1	$\equiv \oint \frac{D_x}{\rho}\,\mathrm{d}s$	$= 2\pi\langle D_x\rangle$
I_2	$\equiv \oint \frac{1}{\rho^2}\,\mathrm{d}s$	$= \frac{2\pi}{\rho}$
I_3	$\equiv \oint \frac{1}{\lvert\rho^3\rvert}\,\mathrm{d}s$	$= \frac{2\pi}{\rho^2}$
I_4	$\equiv \oint \frac{D_x}{\rho}\left(\frac{1}{\rho^2} + \frac{2k}{\rho}\right)\mathrm{d}s$	$= \frac{\alpha_p C}{\rho^2}$
I_5	$\equiv \oint \frac{\mathcal{H}_x}{\rho^3}\,\mathrm{d}s$	$= \frac{2\pi}{\rho^2}\frac{\langle D_x\rangle^2}{\langle\beta_x\rangle}$

Assuming a charged particle q with total energy E at a speed $\beta_r c$, the instantaneous radiated power due to transverse deflection by a magnetic field B is [64]

$$P_\gamma = \frac{q^2c^3}{2\pi\beta_r^2}C_\gamma E^2B^2 = \frac{cC_\gamma}{2\pi}\frac{E^4}{\rho^2}\,, \tag{2.16}$$

where ρ is the bending radius and

$$C_\gamma \equiv \frac{4\pi}{3}\frac{r_p}{(mc^2)^3}\,. \tag{2.17}$$

The energy loss over a full turn in the form of synchrotron radiation is

$$E_{\mathrm{SR}} = \oint \frac{P_\gamma}{c}\,\mathrm{d}s = \frac{C_\gamma E^4}{\rho}\,, \tag{2.18}$$

assuming that all dipoles in the machine have identical curvature radius.

Due to the energy loss in the form of synchrotron radiation, the amplitude of both betatron and synchrotron oscillation are damped like $A_w = A_{w_0}\exp(-t/\tau_{w\mathrm{SR}})$, with *radiation damping times* given by

$$\tau_{w\mathrm{SR}} = \frac{\tau_0}{J_w}, \qquad w = x, y, s\,, \tag{2.19}$$

with $\tau_0 \equiv (2Et_{\mathrm{rev}})/E_{\mathrm{SR}}$ and t_{rev} the revolution period; J_w are the damping partition numbers which, in the case of a planar ring (that is, no vertical bendings and no vertical dispersion), can be expressed in terms of the radiation integrals I_2 and I_4 as follow:

$$J_x = 1 - \frac{I_4}{I_2}, \quad J_y = 1, \qquad \text{and} \quad J_s = 2 + \frac{I_4}{I_2}\,. \tag{2.20}$$

The radiation integrals for a planar ring are defined in Table 2.1, where the last column corresponds to the simplified case where all dipoles have the same bending radius (iso-magnetic ring) [65]. In the table, D_x is the horizontal dispersion function, k is the normalised quadrupolar gradient of the bending magnets ($k = \frac{1}{B\rho}\frac{\partial B_y}{\partial x}$), and

$\mathcal{H}_x = \beta_x {D'_x}^2 + 2\alpha_x D_x D'_x + \gamma_x D_x^2$ with α_x, β_x, γ_x the horizontal Twiss functions, and $\langle\cdot\rangle$ denotes the average value over the dipoles.

The process of quantum excitation yields the emittance to an equilibrium state. The radiation integrals are also useful to express the *equilibrium emittances*, which are reached when the average quantum excitation rate equals the damping rate. For the horizontal and vertical coordinates, their corresponding equilibrium emittances are given by [66]

$$\epsilon_{x_0} = C_q \gamma_r^2 \frac{I_5}{J_x I_2} \qquad \text{and} \qquad \epsilon_{y_0} = \frac{13}{55}\frac{C_q}{J_y I_2}\oint \frac{\beta_y}{|\rho^3|}\,\mathrm{d}s\,, \tag{2.21}$$

respectively, where the C_q is the quantum excitation constant defined as

$$C_q \equiv \frac{55}{32\sqrt{3}}\frac{\hbar c}{mc^2}\,, \tag{2.22}$$

being $\hbar$ the reduced Planck constant.

Thus, the evolution of the transverse emittance taking into account radiation damping and quantum excitation can be written as

$$\epsilon_u(t) = \epsilon_u(0)\exp\left(-\frac{2t}{\tau_{u_{\mathrm{SR}}}}\right) + \epsilon_{u_0}\left[1 - \exp\left(-\frac{2t}{\tau_{u_{\mathrm{SR}}}}\right)\right]\,, \qquad u = x, y\,, \tag{2.23}$$

where $\epsilon_u(0)$ is the emittance at time $t = 0$, and ϵ_{u_0} is the equilibrium emittance.

In the s–δ_E plane (the plane formed by the longitudinal coordinate and the energy deviation), it is possible to define an analogous *longitudinal* emittance[2] ϵ_s in terms of the bunch length $\sigma_s \equiv \sqrt{\langle s^2\rangle}$ and the RMS energy spread $\sigma_{\delta_E} \equiv \sqrt{\langle \delta_E^2\rangle}$:

$$\epsilon_s \equiv \sigma_s \sigma_{\delta_E}\,, \tag{2.24}$$

with units of [m]. Furthermore, following a similar analysis than that applied for for the transverse coordinates, and doting that the synchrotron oscillations are slower than the revolution frequency, the following expressions for the natural energy spread $\sigma_{\delta_{E0}}$ and natural bunch length σ_{s_0} can be derived [50]

$$\sigma_{\delta_{E0}} = \sqrt{C_q \gamma_r^2 \frac{I_3}{J_s I_2}} \qquad \text{and} \qquad \sigma_{s_0} = \frac{c\,\eta}{\omega_s}\sigma_{\delta_{E0}}\,, \tag{2.25}$$

where η is the *phase slip factor*,

$$\eta = \alpha_p + \frac{1}{\gamma^2}\,, \tag{2.26}$$

---

[2] Note that the momentum deviation $\delta_p \equiv \Delta p/p$ is related with the energy deviation $\delta_E \equiv \Delta E/E$ by $\delta_p = \delta_E/\beta_r^2$ and, consequently, the momentum spread and energy spread are related via $\sigma_{\delta_p} \equiv \sqrt{\langle\delta_p^2\rangle} = \sigma_{\delta_E}/\beta^2$. Moreover, there are several definitions for the longitudinal emittance; it can also be defined as $\epsilon_s \equiv \pi\sigma_s\sigma_{\delta_p} p/(\beta c)$ with units of [eV s] or, in terms of the RMS energy, as $\epsilon_s \equiv \sigma_s \sigma_E/\beta^2$. At CERN, it is customary to define the longitudinal emittance in terms of a multiple of the *bunch duration* σ_t (the bunch length expressed in time units of time, $\sigma_t = \sigma_s/c$) [3, 53]:

$$\epsilon \equiv 4\pi\sigma_t\sigma_{\Delta E} = 4\pi\sigma_t\sigma_{\delta_E}E\,.$$

with α_p the *momentum compaction factor*, $\omega_s = 2\pi f_{\rm rev} Q_s$ the longitudinal angular frequency, and Q_s the synchrotron tune. Thus, in the presence of synchrotron radiation and quantum excitation, the longitudinal emittance evolves according to

$$\epsilon_s(t) = \epsilon_s(0) \exp\left(-\frac{2t}{\tau_s}\right) + \epsilon_{s_0}\left[1 - \exp\left(-\frac{2t}{\tau_s}\right)\right] , \tag{2.27}$$

where $\epsilon_{s_0} \equiv \sigma_{s_0}\sigma_{\delta_{E0}}$ is the natural longitudinal emittance.

2.2.2 Intrabeam scattering

The effect of intrabeam scattering (IBS) [67] due to multiple Coulomb small-angle scattering, leads to bunch diffusion. This in turns yields to a change on the beam emittance and the beam dimensions which, ultimately, has an impact on the machine performance. There are different approaches, each with their corresponding approximations, for the computation of the probability of particle scattering, such as the classical Rutherford cross-section and models with quantum considerations. The basic theory on IBS –a classical model– was developed by Piwinksi [68] and extended by Bjorken and Mtingwa [69]; approximations for the case of high energy particles were also developed. The IBS theory was later extended to include (vertical) dispersion and transverse betatron coupling. The latest models allow the computation of the emittance growth times via numerical integration of complicated algebraic expressions averaged over the machine lattice. These models are currently implemented in software for accelerator design such as MAD-X [70].

The emittance growth times in the horizontal, vertical, and longitudinal coordinates ($w = x, y, s$), can be expressed as [67]

$$\frac{1}{\tau_{w_{\rm IBS}}} = \frac{N\pi^2 r_p^2 c\,(\log)}{\gamma_r \Gamma}\left\langle \Delta_w \int_0^\infty \frac{{\rm d}\lambda\ \lambda^{1/2}(a_w\lambda + b_w)}{(\lambda^3 + a\lambda^2 + b\lambda + c)^{3/2}} \right\rangle , \tag{2.28}$$

where N is the bunch population, $\Gamma \equiv (2\pi)^3 \cdot (\beta_r\gamma_r)^3 \epsilon_x\epsilon_y\sigma_s\sigma_{\delta_p}$ is the 6-dimensional invariant phase space volume of the bunch (by a factor of $\sqrt{2}$), (log) is the Coulomb logarithm,[3] and $\langle\cdot\rangle$ denotes an average over the lattice period (the full ring). The term Δ_w depends on the coordinate w as follows:

$$\Delta_x = \frac{\gamma_r^2}{\beta_x} H_x, \qquad \Delta_y = \frac{\gamma_r^2}{\beta_y} H_y, \qquad \text{and} \qquad \Delta_s = \frac{\gamma_r^2}{\sigma_{\delta_p}^2} . \tag{2.29}$$

The eight coefficients a, b, a_w, b_w ($w = x, y, s$) are functions of the lattice optics parameters that depend on the model and/or approximations that are applied; the coefficients implemented in MAD-X, in particular, can be found in Ref. [71]. Finally, the contribution to the emittance growth due to IBS can written as

$$\epsilon_{w_{\rm IBS}}(t) = \epsilon_w(0) \exp\left(\frac{t}{\tau_{w_{\rm IBS}}}\right) . \tag{2.30}$$

---

[3] The Coulomb logarithm is defined as (log) $\equiv \ln(r_{\rm max}/r_{\rm min})$, where $r_{\rm max}$ is the smaller between the RMS beam size σ_x and the Debye length, and $r_{\rm min}$ is the larger between the classical distance of the closest approach and the quantum mechanical diffraction limit from the nuclear radius. [67]

Other effects, such as crab cavity noise [72, 73], can have an impact on the emittance evolution. Their contribution can be modelled in a similar way to the effects described above,

$$\epsilon_{u_{\rm CC}}(t) = \epsilon_u(0)\exp\left(\frac{t}{\tau_{u_{\rm CC}}}\right)\,, \qquad u = x, y\,, \tag{2.31}$$

with $\tau_{u_{\rm CC}}$ the growth time due to the crab cavity, and $\epsilon_u(0)$ the emittance at the start of the fill. The impact of the expected crab cavity noise in the transverse planes for the HL-LHC is described in more detail in Section. 5.3.2.4.

2.3 Luminosity

2.3.1 Instantaneous luminosity

Let us consider n_b pairs of bunches, each with $N_{1,2}$ particles, colliding at a frequency $f_{\rm rev}$ (the revolution frequency around the machine). The instantaneous luminosity at the IP is defined by the general formula [54]

$$\mathcal{L} = f_{\rm rev} n_b N_1 N_2 K \int\limits_{-\infty}^{\infty}\int\limits_{-\infty}^{\infty}\int\limits_{-\infty}^{\infty}\int\limits_{-\infty}^{\infty} \varrho_1(x,y,s,ct)\varrho_2(x,y,s,ct)\,{\rm d}x\,{\rm d}y\,{\rm d}s\,{\rm d}(ct)\,, \tag{2.32}$$

where $\varrho_{1,2}$ are the particle density distributions of the bunches in beam 1 and 2, respectively, and K is a kinematic factor that comes from the fact that the bunches are moving against each other [74]:

$$K = \sqrt{(\vec{v}_1 - \vec{v}_2)^2 - \left(\frac{\vec{v}_1 \times \vec{v}_2}{c}\right)^2}\,. \tag{2.33}$$

If the bunches travel at nearly the speed of light, $|\vec{v}_1| = |\vec{v}_2| = c$, and the kinematic factor K is equal to $2\cos^2\frac{\theta}{2}$. The luminosity is usually expressed in units of $[{\rm cm}^{-2}\,{\rm s}^{-1}]$.

Similarly to Section 2.1, let us consider the crossing ($\times$) and the parallel separation ($\|$) planes to be the horizontal (x) and vertical (y) planes, respectively. Let us also assume the presence of crabbing in both the horizontal and vertical planes, that is, crab crossing and crab kissing, respectively. While the crab crossing allows to compensate, at least partially, the crossing angle, restoring a head-on collision, the crab kissing allows to regulate the pile-up density (Section 2.4) of the bunch crossing. The transformation of coordinates between the reference system of each bunch and the frame (x, y, s, ct) at the IP is [75]

$$\begin{aligned}
x_{1,2} &= x\cos\frac{\theta}{2} \mp s\sin\frac{\theta}{2} \pm \frac{1}{k_x}\sin\{k_x[s \mp (ct + ct_{x_{1,2}})]\}\sin\frac{\theta_x}{2}\,,\\
y_{1,2} &= y + \frac{1}{k_y}\sin\{k_y[s \mp (ct + ct_{y_{1,2}})]\}\sin\frac{\theta_y}{2}\\
s_{1,2} &= s\cos\frac{\theta}{2} \pm x\sin\frac{\theta}{2}\,, \qquad \text{and}\\
ct_{1,2} &= ct\,,
\end{aligned} \tag{2.34}$$

being θ_x and θ_y the crab crossing angle and crab kissing angle, respectively. As the bunches of each beam travel across the CCs, the RF transverse kicks on the particles' trajectories (in the corresponding transverse plane) are exerted, in general, with a time offset $t_{x,y_{1,2}}$. Each of the CC pairs for each beam and plane are assumed to be equal and characterised by their wave numbers

$$k_{x,y} = \frac{\omega_{x,y}}{c} = 2\pi f_{x,y}\ , \tag{2.35}$$

where $f_{x,y}$ and $\omega_{x,y}$ are the frequency and angular frequency, respectively. Each CC pair is also assumed to be synchronised, that is, the time offset of each pair is the same, effectively restoring the bunch original orientation after it exists the interaction region. Assuming a small crossing angle[4]

$$s\cos\frac{\theta}{2} \gg x\sin\frac{\theta}{2}\ , \tag{2.36}$$

a further simplified transformation of the longitudinal coordinates is got, namely,

$$s_{1,2} = s\cos\frac{\theta}{2}\ , \tag{2.37}$$

decoupling, in this way, the transformation of the longitudinal coordinate from the transverse coordinates. Then, it is possible to perform the integrals on the transverse coordinates separately, and to be left with an integrand only dependent on the product of the longitudinal distributions.

Let us also assume separable distributions for each coordinate, equal for both beams,

$$\varrho_{1,2}(x,y,s,ct) = \varrho_x(x_{1,2})\varrho_y(y_{1,2})\varrho_s(s_{1,2},ct_{1,2})\ , \tag{2.38}$$

Due to the bunches moving in opposite direction, the longitudinal densities can rewritten as follows:

$$\varrho_s(s_{1,2},ct) = \varrho_s(s_{1,2} \mp (ct + ct_{0_{1,2}}))\ . \tag{2.39}$$

Here the time offsets $t_{0_{1,2}}$ represent the bunches travelling with a delay with respect to (or travelling ahead of) the ideal time in which the centroid of the bunches cross the lattice IP at $t = 0$ (Section 3.1), and they are different to $t_{x,y_{1,2}}$, the time-offset of the RF kicks exerted by the crab cavities. Finally, assuming equal particle populations in the bunches of both beams ($N = N_1 = N_2$), and Eq. (2.32) can be thus written as

$$\mathcal{L} = f_{\text{rev}} n_b N^2 K \int\limits_{-\infty}^{\infty}\int\limits_{-\infty}^{\infty}\int\limits_{-\infty}^{\infty}\int\limits_{-\infty}^{\infty} \varrho_x(x_1)\varrho_x(x_2)\varrho_y(y_1)\varrho_y(y_2) \cdot \varrho_s[s_1 - (ct + ct_{0_1})]\varrho_s[s_2 + (ct + ct_{0_2})]\,\mathrm{d}x\,\mathrm{d}y\,\mathrm{d}s\,\mathrm{d}(ct)\ . \tag{2.40}$$

For the transverse density profiles, a Gaussian distribution is a common description

$$\varrho_u(u_{1,2}) = \frac{1}{\sqrt{2\pi}\sigma_{u_{1,2}}}\exp\left(-\frac{u_{1,2}^2}{2\sigma_{u_{1,2}}^2}\right), \qquad u_{1,2} = x_{1,2}, y_{1,2}\ . \tag{2.41}$$

After lengthy algebra, the products of the horizontal and vertical densities read

$$\varrho_x(x_1)\varrho_x(x_2) = \frac{1}{2\pi\sigma_x^2} f_x(x,s,ct), \qquad \text{and} \tag{2.42}$$

$$\varrho_y(y_1)\varrho_y(y_2) = \frac{1}{2\pi\sigma_y^2} f_y(y,s,ct), \tag{2.43}$$

---

[4] The validity of this approximation is even more evident when x and s assume the value of the horizontal and longitudinal bunch sizes, respectively, $(\cos^2\frac{\theta}{2})/\sigma_x^2 \gg (\sin^2\frac{\theta}{2})/\sigma_s^2$ since, in general, $\sigma_x \gg \sigma_s$ by several orders of magnitude.

where

$$\begin{aligned} f_x(x,s,ct) = \exp\Bigg[& -x^2\left(\frac{\cos^2\frac{\theta}{2}}{\sigma_x^2}\right) \\ & + x\Bigg\{\frac{2}{k_x\sigma_x^2}\cos\frac{\theta}{2}\cos\left[k_x\left(s+\frac{ct_x^-}{2}\right)\right]\sin\left[k_x\left(ct+\frac{ct_x^+}{2}\right)\right]\sin\frac{\theta_x}{2}\Bigg\} \\ & - \Bigg\{ + \frac{1}{4k_x^2\sigma_x^2}\Big\{2-\cos\{2k_x[s-(ct+ct_{x_1})]\} \\ & \qquad\qquad - \cos\{2k_x[s+(ct+ct_{x_2})]\}\Big\}\sin^2\frac{\theta_x}{2} \\ & \quad - \frac{2s}{k_x\sigma_x^2}\sin\frac{\theta}{2}\sin\left[k_x\left(s+\frac{ct_x^-}{2}\right)\right]\cos\left[k_x\left(ct+\frac{ct_x^+}{2}\right)\right]\sin\frac{\theta_x}{2} \\ & \quad + \frac{s^2}{\sigma_x^2}\sin^2\frac{\theta}{2}\Bigg\}\Bigg], \qquad \text{and} \end{aligned} \tag{2.44}$$

$$\begin{aligned} f_y(y,s,ct) = \exp\Bigg[& -y^2\left(\frac{1}{\sigma_y^2}\right) \\ & - y\Bigg\{\frac{2}{k_y\sigma_y^2}\sin\left[k_y\left(s+\frac{ct_y^-}{2}\right)\right]\cos\left[k_y\left(ct+\frac{ct_y^+}{2}\right)\right]\sin\frac{\theta_y}{2}\Bigg\} \\ & - \Bigg\{ + \frac{1}{4k_y^2\sigma_y^2}\Big\{2-\cos\{2k_y[s-(ct+ct_{y_1})]\} \\ & \qquad\qquad - \cos\{2k_y[s+(ct+ct_{y_2})]\}\Big\}\sin^2\frac{\theta_y}{2}\Bigg\}\Bigg]. \end{aligned} \tag{2.45}$$

with $ct_u^{\pm} = ct_{u_2} \pm ct_{u_1}$ for $u = x, y$. After integration of these expressions, and performing further simplifications using Eq. (2.36) along the process, the formula for the instantaneous luminosity in the presence of the hour-glass effect can be written as as

$$\mathcal{L} = 2\mathcal{L}_0\cos\frac{\theta}{2}\int_{-\infty}^{\infty}\int_{-\infty}^{\infty} g_{s,ct}(s,ct)\,\mathrm{d}s\,\mathrm{d}(ct)\,, \tag{2.46}$$

where the coefficient $\mathcal{L}_0$, given by

$$\mathcal{L}_0 \equiv \frac{f_{\mathrm{rev}} n_b N^2}{4\pi\sigma_x^*\sigma_y^*}\,, \tag{2.47}$$

is the instantaneous luminosity of a head-on collision (in the absence of hour-glass effect) [54]. The integrand

$$g_{s,ct}(s,ct) \equiv F_{x,y}(s,ct)\,\varrho_s[s_1-(ct+ct_{0_1})]\varrho_s[s_2+(ct+ct_{0_2})]\,, \tag{2.48}$$

is the product of the longitudinal densities of the bunches of the two beams, times the contribution of the densities on the transverse coordinates, given by the function,

$$\begin{aligned} F_{x,y}(s,ct) &\equiv \int_{-\infty}^{\infty}\int_{-\infty}^{\infty} f_x(x,s,ct) f_y(y,s,ct)\,\mathrm{d}x\,\mathrm{d}y \\ &= \frac{\exp\left[-\frac{\left\{\frac{1}{k_x}\sin\left[k_x\left(s+\frac{ct_x^-}{2}\right)\right]\cos\left[k_x\left(ct+\frac{ct_x^+}{2}\right)\right]\sin\frac{\theta_x}{2}-s\sin\frac{\theta}{2}\right\}^2}{\sigma_x^{*2}\left[1+\left(s/\beta_x^*\right)^2\right]}\right]}{\sqrt{1+(s/\beta_x^*)^2}} \\ &\quad\cdot\frac{\exp\left[-\frac{\left\{\frac{1}{k_y}\cos\left[k_y\left(s+\frac{ct_y^-}{2}\right)\right]\sin\left[k_y\left(ct+\frac{ct_y^+}{2}\right)\right]\sin\frac{\theta_y}{2}\right\}^2}{\sigma_y^{*2}\left[1+\left(s/\beta_y^*\right)^2\right]}\right]}{\sqrt{1+\left(s/\beta_y^*\right)^2}}\,. \end{aligned} \tag{2.49}$$

It is worth to remember that the assumption made in Eq. (2.37) allowed decoupling the transverse from the longitudinal coordinate transformations. The integrand $g_{s,ct}$, a function of s and ct, has to be evaluated numerically.

2.3.2 Burn-off and luminosity levelling

Particles are lost as result of the bunch collisions, yielding to a decrease of the beam intensity (*burn-off*). There are different models that aim to describe the observed luminosity decay due to burn-off [76, 77]. To derive the model for the present work, notice that luminosity is proportional to the product of the bunch populations ($N = N_1 = N_2$); the time[5] evolution of the luminosity at IP i can thus be written as

$$\mathcal{L}_i(t) = \mathcal{L}_{i_0}\frac{N^2(t)}{N_0^2}\,, \tag{2.50}$$

where $\mathcal{L}_{i_0} = \mathcal{L}_i(t_0)$ and $N_0 = N(t_0)$ for a given time t_0. The number of particles lost due to burn-off is given by $\sigma_{\text{b.o.}}\mathcal{L}_i(t)$, with $\sigma_{\text{b.o.}}$ the cross-section of the collision process. For a machine with more than one IP, the rate of bunch intensity burn-off due to luminosity is

$$r(t) \equiv -\frac{\mathrm{d}N(t)}{\mathrm{d}t} = \sum_i \frac{\sigma_{\text{b.o.}}\mathcal{L}_i(t)}{n_{b_i}}\,, \tag{2.51}$$

where n_{b_i} is the number of colliding bunch pairs at IP i. In the present HL-LHC simulations, a pessimistic total cross-section for burn-off of $\sigma_{\text{b.o.}} = 111\,\text{mb}$ is assumed [3, 77, 78].

Substituting the expression for $\mathcal{L}_i(t)$ on the equation above and solving for $N(t)$,

$$N(t) = \frac{N_0}{1+\frac{r_0}{N_0}t}\,, \tag{2.52}$$

where

$$r_0 \equiv \sum_i \frac{\sigma_{\text{b.o.}}\mathcal{L}_{i_0}}{n_{b_i}}\,. \tag{2.53}$$

---

[5] Note that t in these expressions refers to the time in a collider fill; the time in ct in the expressions for the computation of the instantaneous luminosity in the previous section is a coordinate within the bunch.

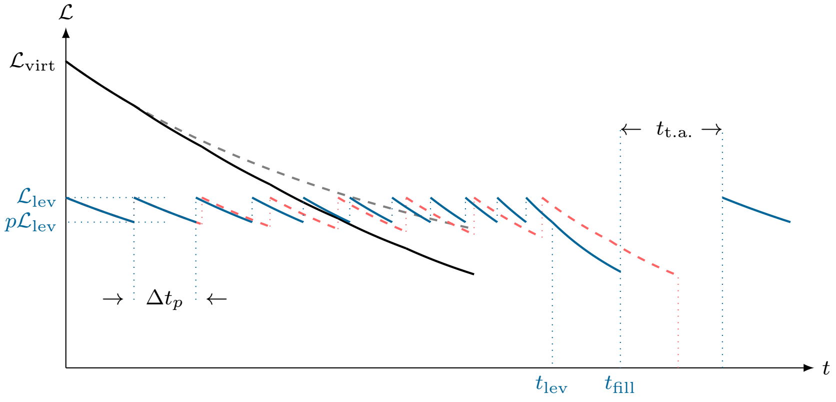

Figure 2.5. Luminosity levelling: in red, luminosity levelling at $\mathcal{L}_{\rm lev}$ with constant-length steps; in blue, levelling with constant luminosity threshold $p\mathcal{L}_{\rm lev}$; luminosity with natural decay (no levelling) from its *virtual* value $\mathcal{L}_{\rm virt}$ [6] according to Eq. (2.54) assuming constant emittance and beam population (in grey) or with re-evaluation of emittance and beam population at constant steps (in black). The levelling and fill duration, and the turn-around time, are denoted by $t_{\rm lev}$, $t_{\rm fill}$, and $t_{\rm t.a.}$, respectively.

Finally, the luminosity at a given IP i as a function of time is given by [77, 79, 80].

$$\mathcal{L}_i(t) = \frac{\mathcal{L}_{i_0}}{\left(1 + \frac{r_0}{N_0}t\right)^2} \,. \tag{2.54}$$

In addition to beam burn-off, the luminosity production is altered throughout the fill due to emittance blow-up. Operation with *levelling* aims at keeping the instantaneous luminosity (and, in consequence, the pile-up, see Section 2.4) within a given threshold of a given value –the levelled luminosity, $\mathcal{L}_{\rm lev}$– , according to detector capabilities.

In the HL-LHC baseline, two levelled luminosities at IP1 and IP5 –corresponding to the location of the ATLAS and CMS detectors, respectively– define the nominal and ultimate operation scenarios (Sections 5.1.1 and 5.1.2) [3]. Levelling can be performed via manipulation of a series of optics parameters. At the two main IPs, in particular, levelling is achieved via step-wise reduction of β^*, which ensures the desired beam size and crossing angles that provide the desired levelled luminosity. At IP8, on the other hand, $\mathcal{L}_{\rm lev} = 2 \times 10^{33}\,{\rm cm}^{-2}\,{\rm s}^{-1}$ is assumed to remain constant for the entire fill duration thanks to levelling with offset (parallel separation [81]).

Assuming the models of beam intensity and luminosity above, a new step (that is, reduction of β^* and the corresponding beam separation) has to be performed once the luminosity has naturally decayed from its initial levelled value of $\mathcal{L}(t_0) = \mathcal{L}_{\rm lev}$ at the beginning of the step ($t = t_0$) to a fraction p of it, given by

$$\mathcal{L}(t_0 + \Delta t_p) = p\mathcal{L}_{\rm lev} \,, \qquad \text{for } 0 < p < 1 \,, \tag{2.55}$$

after a time Δt_p given by

$$\Delta t_p = \frac{N_0}{r_0}\left(\frac{1}{\sqrt{p}} - 1\right) \,, \tag{2.56}$$

with N_0 and r_0 the bunch population and the rate of intensity burn-off, respectively, at time t_0; the transverse and longitudinal emittance are assumed to remain constant (its value is updated at the beginning of each new step) for the duration of the step. The levelling process to restore the luminosity by adjusting the optics settings is repeated until the minimum achievable values of β^* and separation are reached.

Note that, as the fill progresses and the bunch population decreases, the step length Δt_p shortens. Previous works assumed a levelling process with steps of constant duration; in this case, however, the value at which the luminosity has decayed by the end of each step is not constant, but decreases over the fill. Figure 2.5 shows the typical behaviour of levelling luminosity using steps with both fixed duration and with adaptive duration.

Levelling of other figures of merit is also possible; for example, levelling of the peak pile-up density is implemented in the CK scheme discussed in detail in Section 6.5. The evolution of typical fills for any HL-LHC scenario is simulated by a PYTHON routine, based on the original code implemented in Ref. [41], and that has been extended to provide more flexibility and control of the levelling settings. A detailed description of the simulation tools is presented in Chapter 4.

2.3.3 Integrated luminosity

The *integrated luminosity* over a fill is given by

$$\mathcal{L}_{\mathrm{int,fill}} = \int_0^{t_{\mathrm{fill}}} \mathcal{L}(t)\,\mathrm{d}t \ . \tag{2.57}$$

The fill duration t_{fill} is set to maximise the corresponding yearly integrated luminosity, that is, t_{fill} is the duration of the optimum fill.

Once a fill has reached its optimum duration, the burnt-off beams are dumped, and new beams with the original intensity are prepared and injected into the machine. The down time spent between the beam dump and the reaching of flat top energy at the start of collisions with the new beams is known as the *turn-around time* $t_{\mathrm{t.a.}}$. The *yearly integrated luminosity*, usually expressed in [fb^{-1}] is estimated from the extrapolation of the integrated luminosity of a fill [3]:

$$\mathcal{L}_{\mathrm{int}} = \eta\,\frac{t_{\mathrm{year}}}{t_{\mathrm{fill}} + t_{\mathrm{t.a.}}}\,\mathcal{L}_{\mathrm{int,fill}}\,, \tag{2.58}$$

where t_{year} the scheduled time for physics production within a year and η is the efficiency

$$\eta \equiv N_{\mathrm{fill}}\,\frac{t_{\mathrm{fill}} + t_{\mathrm{t.a.}}}{t_{\mathrm{year}}} \times 100\,\%\,, \tag{2.59}$$

with N_{fill} the number of successful fills of duration t_{fill}. The efficiency is related to another useful quantity, the machine availability A, defined as the time spent in physics (fills) divided by the total allocated calendar time, i.e. $A = N_{\mathrm{fill}}\,t_{\mathrm{fill}}/t_{\mathrm{year}}$ [77, 82, 83]. Thus, the yearly integrated luminosity can be written as a function of the availability: $\mathcal{L}_{\mathrm{int}} = A\,t_{\mathrm{year}}\,\mathcal{L}_{\mathrm{ave}}$, where $\mathcal{L}_{\mathrm{ave}}$ is the average instantaneous luminosity over a year. In the following chapters, the estimation of the yearly integrated performance of the HL-LHC baseline and main alternative operational scenarios is conducted and discussed.

2.4 Pile-up and pile-up density

The *pile-up* (PU) μ is defined as the average number of events per bunch crossing; as such, its magnitude is proportional to the instantaneous luminosity $\mathcal{L}(t)$ at time t:

$$\mu(t) = \frac{\sigma \mathcal{L}(t)}{f_{\text{rev}} n_b}\,, \tag{2.60}$$

being σ is the proton-proton inelastic cross-section, n_b is the number of colliding bunches, and f_{rev} is the revolution frequency. A precise and updated characterisation of the PU level of the different HL-LHC operational scenarios is highly relevant for the experiments: the ratio of the reconstructed and identified primary vertices of the events in a collision with respect to the number of simulated vertices depends on the PU and its distribution; its estimate constitutes a critical first step in most detector analyses [30, 31].

The PU can be derived from a 4-dimensional PU density as follows:

$$\mu(t) = \int\int\int\int \rho(x, y, s, ct; t)\, \mathrm{d}x\, \mathrm{d}y\, \mathrm{d}s\, \mathrm{d}(ct)\,, \tag{2.61}$$

where $\rho(x, y, s, t)$ describes the distribution of events in space and time during the collision of two bunches.[6] Then

$$\rho(x, y, s, ct; t) = \frac{\partial^4 \mu(t)}{\partial x\, \partial y\, \partial s\, \partial (ct)}\,. \tag{2.62}$$

The PU density along a single variable, or a set of two or more variables can also be defined. In the following subsection, the line and time PU densities (that is, the corresponding projections along s and $t = (ct)/c$) are discussed, since they are of major interest for the main IPs.

2.4.1 Line and time pile-up densities

The *line PU density*[7] $\rho_s(s; t)$, describes the local distribution of PU events along the longitudinal coordinate s (with the interaction point at $s = 0$), at a given time t during the fill,

$$\mu(t) = \int \rho_s(s; t)\, \mathrm{d}s\,; \tag{2.63}$$

it corresponds to the projection of the general PU density along s. The line PU density is of major interest, in particular, as the experimental tracking detectors are sensitive to this quantity.

Using the proportionality relation between the PU and the luminosity in Eq. (2.60) and the expression for the instantaneous luminosity in Eq. (2.46) in the equation above,

$$\rho_s(s; t) \equiv \frac{\partial \mu(t)}{\partial s} = \frac{2\sigma \mathcal{L}_0(t)}{f_{\text{rev}} n_b} \cos\frac{\theta(t)}{2} \int g_{s,ct}(s, ct; t)\, \mathrm{d}(ct)\,, \tag{2.64}$$

---

[6] As pointed out before, it is important to note that coordinate ct in ρ and its integral refers to the time it takes for a bunch pair to collide. The variable t has been included to make explicit the fact that the 4D-density changes its shape as the fill evolves (with the beam and optics parameters changing due to levelling, emittance growth, etc.

[7] When mentioned as simply *PU density*, it refers to the *line* PU density, as this quantity is of more interest than its time counterpart.

where $g_{s,ct}(s,ct) \equiv F_{x,y}(s,ct)\,\varrho_{s_1}(s,ct)\varrho_{s_2}(s,ct)$; the factor $F_{x,y}(s,ct)$ is given by Eq. (2.49) and the distributions $\varrho_{s_{1,2}}$ depend on the longitudinal bunch profile (Sections 3.1.1 to 3.1.3). Thus, the line PU density can be easily computed by numerically integrating the corresponding integrand over only the time coordinate; its units are [m^{-1}], understood as events/m.

Similarly, the time PU density $\rho_{ct}(ct;t)$ at time t represents the local distribution of events per bunch crossing around ct (with the interaction point at $ct = 0$):

$$\rho_{ct}(ct;t) \equiv \frac{\partial\mu(t)}{\partial(ct)} = \frac{2\sigma\mathcal{L}_0(t)}{f_{\mathrm{rev}}n_b}\cos\frac{\theta(t)}{2}\int g_{s,ct}(s,ct;t)\,\mathrm{d}s\,, \tag{2.65}$$

or in time units, $\rho_t = c\rho_{ct}$ gives the distribution in events/s^{-1}. In the case of the time PU density, the corresponding integrand describing the case of interest is integrated over only the longitudinal coordinate.

The *peak line (time) PU density* is the value of the line (time) PU density at its peak; in general, this peak occurs at $s = 0$ ($ct = 0$):

$$\hat{\rho}_v(t) = \rho_v(v = 0;t)\,, \qquad v = s, ct\,, \tag{2.66}$$

and its units are naturally the same as the line (time) PU density.

As mentioned earlier, projections of the 4D PU density in more than one coordinate can also be defined. In particular, the study of the 2D PU density in both s and ct is of interest, and its is given by

$$\rho_{s,ct}(s,ct;t) \equiv \frac{\partial\mu(t)}{\partial s} = \frac{2\sigma\mathcal{L}_0(t)}{f_{\mathrm{rev}}n_b}\cos\frac{\theta(t)}{2}g_{s,ct}(s,ct;t); \tag{2.67}$$

the event distribution $\rho_{s,ct}(s,ct;t)$ is typically expressed in units of [$\mathrm{m}^{-1}\,\mathrm{s}^{-1}$], after transforming ct into t. In this case, no integration is needed.

2.4.2 Transverse pile-up densities

Following the logic in the previous subsection, similar projections of the PU density can be made for the transverse coordinates, that is, $\mu(t) = \int \rho_u(u;t)\,\mathrm{d}u$ for $u = x, y$, or

$$\rho_u(u;t) = \frac{\partial\mu(t)}{\partial u} = \frac{\sigma}{f_{\mathrm{rev}}n_b}\frac{\partial\mathcal{L}(t)}{\partial u}, \qquad u = x, y. \tag{2.68}$$

In this case however, the integrand of the luminosity integral does not correspond to $F_{x,y}\,\varrho_{s_1}\varrho_{s_2}$ because the term $F_{x,y}$ comes from the integral over both x *and* y; thus, a step back has to be taken: the corresponding transverse coordinate has to remain not integrated, which yields to more complicated expressions for the full integrand. The result, however, can still be integrated numerically: in this case the integral is performed over s, ct, and the reminding transverse coordinate (either y or x, for the horizontal or vertical PU density, respectively).

A simplified case corresponds to the scenario of collision without crabbing. This is in fact the situation at IP8, where the transverse PU densities are of interest for a potential high-luminosity LHCb experiment [40] (Section 5.6) due to the larger beam sizes.

2.5 Luminous region and luminous time

Other related quantities of interest are the RMS luminous sizes [84], as they characterise the dimensions of the space-time region around the IP where the collisions take place. As in the case of the PU densities, the RMS luminous size can also be defined for one or more coordinates, mirroring the line and time PU densities. The RMS luminous sizes in s and ct:

$$\sigma_v^{\mathrm{lum}}(t) = \sqrt{\frac{1}{\mu(t)} \int v^2 \rho_v(v;t)\,\mathrm{d}v}\,, \qquad v = s, ct\,. \tag{2.69}$$

The factor $1/\mu(t)$ normalises the PU density at t to the total number of PU events at t. The RMS luminous size in s is commonly called the *RMS luminous region*. The *RMS luminous time* as given by the expression above must be divided by c to express this quantity in time units.

Finally, another useful quantity, namely, the peak luminous size in u is defined by

$$\hat{\sigma}_u^{\mathrm{lum}}(t) = \frac{1}{\mu(t)} \int \rho_{u,v}(u=0,v;t)\,\mathrm{d}v\,, \qquad u,v = s, ct, \text{ or } u,v = ct, s\,. \tag{2.70}$$

The peak luminous region (in s) and peak luminous time (in t) allows the easy computation of the corresponding peak PU densities since $\rho_u(u=0;t) = \int \rho_{u,v}(u=0,v;t)\,\mathrm{d}v$ and, after substitution of Eq. (2.66),

$$\hat{\rho}_v(t) = \mu(t)\,\hat{\sigma}_v^{\mathrm{lum}}(t)\,, \qquad v = s, ct\,. \tag{2.71}$$

for a given t during the fill.

Each operational scenario delivers local PU densities with particular characteristics. As in the case of the total PU, a detailed study of these quantities is needed in order to provide the input for accurate simulations of the detector performance for different detector configurations.

Chapter 3

Luminosity formulae and effective pile-up density

In the first section of this chapter, the known equations for the computation of the luminosity with both crab crossing and crab kissing are derived. For this work, these formulae were then extended to include beam time offsets and for different longitudinal bunch profiles. The analytic case of the q-Gaussian distribution is studied, in particular, in greater detail as it better describes the longitudinal profile of the bunches in the LHC (and thus assumed for the simulations of the HL-LHC in Chapter 5). In the second section, the concept of **effective pile-up density** is introduced as a complimentary parameter to estimate the integrated performance in terms of the pile-up density –associated with the expected detector performance–, allowing to characterise each machine operational scenario of the HL-LHC. This new figure-of-merit constitutes the main analytic contribution of this thesis.

3.1 Luminosity formulae

Although Gaussian is a common description of the longitudinal bunch profile, simulations and measurements show that a q-Gaussian distribution provides a better description [33, 85]; this is the case at least at the beginning of the fill, with the profile tending to Gaussian by the end of it. Other profiles have been developed to optimise other configurations; for example, a particular case of the super-Gaussian distribution is adopted for the crab kissing scheme [86]. The properties and relations of these three main distributions are described in the Appendix A. The forms taken by luminosity equation for each of these cases are summarised below. The q-Gaussian case is studied in more detail, as it constitutes the distribution assumed for the simulations of the HL-LHC baseline and most of the alternative scenarios.

3.1.1 Gaussian

A Gaussian longitudinal profile is described by

$$\varrho_s[s_{1,2} \mp (ct + ct_{0_{1,2}})] = \frac{1}{\sqrt{2\pi}\sigma_s} \exp\left(-\frac{[s_{1,2} \mp (ct + ct_{0_{1,2}})]^2}{2\sigma_s^2}\right) , \tag{3.1}$$

where σ_s is the RMS value of the Gaussian distribution. After performing the product of the corresponding densities of the bunches of the two beams, and plugging it into the expression for the instantaneous luminosity,

$$\mathcal{L} = \frac{\mathcal{L}_0}{\pi\sigma_s^2} \cos\frac{\theta}{2} \int_{-\infty}^{\infty}\int_{-\infty}^{\infty} F_{x,y}(s, ct) f_{s,ct}(s, ct)\, \mathrm{d}s\, \mathrm{d}(ct) , \tag{3.2}$$

where

$$f_{s,ct}(s, ct) = \exp\left(-\frac{[s\cos\frac{\theta}{2} - (ct + ct_{0_1})]^2 + [s\cos\frac{\theta}{2} + (ct + ct_{0_2})]^2}{2\sigma_s^2}\right) , \tag{3.3}$$

and $\mathcal{L}_0$ and $F_{x,y}(s, ct)$ are given by Eqs. (2.47) and (2.49), respectively.

3.1.2 q-Gaussian

In the case of the q-Gaussian distribution (see Appendix A.2), the longitudinal bunch density is

$$\varrho_s[s_{1,2} \mp (ct + ct_{0_{1,2}})] = \frac{1}{\mu(\lambda\sigma_s)} \left(1 - \frac{4[s_{1,2} \mp (ct + ct_{0_{1,2}})]^2}{(\lambda\sigma_s)^2}\right)^{5/2} , \tag{3.4}$$

where the parameters $\mu \equiv 5\pi/32$ and $\lambda \equiv 2\left[(2\ln 2)/(1 - 2^{-2/5})\right]^{1/2}$ ensure that its *full width at half maximum* (FWHM) equals the FWHM of the corresponding Gaussian distribution, $2\sigma_s\sqrt{2\ln 2}$ [75]. The luminosity can be written then as

$$\mathcal{L} = \frac{2\mathcal{L}_0}{\mu^2(\lambda\sigma_s)^2} \cos\frac{\theta}{2} \iint_D F_{x,y}(s, ct) f_{s,ct}(s, ct)\, \mathrm{d}s\, \mathrm{d}(ct) , \tag{3.5}$$

with

$$f_{s,ct}(s, ct) \equiv \left[\left(1 - \frac{4[s\cos\frac{\theta}{2} - (ct + ct_{0_1})]^2}{(\lambda\sigma_s)^2}\right)\left(1 - \frac{4[s\cos\frac{\theta}{2} + (ct + ct_{0_2})]^2}{(\lambda\sigma_s)^2}\right)\right]^{5/2} . \tag{3.6}$$

Note that, unlike the Gaussian distributions, the domain D on s-ct of the q-Gaussian function (and their product for two bunches) is finite. Moreover, the integrand must be real to have a physical meaning. Therefore the integrals over s and ct in the formula of the instantaneous luminosity have to be performed within these limits. In order to determine the integration limits, it is useful to rewrite the q-Gaussian bunch profiles in a factorised way,

$$\begin{aligned}&\varrho_s[s_{1,2} \mp (ct + ct_{0_{1,2}})]\\ &\quad= \frac{1}{\mu(\lambda\sigma_s)} \left(\frac{2}{(\lambda\sigma_s)}\right)^5 \left[-\prod_{i=0}^{1}\left((ct + ct_{0_{1,2}}) \mp s_{1,2} + (-1)^i\frac{(\lambda\sigma_s)}{2}\right)\right]^{5/2} ,\end{aligned} \tag{3.7}$$

Table 3.1. Properties of the sub-regions in the domain of $f_{s,ct}(s,ct)$.

Combinat.	Inters.	$f_{s,ct}$	Bounded	Combinat.	Inters.	$f_{s,ct}$	Bounded
$++++$	1	$\mathbb{R}$	No	$-+++$	4	$\mathbb{C}$	
$+++-$	$\varnothing$			$-++-$	$\varnothing$		
$++-+$	2	$\mathbb{C}$		$-+-+$	5 (D)	$\mathbb{R}$	Yes
$++--$	3	$\mathbb{R}$	No	$-+--$	6	$\mathbb{C}$	
$+-++$	$\varnothing$			$--++$	7	$\mathbb{R}$	No
$+-+-$	$\varnothing$			$--+-$	$\varnothing$		
$+--+$	$\varnothing$			$---+$	8	$\mathbb{C}$	
$+---$	$\varnothing$			$----$	9	$\mathbb{R}$	No

which yields to

$$\mathcal{L} = \frac{2\mathcal{L}_0}{\mu^2(\lambda\sigma_s)^2}\left(\frac{2}{(\lambda\sigma_s)}\right)^{10}\cos\frac{\theta}{2}\iint_D F_{x,y}(s,ct)f_{s,ct}(s,ct)\,\mathrm{d}s\,\mathrm{d}(ct)\,, \tag{3.8}$$

where

$$\begin{aligned} f_{s,ct}(s,ct) = \Bigg[&\left((ct+ct_{0,1}) - s\cos\frac{\theta}{2} - \frac{(\lambda\sigma_s)}{2}\right)\left((ct+ct_{0,1}) - s\cos\frac{\theta}{2} + \frac{(\lambda\sigma_s)}{2}\right) \\ &\cdot\left((ct+ct_{0,2}) + s\cos\frac{\theta}{2} + \frac{(\lambda\sigma_s)}{2}\right)\left((ct+ct_{0,2}) + s\cos\frac{\theta}{2} + \frac{(\lambda\sigma_s)}{2}\right)\Bigg]^{5/2}\,. \end{aligned} \tag{3.9}$$

As pointed out before, the approximation Eq. (2.36) allows to decouple the transformation of the horizontal and longitudinal coordinates. Below, the domain D of the function $f_{s,ct}(s,ct)$ is studied in more detail.

The four factors inside brackets in Eq. (3.9) can be either positive (+) or negative (−); this results in the sixteen possible combinations listed in Table 3.1 (each sign corresponds, in the same order, to each factor in $f_{s,ct}(s,ct)$). Not all combinations are possible, though, as for some of them there are no pairs of points (s,ct) that satisfy the corresponding signs of the four factors simultaneously. Equating each of the factors in Eq. (3.9) to zero defines four lines (written as function of s in the plane s-ct):

$$ct = s\cos\frac{\theta}{2} + \frac{(\lambda\sigma_s)}{2} - ct_{0_1} \equiv A_{ct}(s)\,, \tag{3.10}$$

$$ct = s\cos\frac{\theta}{2} - \frac{(\lambda\sigma_s)}{2} - ct_{0_1} \equiv B_{ct}(s)\,, \tag{3.11}$$

$$ct = -s\cos\frac{\theta}{2} + \frac{(\lambda\sigma_s)}{2} - ct_{0_2} \equiv C_{ct}(s)\,, \qquad \text{and} \tag{3.12}$$

$$ct = -s\cos\frac{\theta}{2} - \frac{(\lambda\sigma_s)}{2} - ct_{0_2} \equiv D_{ct}(s)\,. \tag{3.13}$$

Each of the regions defined by the equations above can be seen in Fig. 3.1a. The (+) or (−) signs correspond to the semi-planes *above* or *below* the corresponding lines. The seven empty intersections are indicated by $\varnothing$ in Table 3.1, and they are discarded. For the reminding regions, note that $f_{s,ct}(s,ct) : \mathbb{R}\times\mathbb{R}\to\mathbb{C}$, that is, for s and ct reals,

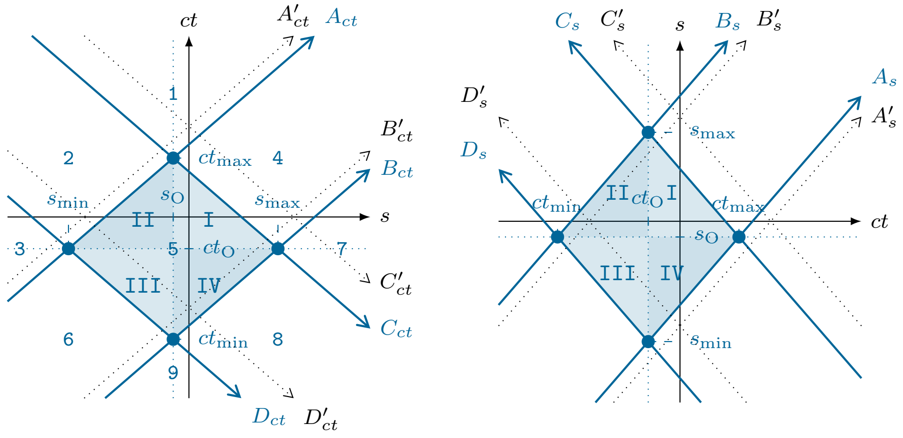

(a) Domain of $f_{s,ct}(s, ct)$.

(b) Domain of $f_{ct,s}(ct, s)$.

Figure 3.1. Domain of the q-Gaussian function: **(a)** $f_{s,ct}(s, ct)$ and **(b)** $f_{ct,s}(ct, s)$.

Eq. (3.9) is in general a function in the complex plane $\mathbb{C}$. To be physically meaningful, the domain has to be restricted to those values of s and ct for which the integrand function is real. Since $f_{s,ct}(s, ct)$ is imaginary when the number of positive (or negative) terms is even (e.g. the first term being positive and the reminding three all negative, and so on), four more regions can be discarded, as they deliver a complex result (some of the original combinations could also be directly discarded for this reason). Finally, only the regions where $f_{s,ct}(s, ct)$ is bounded and its integral converges are of interest; this does not occur in the regions 1, 3, 7, nor 9, and thus only one region is left:

$$- + - + \,.$$

This region, called D, is shaped as a parallelogram, and its boundaries define the limits of integration over s and ct for the luminosity calculation. The choice of this region is also intuitive, as it is the bounded region around the origin. Although the function $f_{s,ct}$ is defined in other regions, this is a purely mathematical result from its own definition; the physical density distribution is described by this function only by the aforementioned region of interest, and it is assumed zero elsewhere.

The ratio between the height and width of the parallelogram is determined by the angle θ which, in general, is a small crossing angle (the region is a square for head-on collisions). The offset of the parallelogram centre $(s_{\mathrm{O}}, ct_{\mathrm{O}})$ with respect to the centre of the coordinate system is determined by the time offsets $t_{0_{1,2}}$:

$$s_{\mathrm{O}} = -\frac{ct_{0_2} - ct_{0_1}}{2\cos\frac{\theta}{2}}\,, \qquad \text{and} \qquad ct_{\mathrm{O}} = -\frac{ct_{0_2} + ct_{0_1}}{2}\,. \tag{3.14}$$

The vertices of the parallelogram also define the following quantities:

$$\begin{aligned} s_{\min} &= -\frac{(\lambda\sigma_s) - (ct_{0_2} - ct_{0_1})}{2\cos\frac{\theta}{2}} & ct_{\min} &= -\frac{(\lambda\sigma_s) - (ct_{0_2} + ct_{0_1}:)}{2} \\ s_{\max} &= \frac{(\lambda\sigma_s) - (ct_{0_2} - ct_{0_1})}{2\cos\frac{\theta}{2}} & ct_{\max} &= \frac{(\lambda\sigma_s) - (ct_{0_2} + ct_{0_1})}{2}\,. \end{aligned} \tag{3.15}$$

Note that $(ct_{\max} - ct_{\min})/(s_{\max} - s_{\min}) = \cos\frac{\theta}{2}$.

In some cases, it is more useful to study the domain of the integrand function in the reflected *ct*-*s* plane (Fig. 3.1b). In this case, the equations of the bordering lines of the region D are

$$s = \frac{1}{\cos\frac{\theta}{2}}\left[(ct + ct_{0_1}) - \frac{(\lambda\sigma_s)}{2}\right] \equiv A_s(ct)\,, \tag{3.16}$$

$$s = \frac{1}{\cos\frac{\theta}{2}}\left[(ct + ct_{0_1}) + \frac{(\lambda\sigma_s)}{2}\right] \equiv B_s(ct)\,, \tag{3.17}$$

$$s = \frac{1}{\cos\frac{\theta}{2}}\left[-(ct + ct_{0_2}) - \frac{(\lambda\sigma_s)}{2}\right] \equiv C_s(ct)\,, \qquad \text{and} \tag{3.18}$$

$$s = \frac{1}{\cos\frac{\theta}{2}}\left[-(ct + ct_{0_2}) + \frac{(\lambda\sigma_s)}{2}\right] \equiv D_s(ct)\,, \tag{3.19}$$

and they are functions of *ct*; the expressions in Eqs. (3.14) and (3.15) are, of course, still valid.

The region of interest in the plane *s*-*ct* can be further split into four quadrants, see Fig. 3.1. The integrals over s and ct in the domain D are thus understood as

$$\iint_D \mathrm{d}(ct)\,\mathrm{d}s = \sum_{i=\mathtt{I}}^{\mathtt{IV}} \iint_i \mathrm{d}(ct)\,\mathrm{d}s\,, \tag{3.20}$$

in the *s*-*ct* plane, where

$$\iint_i \mathrm{d}(ct)\,\mathrm{d}s = \begin{cases} \int_{s_\mathrm{O}}^{s_{\max}}\int_{ct_\mathrm{O}}^{C_{ct}(s)} \mathrm{d}(ct)\,\mathrm{d}s, & \text{for} \quad i = \mathtt{I} \\ \int_{s_{\min}}^{s_\mathrm{O}}\int_{ct_\mathrm{O}}^{A_{ct}(s)} \mathrm{d}(ct)\,\mathrm{d}s, & \text{for} \quad i = \mathtt{II} \\ \int_{s_{\min}}^{s_\mathrm{O}}\int_{D_{ct}(s)}^{ct_\mathrm{O}} \mathrm{d}(ct)\,\mathrm{d}s, & \text{for} \quad i = \mathtt{III} \\ \int_{s_\mathrm{O}}^{s_{\max}}\int_{B_{ct}(s)}^{ct_\mathrm{O}} \mathrm{d}(ct)\,\mathrm{d}s, & \text{for} \quad i = \mathtt{IV} \end{cases}\,. \tag{3.21}$$

When reflecting the *s*-*ct* plane, and thus inverting the order of integration –to be consistent with the order in Eq. (3.8), which is the same order that has been used in the Gaussian and super-Gaussian cases–, the limits of integration of each of the regions of D are

$$\iint_i \mathrm{d}s\,\mathrm{d}(ct) = \begin{cases} \int_{ct_\mathrm{O}}^{ct_{\max}}\int_{s_\mathrm{O}}^{C_s(ct)} \mathrm{d}s\,\mathrm{d}(ct), & \text{for} \quad i = \mathtt{I} \\ \int_{ct_{\min}}^{ct_\mathrm{O}}\int_{s_\mathrm{O}}^{B_s(ct)} \mathrm{d}s\,\mathrm{d}(ct), & \text{for} \quad i = \mathtt{II} \\ \int_{ct_{\min}}^{ct_\mathrm{O}}\int_{D_s(ct)}^{s_\mathrm{O}} \mathrm{d}s\,\mathrm{d}(ct), & \text{for} \quad i = \mathtt{III} \\ \int_{ct_\mathrm{O}}^{ct_{\max}}\int_{A_s(ct)}^{s_\mathrm{O}} \mathrm{d}s\,\mathrm{d}(ct), & \text{for} \quad i = \mathtt{IV} \end{cases}\,. \tag{3.22}$$

Depending on the parameters of the crab cavities, the integral of $F_{x,y}f_{s,ct}$ can be further simplified by exploiting the parity of the integrand. This is indeed the case in the developed simulation tools to optimise the computation of the numerical integration, as described in the following chapter. Lastly, substitution of Eq. (3.20) in (3.8) gives the final expression to compute the instantaneous luminosity for bunches with q-Gaussian longitudinal profile.

3.1.3 Super-Gaussian

A longitudinal bunch profile with super-Gaussian distribution is described by

$$\varrho_s[s_{1,2} \mp (ct + ct_{0_{1,2}})] = \frac{1}{\nu(\kappa\sigma_s)} \exp\left(-\frac{[s_{1,2} \mp (ct + ct_{0_{1,2}})]^4}{2(\kappa\sigma_s)^4}\right) , \tag{3.23}$$

with $\nu \equiv 2^{5/4}\,\Gamma\,({}^5\!/\!_4)$, $\kappa \equiv \left\{\Gamma({}^1\!/\!_4)/\left[\sqrt{2}\,\Gamma({}^3\!/\!_4)\right]\right\}^{1/2}$ and $\Gamma(\cdot)$ is the gamma function [75]. These parameters ensure that the RMS the super-Gaussian distribution is equal to σ_s –the RMS of the equivalent Gaussian distribution–, see Appendix A.3. The instantaneous luminosity in this case is

$$\mathcal{L} = \frac{2\mathcal{L}_0}{\nu^2(\kappa\sigma_s)^2} \cos\frac{\theta}{2} \int_{-\infty}^{\infty}\int_{-\infty}^{\infty} F_{x,y}(s,ct) f_{s,ct}(s,ct)\,\mathrm{d}s\,\mathrm{d}(ct) , \tag{3.24}$$

where

$$f_{s,ct}(s,ct) \equiv \exp\left(-\frac{[s\cos\frac{\theta}{2} - (ct + ct_{0_1})]^4 + [s\cos\frac{\theta}{2} + (ct + ct_{0_2})]^4}{2(\kappa\sigma_s)^4}\right) . \tag{3.25}$$

3.2 Effective pile-up density

Since the longitudinal resolution of the tracker (around 0.1 mm) is significantly smaller than the average distance between PU vertices [87], it was reasonable for the experiments at the LHC to assume the impact of PU density on the detector efficiency to be linear (in the current range of HL-LHC collision scenarios). Several quantities were preliminary studied as a function of the PU density. It was found that the local efficiency of reconstructed events indeed exhibited an approximately linear relation with the PU density [30, 31, 88], confirming this simple but novel hypothesis. Based on these observations, a new figure-of-merit, the *effective* PU density, was proposed to quantify the integrated effect of the local event distributions on detector efficiency, as derived below. The effective PU density mirrors the integrated luminosity as a more interesting parameter for the experiments than the peak magnitude of the corresponding parameter [89] (namely, the peak instantaneous luminosity or the peak PU density).

The useful data quantity for analysis, represented by $\mathcal{L}'_{\text{int,fill}}$, can be parametrised as a fraction of the delivered integrated luminosity $\mathcal{L}_{\text{int,fill}}$ for a fill duration t_{fill} (see Eq. (2.57)) via a function f of the PU μ and the local density ρ_s,

$$\mathcal{L}'_{\text{int,fill}} = \int_0^{t_{\text{fill}}} \int f(\mu,\rho)\,\mathcal{L}(s;t)\,\mathrm{d}s\,\mathrm{d}t\ . \tag{3.26}$$

Expanding f around $\rho_s = 0$,

$$f(\mu,\rho_s) \approx f(\mu,0) + \left.\frac{\partial f(\mu,\rho_s)}{\partial\rho_s}\right|_{\rho_s=0} \rho_s(s;t)\,. \tag{3.27}$$

At constant PU $\mu(t) = \mu_0$ –which is the case in the HL-LHC for most of the fill duration due to luminosity levelling (Section 5.1)–, the integrals over the first term can be approximated as

$$\int_0^{t_{\text{fill}}} \int f(\mu(t),0)\,\mathcal{L}(s,t)\,\mathrm{d}s\,\mathrm{d}t \approx f(\mu_0)\mathcal{L}_{\text{int,fill}}\,, \tag{3.28}$$

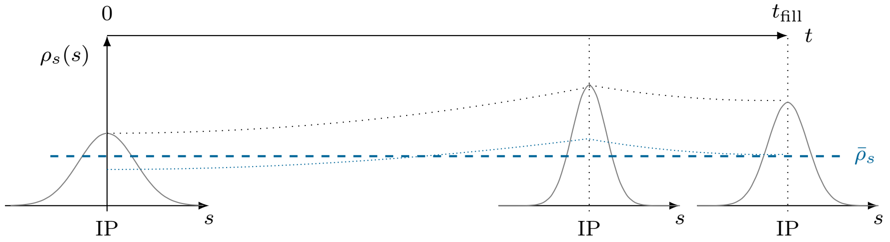

Figure 3.2. Effective line pile-up density as the average line pile-up density over the fill weighted by the corresponding integrated luminosity.

and

$$\int_0^{t_{\rm fill}} \int \left.\frac{\partial f(\mu_0,\rho_s)}{\partial \rho_s}\right|_{\rho_s=0} \rho_s(s;t)\mathcal{L}(s;t)\,\mathrm{d}s\,\mathrm{d}t \approx -\varepsilon \int_0^{t_{\rm fill}} \int \rho_s(s;t)\,\mathcal{L}(s;t)\,\mathrm{d}s\,\mathrm{d}t \equiv -\varepsilon\bar{\rho}_s\mathcal{L}_{\rm int,fill}\,, \quad (3.29)$$

where

$$\varepsilon \equiv -\left.\frac{\partial f(\mu_0,\rho_s)}{\partial \rho_s}\right|_{\rho_s=0}\,. \quad (3.30)$$

The useful integrated luminosity in Eq. (3.26) can be rewritten as

$$\mathcal{L}'_{\rm int,fill} \approx [\,f(\mu_0) - \varepsilon(\mu_0)\bar{\rho}_s\,]\,\mathcal{L}_{\rm int,fill}\,, \quad 0 \le f(\mu_0) \le 1\,, \quad \varepsilon > 0\,, \quad (3.31)$$

and therefore it allows to compare different scenarios in terms of the integrated luminosity and a parameter $\bar{\rho}_s$ for constant PU μ_0. Equation (3.29) defines the *effective (line) pile-up density* $\bar{\rho}_s$, the average of the PU density over the fill, weighted by the integrated luminosity (or equivalently, the integrated PU in the fill) [90],

$$\bar{\rho}_s \equiv \frac{\displaystyle\int_0^{t_{\rm fill}} \int \rho_s^2(s;t)\,\mathrm{d}s\,\mathrm{d}t}{\displaystyle\int_0^{t_{\rm fill}} \mu(t)\,\mathrm{d}t} = \frac{\displaystyle\int_0^{t_{\rm fill}} \mu(t)\,\mathrm{E}[\rho_s(s;t)]\,\mathrm{d}t}{\displaystyle\int_0^{t_{\rm fill}} \mu(t)\,\mathrm{d}t}\,, \quad (3.32)$$

see Fig. 3.2. In the second identity, the effective line PU density has been rewritten in terms of the expected value of ρ_s over s with probability $\rho(s;t)/\mu(t)$:

$$\mathrm{E}[\rho_s(s;t)] = \int_{-\infty}^{\infty} \rho_s(s;t)\,\frac{\rho_s(s;t)}{\mu(t)}\,\mathrm{d}s\;. \quad (3.33)$$

The common units of $\bar{\rho}_s$ are [mm^{-1}], understood as [events/mm]. The lower the effective PU density is, the higher the detector efficiency becomes for the reconstruction of event vertices, i.e. higher data quality. It has to be noted that for other experimental quantities, such as those not relying on the tracker, only the PU level is relevant.

Naturally, the concept of the effective line PU density can be extended to the temporal coordinate (or even the transverse coordinates). In this case, the effective

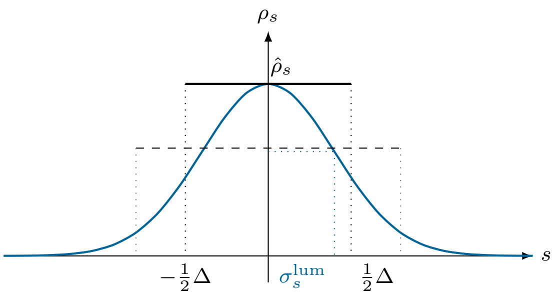

Figure 3.3. Two functions to approximate the pile-up density: in blue, a Gaussian distribution; in black; two cases of box distributions (solid and dashed lines). All densities shown correspond to a fixed time $t = t_0$, and are normalised to the same PU.

time PU density is given by

$$\bar{\rho}_t = c\,\frac{\displaystyle\int_0^{t_{\text{fill}}} \int \rho_{ct}^2(ct;t)\,\mathrm{d}(ct)\,\mathrm{d}t}{\displaystyle\int_0^{t_{\text{fill}}} \mu(t)\,\mathrm{d}t}\,, \tag{3.34}$$

and it is commonly expressed in $[\text{ns}^{-1}]$.

3.2.1 Approximations

In general, the line PU density is a complicated function of the beam and optics parameters at the IP. However, a Gaussian description with peak $\hat{\rho}(t)$ and RMS value given by $\sigma_{s,\text{lum}}(t)$,

$$\rho_s(s;t) = \hat{\rho}_s(t)\exp\left(-\frac{s^2}{2(\sigma_s^{\text{lum}})^2(t)}\right)\,, \tag{3.35}$$

is often a good approximation even when considering realistic simulations [32, 85]. In this case, Eq. (3.32) can be simplified to

$$\bar{\rho}_s = \frac{1}{\sqrt{2}}\,\frac{\displaystyle\int_0^{t_{\text{fill}}} \hat{\rho}_s^2(t)\,\mathrm{d}t}{\displaystyle\int_0^{t_{\text{fill}}} \hat{\rho}_s(t)\,\mathrm{d}t}\,. \tag{3.36}$$

A flatter event distribution is observed, for example, in the crab kissing scheme at the start of the levelling [86]. In order to analytically derive the effective PU, the extreme case of a flat (box) function with full width $\Delta(t)$ –as seen in Fig. 3.3– is considered,

$$\rho_s(s;t) = \hat{\rho}_s(t)\,\text{box}[s,\Delta(t)]\,. \tag{3.37}$$

In this case, the effective PU density is given by

$$\bar{\rho}_s = \frac{\displaystyle\int_0^{t_{\text{fill}}} \hat{\rho}_s^2(t)\,\mathrm{d}t}{\displaystyle\int_0^{t_{\text{fill}}} \hat{\rho}_s(t)\,\mathrm{d}t}\,. \tag{3.38}$$

Comparing Eqs. (3.36) and (3.38) it is observed that $\hat{\rho}$ is not a robust figure-of-merit and it is too pessimistic by about a factor of $\sqrt{2}$ for the cases with approximately Gaussian event distributions, such as the HL-LHC baseline. For this reason, $\bar{\rho}$ has been introduced to replace the peak PU density as a figure-of-merit to evaluate scenarios in terms of the expected detector performance at constant pile-up.

Chapter 4

LEVELLING program

In order to simulate the optimum fills of the different HL-LHC operational scenarios studied in this work, a series of scripts were developed, jointly known as the LEVELLING program. The program offers the large flexibility needed to simulate the wide set of parameters and operation modes that the baseline and the alternative scenarios encompass. In this chapter, the main modules of LEVELLING are described in the order of the work-flow of a typical simulation. The formulae implemented in the code is based in the accelerator theory in Chapter 2, as well as the new concepts in Chapter 3.

The LEVELLING program [91] was developed at CERN; the initial scripts –used on the first studies of the performance assessment of the HL-LHC alternative scenarios [41]– were considerably extended and improved for the present work. The program is comprised of four main modules, namely `Levelling_Run.py`, `Levelling_Config.py`, `Levelling_Beam.py`, and `Levelling_Luminosity.py`, as well other modules with auxiliary functions and files. Figure 4.1 shows a high-level and non-exhaustive overview[1]of the main modules, functions, and their relations, as well as a simplified work-flow.

LEVELLING is written mainly in PYTHON 2 (the NUMPY and SCIPY packages are prerequisites), with some functions written in BASH, and some auxiliary files in the format of the MAD-X accelerator program (a prerequisite, executed internally) [70, 92–94]. Simulation results are written into two main text files:

- A *table* file containing a list of the simulation settings (the parameters that define the scenario: beam, levelling options, assumptions for the estimate of the integrated performance, etc.), the *virtual* magnitude (see Section 4.5.8) of a wide set of parameters (optics, instantaneous luminosity, PU, and related quantities), and final results (integrated luminosity and effective PU densities, number of levelling and total steps, etc.); and

---

[1] The diagram does correspond to a programming standard (such as an entity-relationship model or ER, or Structured Query Language or SQL).

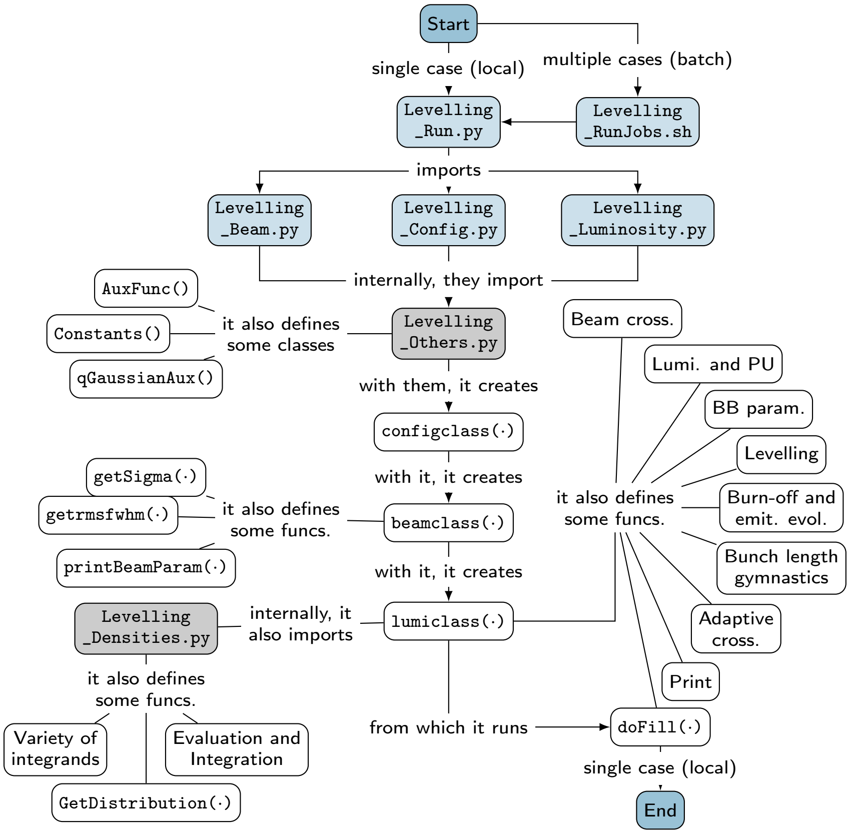

Figure 4.1. Work-flow of the `Levelling` program: main modules and functions.

- A *level* file, where the evolution of the parameters at each time step of the optimum fill.

Both files are combined into a single *results* file at the end of the simulation. Other additional result files are also created, each explained in the corresponding sections; for example, the derived pile-up densities for a given scenario, computed from the results file by the `Levelling_Densities.py` auxiliary module with the aid of MAPCLASS2 (another prerequisite) [95].

4.1 `Levelling_Run.py`

This module starts the simulation of a single scenario. It imports the other three main LEVELLING modules –described in the following sections– and creates an object (instance) of the class defined in each of them. `Levelling_Run.py` is called with two main options: `-n` (`--name`), the name of the scenario to be run, and `-t` (`--table`), an optional flag to only compute and return a table with the initial and virtual parameters of interest (the fill evolution is not simulated). The module then proceeds to run the `doFill(·)` method of the created `Luminosity` object, thus starting the simulation of the requested scenario.

4.2 Levelling_Config.py

It defines the `Config` class which includes a list of basic parameters (beam, machine, levelling options, etc.), in the form of attributes of the object (`self`); the default values of these parameters correspond to the HL-LHC baseline at nominal levelling, see Table 4.1 and Chapter 5. The different available scenarios (Chapter 6) are stored in the form of methods of the `Config` class. The creation of an instance of `Config` in the `Levelling_Run.py` module for a particular scenario (`name`) calls the corresponding method, overwriting the default parameters that define the particular scenario of interest.

4.3 Levelling_Beam.py

This module defines the `Beam` class which contains parameters directly inherited from the `Config` instance (such as the momentum `_momeV`, the bunch population `_ppb`, etc.), and parameters computed when initialised: Similarly to `Config`, the parameters in `Beam` are stored as attributes of the object itself. `Levelling_Beam.py` also imports (as `cst`) physical constants from the `Levelling_Others.py` module (Section 4.6.1). The first dependent parameters that are computed are reproduced below:

```
self._frev      = cst.clight / config._circ
self._betaver   = config._circ/(2.*np.pi) / config._tuneb
self._dx        = config._circ/(2.*np.pi) * config._alfmom
self._gamma     = config._momeV / cst.pmass + 1.
self._betarel   = np.sqrt( 1. - 1./(self._gamma**2.) )
self._totalpart = self._Nbunch * self._ppb
self._current   = self._totalpart * 1.815e-15
```

where `_frev` is the revolution frequency (in [Hz]); `_betaver` and `_dx`, the average betatron and dispersion functions (in [m]); `_gamma` and `_betarel`, the Lorentz relativistic factors (in [1]); `_totalpart`, the beam intensity, that is, the total number of particles in all bunches; and `_current`, the beam current (in [A]).

Regarding optics (transverse) parameters, the minimum β^* (`_betamin`) is initially stored as a copy of the input `_beta`, a parameter that will vary during the levelling. A new variable, the parallel separation `_parsep` (in [m]) is declared with an initial value of zero, as it is needed for levelling at IP8. The initial value of the BBLR separation (`_initsepLR`, in [σ]), the crossing angle (`_initphi`, in [rad]), the crab crossing and crab kissing angles (`_initphiCR` and `_initphiCK`, respectively, both in [rad]), and the crab crossing and crab kissing fractions with respect to the crossing angle (`_initoncc` and `_initonck`, respectively, both in [1]) are also stored.

```
self._initsepLR = [];  self._initoncc = []
self._initphi   = [];  self._phi      = []
self._initphiCR = [];  self._phiCR    = []
for i in range(self._nip):
  self._initsepLR.append(self._sepLR[i])
  diver = np.sqrt( self._epsn[self._xplane[i]] / (self._gamma*self._betarel)
                   / self._beta[i][self._xplane[i]] )
  self._initphi.append(diver * self._sepLR[i])
  self._phi.append(self._initphi[i])
  self._initoncc.append(self._oncc[i])
```

Table 4.1. Default parameters in the `Config` class (corresponding the HL-LHC baseline standard at nominal levelling).

Variable	Default value	Unit or Options	Meaning
`_momeV`	`7000.0e9`	eV	Momentum
`_ppb`	`2.2e11`	1	Bunch population (protons per bunch)
`_dpp`	`0.0001074259105`	1	Energy spread
`_sigs`	`0.09`	m	(Equivalent) Gaussian RMS bunch length
`_epsn`	`[2.5e-6,2.5e-6]`	m	Horizontal and vertical normalised emittance

`_beta`	`[[0.15, 0.15],`
	`[0.15, 0.15],`
	`[3.00, 3.00]]`
		m	Minimum $\beta^*_\times$ and $\beta^*_\parallel$, per IP

`_tau_obs`	`[None, None]`	`None` or in h	Horizontal and vertical normalised emittance growth time*
`_tau_cc`	`None`	`None` or in %/h · m/rad^2	Inverse of the normalised emittance growth time due to the CCs for both crab crossing and/or crab kissing) in the plane with CCs
`_kappac`	`0.1`	1	Ratio between the horizontal over the vertical IBS lifetime
`_t1 (_t2)`	`0.0`	s	Time delay of the bunches of beam 1 (2)
`_incroncc`	`[False, False, False]`	`False` or in `rad`	Flag to increase the crabbing angle from the initial value (given) until reaching the crossing angle (`oncc` $= \theta_{\mathrm{CC}}/\theta = 1$)
`_incronccrate`	`0.0`	1	Fractional increment of `oncc` per step**
`_niterlev`	`1`	1	Number of iterations of the minimisation process for levelling***
`_IBSRF`	`True`	`True` or `False`	Logical flag to include the contributions of the IBS and SR to the evolution of the emittance growth
`_adaptivexsing`	`[False, False, False]`	`True` or `False`	Logical flag to perform adaptive crossing
`_opticsfile`	`"opt_round.madx"`	N/A	Optics file with the MAD-X sequence of the machine
`_circ`	`26658.8832`	m	Machine circumference
`_rho`	`2804`	m	Curvature radius
`_alfmom`	`3.225e-4`	1	Momentum compaction
`_tuneb`	`64.31`	1	Horizontal betatron tune
`_tunes`	`0.002342`	1	Synchrotron tune
`_Nbunch`	`2760`	1	Total number of bunches
`_ipnames`	`["IP1", "IP5", "IP8"]`	N/A	IP names
`_nip`	`len(ipnames)`	1	Number of IPs
`_nbunch`	`[2748, 2748, 2572]`	1	Number of colliding bunches, per IP
`_xplane`	`[0, 0, 0]`	*(see Meaning)*	Crossing plane, per IP, `0` for horizontal (H), `1` for vertical (V)
`_sepLR`	`[10.5, 10.5, 21.8]`	σ	Long-range beam-beam separation, per IP
`_wcc`	`400.0e6`	Hz	Crab cavity frequency****
`_sepLRsteptime`	`[False for i in range(nip)]`	`False` or in s	Trigger time for reduction of BBLR separation, per IP

* The *observed* emittance – a large value will dominate over the effect of IBS and syncrhtotron radiation

** E.g. the value `0.005` $= 0.12/24$ will result in an increment of 0.12 –as in `oncc` $= 0.8$ to 1.0– in around 24 steps (penalty steps are not counted).

*** Useful for mutiparametric levelling where, for example, the crab crossing and crab kissing are levelled simultaneously

**** In the case of IP8, the value is set *ad hoc* to correspond to the full crossing angle calculated from the external and crossing angles.

Variable	Default value	Unit or Options	Meaning
`_sepLRstep`	`[0.0   for i in range(nip)]`	σ	Step for reduction of BBLR separation, per IP
`_oncc`	`[0.7657, 0.7657, 0.0]`	1	Ratio between crabbing angle and crossing angle, per IP*
`_tcc1` (`tcc2`)	`[[0.0,0.0], [0.0,0.0], [0.0,0.0]]`	s	Time delay of the CCs for beam 1 (2) in the horizontal and vertical planes, per IP
`_levtech`	`["levlumi" for i in range(nip)]`	*(see Meaning)*	Levelling technique, per IP, `"levlumi"` for luminosity levelling or `"levppus"` for levelling of peak pile-up density
`_levvar`	`["Beta", "Beta", "ParSep"]`	*(see Meaning)*	Levelling parameter, per IP, `"Beta"` for β^*, `"PhiCR"` for θ_{CC}, `"PhiCK"` for θ_{CK}, or `"ParSep"` for $d_\parallel$
`_levlumi`	`[5.00e34, 5.00e34, 2.00e33]`	$\mathrm{cm}^{-2}\,\mathrm{s}^{-1}$	Levelled luminosity, per IP
`_levppus`	`[1.30, 1.30, None]`	mm^{-1}	Levelled peak pile-up density, per IP
`_ck`	`[False for i in range(nip)]`	`True` or `False`	Flag for levelling with crab kissing in the separation plane, per IP
`_constbetar`	`[True  for i in range(nip)]`	`True` or `False`	Flag to keep the ratio of the horizontal/vertical β^* constant throughout levelling, per IP
`_sepLRconst`	`[False for i in range(nip)]`	`True` or `False`	Flag to keep the crossing angle (in rad) constant and the BBLR separation (in σ) variable (`False`) or vice versa if `True`, per IP
`_longdens`	`"qGaussian"`	*(see Meaning)*	Type of longitudinal density, `"Gaussian"`, `"RF800"` for super-Gaussian**, or `"qGaussian"` for q-Gaussian
`_p`	`0.98`	1	Luminosity step for levelling, that is, the reduction in percentage of the luminosity that triggers a new levelling step (it is the same for all IPs)
`_step`	`600.0`	s	Time step (in case `p` = 1.0)
`_optimumfill`	`True`	`True` or `False`	Flag to run for the optimum fill (`True`) or a given fill duration `maxfill` (`False`)
`_maxfill`	`20.0*3600.0`	s	Maximum fill duration (aside from being used for the simulation of a fixed-duration run, it is used to prevent a simulation to run indefinitly)
`_penstp`	`True`	`True` or `False`	Flag to include penalty steps
`_timepenstp`	`0.0`	s	Duration of penalty steps
`_updatepenstp`	`False`	`True` or `False`	Flag to update the parameters related to the emittance evolution in the penalty steps
`_constlong`	`True`	`True` or `False`	Flag to keep the bunch length (and in consequence the FWHM) constant throughout the fill
`_ppblong`	`0.0`	1	Bunch intensity that triggers bunch length shortening
`_redlong`	`0.0`	1	Fractional reduction for bunch length and energy spread
`_minlong`	`sigs`	m	Minimum (equivalent) Gaussian bunch length or FWHM
`_redsepLR`	`[False for i in range(nip)]`	`True` or `False`	Flag to keep the BBLR separation constant
`_minsepLR`	`[None for i in range(nip)]`	σ/h	Minimum BBLR separation
`_ratesepLR`	`[None for i in range(nip)]`	σ/h	Rate of the reduction of BBLR separation
`_xsec`	`81.0`	mb	Cross-section (inelastic) for pile-up
`_xsecburn`	`111.0`	mb	Cross-section (total) for burn-off
`_days`	`160.0`	1	Dedicated time to physics (days per year)
`_eff`	`0.5`	1	Efficiency
`_turnar`	`145./60.`	h	Turn-around time

* In order to provide a crabbing angle of 380 µrad (exact), `oncc` is defined in the code as

```
[ 380.e-6/( sepLR[0] * np.sqrt( epsn[0]/(momeV/cst.pmass)/beta[0][0]) ), 380e-6/( sepLR[1] * np.sqrt( epsn[1]/(momeV/cst.pmass)/beta[1][0]) ), 0.]
```

** The label `"RF800"` is motivated by the additional 800 MHz-RF system needed to shape the longitudinal bunch profile into a super-Gaussian distribution.

```
    self._initphiCR.append(self._initoncc[i] * self._initphi[i])
    self._phiCR.append(self._initphiCR[i])
  self._phiCK     = [0.]*self._nip;  self._onck     = [0.]*self._nip
  self._initphiCK = [0.]*self._nip;  self._initonck = [0.]*self._nip
```

The parameters `_phi`, `_phiCR`, `_phiCK`, and `_onck` are created as a copy of their input initial values, and they constitute the variables to be adjusted during the levelling process.[2] Similarly, the initial values of the longitudinal variables are also stored:

```
self._initsigs   = self._sigs;        self._initdpp    = self._dpp
self._mindpp     = self._initdpp;     self.flagminlong = False
self._constlong0 = config._constlong
```

where `_mindpp` is the minimum energy spread.[3]

Then, the `Beam` module initialises the damping times due to IBS (`_tau_ibs`) and SR. For the former, `_tau_ibs` is a list that will contain the horizontal and vertical components (in [h]) as they are computed at every step. For the latter, the relative energy loss by SR is estimated first with Eq. (2.18), and then used to define the three transverse components of `_tau_sr` (in [h]) according to Eqs. (2.19) and (2.20):

```
dEsr = cst.e**2 * self._betarel**3 * self._gamma**4
       / (3.*cst.eps0*self._rho) / cst.e / self._momeV
taux_sr = 2./(dEsr*self._frev*3600.)
tauy_sr = 2./(dEsr*self._frev*3600.)
tauz_sr = 1./(dEsr*self._frev*3600.)
self._tau_sr = [taux_sr, tauy_sr, tauz_sr]
```

With the aid of the radiation integrals in Table 2.1, the equilibrium transverse emittances (`_eps0`, in [m]), bunch length (`_sigs0`, in [m]) and energy spread (`_dpp0`, in [1]) are estimated following Eqs. (2.21) and (2.25):

```
self._dpp0  = np.sqrt( cq * self._gamma**2 * I3/(2*I2) )
self._sigs0 = self._alfmom * cst.clight
              /(2.*np.pi * self._tunes * cst.clight/self._circ) * self._dpp0
epsx0 = cq * self._gamma**2 * I5/I2 * self._betarel*self._gamma
epsy0 = 13./55. * cq/I2 * self._betaver
        / self._rho**2 * 2.*np.pi * self._betarel*self._gamma
self._eps0 = [epsx0, epsy0]
```

where `cq` is the constant in Eq. (2.22).

For the case of the CC noise contribution to the emittance growth (if the option `_tau_cc` is not `None`), the associated damping time is not directly passed as it depends on the magnitude of the betatron function and crabbing angle, which vary along the fill according to Eq. (5.3). In this case, the growth rate `_tau_cc_mh` (in [m/h]) is passed instead, i.e. the inverse of the normalised emittance growth time due to the CCs in the plane that features them:

```
self._tau_cc_mh = self._epsn[0]/( self._tau_cc * 0.15/380.e-6**2 )
```

Two more variables, `_tau_cc_0` and `_tau_cc_0`, will store the inverse of the normalised emittance growth times due to the CCs for crab crossing and crab kissing at the main IPs (at $\beta^* = 15\,\mathrm{cm}$ and 380 µrad of crabbing for both effects), respectively, as

---

[2] All the optics list-type parameters described above are used to define a logical flag `_identicalIP01` that evaluates if their first pair of elements (corresponding to IP1 and IP5) are identical; if `True`, computations are performed only for the first IP, with the results being copied to the second IP (IP5), thus speeding up the running time. The third element in these list-type parameters corresponds to IP8. IP2 is omitted due to its low luminosity and negligible effect on the machine performance in comparison with the other IPs.

[3] This variable is redefined to the corresponding value once the bunch length `_sigs` reaches its minimum `_minlong` during a fill when the scenario does not require the bunch length to remain constant; the flag `flagminlong` also turns `True`.

they evolve throughout the simulation (IP8 does not feature CCs). Lastly, all the variables for the contributions to the emittance growth from the different processes discussed above are declared as lists containing their respective horizontal and vertical components, to be used to track their evolution throughout the fill.

Two useful functions are defined as methods of the current class, namely `getsigma(self, ip)` and `getrmsfwhm(self, longdens)`; they are called at each step of the simulation to update the magnitude of the beam size at the requested `ip` and the corresponding FWHM (depending on the longitudinal density profile `longdens`, see Appendix A). The variables `_initrmssigs` and `_initfwhm` store the initial values of the aforementioned parameters. One final function, `printBeamParam`, prints the values of all the variables in the `Beam` object to both the standard output (the default terminal) and, if requested, to the table output file.

4.4 Levelling_Densities.py

The auxiliary `Levelling_Densities.py` module defines the `Densities` class which includes functions (methods) that define the luminosity integrands of a wide range of cases (depending mainly on the type of the longitudinal bunch profile and the presence or absence of crab cavities for crab crossing and/or crab kissing); the full list of integrands and their corresponding arguments is shown in Table 4.2. When initialised, this module imports several auxiliary functions from the `Luminosity_Others.py` module, in particular, `qGaussianAux` for the computation of the limits of the finite domain of the q-Gaussian distribution. Numerical integration in one (`quad`) and two dimensions (`dblquad`) is performed with the aid of the SCYPY module.

As an example, the integrand for q-Gaussian bunches colliding with crab crossing is described below in more detail; all other integrands are defined in a similar way. The integrand is a function of the longitudinal and temporal coordinates (`s` and `ct`), beam and optics parameters,[4] and the time offsets for the bunches of each beam (`t1` and `t2`) and the CCs (`t1c` and `t2c`). As a first step, derived and auxiliary quantities (those present in the function $F_{x,y}(s, ct)$ in Eq. (2.49), resulting from the integration of the transverse coordinates) are calculated: the associated wave numbers of the CCs, the hour-glass effect factor, the scaling factor for the equivalence between Gaussian and q-Gaussian bunch lengths, etc.:

```
def integrand_CC_qGaussian(self, ct, s, phi, sigs, betc, sigc, betp, t1, wcc, phiCR, ...):

  kCR  = wcc/cst.clight * 2.*np.pi;   sigs2  = sigs**2
  hgc2 = 1. + (s/betc)**2;            sinPHh = np.sin(phi/2.);
  ct1  = cst.clight*t1;               FactFWHMGauss2 = cst.FactFWHMGauss**2; ...
  const = 2./(cst.NormFWHMGauss**2*FactFWHMGauss2*sigs2) * (2.**10/FactFWHMGauss10/sigs10)

  result = const*( ((ct+ct1) - s*cosPHh - 0.5*cst.FactFWHMGauss*sigs) * ...)**(5./2.)
            * np.exp( - (( (1./kCR)*sinCRh * np.sin(kCR*(s+0.5*(ct2c-ct1c)))
                          * np.cos(kCR*(ct+0.5*(ct2c+ct1c))) - s*sinPHh )**2
                         )/ sigc2/hgc2
                    ) / hgc/hgp
  return result
```

The integrand is then constructed from the Eq. (2.46); in this case, in particular, the function of the longitudinal coordinates is given by Eqs. (3.2) and (3.3).

---

[4] The endings `-c` and `-p` in several optics parameters denote the crossing and parallel planes, respectively, e.g. $\beta^*_\times$ =`betc` and $\beta^*_\parallel$ =`betp`.

Table 4.2. Integrands available in the `Densities` class.

Integrand	ct	s	x	y	phi	sigs	betc	sigc	betp	sigp	parsep	t1	t2	wcc	phiCR	t1c	t2c	phiCK	t1p	t2p
integrand_noCC_Gaussian		●			●	●	●	●	●			●	●							
integrand_noCC_parsep_Gaussian		●			●	●	●	●	●	●	●	●	●							
integrand_noCC_RF800	●	●			●	●	●	●	●											
integrand_noCC_parsep_RF800	●	●			●	●	●	●	●	●	●									
integrand_noCC_qGaussian	●	●			●	●	●	●	●			●	●							
integrandwithx_noCC_qGaussian	●	●	●		●	●	●	●	●			●	●							
integrandwithy_noCC_qGaussian	●	●		●	●	●	●	●	●	●		●	●							
integrand_noCC_parsep_qGaussian	●	●			●	●	●	●	●	●	●	●	●							
integrandwithx_noCC_parsep_qGaussian	●	●	●		●	●	●	●	●	●	●	●	●							
integrandwithy_noCC_parsep_qGaussian	●	●		●	●	●	●	●	●	●	●	●	●							
integrand_CC_Gaussian	●	●			●	●	●	●	●			●	●	●	●	●	●			
integrand_CC_parsep_Gaussian	●	●			●	●	●	●	●	●	●	●	●	●	●	●	●			
integrandwithx_CC_Gaussian	●	●	●		●	●	●	●	●			●	●	●	●	●	●			
integrandwithy_CC_Gaussian	●	●		●	●	●	●	●	●	●		●	●	●	●	●	●			
integrand_CC_RF800	●	●			●	●	●	●	●					●	●					
integrand_CC_parsep_RF800	●	●			●	●	●	●	●	●	●			●	●					
integrand_CC_qGaussian	●	●			●	●	●	●	●			●	●	●	●	●	●			
integrandwithx_CC_qGaussian	●	●	●		●	●	●	●	●			●	●	●	●	●	●			
integrandwithy_CC_qGaussian	●	●		●	●	●	●	●	●	●		●	●	●	●	●	●			
integrand_CC_CK_Gaussian	●	●			●	●	●	●	●	●		●	●	●	●	●	●	●	●	●
integrand_CC_CK_RF800	●	●			●	●	●	●	●	●				●	●	●	●	●		
integrand_CC_CK_qGaussian	●	●			●	●	●	●	●	●		●	●	●	●	●	●	●	●	●

These integrands are used for the computation of the luminosity and PU densities, which are obtained either by a simple evaluation at a given space-time point (`Evaluate_integrand(·)`), or by numerical integration for a given coordinate (`IntCT(·)`) and `IntS(·)`) or for a set of coordinates (`IntAll(·)`, `IntAll_withx(·)`, and `IntAll_withy(·)`). The functions performing these actions take the necessary sub-set of parameters as attributes;[5] in all cases, these functions first determine the type scenario based on the IP (IP8, for example, uses parallel separation), the presence and type of crabbing, and the longitudinal bunch profile.

While `Evaluate_integrand(·)` is needed for the computation of the 2D *s*-*t* PU density, the integrals on `ct` and `s` are allow the computation of the line and time PU densities, respectively. An extract of the `IntCT(·)` function is shown below (note the variable *s* as first argument) as an example:

```
def IntCT(self, s, phi, ...):
  ...
  elif longdens == "qGaussian":
    qGAux = qGaussianAux(sigs, phi, t1, t2)
    if  s >= qGAux.szero:
```

---

[5] The list of attributes is denoted here by "(·)" for simplicity.

```
        result1 = quad(lambda ct: self.integrand_CC_qGaussian(ct, s, ...),
                              qGAux.Zct(s), qGAux.Cct(s))
        result4 = quad(lambda ct: self.integrand_CC_qGaussian(ct, s, ...),
                              qGAux.Bct(s), qGAux.Zct(s))
        result = (result1[0]+result4[0],)
      else:
        result2 = quad(lambda ct: self.integrand_CC_qGaussian(ct, s, ...),
                              qGAux.Zct(s), qGAux.Act(s))
        result3 = quad(lambda ct: self.integrand_CC_qGaussian(ct, s, ...),
                              qGAux.Dct(s), qGAux.Zct(s))
        result = (result2[0]+result3[0],)
    ...
    return result[0]
```

The case with `qGaussian` profile has been chosen because special care has to be taken in it due to its finite domain (and its importance as the HL-LHC baseline). The integrals (`quad`) on the different regions described in Section 3.1.2 over the `lambda` variable `ct` are performed first within the corresponding limits (defined in the auxiliary class `qGaussianAux`), and then they are summed up. The result has then to be doubled at the instance where `IntCT(·)` is originally called, as the integral is only computed over two regions (taking advantage of domain symmetry when one of the variables is absent). In the case of distributions with a infinite domain such as Gaussian, the integral is straightforward:

```
result = quad(lambda ct: self.integrand_CC_CK_Gaussian(ct, s, ...), -np.inf, np.inf)
```

The definition of the function `IntS(self, ct, phi, ...)` is similar, but with the `lambda` variable `s` instead, and the corresponding integration limits. The returned result by the `Evaluate_integrand(·)` function is given in $[\mathrm{m}^{-2}]$, but it can be converted into $[\mathrm{m}^{-1}\,\mathrm{s}^{-1}]$ since $t = \mathtt{ct}/c$. For the integrals on `ct` and `s`, the result is in $[\mathrm{m}^{-1}]$, but for the latter, it is usually converted into $[\mathrm{s}^{-1}]$.

The integral over *all* coordinates, that is, both s and ct, on the other hand, is conducted by `IntAll(self, phi, ...)` (note the absence of s and ct, and their presence as `lambda` variables) via a double integral (`dblquad`) over the corresponding limits of each coordinate:

```
result1 = dblquad(lambda s, ct: self.integrand_CC_qGaussian(ct, s,
                              ...), qGAux.ctzero, qGAux.ctmax, qGAux.Zs, qGAux.Cs)
...
result = (result1[0]+result2[0]+result3[0]+result4[0],)
```

For the q-Gaussian the four regions are computed and added up. The returned results is used in the computation of luminosity and PU.

Two more functions are defined for the integral over `s` and `ct` which take, in addition, either `x` or `y` as variables: `IntAll_withx(self, phi, ..., x)` and `IntAll_withy(self, phi, ..., y)`; the transverse coordinate is, in turn, passed to the corresponding integrand. These functions are needed for the numerical calculation of the 1D horizontal and vertical PU densities. The result of the integrals on both s and ct are dimensionless, understood as number of events. A last function, `GetDistribution(·)` generates, for a given IP and at a given fill step, tables with the 1D and 2D PU densities as a function of their corresponding variables, over given ranges. It is discussed in more detail in Section 4.6.4.

4.5 Levelling_Luminosity.py

The `Levelling_Luminosity.py` module defines the `Luminosity` class; one of its methods, `doFill(·)`, is the core function of the LEVELLING program, as it is in charge of performing the simulation of the fill evolution and controlling the levelling process throughout it. The `Luminosity` class also defines many auxiliary functions. According to the type of parameters they compute, these functions can be grouped into the following categories: for a) beam crossing parameters; b) luminosity and PU-related parameters; c) the beam-beam parameter; d) levelling; e) burn-off and emittance evolution; f) bunch length gymnastics; and g) adaptive crossing. The functions in each of the groups above are described in the following subsections.

The preamble of the `Luminosity` module loads common packages for I/O file management and to perform mathematical operations (namely, `numpy`, `fminbound` from `scipy.optimize`,[6] and `quad`, `dblquad`, and `fixed_quad` from `scipy.integrate`), as well as the `Levelling_Others.py` and `Levelling_Densities.py` modules. LUMINOSITY also defines several parameters (either new or directly copied from `Config`) in the form of attributes of the class itself (mainly auxiliary flags and ID labels for output files).

4.5.1 Functions for beam crossing parameters

During the levelling process, the magnitude of the crossing angle at a given IP may change as a result of the variation of the emittance and/or β^*. This in turn leads to a change of the ratio between the crabbing and crossing angle, which would need to be recomputed (with the restriction that the fraction of compensation cannot go above the unity). This is performed by the `GetPhi(·)` and `GetOnccDueToPhi(·)` functions, respectively. Conversely, changes in the crossing angle or the crabbing angle demand updating the ratio `_oncc`, operation that is conducted by `GetOnccDueToPhiCR(·)`. Naturally, a change on the crabbing fraction requires the recalculation of the crabbing angle (`GetPhiCR(·)`). To update all crossing parameters after a levelling step, all the aforementioned functions can be collectively called at once by using the `GetNewPhi(·)` function, assuming that the BBLR separation remains constant. If this is not the case, `GetNewSepLR(·)` allows to update the BBLR separation. Two other functions, `GetOnckDueToPhiCK(·)` and `GetPhiCRDueToAdaptive(·)` deal with the computation of the fraction of crab crossing and kissing angles when adaptive crossing is requested (Section 4.5.7).

4.5.2 Functions for luminosity and PU-related parameters

As described in Section 4.4, the functions in `Densities` are the integrands of the luminosity integral for different cases. The luminosity is found as the product of the luminosity of a *head-on* collision (which in turn is defined as the product of a numerical factor –which accounts for the number of bunches, the bunch population, the revolution frequency, and beam sizes– and the kinematic factor), times a dimensionless reduction factor (which accounts for the hour-glass effect, crabbing, parallel separation, etc.). These factors are computed from Eqs. (2.33), (2.46), and (2.47), although their definitions have been slightly adapted with the aim to optimise numerical computations:

---

[6] To be used with SCIPY version 0.15.1; use `minimize_scalar` for version 0.17.0 or higher.

```
def KinFact(self, beam, ip):
  ...
  k = 2.*np.cos(phi/2.)
  return k

def GetL0(self, beam, ip):
  ...
  L0 = k * ppb**2 * frev * nbunch
         / (8.*np.pi*sig[0]*sig[1])*1.e-4
  return L0

def GetReduc(self, beam, ip):
  ...
  densities = Densities()
  l0    = self.GetL0(beam,ip)
  reduc = densities.IntAll(phi, ..., ip)
  return reduc
```

```
def getlumi(self, beam):
  lumi  = []
  lumi0 = []
  reduc = []
  for i in range(beam._nip):
    if (i != 1 or not beam._identicalIP01):
      r  = self.GetReduc(beam,i)
      l0 = self.GetL0(beam,i)
    lumi.append(l0*r);
    lumi0.append(l0);
    reduc.append(r)
  return lumi, lumi0, reduc

def getlumiip(self, beam, ip):
  r  = self.GetReduc(beam,ip)
  l0 = self.GetL0(beam,ip)
  return l0*r, l0, r
```

The functions `getlumi(·)` and `getlumiip(·)` allow to compute the luminosity either at all the IPs, or a given IP, respectively. For a given luminosity (either levelled or instantaneous), the calculation the PU is straightforward:

```
def GetPileUp(self, frev, lumi, nbunch):
  return lumi * self._xsec*1.e-27 / nbunch / frev
```

Computation of the luminous region and luminous time, as well as their corresponding peak values at a given IP is conducted by `GetLumRegion(·)`, `GetLumTime(·)`, `GetPeakLumRegion(·)`, and `GetLumTime(·)` functions. Depending on the settings of the given scenario, this is performed with the associated integrand in the `Densities` class. The computation of the luminous region by `GetLumRegion(·)` following Eq. (2.69) for the case of q-Gaussian bunches with crab crossing is shown below as an example:

```
def GetLumRegion(self, beam, ip):
  ...
  densities = Densities()
  norm = densities.IntAll(phi, ..., longdens, ip)
  ...
    elif longdens == "qGaussian":
      qGAux = qGaussianAux(sigs, phi, t1, t2)
      i1 = dblquad(lambda s, ct: s**2*densities.integrand_CC_qGaussian(ct, s, phi, ...),
                                   qGAux.ctzero, qGAux.ctmax,  qGAux.Zs,  qGAux.Cs )
      ...
      i = (i1[0]+i2[0]+i3[0]+i4[0],)
  ...
  result = np.sqrt(i[0]/norm)
  return result
```

The peak luminous region, Eq. (2.70), is defined following a similar structure, (but with $s = 0$ and only over two regions of the domain thanks to symmetry):

```
def GetPeakLumRegion(self, beam, ip):
    ...
      i12 = quad(lambda ct: densities.integrand_CC_qGaussian(ct, 0, phi, ...),
                              qGAux.ctzero, qGAux.ctmax)
      ...
      i = (i12[0]+i34[0],)
    ...
  result = i[0]/norm
  return result
```

The definition of the luminous time and peak luminous time are analogous, but with `s` and `ct` interchanged (except on the arguments of the integrands which are positional), and the integration performed over the corresponding limits.

Two more functions are included to compute the integral on s or ct of the squared of the line or time PU densities for a given IP. These quantities are needed for the computation of the effective PU densities (Section 4.5.9):

```
def GetIntSPUS2(self, beam, ip, pu):
  ...
  pus2 = lambda  s: pow(pu * densities.IntCT(s, phi, sigs, ...)/norm, 2)
  ...
      elif longdens == "qGaussian":
        qGAux = qGaussianAux(sigs, phi, t1, t2)
        result1 = quad(lambda  s: pus2(s), qGAux.szero, qGAux.smax )
        result2 = quad(lambda  s: pus2(s), qGAux.smin,  qGAux.szero)
        result = (result1[0]+result2[0],)
  ...
  return result[0]
```

with an analogous definition for its time counterpart, `GetIntCTPUT2(·)`.

4.5.3 Function for the beam-beam parameter

The `GetBBParam(·)` function computes the linear beam-beam parameter (neglecting hour-glass) for a given IP. It first computes a geometrical factor given, in the case `xplane == 0`, by

```
  geomx = np.sqrt(1. + (sigs2)/(sigx2) * np.tan((1.0-oncc)*phi/2.)**2);  geomy = 1.0
```

and then proceeds to `xix` and `xiy` according to Eq. (2.14). A list `xi = [xix, xiy, xim]` is returned, with `xim` the mean of the transverse factors.

4.5.4 Functions for levelling

These set of functions handle the levelling variables (possible parameters are β^*, crabbing or kissing angles, or parallel separation), according to the requested target (instantaneous luminosity or peak line PU density). The `FuncVar(·)` function assigns, for a given IP, the value `lambdavar` of a `lambda` variable created beforehand in the `GetLevel(·)` function (explained below), to the corresponding optics variable, according to the option `levvar`. In the case of levelling with β^*, the choice of crossing/parallel separation planes and the use of round/flat optics are taken into account. Optics parameters that depend on the selected levelling variable have to be updated after the `lambda` variable assignation (for example, update the crossing angle if the β^* changes, or `oncc` if the crossing angle changes, etc.):

```
def FuncVar(self, lambdavar, beam, ip, levtech, levvar, roundorflat=None, kbeta=None):
  if levvar == "Beta":
    ...
    if xplane == 0:
      beam._beta[ip][1] = lambdavar;  beam._beta[ip][0] = lambdavar/kbeta
    ...
  elif levvar == "PhiCR":
    beam._phiCR[ip] = lambdavar;  self.GetOnccDueToPhiCR(beam, ip)
  ...
```

After these assignations, the luminosity is computed with `getlumiip(·)` and returned if luminosity is the levelling target; conversely, if the line PU density is the levelling target, the luminosity is used to calculate the PU first and, after computing the peak luminous region via `GetPeakLumRegion(·)`, the line PU density is calculated using Eq. (2.71) and returned. For the case with levelling with β^*, in particular, another

Table 4.3. Conditions on the optics and target parameters for levelling.

Parameter	Conditions	
N/A	`condition1 = lumi/levlumi < levlumitol`	
`levtech == "levlumi"`	`condition2 = True`	
`levtech == "levppus"`	`condition2 = ppus/levppus < levppustol`	
`levvar == "Beta"`	`condition3 = beta   == bmin`	`condition4 = beta   > bmin`
`levvar == "PhiCR"`	`condition3 = phiCR  == initphi`	`condition4 = phiCR  > 0.`
`levvar == "PhiCK"`	`condition3 = phiCK  == 0.`	`condition4 = phiCK  > 0.`
`levvar == "ParSep"`	`condition3 = parsep == 0.`	`condition4 = parsep > 0.`

`levppustol = 0.999`; `levlumitol = 0.999` for IP1/5 and `levlumitol = 0.995` for IP8.

Table 4.4. Limits on the levelling parameters.

`levvar`	`boundmin`	`boundmax (t == 0.)`	`boundmax (t != 0.)`	Limit to reset
`"Beta"`	`_betamin[ip][1-xplane]`	`100.*boundmin`	`1.5*beta[1-xplane]`	`_beta[ip]  = bmin`
`"PhiCR"`	`0.`	`phi`	`phi`	`_phiCR[ip] = phi`
`"PhiCK"`	`0.`	`2.5*initphi`	`1.5*initphi`	`_phiCK[ip] = 0.`
`"ParSep"`	N/A	N/A	N/A	`_parsep    = 0.`

method is included: `GetBetaMin(·)`, which returns either the minimum betatron function for a given IP, or assigns it the corresponding `_betamin` value (a function of the bunch intensity, defined as a dictionary, optionally declared in `Config`).

The conditions that the levelling variable for a given IP has to fulfil in order to proceed (or not) to perform a levelling step are returned by the `GetConditionsLevel(·)` function; the four possible conditions, depending on the levelling variable, are listed in Table 4.3. The first and second conditions –which apply to any levelling variable– refer to the magnitude of the luminosity and peak PU densities at the current step remaining inside tolerance thresholds (the second is always satisfied when luminosity levelling is the target). Conditions 3 and 4 deal with the initial value of the levelling parameter, or with it remaining larger than a minimum value (zero, for example).

The following method, `GetLevel(·)`, is the core function in charge of the levelling computation at each step of the fill simulation conducted by `DoFill(·)`. It finds by an optimisation process the value of the desired levelling variable (β^*, crab crossing or kissing angle, etc.) for a given IP, such that the either the levelled luminosity is met, or the peak line PU density is kept under its levelled value (depending on the input settings). The magnitude of the levelling parameter is updated directly in the `Beam` class instance. If the variable reaches its limit during the optimisation and the levelling target has not been reached, it is assigned the default limit in Table 4.4 instead.

Figure 4.2 shows the simplified work-flow of `GetLevel(·)`. The function starts by reading the current beam and optics parameters for the IP to be levelled, and additional dependent parameters computed from them (for example, the ratio $\beta^*_{\parallel}/\beta^*_{\times}$); then, it proceeds to calculate the current luminosity and peak PU density using the functions in Section 4.5.2. The conditions to proceed (or not) with the levelling computation are evaluated by `GetConditionsLevel(·)` as described before. A first check (`condition1 and condition2 and condition3`) is conducted; if the three first conditions are met, it means that the levelling variable has reached its limit, but the luminosity (and the peak line PU density, if applicable) is lower than its levelled threshold, in which case levelling is no longer possible. Conversely, if the conditions

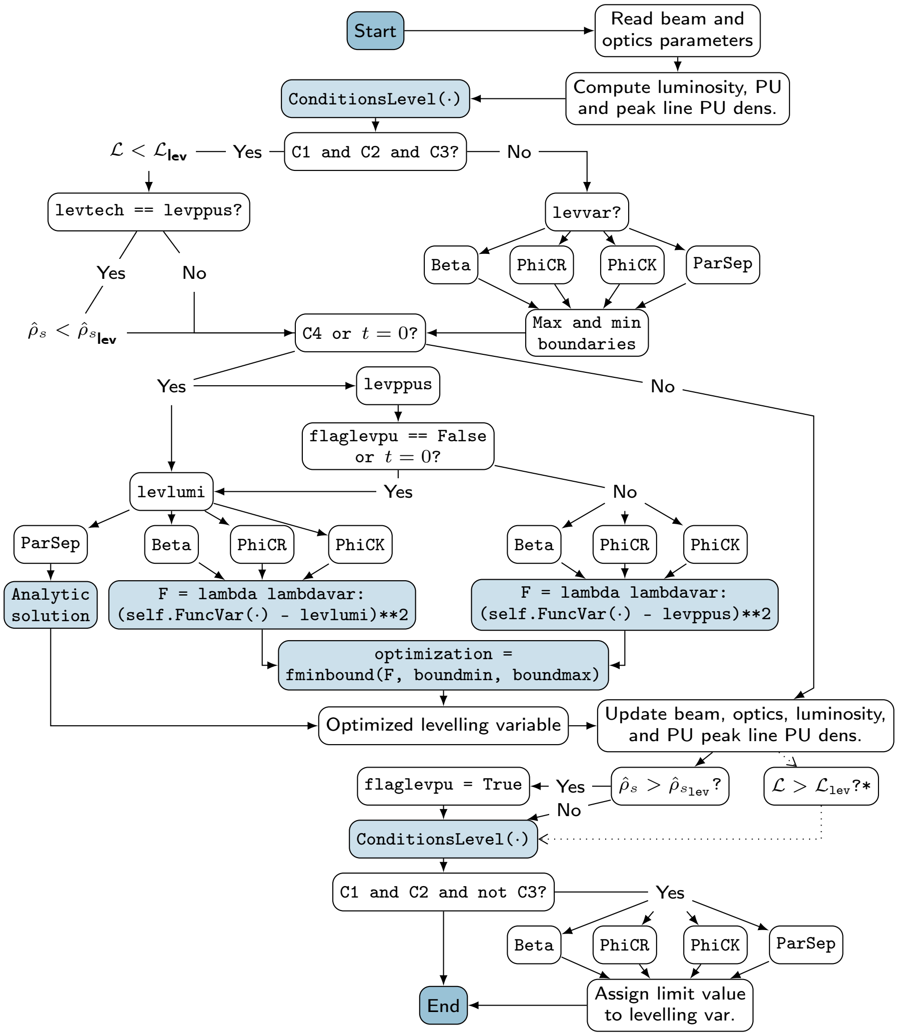

Figure 4.2. Work-flow of the `GetLevel` function.

are not met, the corresponding limit of the levelling variable is assigned.

The levelling process is conducted at the first step of levelling, or while the levelling parameter remain within its range. The case of luminosity levelling starts by defining the function `F` to be minimised, namely the square of the difference of the current luminosity with respect to the target levelled value:

```
F = lambda betavar: (self.FuncVar(betavar, beam, ip, "levlumi", levvar) - levlumi)**2
```

`F` is a function of the requested levelling variable, defined as a `lambda` variable. When levelling of the peak line PU separation is requested instead, the process is conducted only after a first stage of luminosity levelling has been performed (as described before), since during this stage the peak line PU luminosity is naturally smaller than the levelled peak line PU density threshold. When the peak line PU density has finally reached its limit, a flag `flaglevpu` is raised (from `False` to `True`), and the levelling with peak line PU density formally starts. This process makes use of a similar minimisation function:

```
F = lambda betavar: (self.FuncVar(betavar, beam, ip, "levppus", levvar) - levppus)**2
```

Once the corresponding minimisation function has been defined, the optimisation process is conducted via the `fminbound` function of the SCIPY V0.15.1 package[7] (the default tolerance is `xtol = 1.0e-5`):

```
optimization = fminbound(F, boundmin, boundmax, full_output=1, disp=3, xtol=1e-8)
```

Thus, the optimum magnitude of the levelling parameter is obtained by the method of least squares. Different ranges are given for the different variables to speed up the optimisation process (at the first step, for example, a larger range is used). When the calculation is finished, the levelling variable will contain the optimised value that minimises `F`. Then, an update of optics parameters is required to reflect the effect of its new value, followed by a re-evaluation of the luminosity, PU, etc. The magnitude of the latter parameter is used, in particular, to rise a flag (`flaglevpu`) when it surpasses the levelled line PU density; simultaneously, the time (in hours) at which this event takes place is stored in `_timeppuslev`.

Luminosity levelling by parallel separation profits from the exact analytic solution in the case of no CCs and no minimisation function is required:

```
sigp       = beam.getsigma(ip)[1]
sepfact    = np.exp( -beam._parseptmp**2 /4./sigp**2 )
lumitottmp = self.getlumiip(beam, ip)[0]/sepfact
if lumitottmp >= levlumi:
  beam._parsep = 2.*sigp*np.sqrt( np.log(lumitottmp/levlumi) )
else:
  beam._parsep = 0.
  if self._flagsteplev2 == False:
    self._flagsteplev2 = True
lumitot = self.getlumiip(beam, ip)
beam._parseptmp = beam._parsep
```

The parallel separation at the current step is stored in a temporary variable, and a special flag is raised when it reaches zero.

Once all parameters have been updated, the levelling conditions, as given by `GetConditionsLevel(·)` are also re-evaluated. As before, if the luminosity and peak line PU density (when relevant) are lower than their levelled thresholds, it means that the optimisation function was not able to reach a satisfactory solution and the levelling variable is reset then to its limit. Lastly, note that if `condition4` is `False`, that is, the levelling variable has reached its limit, the optimisation process is skipped entirely (the update of the parameters is still performed). The `GetLevel(·)` function finishes by returning the luminosity at the current step.

4.5.5 Functions for burn-off and emittance evolution

After a levelling step, beam parameters such as bunch population, emittance, and bunch length, have to be updated as a function of the step duration. For example, the bunch population decreases over time due to the simultaneous luminosity burn-off at all the IPs (Section 2.3.2). The function `GetPPBNew(·)` computes `_ppb` after a time `t`, as given in Eq. (2.52),

---

[7] For the SCIPY V0.17.0 or higher, use `optimization = minimize_scalar(F, bounds = (boundmin, boundmax), method = 'bounded')` instead.

```
def GetPPBNew(self, t, lumiall, beam):
  rate = 0.
  for i in range(beam._nip):
    rate = rate + lumiall[i]*(self._xsecburn*1.0e-27) / beam._nbunch[i]
  beam._ppb = beam._ppb / (1. + t * rate/beam._ppb)
```

In the linear approximation, this reduces to `beam._ppb = beam._ppb - t*rate`, a common model for intensity burn-off.

Meanwhile, the beam emittance changes over time due to two main processes described in Section 2.2: IBS and synchrotron radiation. In order to estimate the growth times due to IBS, Levelling makes use of MAD-X. The `IBStauxz(·)` function creates several auxiliary files: `NAMEupdateIBS` stores the relevant beam paramters at the current step; `NAMEjobfile` is a copy of the `Levelling_jobtau.madx` mask that contains the minimum set of commands to compute the IBS (edited with the unique I/O file names for the particular case that is running, described in more detail in Section 4.6.2); and `NAMEtauxz` will contain the corresponding results for the transverse and longitudinal growth IBS growth times at the current step. `IBStauxz(·)` then runs MAD-X internally with the `NAMEupdateIBS` file as input, and it waits for the process to finish:

```
cmd = ["/afs/cern.ch/user/m/mad/bin/madx", NAMEjobfile]
process = subprocess.Popen(cmd, stdout = subprocess.PIPE)
process.wait()
```

Once MAD-X computations are finished and the results for the emittance growth times (in [h]) are stored in `NAMEtauxz`, their magnitudes are read and assigned to their corresponding variables back in `IBStauxz(·)` function:

```
beam._tau_ibs[0] = float(data[0][2]);  beam._tau_ibs[1] = beam._tau_ibs[0]/beam._kappac;
beam._tau_ibs[2] = float(data[1][2]);
```

The vertical emittance growth time, in particular, is derived via the coupling factor `kappac` defined in `Config`. Computation of the IBS growth times by means of this method improves the result with respect to earlier versions of Levelling, where an approximate analytic formula was used instead; this led, however, to a increase of the simulation duration.

The `EmitGrowth(·)` function computes the emittance evolution taking into account IBS, SR, CC noise (and optionally, of an *observed* emittance growth). The emittance growth due to IBS and SR can be neglected via the `Config` flag `IBSRF`. When being taken into account, their contributions after a time interval `steph` (in [h]) are computed following Eqs. (2.28) and (2.27):

```
def EmitGrowth(self, t, beam):
    steph = t/3600.
    beam._epsn_ibs  = [beam._epsn[0]*(steph/beam._tau_ibs[0]),
                       beam._epsn[1]*(steph/beam._tau_ibs[1])]
    beam._epsn_sr   = [-2*steph*(beam._epsn[0] - beam._eps0[0])/beam._tau_sr[0],
                       -2*steph*(beam._epsn[1] - beam._eps0[1])/beam._tau_sr[1]]
```

For the IBS, results from `IBStauxz(·)` are used, while for SR, the equilibrium emittances `eps0` –calculated beforehand in the `Beam` module (Section 4.3)– are required.

For the CC noise, the effects of crab crossing and crab kissing are assumed to be in opposite planes in both main IPs (VH crossing, equivalent to HV crossing for identical IPs). The growth time due to CCs noise (in [h)] is computed from `_tau_cc` (the growth rate estimated for a given β^* and crabbing angle, expressed in [%/h], defined in `Config`), scaling it with the betatron function at the IP and crabbing angle at the current step:

```
if beam._phiCK[0] > 0: taux0 = beam._tau_cc/(beam._phiCK[0]**2/beam._beta[0][1])
else:                  taux0 = 1.e8
if beam._phiCR[0] > 0: tauy0 = beam._tau_cc/(beam._phiCR[0]**2/beam._beta[0][0])
else:                  tauy0 = 1.e8
...
beam._tau_cc_0 = [taux0, tauy0];  beam._tau_cc_1 = [taux1, tauy1]
```

The absence of CCs in one of the planes can be treated as an infinite emittance growth time in that plane (for practical purposes, 10^8 is taken). The emittance growth due to CC noise after a time interval `steph` is, according to Eq. (2.31),

```
beam._epsn_cc_ip0 = [ beam._initepsn[0]*(steph/beam._tau_cc_0[0]),
                      beam._initepsn[1]*(steph/beam._tau_cc_0[1]) ]
beam._epsn_cc_ip1 = [ beam._initepsn[0]*(steph/beam._tau_cc_1[0]),
                      beam._initepsn[1]*(steph/beam._tau_cc_1[1]) ]
```

This contribution is additive, hence it is computed from the initial emittance.

Lastly, an additional source of transverse emittance growth can be input; it is computed in a similar way than the other contributions described above for its characteristic *observed* growth time `_tau_obs`. Before being updated, the current value of the emittance is stored (`_epsn_0`) for reference. `EmitGrowth(·)` then adds (in a linear approximation), all the contributions to the beam emittance growth for each transverse plane:

```
for i in range(2):
  epsni =   beam._epsn_0[i]   + beam._epsn_ibs[i]   + beam._epsn_sr[i]
         + beam._epsn_obs[i] + beam._epsn_cc_ip0[i] + beam._epsn_cc_ip1[i]
  beam._epsn[i] = epsni
```

The `EmitGrowth(·)` function not only updates the value of the horizontal and vertical emittances, but also acts on the longitudinal parameters (bunch length and momentum spread), computing their corresponding updated values due to IBS and SR after a given time step. As for their transverse counterparts, the effect of the former on the longitudinal emittance is computed from the longitudinal growth time obtained from MAD-X, while the contribution from the latter exploits the analytic derivation involving the equilibrium emittance:

```
  epss  = beam._sigs*beam._dpp * (1 + steph/beam._tau_ibs[2])
           -  2.*steph/beam._tau_sr[2] * (beam._sigs*beam._dpp - beam._sigs0*beam._dpp0)
  sigs1 = np.sqrt( epss*beam._sigs/beam._dpp )
  dpp1  = np.sqrt( epss*beam._dpp /beam._sigs )
  beam._sigs  = sigs1
  beam._dpp   = dpp1
```

For the particular case of a q-Gaussian longitudinal density, the q-Gaussian RMS bunch length has to be used in the computations (`sigs` is the Gaussian-equivalent RMS). With all the parameters of interest being updated directly in the `beam` instance, `EmitGrowth(·)` finishes by printing their magnitude to the standard output.

After each step of the fill simulation, all the beam parameters handled by the `GetPPBNew(·)` and `EmitGrowth(·)` functions can be updated simultaneously by calling the single `ParametersEvolution(·)` function, described in the following. This function calls the aforementioned methods with the appropriate time interval, depending on the type of current step (their duration are different if they are levelling, decaying, or penalty steps, identified with the associated label (`"LEVEL"`, `"DECAY"`, or `"PENAL"`, respectively) assigned during the fill simulation conducted by `DoFill(·)`. For penalty steps, the beam parameters are always updated, since this type of steps follow levelling (or decaying) steps which are longer in duration; `GetPPBNew(·)` and `EmitGrowth(·)` are called with a time step equal to `timedecay` ($\gg$ `timepenstp`), the time the luminosity spends decaying from its original value at the start of the step (the levelled luminosity in the case of `LEVEL`, or its last value of in the case of `DECAY`):

```
def ParametersEvolution(self, beam, typestep, timedecay, listLUMITOTi):
  if (typestep == "PENAL"):
    self.GetPPBNew(timedecay, listLUMITOTi[-1], beam)
    self.EmitGrowth(timedecay, beam)
```

If the step is a levelling step, the parameter update is optional via the `updatepenstp` flag in `Config` (potentially allowing to speed up the overall simulation). This is possible since levelling steps can follow penalty steps, where an update of the parameters is always conducted; moreover, they are short in duration (`timepenstp`), and therefore the parameters are not expected to change significantly. If the inclusion of penalty step has not been requested –which means the levelling step comes right after a levelling step of duration `timedecay`, then updating the parameters is mandatory:

```
  elif (typestep == "LEVEL"):
    if (self._penstp == True):
      if (self._updatepenstp == True):
        self.GetPPBNew(self._timepenstp, listLUMITOTi[-2], beam)
        self.EmitGrowth(self._timepenstp, beam)
    else:
      self.GetPPBNew(timedecay, listLUMITOTi[-1], beam)
      self.EmitGrowth(timedecay, beam)
```

Lastly, in the case of a decaying step, the beam parameters have to be updated only if penalty steps have not been requested; in this case, they follow a previous `DECAY` step of a duration `timedecay`:

```
  elif (typestep == "DECAY"):
    if (self._penstp == False):
      self.GetPPBNew(timedecay, listLUMITOTi[-1], beam)
      self.EmitGrowth(timedecay, beam)
```

4.5.6 Function for bunch length gymnastics

The bunch length (and momentum spread) can be manipulated during the fill to either remain constant or to decrease its magnitude, simulating with this the counteraction of IBS due to external means (such as RF manipulations). These effects are handled by the `BunchLengthGymnastics(·)` function, which vary depending on the type of step. If in the current step (`LEVEL` and `DECAY` steps) the bunch length is larger than its minimum threshold (`_minlong`, defined in `Config`), the current bunch intensity is larger than the user-defined threshold that triggers the bunch length reduction, and the bunch length has been requested to remain constant via the flag `_constlong`, then both `_sigs` and `_dpp` are reset to their minimum limits:

```
beam._sigs = beam._initsigs;  beam._dpp  = beam._initdpp
```

Once the bunch population has shrunk below the threshold, the bunch length and energy spread are reduced at each step until they reach their minimum magnitudes (marked by flag `_flagminlong`); the fractional reduction applied for both is `_redlong`, also defined in `Config`:

```
beam._sigs = beam._sigs*(1. - beam._redlong);  beam._dpp  = beam._dpp*(1. - beam._redlong)
```

The bunch length is reset to its minimum limit when, at a given step, it decreases below its limit following a bunch length reduction step. The energy spread at the current step is stored and assigned as the new minimum threshold of `_dpp`. At this step, two additional flags are raised: one to mark the time of this event (`_flagminlong = True`), and to stop further bunch length gymnastics in subsequent steps (`_constlong`).

If the bunch length at the current step (`LEVEL` and `DECAY`) is no larger than the minimum bunch length and constant longitudinal parameters were requested, the bunch length and energy spread have to be set to their minimum values. The function finishes by printing the current value of the bunch length and energy spread after the corresponding changes have been applied; no parameters are returned, as the function operates directly on the parameters of the `Beam` instance.

4.5.7 Functions for adaptive crossing

The manipulation of the crossing angle (or alternatively, the BBLR separation) at a given IP along the fill is conducted by `StepReductionSeparation(·)` in a step-wise process. If the reduction of the BBLR separation has been requested (via `_sepLRsteptime`, indicating the time that triggers the reduction), and the current step has reached or surpassed the trigger time, `_sepLR` is reduced by `_sepLRstep` (in $[\sigma]$):

```
beam._sepLR[ip] = beam._sepLR[ip] - beam._sepLRstep[ip]
self.GetNewPhi(beam, ip)
```

Alternatively, `ReductionSeparation(·)` allows to decrease the BBLR separation at an IP at a rate `_ratesepLR` (in $[\sigma/\text{hour}]$, instead of step by step),

```
beam._sepLR[ip] = beam._sepLR[ip] - beam._ratesepLR[ip]*time/3600.
```

until it reaches the minimum value `_minsepLR`. When the BBLR separation goes below its threshold (this can occur, for example, due to other beam parameters changing as a result of levelling), it is then reset to `_minsepLR`. Similar to the previous function, the crossing angle has to be re-evaluated via `GetNewPhi(·)` following any change on the BBLR separation.

The crabbing fraction (`_oncc`) can also be manipulated. This is performed by the `IncrOncc(·)` function, which increases the crabbing angle along the fill at a rate `_incronccrate` from an initial value and until it reaches full-crabbing ($\theta_{\text{CC}} = \theta$):

```
beam._oncc[j] = beam._oncc[j] * (1 + self._incronccrate)
```

When full crabbing is achieved, `_oncc` no longer increases, but remains equal to the unity. Following a change of the crabbing fraction, the crabbing angle has to be updated accordingly using `GetPhiCR(·)`.

An additional function is included to handle a specific *adaptive* crossing program: with `GetPhiFromPPBFor6sigmaDA(·)`, the crossing angle `_phi` is updated with the interpolated value obtained from the following step-wise function of the bunch intensity:

```
def GetPhiFromPPBFor6sigmaDA(self, beam, ip):
  phiold   = beam._phi[ip]
  ...
  if   beam._ppb > 2.2e11: phi =  308.e-6
  elif beam._ppb > 1.9e11: phi = (366.e-6 - 308.e-6) / (1.9e11 - 2.2e11)
                                 *(beam._ppb - 2.2e11) + 308.e-6
  ...
  elif beam._ppb > 0.8e11: phi = (418.e-6 - 418.e-6) / (0.8e11 - 0.9e11)
                                 *(beam._ppb - 0.9e11) + 418.e-6
  else:                    phi =  418.e-6
  beam._phi[ip] = phi
  self.GetNewSepLR(beam, ip)
  self.GetPhiCRDueToAdaptive(beam, ip)
  self.GetOnccDueToPhiCR(beam,ip)
```

This program, developed via simulations, ensures, in particular, that the dynamic aperture remains at least 6σ at any time during the fill [96, 97]. The BBLR separation, crabbing angle, and `_oncc` have to be updated accordingly at each step. Results for this HL-LHC scenario are discussed in Section 5.4.2. The `GetPhiFromPPBFor6sigmaDA(·)` function can be easily modified to perform any other adaptive crossing program.

4.5.8 Print functions

The `PrintLumiParam(·)` function prints the simulation settings to both to the standard output and, if requested via the `tofile` flag in `Config`, to the table file (`foutname`). `PrintVirtualLumiParam(·)`, on the other hand, computes the *virtual* optics parameters (beam sizes, Piwinski angle, etc.), instantaneous luminosity, PU, peak PU densities, etc. at each IP, and prints them to the standard output and to the table file (if requested). The virtual magnitude of a parameter is defined as the result of the evaluation of the parameter with the minimum magnitude of the levelling variable (for example, minimi β^*) before levelling (initial emittance, bunch length, full intensity, etc.).

```
def PrintVirtualLumiParam(self, beam, foutname):
   sig        = [];  piw         = []
   lumiall    = [];  puall       = [];
   lregionall = [];  plregionall = [];
   xiall      = []
   ...

   for i in range(beam._nip):
     sig.append(beam.getsigma(i))
     sigsrms = beam._sigsrms * cst.FactFWHMGauss/4./np.sqrt(2.)
     piw.append(sigsrms*beam._phi[i]/sig[i][beam._xplane[i]]/2.,)
     ...
     lumiall.append( self.getlumiip(beam, i) )
     puall.append( self.GetPileUp(beam._frev, lumiall[i][0], beam._nbunch[i]) )
     lregionall.append( self.GetLumRegion(beam, i) )
     plregionall.append( self.GetPeakLumRegion(beam, i) )
     ppusall.append( puall[i]*plregionall[i]/1.e3 )
     xiall.append( self.GetBBParam(beam, i) )
     ...

   print "{0:36} {1:10}".format("Virtual sigma horizontal", "m"),
   for i in range(beam._nip):
     print beam._ipnames[i] + ":", "{0:12}".format("%1.4e" %sig[i][0]),
     print >> foutname, "@", "{0:22} {1:4}".format("virtsigx"+str(i), "%le"), sig[i][0]
   ...
```

Additionally, this function computes the virtual transverse BB parameters and the virtual IBS growth times using `GetBBParam(·)` and `IBStauxz(·)`, respectively. The luminosity- and PU-related parameters are also computed, for reference, without crabbing (if this is not the case already). After storing a temporary copy of the current crabbing ratio (`save_oncc = beam._oncc[i]`), `_oncc` is set to zero at all IPs and all the parameters are re-evaluated. Results are then printed to the default terminal and eventually to the output file, after which the original crabbing is restored and the simulation of the levelling process is resumed.

A third function, `WriteFILElevelHeaders(·)`, prints the headers of the table columns in the level output file; each column corresponds to a parameter that evolves throughout the fill (listed in Table 4.5), as they are computed by the `DoFill(·)` function:

```
def WriteFILElevelHeaders(self, FILElevel, beam):
  print >> FILElevel, "{0:14}".format("TIME"),
  ...
  print >> FILElevel, "{0:13} ".format("%le"),
  ...
```

In the second row, a tag describing the type of data of the associated parameter is assigned: `%s` for strings and `%le` for floats.

Table 4.5. Parameters in the output file of the `Levelling` class with the results: column number, variable name, and unit.

No.	Variable	Unit	No.	Variable	Unit	No.	Variable	Unit	No.	Variable	Unit
1	`TIME`	h	28	`LUMITOT0`	cm^{-2} s^{-1}	55	`ONCK2`	1	82	`XIY1`	1
2	`PPB`	1	29	`REDUC0`	1	56	`PARSEP2`	1	83	`XIM1`	1
3	`SIGS`	m	30	`BETX1`	m	57	`LREGION0`	m	84	`XIX2`	1
4	`RMSSIGS`	m	31	`BETY1`	m	58	`PLREGION0`	m^{-1}	85	`XIY2`	1
5	`FWHM`	m	32	`LUMITOT1`	cm^{-2} s^{-1}	59	`LTIME0`	s	86	`XIM2`	1
6	`DPP`	1	33	`REDUC1`	1	60	`PLTIMEN0`	s^{-1}	87	`XIXTOT`	1
7	`EPSXN`	m	34	`BETX2`	m	61	`PU0`	1	88	`XIYTOT`	1
8	`EPSYN`	m	35	`BETY2`	m	62	`PPUS0`	mm^{-1}	89	`XIMTOT`	1
9	`EPSXNIBS`	m	36	`LUMITOT2`	cm^{-2} s^{-1}	63	`PPUT0`	ns^{-1}	90	`LINT0`	fb^{-1}
10	`EPSYNIBS`	m	37	`REDUC2`	1	64	`LREGION1`	m	91	`LINT1`	fb^{-1}
11	`EPSXNSR`	m	38	`PHI0`	rad	65	`PLREGION1`	m^{-1}	92	`LINT2`	fb^{-1}
12	`EPSYNSR`	m	39	`SEPLR0`	σ	66	`LTIME1`	s	93	`LINT`	fb^{-1}
13	`EPSXNOBS`	m	40	`PHICR0`	rad	67	`PLTIMEN1`	s^{-1}	94	`RATE`	s^{-1}
14	`EPSYNOBS`	m	41	`ONCC0`	1	68	`PU1`	1	95	`LLIFETIME`	h
15	`EPSXNCC0`	m	42	`PHICK0`	rad	69	`PPUS1`	mm^{-1}	96	`STEPLENGTH`	s
16	`EPSYNCC0`	m	43	`ONCK0`	1	70	`PPUT1`	ns^{-1}	97	`LUMIINTSTEP`	cm^{-2}
17	`EPSXNCC1`	m	44	`PHI1`	rad	71	`LREGION2`	m	98	`PUINT0`	s
18	`EPSYNCC1`	m	45	`SEPLR1`	σ	72	`PLREGION2`	m^{-1}	99	`EPPUS0`	mm^{-1}
19	`TAUXIBS`	h	46	`PHICR1`	rad	73	`LTIME2`	s	100	`EPPUT0`	ns^{-1}
20	`TAUYIBS`	h	47	`ONCC1`	1	74	`PLTIMEN2`	s^{-1}	101	`PUINT1`	s
21	`TAUZIBS`	h	48	`PHICK1`	rad	75	`PU2`	1	102	`EPPUS1`	mm^{-1}
22	`TAUXCC0`	h	49	`ONCK1`	1	76	`PPUS2`	mm^{-1}	103	`EPPUT1`	ns^{-1}
23	`TAUYCC0`	h	50	`PHI2`	rad	77	`PPUT2`	ns^{-1}	104	`PUINT2`	s
24	`TAUXCC1`	h	51	`SEPLR2`	σ	78	`XIX0`	1	105	`EPPUS2`	mm^{-1}
25	`TAUYCC1`	h	52	`PHICR2`	rad	79	`XIY0`	1	106	`EPPUT2`	ns^{-1}
26	`BETX0`	m	53	`ONCC2`	1	80	`XIM0`	1	107	`STEP`	-
27	`BETY0`	m	54	`PHICK2`	rad	81	`XIX1`	1	108	`TYPESTEP`	-

4.5.9 Fill evolution: the `DoFill` function

The `DoFill(·)` function starts by creating the table output file (`NAMEtable`) containing the simulation settings (as printed by **`PrintLumiParam(·)`**) and virtual parameters (as computed by **`PrintVirtualLumiParam(·)`**):

```
def DoFill(self, beam):
  NAMEtable = "table_" + self._ID + ".out"
  FILEtable = open(NAMEtable, "w")
  beam.printBeamParam(self._longdens, tofile = True, foutname = FILEtable)
  ...
  self.PrintLumiParam(beam, tofile = True,  foutname = FILEtable)
  self.PrintVirtualLumiParam(beam, FILEtable)

  if self._table == True: sys.exit()
```

The Levelling program can be used to compute the virtual parameters only, that is, without performing the simulation for the entire fill (this is the case when the parameter **`table`** is **`True`** in **`Config`**). The full work-flow of the **`doFill(·)`** function is presented in Fig. 4.3. Aside from the level output file (**`NAMElevel`**) –the table to which the time-step evolution of each of the parameters in Table 4.5 will be written–, two additional auxiliary files are initialised:

```
  NAMElevel = "level_" + self._ID + ".out"
  FILElevel = open(NAMElevel, "w")
  self.WriteFILElevelHeaders(FILElevel, beam)
  ...
  NAMEupdateIBS = "updateIBS_" + self._ID + ".madx"
  FILEupdateIBS = open(NAMEupdateIBS, "w")
```

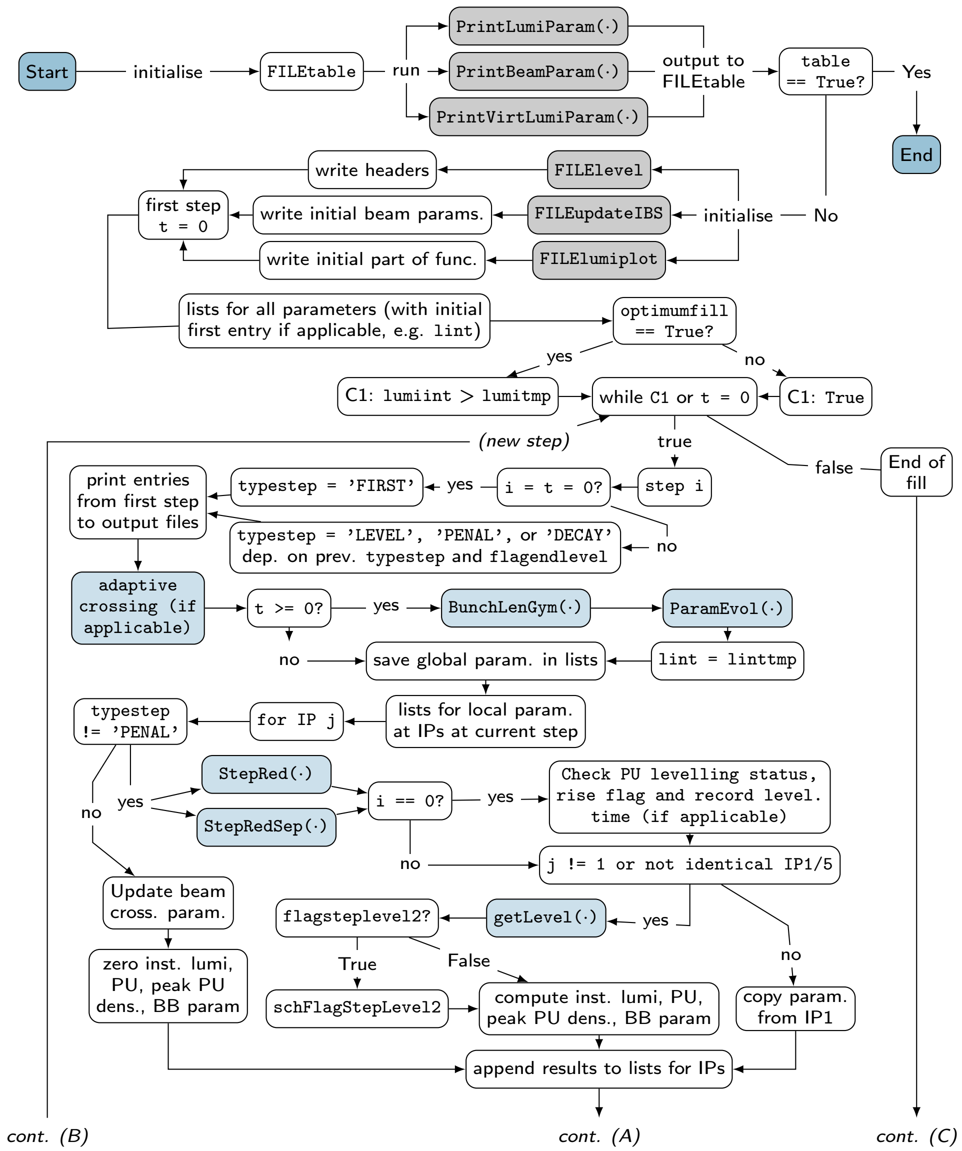

Figure 4.3. Work-flow of the `doFill1` function

```
print >> FILEupdateIBS, "! 0.0"
print >> FILEupdateIBS, "epsxn =", beam._epsn[0], ";"
...
NAMElumiplot = "lumiplot_" + self._ID + ".gnu"
FILElumiplot = open(NAMElumiplot, "w")
print >> FILElumiplot, "L_" + auxfuncclass.DotToDash(self._ID) + "(x,SECtoHR) = ",
print >> FILElumiplot, "x < 0 ? NaN : ",
```

`NAMEupdateIBS` stores the necessary beam parameters for the computation of the IBS

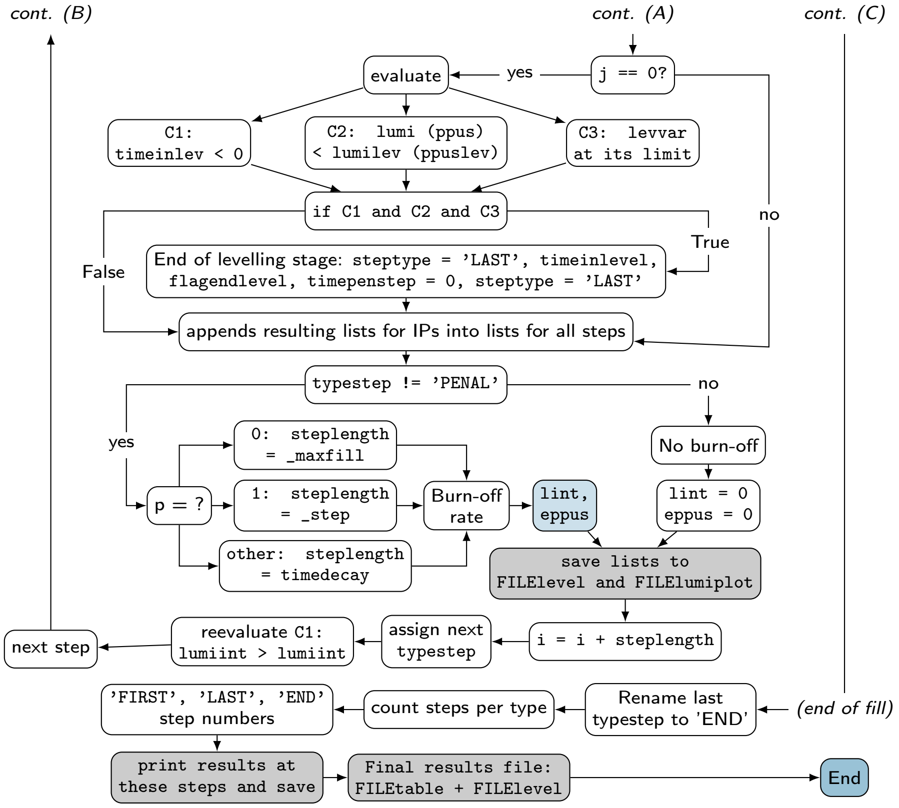

Figure 4.3. Work-flow of the `doFilll` function *(cont.)*

growth times at the first levelling step (`IBStauxz(·)` will append their magnitude in subsequent steps). `NAMElumiplot` is a file that stores a step-wise Gnuplot function describing the luminosity (in [$\mathrm{cm}^{-2}\,\mathrm{s}^{-1}$]) vs. time (in [s]), for plotting.

Prior to the start of the levelling loop, a series of auxiliary variables (counters and flags) are initialised, together with a series of lists that will store the values of all the parameters of interest at each step:

```
i = 0.;
countsteps = 0;  typestep = "FIRST";  timeinleveling = -1;  flagendlevel = False; ...
listTIME = [];  listPPB  = [];  listSIGS = [];  ...
```

In particular, `i` is the current step in the simulation, with an associated time (in [s]), and `typestep` is the type of step (see Table 4.6). The variable `timeinleveling` has the arbitrary value `-1` at the start of the fill, which will be replaced by the end time of the levelling stage. Due to the integrated luminosity at IP1 (or IP5, if identical) driving the optimum fill duration, special variables to monitor this quantity are defined, tracking its current and previous magnitude:

```
lint     = 0.;  linttmp     = 1.e-9
lintiall = [];  lintialltmp = [0.]*self._nip
puint    = [0.]*beam._nip;  eppus = [0.]*beam._nip;  epput = [0.]*beam._nip
ltot     = self._eff * self._days * 24*3600.
```

Table 4.6. Step types in the fill simulation.

`typestep`	Meaning
`"LEVEL"`	A levelling step (the levelling optics variable is adjusted such as the levelling target (luminosity or peak line PU density) matches its levelled threshold.
`"FIRST"`	The first step of the simulation (usually a `LEVEL` step).
`"PPUSL"`	If applicable, the first formal `LEVEL` step with levelling of the peak line PU density (after a first stage luminosity levelling).
`"LAST"`	The last `LEVEL` step of the levelling stage.
`"DECAY"`	A step where luminosity naturally decays after the levelling stage has concluded.
`"PENAL"`	If requested, a penalty step interleaved with `LEVEL` to simulate the loss on instantaneous luminosity (for a short period of time) due to the switch of optics corresponding to two consecutive levelling steps. Between two `DECAY` steps, its length is automatically set to zero in order to be neglected.
`"END"`	The last step of the simulation.

Also, special attention is given to the effective line and time PU densities at each IP, whose values are tracked by `eppus` and `epput`. The factor `ltot` is used for the extrapolation of the integrated luminosity per fill to the yearly integrated luminosity.

The program then proceeds to run the simulation of the fill, running as a loop in which the stop condition is determined by the `optimumfill` flag of `Config`: if `True`, the fill simulation stops once its duration corresponds to the optimum fill duration that maximises the yearly integrated luminosity (`linttmp > linttmpall`); otherwise, the simulation runs for a fixed fill duration `_maxfill`. Once inside the levelling loop, the `NAMElevel` and `NAMElumiplot` files are open to append the results to be obtained in the simulation of the current step. At the begining of each step, and before performing levelling, the different functions that update the beam parameters (emittance, bunch population, etc), or manipulate the bunch crossing angle or bunch length are called. The adjustment of the adaptive crossing angle is the first to be executed, followed by the bunch length and the parameter time evolution:

```
for j in range(beam._nip):
  if self._adaptivexsing[j] == True:
    self.GetPhiFromPPBFor6sigmaDA(beam, j)
if (i > 0.):
  self.BunchLengthGymnastics(beam, typestep)
  self.ParametersEvolution(beam, typestep, timedecay, listLUMITOTi)
  lint = linttmp
```

The latter functions are only applied for the second step onwards, together with the assignment of the value of the integrated luminosity in the previous step as the current one.

Once the series of updates above have been conducted, the global beam parameters are appended to their corresponding lists:

```
listTIME.append(i/3600.);  listPPB.append(beam._ppb);  listSIGS.append(beam._sigs); ...
```

A list for each of the optics- and luminosity-, and PU-related parameters of interest are then declared; these store the values of the corresponding variable for all IPs at the current step. At the end of present step, the entries of these lists are appended to the lists above:

```
betxall = [];  phiall = [];  ...;  lumiall = [];  lregionall = [];  puall = [], ...
```

Similarly to the general beam parameters, an update of the optics parameters at each IP has to be conducted, in particular, if the scenario features reduction of the normalised BBLR separation (either via the `StepReductionSeparation(·)` or the

`ReductionSeparation(·)` functions) or a program for the increase of the crabbing angle (executed by `IncrOncc(·)`) throughout the fill.

In the case of peak line PU density levelling, a special check has to be conducted at the beginning of each step to verify if this parameter has reached its maximum levelled threshold; if true, a flag (`_flagtimeppuslev`) is raised, and the current step is relabel as `"PPUSL"`. One more condition is checked before performing the levelling process; this allows to verify if the first and second IPs (associated to IP1 and IP5) are identical. If this is the case, the program can skip the calculations involved for the latter, and the results for its parameters can be directly inherited from the corresponding parameters for the first IP.

Finally, the levelling routine, conducted by the `GetLevel(·)` function (Section 4.5.2) is executed.[8] If the current step is a `LEVEL` (or `DECAY`) step:

```
if (typestep != "PENAL"):
  ...
  if (j != 1 or not beam._identicalIP01):
    if len(self._levtech[j]) > 1:
      for m in range(self._niterlev):
        for k in range(len(self._levtech[j])):
          lumitot = self.GetLevel(beam, j, self._levtech[j][k], self._levvar[j][k], i)
```

Once the levelling routine is completed, an additional check is conducted for IP8 to record the ending time of the levelling process at this IP (`_timesteplev2`, raising a flag (`_flagsteplev2`) and to count the number of elapsed steps (`_steplev2`); a similar check –discussed later– is also performed for the main IPs at the end of the `while` loop.

Regardless of the IP, at the end of the `GetLevel(·)` routine the magnitude of the levelling variable in the `Beam` class is as follows: if the current step is a `LEVEL` step, it is such that the levelled luminosity or levelled peak line PU density (depending on the requested case) are met; if the current step is a `DECAY` step, however, it corresponds to its limit (minimum or maximum, depending on the levelling variable), since the levelling stage has concluded at this point. For all cases the dependent beam parameters are subsequently updated, alongside the (peak) luminous region/time, PU, and PU densities.

```
    lregion  = self.GetLumRegion(beam, j)
    plregion = self.GetPeakLumRegion(beam, j)
    ...
    pu       = self.GetPileUp(beam._frev, lumitot[0], beam._nbunch[j])
    ppus     = pu*plregion/1e3
    ...
```

On the other hand, If the current step is a penalty step, an arbitrary zero-value is assigned to the luminosity and PU-related variables:

```
else:
  ...
  lumitot  = [0.]*self._nip;
  lregion = 0.;  plregion = 0.;  ...; pu  = 0.0;  ppus = 0.; ...
```

Independently of the type of step, the current value of each of the parameters at each IP at the end of the step is printed to the standard output, and appended to the corresponding list:

---

[8] `GetLevel(·)` is executed one or more times, depending on the requested `_niterlev` time; a number larger than one might be needed if more than one variable is used for the levelling (e.g. a scenario with the crab crossing and kissing angles), in order to find an optimum solution in a recursive way.

```
print "{0:36} {1:10}".format("Beta horizontal", "m"), "%1.8f" %beam._beta[j][0]
betxall.append(beam._beta[j][0]);
...
print "{0:36} {1:10}".format("Luminosity", "cm-2 s-1"),  "%1.6e" %lumitot[0]
lumiall.append(lumitot[0])
...

xi = self.GetBBParam(beam, j)
print "{0:36} {1:10}".format("BB tune-shift horizontal", "1"), "%1.4e" %xi[0]
xixall.append(xi[0])
...
```

Additionally, the transverse tune-shifts due to the beam-beam interactions are computed.

The duration of the fill simulation is driven by the first IP (either for an optimum fill or for a fixed fill duration). In order to determine the step that breaks the `while` levelling loop, several conditions are checked. While at this step, the `condition timeinleveling < 0` is technically still `True` (it will be `False` in subsequent steps, as the parameter `timeinleveling` will be assigned the time of the last step of levelling), two other conditions might not hold: the current luminosity (or peak PU density) being lower than its levelled threshold, and the levelling parameter reaching its limit:

```
if (j == 0):
  condition = timeinleveling < 0

  for k in range(len(self._levtech[j])):

    if self._levtech[j][k] == "levlumi":
      condition = condition and lumitot[0] < self._levlumi[j]
    elif self._levtech[j][k] == "levppus":
      condition = condition and ppusall[j] < self._levppus[j]

    if self._levvar[j][k] == "Beta":
      condition = condition and beam._beta[j][1-beam._xplane[j]] <=
                                beam._betamin[j][1-beam._xplane[j]]
    elif self._levvar[j][k] == "PhiCR":
      condition = condition and beam._phiCR[j] == beam._phi[j]
    elif self._levvar[j][k] == "PhiCK":
      condition = condition and beam._phiCK[j] == 0.0

  if condition:
    timeinleveling = i/3600.; flagendlevel = True
    self._timepenstp = 0.;    typestep     = "LAST"
```

When all this conditions are met, a flag `flagendlevel` is raised to indicate the last step of the levelling mode (the type of step is also relabeled as `"LAST"`), and the current time –i.e. the levelling time– is stored in `timeinleveling` parameter. Additionally, in case penalty steps were requested in the simulation, their duration is set to zero, as they are not necessary during the upcoming decaying stage of the fill (since they represent the time needed to pass from one levelling optics to the following). Independently of the type of step, the integrated luminosities at the IPs from previous step are then assigned as the current integrated luminosities, `lintiall.append(lintialltmp[j])`.

With the results for all the optics-, luminosity-, and PU-related parameters for all the IPs computed, they are then appended in the form of a list (for the current step) to the corresponding variable list:

```
listBETXi.append([]); ...; listLUMITOTi.append([]); ...,
listXIXi.append([]);  ...; listLINTi.append([])
...
for j in range(beam._nip):
  listBETXi[-1].append(betxall[j]); ...;  listLUMITOTi[-1].append(lumiall[j]); ...
  listXIXi[-1].append(xixall[j]);   ...;  listLINTi[-1].append(lintiall[j])
```

```
xixtot = sum(listXIXi[-1])
listXIXTOT.append(xixtot)

listLINT.append(lint)
```

From the beam-beam tune-shifts, an additional parameter for each coordinate is computed, the total tune shift. The lists containing the current contribution to the integrated luminosity at each IP (`listLINTi`) and the total integrated luminosity from all IPs (`listLINT`) are also appended to their corresponding lists. However, these are formally the luminosities integrated until right before the present step, as computed at the previous step. The contributions to the integrated luminosity from the current step will be computed later, and they will be passed to the following step as its *current* integrated luminosities. Once all the parameters have been appended in their corresponding list for the current step (including the general beam parameters), their values are saved in the `FILElevel` output file:

```
print >> FILElevel, "{0:16}".format("%1.8f" %listTIME[-1]),; ...;
for j in range(beam._nip):
  print >> FILElevel, "{0:16}".format("%1.8f" %(listBETXi[-1][j])),; ...;
  print >> FILElevel, "{0:16}".format("%1.8f" %(listLINTi[-1][j]*1e-39)),
print >> FILElevel, "{0:16}".format("%1.8f" %(listLINT[-1]*1e-39)),
```

The next task in the current step is precisely the computation of the total integrated luminosity (per fill), which depends on the instantaneous luminosity at each IP, the type of step and its duration `steplength`; the latter two are associated to the first IP only. For `LEVEL` steps (including `FIRST`, `LAST`, and `DECAY`), the step duration is the time (in [second]) it takes for the luminosity to decay to a fraction `_p` (defined in `Config`) of its original levelled value, as explained in Section 2.3.3. The loss rate of bunch particle population due to luminosity burn-off (in [s^{-1}], undestood as [ppb/s]) from all IPs is, according to Eq. (2.53),

```
rate = 0.
if (typestep != "PENAL"):
  for j in range(beam._nip):
    rate = rate + lumiall[j]*(self._xsecburn*1.e-27) / beam._nbunch[j]
```

Three cases of levelling at the first IP have to be distinghised. The case `_p = 0` corresponds mathematically to a step of infinite duration, at the end of which the instantaneous luminosity has decayed to zero (since the simulation cannot extend to infinite, the maximum fill duration `maxfill` is used instead); therefore, this case is equivalent to the absence of levelling, corresponding to a fill with natural decay only. The case `_p = 1` represents infinitely-short steps that keep the instantaneous luminosity exactly equal to its levelled value at all times (since reproducing this is not possible either, the simulation is conducted with steps of a fixed duration `_step`). For any case in between, the decaying time `timedecay` is computed from the solution of the analytic model for burn-off in Eq. (2.56):

```
  if (self._p != 0.):
    if (self._p != 1.): timedecay = (np.sqrt(1./self._p) - 1.) * beam._ppb/rate
    else:               timedecay = self._step
  else:                 timedecay = self._maxfill
  steplength = timedecay
```

Therefore, in case the current step is a levelling (or decaying) step, it will extend from time `i` to `i+timedecay`. This branch of the step-wise luminosity function at the first IP (IP1 and IP5, if identical) is appended in the `FILElumiplot` output file:

```
  print >> FILElumiplot, "x <=", str(i+timedecay)+"/SECtoHR", "?",
                         lumiall[0], "/ ( 1. + ( x -", str(i)+"/SECtoHR", ")*",
                         str(rate)+"*SECtoHR", "/", beam._ppb, ")**2", ": "  ,
```

The function describing the luminosity decay at each IP is then numerically integrated, and all the results summed to obtained the total integrated luminosity (per fill) at the current step:

```
for j in range(beam._nip):
  integrand = lambda t: lumiall[j] / (1. + (t-i)*rate/beam._ppb)**2
  linti = quad(integrand, i, i+timedecay)
  lintiall[j] = lintiall[j] + linti[0]
```

The contribution to the integrand luminosity from the first IP at the end of the current step is given special monitoring:

```
lumiint = lumiall[0]*beam._ppb/rate * ( 1. - 1./(1. + timedecay*rate/beam._ppb) )
```

To extrapolate the integrated luminosity per fill above to the yearly integrated luminosity, two factors that take into account the turn-around time are computed: one corresponding to the start of the current step (`factbef`) and the other to its expected ending (`factnow`):

```
factnow = ltot/ (i + timedecay + self._turnar*3600.)
factbef = ltot/ (i             + self._turnar*3600.)
```

These factors are also necessary to monitor the change in the slope of the yearly integrated luminosity with time.

The duration of `PENAL` steps, on the other hand, is simply `_timepenstp`, as specified in `Config`. In this case, no contribution is added to the integrated luminosity and the branch added to the step-wise function in `FILElumiplot` is a constant zero extending for the duration of the step. The `factnow` and `factbef` factors are also re-evaluated. For any type of step, the estimate on the total yearly integrated luminosity is stored in the temporary variable `lintialltmp`, and the results printed to the standard output. Another related parameter, the luminosity lifetime (in [h]) at the driving IP, is computed as follows:

```
if rate != 0.0: llifetime = beam._ppb/2./rate/3600.
else:           llifetime = 0.0
```

Its magnitude, together with the other luminosity-related parameters, is appended to their corresponding lists and stored in the `FILElevel` output file:

```
listRATE.append(rate);              listLLIFETIME.append(llifetime)
listSTEPLENGTH.append(steplength);  listLUMIINTSTEP.append(lumiint)
print >> FILElevel, "{0:16}".format("%1.8e" %listRATE[-1]),
...
```

As mentioned before, the computation of the extrapolated yearly integrated luminosity is conducted one step ahead:

```
linttmp = factnow*(linttmp/factbef) + factnow*lumiint
linttmpall.append(linttmp)
```

Its units are [cm^{-2}] per year, although it is usually expressed as [fb^{-1}/160 days] with the assumed number of days for physics within a year made explicit. At the end of each step, the ratio between the current integrated luminosity and its magnitude at the previous step monitors the fraction of the yearly integrated luminosiy corresponding to an optimum fill. Therefore, the `while` loop is broken once this fraction reaches 100 %.

Once the performance at the current step in terms of luminosity has been assessed, the performance in terms of the effective line and time PU densities (Section 3.2) is estimated using Eq. (3.32) as follows: for all IPs, the integral over the corresponding variable (s or t) of the PU density times the square of the variable is performed by the `GetIntSPUS2(·)` or `GetIntSPUS2(·)` functions; the result is then integrated over the duration of the current step (`listSTEPLENGTH[-1]`), normalised to the total integrated pile-up `puint`, and finally added to its former magnitude. Results for each IP (in the usual units of [events/mm^{-1}] and [events/ns^{-1}]) are appended to their respective lists:

```
puintall = [];  eppusall = [];  epputall = []
for j in range(beam._nip):
  intpus2 = self.GetIntSPUS2( beam, j, listPUi[-1][j]) /1e3
  intput2 = self.GetIntCTPUT2(beam, j, listPUi[-1][j]) /1e9
  if i == 0.0:
    puint =   listSTEPLENGTH[-1]*listPUi[-1][j]
    eppus = ( listSTEPLENGTH[-1]*intpus2 ) /puint
    epput = ( listSTEPLENGTH[-1]*intput2 ) /puint
  else:
    puint =                     listPUINTi[-1][j] + listSTEPLENGTH[-1]*listPUi[-1][j]
    eppus = ( listEPPUSi[-1][j]*listPUINTi[-1][j] + listSTEPLENGTH[-1]*intpus2 ) /puint
    epput = ( listEPPUTi[-1][j]*listPUINTi[-1][j] + listSTEPLENGTH[-1]*intput2 ) /puint
  puintall.append(puint);  eppusall.append(eppus);  epputall.append(epput)
```

In turn, results for all IPs at the current step are appended to `FILElevel`:

```
listPUINTi.append([]);  listEPPUSi.append([]); ...
for j in range(beam._nip):
  listPUINTi[-1].append(puintall[j]); listEPPUSi[-1].append(eppusall[j]); ...
  print >> FILElevel, "{0:16}".format("%1.8e" %listPUINTi[-1][j]),
  print >> FILElevel, "{0:16}".format("%1.8f" %listEPPUSi[-1][j]),
  ...
```

To conclude the current step of the simulation, a few last tasks have to be performed. First, the number and type of step is stored in `listSTEP` and `listTYPESTEP`, respectively, and saved in the levelling file. Second, the time variable `i` is updated depending on the type of step that is about to conclude and if penalty steps were requested:

```
if (typestep != "PENAL"):
  i = i + timedecay
  if (self._penstp == True):    typestep = "PENAL"
  else:
    if (flagendlevel == False): typestep = "LEVEL"
    else:                       typestep = "DECAY"
else:
  i = i + self._timepenstp
  if (flagendlevel == False):   typestep = "LEVEL"
  else:                         typestep = "DECAY"
countsteps = countsteps + 1
```

Lastly, the condition driving the loop of the simulation has to be re-evaluated with the current estimate on the yearly integrated lumnosity (if simulation of optimum fill was requested):

```
if self._optimumfill == True: cond1 = linttmp > linttmpall[-3] or linttmp == 0.0
else:                         cond1 = not self._optimumfill
```

The last step in `listTYPESTEP` is re-labelled as `"END"`, and a last branch to the step-wise function of the luminosity is appended. After appending its last contributions, the output files are closed for the present step. With this, the simulation of the next step is ready, and it will be performed if the conditions are met.

Upon completition of the fill simulation, some computations are conducted using the resulting lists containing the time-step-evolution of the parameters as input. The number steps spent in the levelling (`nls`), penalty (`nps`), decay (`nps`) stages (applicable for the driving IP), are then counted from the same list, and the total number of steps in the simulation is their sum. For IP8, the number of levelling steps and the corresponding time is determined using its associated flags (if a null separation was not reached before the fill ended, the total number of steps and the fill duration, respectively, are assigned instead).

The maximum value of the (peak) luminous region (time), PU, and peak line (time) PU density at each IP (as well as tune shift due to BB) are of special interest. These are easily found from their corresponding lists, and the results are appended to the `NAMEtable` output file. The values of all parameters at the start and at the end of the fill, as well as the end of the levelling mode, are also of special interest. To read them from their corresponding lists, the indices associated to those steps can be used. For the start and the end of the fill, the indices are straightforward: `k = 0` and the last index (the list length minus one), respectively. For the last step of levelling, the index is `k = 2*(nls-2)` if penalty steps were requested, and `nls-1` otherwise. The results are printed to the standard output and recorded in the `FILEtable` with the `fle` tag (`"first"`, `"last"`, or `"end"`) appended at the beginning of each variable name:

```
for k in [0, lastindex, endindex]:

  if   k == 0:               fle = "first"
  elif k == lastindex:       fle = "last"
  else:                      fle = "end"

  print >> FILEtable, "@", "{0:22} {1:4}".format(fle+"time",  "%le"), listTIME[k]
  print >> FILEtable, "@", "{0:22} {1:4}".format(fle+"ppb",   "%le"), listPPB[k]
  print >> FILEtable, "@", "{0:22} {1:4}".format(fle+"sigs",  "%le"), listSIGS[k]
  print >> FILEtable, "@", "{0:22} {1:4}".format(fle+"epsxn", "%le"), listEPSN[k][0]
  ...
  for j in range(beam._nip):
    print >> FILEtable, "@", "{0:22} {1:4}".format(fle+"betx"+str(j), "%le"), listBETXi[k][j]
    print >> FILEtable, "@", "{0:22} {1:4}".format(fle+"phi" +str(j), "%le"), listPHIi[k][j]
    print >> FILEtable, "@", "{0:22} {1:4}".format(fle+"lumi"+str(j), "%le"), listLUMITOTi[k][j]
    print >> FILEtable, "@", "{0:22} {1:4}".format(fle+"pu"  +str(j), "%le"), listPUi[k][j]
    ...
    print >> FILEtable, "@", "{0:22} {1:4}".format(fle+"lintfb"+str(j), "%le"), listLINTi[k][j]*1.e-39
```

Lastly, the final results related to the driving IP (such as the total fill duration, the counts of the different type of steps, the performance in terms of the total yearly integrated luminosity and effective line (time) PU density, as well as the state of several flags) are also output to the table file:

```
print >> FILEtable, "@", "{0:22} {1:4}".format("filltime", "%le"), listTIME[-1]
print >> FILEtable, "@", "{0:22} {1:4}".format("lintfb",   "%le"), listLINT[-1]*1.0e-39
print >> FILEtable, "@", "{0:22} {1:4}".format("nls",      "%d" ), nls
...
for j in range(beam._nip):
  print >> FILEtable, "@", "{0:22} {1:4}".format("puint"+str(j),      "%le"), listPUINTi[-1][j]
  print >> FILEtable, "@", "{0:22} {1:4}".format("maxlregion"+str(j), "%le"), maxlregion[j]
  print >> FILEtable, "@", "{0:22} {1:4}".format("maxxixtot",         "%le"), maxxixtot
  ...
```

The table and level files are then joined into a single final results file (`NAMEresults`).

4.6 Other modules

4.6.1 `Levelling_Others.py`

This module defines several classes. The `Constants` class provides a lists of physical and mathematical constants (including the proportionality factors between the different density distributions: Gaussian, super-Gaussian of order 4, and q-Gaussian). `qGaussianAux` defines functions that describe the limit of integration of a q-Gaussian distribution. `Banners` handle the printing of banners –with several formats– in the default output to report the simulation progress. Lastly, `AuxFunc` defines several functions with general purposes (to interpret input in `Levelling_Run.py`, to format labels, etc.).

4.6.2 `Levelling_jobtau.madx`

The `Levelling_jobtau.madx` file contains a mask used for the calculation of the IBS growth times with MAD-X (Section 2.2.2). The mask calls the files that defines the machine lattice of interest (defined in `Config`) and the beam parameters at the step in which it is called (as created by `IBStauxz(·)`). After loading the sequence, it creates the `beam` object with the loaded beam parameters (energy, bunch population, beam size and energy spread, and transverse emittances). The `twiss` function is then run, followed by the `ibs` command [70]. The resulting horizontal and vertical IBS times, expressed in [h], are stored in an output file that will in turn be called by `ParametersEvolution(·)` for the computation of the emittance evolution in the following step.

4.6.3 `Levelling_RunJobs.sh`

`Levelling_RunJobs.sh` is a script written in `Bash` which handles the run in parallel of multiple scenarios (listed in the `Levelling_List.txt` input file). For each case, a unique directory storing a temporary copy of the different Levelling scripts is created in the home directory `HOMEDIR`. From each directoy, the simulation is submitted as a parallel job in the batch service of CERN AFS service [98], with `8nh` the default queue[9] –available for 8 h– as simulations typically run from 15 min to a couple of hours. Each job runs the local `Levelling_Run.py` module for the corresponding scenario using the `-n` option. Once a simulation is finished, results are copied from their temporary location in the remote host to their corresponding directory in `HOMEDIR`, and all temporary files are deleted.

4.6.4 `Levelling_Distributions.py`

Once the simulation of the optimum fill of a given scenario is completed, the `Levelling_Distributions.py` module can be run separately to compute the 1D and/or 2D PU densities (Section 2.4) for a given IP and step. The module can be called with several options: `-n` (`--name`), the name of the results file; `-i` (`--ip`), the number of the IP (`0`, `1`, or `2` for IP1, IP2, or IP8, respectively); and `-s` (`--step`), the step of levelling process (use `FIRST` or `LAST` or an integer for the step number). These options are then used to create an instance of the `Densities` class, from which the `GetDistribution(·)` method is called (Section 4.4) which reconstructs of the PU densities as described below.

First, the relevant beam and optics parameters at the chosen IP and at the requested step are read from the results file (imported as a table using Mapclass). The default ranges of the four different coordinates over which the PU densities will be computed, as well as their resolution (`nstep0`) are the following:

```
nstep0 = 200;  xrang0 = 100.e-6;  yrang0 = 100.e-6;  srang0 = 250.e-3;  trang0 = 1.e-9
```

The normalisation factor of the PU densities (in units of [1/events]) is then computed using the integral of the event density over all the variables:

---

[9] Other available queues are, for example, `1nd` and `2nd`, for one and two days, respectively.

```
norm = self.IntAll(phi, sigs, betc, ..., parsep) / pu
```

While for IP8 (where levelling is performed exclusively with parallel separation) the 1D projections for all the coordinates are computed, only the line and time PU densities are currently available for IP1/5 (due to the more complex nature of the collision which can include also crab crossing and crab kissing); the 2D projection in $s - t$, however, is computed for all IPs.

The computation of the 1D PU density for any given coordinate is described in the following, using the longitudinal coordinate `s`, Eq. (2.64), as example. Running a loop over the range of the variable in question in steps, the corresponding integral over the density is performed (in this example, the integral over time), and the results stored in the `NAMEdenss` output file:

```
NAMEdenss = resultsname + "." + str(ip) + "." + ’s’ + "." + str(step)
FILEdenss = open(NAMEdenss, "w")
print >> FILEdenss, "* {0:12} {1:14}".format("S",   "PUS")
print >> FILEdenss, "$ {0:12} {1:14}".format("%le", "%le")
srang  = srang0;  snstep = nstep0
for s in np.arange(-srang, srang*(1.+2./snstep), 2*srang/snstep):
  pus = self.IntCT(s, phi, sigs, ..., parsep) / norm
  print >> FILEdenss, "{0:14} {1:14}".format(%s, %pus)
FILEdenss.close()
```

The units of `S` and `PUS` are [m] and [m^{-1}], respectively. A similar computation is performed to obtain the time PU density, Eq. (2.65); in this case, however, the integral is performed over the longitudinal coordinate, and the results for `T` and `PUT` are given in [s] and [s^{-1}], respectively. In the case of the projections of the PU density along the horizontal or vertical coordinates, Eq. (2.68), the integrals are performed with `IntAll_withx(·)` or `IntAll_withy(·)` (which have `x` or `y` as explicit variables of the density), and the units `X` and `PUX` (or `Y` and `PUY`) are [m] and [m^{-1}], respectively.

Lastly, a simple evaluation of the integrands is enough for the computation of the 2D PU density (see Eq. (2.67)), as they are defined as a function of s and t. However, special attention has to be given to the cases with integrands with q-Gaussian bunch profiles, as the domain is finite:

```
for s in np.arange(-srang, srang*(1.+2./snstep), 2*srang/snstep):
  for t in np.arange(-trang, trang*(1.+2./tnstep), 2*trang/tnstep):
    ...
    if longdens == "qGaussian":
      ...
      if((s >= qGAux.szero and (ct <= qGAux.Cct(s)and ct >= qGAux.Bct(s))) or
         (s <  qGAux.szero and (ct <= qGAux.Act(s) and ct >= qGAux.Dct(s))) ):
        pust = self.Evaluate_integrand(ct, s, phi, ...) / norm * cst.clight
      else: pust = np.NaN
    else:
      pust = self.Evaluate_integrand(ct, s, phi, ...) / norm * cst.clight
    print >> FILEdens, "{0:14} {1:14} {2:14}".format(%s, %t, %pust)
```

In this case, the output file has three columns: the value of the longitudinal and time coordinates at each step (in the same units described above), and the PU density, expressed in [$\mathrm{m}^{-1}\,\mathrm{s}^{-1}$]. The `GetDistribution(·)` function can be expanded to include the computation of 2D projections in any pair of coordinates (e.g. x–t or y–t), for which the proper integrands have first to be found and then to be included in `Densities(·)`.

Chapter 5

Performance of the HL-LHC baseline

The HL-LHC baseline parameters with *standard* filling scheme for both the nominal and ultimate levelling operation are presented in Section 5.1. Using the tools presented in the previous chapter, simulations of the corresponding optimum fill are conducted and the parameters evolution are described in detail. Special emphasis is given to the estimation of the performance at the two main IPs, evaluated in terms of two main figures-of-merit, namely the integrated luminosity and the effective PU density. Results for the baseline constitute the reference frame for the comparisons of all other operational scenarios in this work. To enrich the baseline framework, an intensive study on the sensitivity of its parameters is also presented. The case of the so-called BCMS filling scheme, two cases aiming at the improvement of the performance (with electromagnetic wires and adaptive crossing angle), and the case of operation at a beam energy of 7.5 TeV, are of special interest and they are analysed afterwards. Lastly, the baseline operation of IP8 is reviewed and compared against a series of proposed alternative configurations that aim at delivering high luminosity for the LHCb experiment.

5.1 Standard parameters

The latest HL-LHC baseline parameters [3] aim at meeting the original project's goals with only two crab cavities per beam and per IP side [37, 90]. In the following, the main beam and optics parameters, summarised in Tables 5.1 and 5.2, are described in detail. These parameters constitute the input for the simulation of the baseline optimum fill and the estimation of its performance using the LEVELLING program.

Table 5.1. General parameters of the HL-LHC baseline standard and BCMS.

Parameter	Unit	Standard	BCMS
Beam energy	TeV	7.0	7.0
Total number of bunches per beam	1	2760	2748
Bunch population (ppb)	10^{11}	2.2	2.2
Total beam current	A	1.10	1.10
Longitudinal profile	–	q-Gaussian	q-Gaussian
RMS bunch length	cm	7.6	7.6
Full width at half maximum	cm	21.2	21.2
Relative energy spread	10^{-4}	1.07	1.07
Normalised transverse emittance	µm	2.5	2.5

Table 5.2. Optics and virtual parameters at IP1/5 of the scenarios in Table 5.1.

Parameter	Unit	Standard	BCMS
Number of colliding bunches	1	2748	2736
Minimum $\beta^*_{\times,\parallel}$	cm	15.0	15.0
Full crossing angle	µrad	500	500
Minimum norm. BBLR separation	σ	10.5	10.5
Piwinski parameter	1	2.66	2.66
Full crabbing angle	µrad	380	380
Virtual luminosity	$10^{34}\,\mathrm{cm}^{-2}\,\mathrm{s}^{-1}$	16.95	16.88
Virtual pile-up	1	444	444
Virtual loss factor	1	0.716	0.716
Virtual beam-beam	10^{-2}	0.86	0.86

Operating at the design LHC beam energy of 7.0 TeV, the current HL-LHC baseline features increased bunch populations (2.2×10^{11} protons per bunch ppb) and a small β^* and crossing angles at the IP1 and IP5 (where the ATLAS and CMS experiments are located, respectively) with respect to the LHC. A normalised transverse emittance of 2.5 µm is assumed at the beginning of the fill. For the current HL-LHC parameters, an increased number of colliding bunches at the two main IPs and shorter turn-around times with respect to the original HL-LHC design are also assumed [99].

As presented in Section 2.3.1, the transverse bunch density is well described by Gaussian distributions. Previous works considered also a Gaussian distribution for the modelling of the longitudinal profile [34]. Based on observations in the LHC [33], however, the latter is better described by a q-Gaussian distribution (Appendix A.1),

$$\varrho_s^{\mathrm{qG}}(s) \equiv \frac{\sqrt{32}}{5\pi\sigma_{s_{\mathrm{qG}}}}\left(1 - \frac{s^2}{8\sigma^2_{s_{\mathrm{qG}}}}\right)^{5/2} \quad , \quad |s| \leq \sqrt{8}\sigma_{s_{\mathrm{qG}}} \; , \tag{5.1}$$

with a q-Gaussian RMS bunch length of $\sigma_{s_{\mathrm{qG}}} = 7.61\,\mathrm{cm}$ (for a Gaussian-equivalent RMS bunch length of 9.0 cm [100]). Together with the bunch length, the full width at half maximum of FWHM = 21.19 cm –a parameter of interest due to its relation with the longitudinal beam stability [32, 85, 100]– is kept constant along the fill.

With the *standard* filling scheme [35, 36, 101], 2748 bunches pairs collide at IP1 and IP5. The HL-LHC baseline makes use of round optics with minimum β^* =

Table 5.3. Parameters for the estimation of the yearly integrated luminosity at IP1/5 of the HL-LHC operational scenarios at nominal and ultimate levelling.

Parameter	Unit	Nominal	Ultimate
Days in physics (within a year)	days	160	160
Efficiency	%	50	50
Turn-around time	min	145	150

15 cm; this value, however, is larger at the beginning of the fill due to luminosity levelling. Collisions at the main IPs are performed with a constant full crossing angle of 500 µrad throughout the fill (or equivalently, with a beam-beam normalised separation of 10.5σ for the minimum β^*). The two CCs per beam per IP side with an RF voltage of 3.4 MV [102] allow to rotate the colliding bunches by 380 µrad, thus partially compensating the crossing angle and allowing to reach a virtual luminosity of almost $17 \times 10^{34}\,\mathrm{cm^{-2}\,s^{-1}}$.

For the simulation of the fill evolution, the effects of radiation damping and IBS, as described in Section 2.2, are taken into account for both transverse planes and assuming a vertical/horizontal coupling factor of $1/\kappa_c = 10$. Unlike previous studies [103, 104], no additional source of vertical emittance growth is included. To compensate for the luminosity decay due to beam burn-off (computed with a conservative total cross-section of 111 mb), luminosity levelling with β^* and a luminosity step of 2 % ($p = 0.98$) is assumed (Section 2.3.2). Two levelled luminosities, namely $5.0 \times 10^{34}\,\mathrm{cm^{-2}\,s^{-1}}$ and $7.5 \times 10^{34}\,\mathrm{cm^{-2}\,s^{-1}}$ –or their corresponding PU levels– define the *nominal* and *ultimate* operation,[1] respectively, for the baseline and any alternative scenario.

The relevant parameters for the estimation of the yearly integrated luminosity $\mathcal{L}_{\mathrm{int}}$ via extrapolation of its corresponding integrated luminosity per fill –according to Eq. (2.58)– are listed in Table 5.3 [3].The difference of five minutes of turn-around time between nominal and ultimate operation derives from the additional squeeze necessary at the latter operation. The reduction of the turn-around times from 3 h in the original HL-LHC design to the current estimates is a result from the foreseen implementation of a combined ramp and squeeze, shortening of the squeeze time, and the reduction of the ramp-down time after a physics fill [99].

5.1.1 Nominal

In the following, the evolution of the optimum fill for the HL-LHC baseline at nominal levelling –as seen in Fig. 5.1– is described in detail. As the fill progresses, the bunch population is burned-off in an almost linear fashion, only slightly deviating from such behaviour by the end of the fill. Despite the normalised emittance starting at 2.5 µm in both transverse directions, its evolution for each coordinate is different: horizontal emittance is initially dominated by IBS and grows until reaching a maximum of around 2.67 µrad after 6 h; after this point, SR dominates, and it begins to shrink. Due to the effect of IBS being a factor of 10 smaller for the vertical plane with respect to the

---

[1] Previous works conducted with higher estimates of the cross-section for PU [86] and/or slightly higher $\mathcal{L}_{\mathrm{lev}}$ [105], provided $\mu = 140$ (200) events per bunch crossing for the nominal (ultimate) operation. These values, slightly above the current estimates, are still commonly used in studies on the detector performance in the HL-LHC era by the experiments.

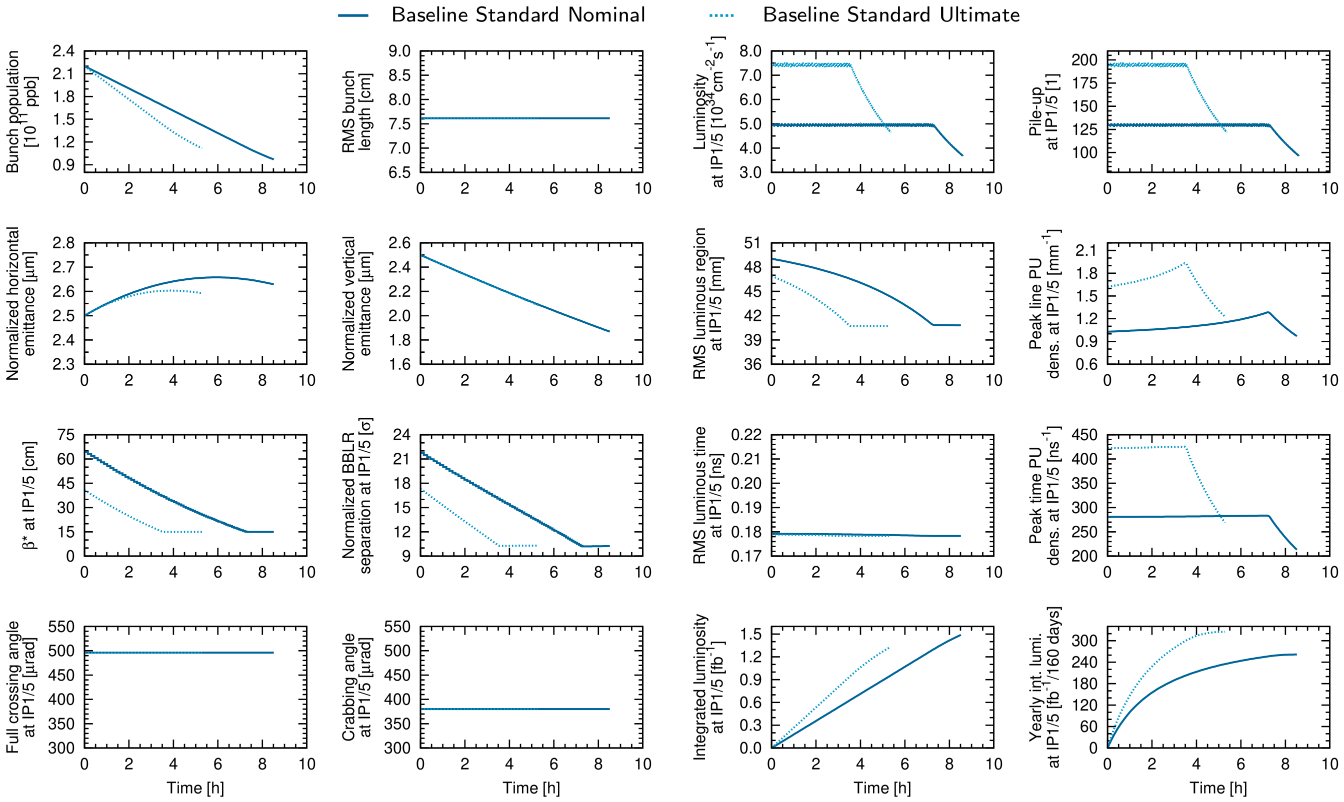

Figure 5.1. Evolution at IP1/5 of the optimum fill in the HL-LHC baseline standard at nominal and ultimate levelling.

Table 5.4. Performance at IP1/5 of the scenarios in Table 5.2.

Parameter	Unit	Standard		BCMS	
		Nominal	Ultimate	Nominal	Ultimate
Levelled luminosity	$10^{34}\,\mathrm{cm^{-2}\,s^{-1}}$	5.0	7.5	5.0	7.5
Levelled pile-up	1	131	197	132	197
At the start of the fill					
$\beta^*_{\times,\parallel}$	cm	64.1	40.7	64.1	40.7
Norm. BBLR sep.	σ	21.7	17.3	21.7	17.3
RMS luminous region	mm	49.0	46.9	49.0	46.9
RMS luminous time	ns	0.179	0.179	0.179	0.179
Peak line PU density	$\mathrm{mm^{-1}}$	1.03	1.63	1.03	1.63
Peak time PU density	$\mathrm{ns^{-1}}$	282	424	282	424
At the end of the levelling					
$\beta^*_{\times,\parallel}$	cm	15.0	15.0	15.0	15.0
Norm. BBLR sep.	σ	10.2	10.3	10.2	10.3
RMS luminous region	mm	40.9	40.7	40.9	40.7
RMS luminous time	ns	0.178	0.178	0.178	0.178
Peak line PU density	$\mathrm{mm^{-1}}$	1.29	1.94	1.29	1.94
Peak time PU density	$\mathrm{ns^{-1}}$	285	427	285	427
Fill duration	h	8.5	5.3	8.4	5.3
Levelling time	h	7.3	3.5	7.2	3.5
Number of levelling steps	1	67	44	67	44
Integrated luminosity per fill	$\mathrm{fb^{-1}}$	1.49	1.32	1.47	1.31
Yearly integrated luminosity	$\mathrm{fb^{-1}}$/160 days	262	325	261	324
Diff. w.r.t. base. std. nom.	%	ref.	+24.4	−0.2	–
Diff. w.r.t. base. std. ult.	%	–	ref.	–	−0.3
Effective line PU density	$\mathrm{mm^{-1}}$	0.79	1.20	0.80	1.20
Diff. w.r.t. base. std. nom.	%	ref.	+50.9	+0.6	–
Diff. w.r.t. base. std. ult.	%	–	ref.	–	+0.4
Effective time PU density	$\mathrm{ns^{-1}}$	200	288	201	289
Diff. w.r.t. base. std. nom.	%	ref.	+44.4	+0.6	–
Diff. w.r.t. base. std. ult.	%	–	ref.	–	+0.3

horizontal, the vertical emittance is dominated by SR, which yields to a continuous reduction down to 1.87 µm by the end of the fill.

Due to the implementation of β^*-levelling, the betatron function at the main IPs is larger than its minimum value of 15 cm at the beginning of the fill. With nominal operation, $\beta^* = 64\,\mathrm{cm}$ accomplishes the reduction of the luminosity from its virtual to its levelled values. Since the crossing angle is kept constant at 500 µrad for the baseline, this corresponds to a normalised BBLR separation of 21.8σ at the beginning of the fill (instead of its minimum of 10.5σ). Similarly, the full crossing angle and crabbing angle at IP1/5 (as well as the RMS bunch length) are kept constant along the fill. Thus, the compensation of the crossing angle by the CCs ($\theta_{\mathrm{CC}}/\theta \approx 76\,\%$), remains always constant. The minimum β^* is reached after 7.3 h of levelling, during which 67 steps are implemented to keep the luminosity within a 2 %-margin from its levelled value. After the minimum β^* has been reached, the instantaneous luminosity is left to naturally decay for another 1.2 h, corresponding to the optimum fill duration. It is important to note that a large number of levelling steps might pose an operational challenge, as each of them represents a different optics for commissioning [6, 9, 10, 106, 107].

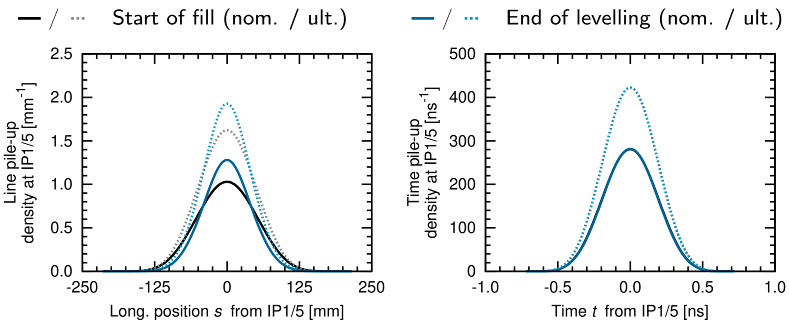

Figure 5.2. Line and time PU densities at IP1/5 at the start of the fill and at the end of the levelling in the HL-LHC baseline. Both the nominal or ultimate time PU densities remain almost unchanged throughout the fill.

The nominal levelled luminosity of $5.0 \times 10^{34}\,\mathrm{cm}^{-2}\,\mathrm{s}^{-1}$ yields a PU of $\mu = 131$ events per bunch crossing at IP1/5, an acceptable number in view of the detector capabilities. The integrated luminosity per fill at each of the main IPs grows linearly as the fill evolves due to levelling, only slowing down its rate at the second stage of the fill when the luminosity is left to naturally decay. The optimum fill duration for the baseline nominal with the current set of parameters is around 8.5 h, delivering $1.5\,\mathrm{fb}^{-1}$ per fill. Assuming the efficiency discussed above, the corresponding estimate for $\mathcal{L}_{\mathrm{int}}$ of the HL-LHC baseline at nominal levelling via extrapolation of the latter is $262\,\mathrm{fb}^{-1}$, thus surpassing the project's current goal.

As pointed out before, the integrated luminosity is a parameter of interest due to its relation with the number of events to be recorded by the two main experiments; its current estimate has profited from a series of changes to the baseline parameters. Reduction of the turn-around time to the current values for the nominal (and ultimate) operations have led to an increment of around 6 % with respect to estimates with the previously-assumed 3.12 h (or 187 min). The adoption of a q-Gaussian bunch profile for simulations is solely responsible, on the other hand, of a 2 % increase on the estimate of the nominal integrated performance when compared to a Gaussian longitudinal density (9 cm bunch length). The reduction of β^* from 20 cm (assumed in Ref. [104]) to 15 cm yields to a gain of roughly 3 % on the nominal $\mathcal{L}_{\mathrm{int}}$. Further performance increments ranging from 3 % to 23 % can be expected under a series of conservative or relaxed configurations, according to several studies on machine availability [82, 108, 109].

Regarding the second figure-of-merit, the effective PU density –the parameter related to the quality of the data at the detectors–, current estimates are found to be around $\bar{\rho}_s = 0.80\,\mathrm{mm}^{-1}$ and $\bar{\rho}_t = 200\,\mathrm{ns}^{-1}$, respectively, for its line and time projections. The comparisons of the performance of several alternative operational scenarios with the baseline are presented, in the following sections and chapters, in terms of the yearly integrated luminosity and the effective line PU density.

A detailed characterisation of the multidimensional distribution of event vertices is of great interest for the experiments [17, 20] as it is crucial to perform realistic detector simulations, and it is described below for the baseline nominal. At the start of the fill, the RMS luminous region (projection along s) is 49 mm, but it shortens to about 41 mm by the end of the levelling process, after which it remains almost constant. Due to this, the peak of the line PU density grows from its initial value of around

Table 5.5. Parameters of the Gaussian fits of the line and time PU densities at IP1/5 of the scenarios in Fig. 5.2.

Parameter	Unit	At the start of the fill Nominal	 Ultimate	At the end of levelling Nominal	 Ultimate
σ_s	mm	50.9	48.5	40.8	40.7
σ_t	ns	0.186	0.186	0.184	0.184
$\hat{\rho}_s$	mm^{-1}	1.04	1.63	1.27	1.91
$\hat{\rho}_t$	ns^{-1}	284	426	284	426

$1\,\mathrm{mm}^{-1}$ to a maximum of $1.28\,\mathrm{mm}^{-1}$ (when the RMS luminous region is minimum) and then it proceeds to decay. It was found that the adoption of the q-Gaussian bunch density is responsible of a slight decrease of the RMS luminous region and, in consequence, an increase of a few percent on $\bar{\rho}_s$ as compared with simulations with Gaussian longitudinal densities. In the case of the RMS luminous time and peak time PU density, they remain almost constant at around 0.180 ns and $280\,\mathrm{ns}^{-1}$, respectively, along the fill, although the latter starts to decay as the luminosity naturally decays. The main parameters described above are summarised in Table 5.4 for reference.

Figure 5.2 shows the one-dimensional event distribution on the longitudinal and temporal coordinates at the beginning of the fill and at the end of the levelling. The most critical stage for the experiments takes place at the end of the fill as the line PU density sharpens: the peak number of events reaches its maximum, and they are distributed in a narrower region. Due to the observed shape of these densities, Gaussian fits (see Eq. (3.35)) of the form

$$\rho_v(v) = \hat{\rho}_v \exp\left(-\frac{v^2}{2\sigma_v^2}\right), \qquad v = s, t, \tag{5.2}$$

obtained by the optimisation method of least squares, were applied with the aim of providing the experiments with the parameters to realistically reproduce the luminous region and time. Table 5.5 lists the resulting parameters of the corresponding Gaussian fits; comparison between $\hat{\rho}_u$ and σ_u with the corresponding peak line/time PU densities and RMS luminous region/time in Table 5.4 –which were computed numerically directly from the luminosity integral– shows a good agreement. An illustrative two-dimensional projection of the PU density in both the s and t coordinates is shown in Fig. 5.3, where a common scale has been employed for all the cases to better appreciate its evolution.

5.1.2 Ultimate

The ultimate operation of the HL-LHC baseline with standard filling scheme exhibits a similar general behaviour than the nominal, as seen in Fig. 5.1. The levelling time and fill duration, however, are shorter due to the larger levelled luminosity, namely 5.3 h and 3.5 h. In ultimate operation, the levelled luminosity of $7.5 \times 10^{34}\,\mathrm{cm}^{-2}\,\mathrm{s}^{-1}$ corresponds to a PU of around $\mu = 200$ events per bunch crossing, the maximum value tolerable by the experiments. Regarding the optics, β^* and d_{BBLR} are 41 cm and 17.3σ, respectively, at the start of the process, while the full crossing angle and crabbing angle, as well as the minimum β^* and minimum d_{BBLR} remain equal to the nominal operation at the end of the levelling stage (which involves 44 steps).

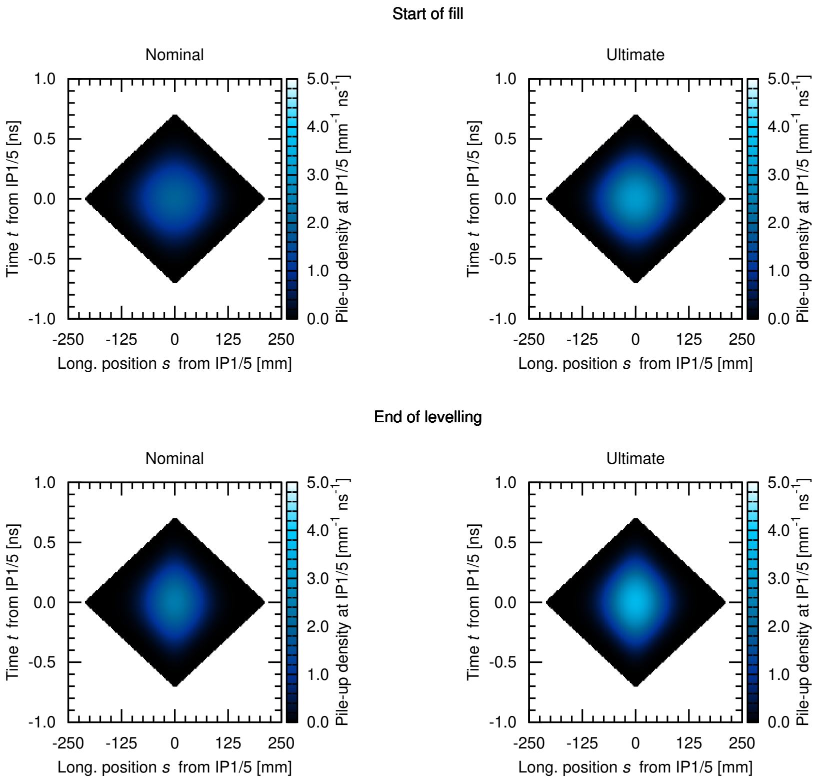

Figure 5.3. Line-time PU densities at IP1/5 at the start of the fill and at the end of the levelling in the HL-LHC baseline.

Due to the larger PU level, a significant increment is experienced by the line PU density, which reaches a maximum of $1.93\,\mathrm{mm}^{-1}$ at the end of the levelling. As in the nominal operation, the local densities of events are well-described by Gaussian distributions. The yearly integrated luminosity of the HL-LHC baseline ultimate is found to be $325\,\mathrm{fb}^{-1}$, thus meeting the current goal for this levelling; this represents an increment of 24 % with respect to the nominal. While the effect on performance from the use of a q-Gaussian bunch profile instead of Gaussian is found to be negligible at ultimate operation, reduction of the turn-around time to the current ultimate value is responsible of a 7 % increase on $\mathcal{L}_{\mathrm{int}}$; the reduction of β^* from 20 cm to 15 cm, on the other hand, is responsible of a gain of more than 6 %. At ultimate operation, the effective PU density is $\bar{\rho} = 1.20\,\mathrm{mm}^{-1}$, that is, it rises by around 50 % with respect to the nominal. A detailed characterisation of the line and time PU densities with the parameters of the corresponding Gaussian fits at the beginning and at the end of the levelling process for ultimate operation has been included in Table 5.5.

5.2 BCMS parameters

Operation with the bunch-compression-merge-and-split (BCMS) filling scheme [35, 36, 101, 110] results in a slightly lower total number of bunches in each beam (2748) and colliding pairs at the two main IPs (2736), which in turn translates into a slight reduction of the virtual luminosity ($\mathcal{L}_{\mathrm{virt}} = 16.88 \times 10^{34}\,\mathrm{cm}^{-2}\,\mathrm{s}^{-1}$). Similar simulations to the baseline standard are performed for the BCMS case, and the results are included in Table 5.4. Small to negligible differences are found for the values of the β^* and normalised separation and the beginning of the fill, as well as for the RMS luminous region/time and peak line/time PU densities, at both nominal and ultimate operation. The reduction of $\mathcal{L}_{\mathrm{int}}$ with the BCMS filling scheme remains below 0.3 % for both levelling operations with respect to the standard filling scheme. The effective line and PU densities at nominal and ultimate operation, on the other hand, increase by around 0.6 % and 0.3-0.4 %, respectively, with respect to their standard counterparts.

5.3 Sensitivity studies

In this section, the effect on the performance of the HL-LHC baseline[2] from the variation of the magnitude of several beam, machine, and operational parameters is studied. When applicable, the dependency of the virtual luminosity at the main IPs with the parameter under consideration is first examined; then the effects on the fill duration, levelling time, and performance are reviewed. These studies allow to better understand the risks of the current baseline configuration, as well as mapping its potential improvements.

5.3.1 Beam and optics parameters at IP1/5

Beam parameters such as bunch population, transverse emittance and bunch length is reviewed first, followed by the study of the effect of different β^* and crossing angles, as well as the fraction of compensation by means of bunch crabbing.

5.3.1.1 Bunch population

The HL-LHC aims at operating at a bunch population of 2.2×10^{11} ppb, almost doubling that of the LHC design. The top-left plot of Fig. 5.4 shows a scan of $\mathcal{L}_{\mathrm{virt}}$ for the *baseline* as a function of initial bunch population while keeping all the other parameters unchanged (in particular, the luminosity step of 2 %). A reduction of the bunch population to 1.5×10^{11} ppb results in a reduction of more than 50 % of virtual luminosity. Pushing the bunch population to 2.5×10^{11} ppb, on the contrary, yields to an increase of almost 30 %. These variations, however, do not automatically translate into the same increments/decrements of $\mathcal{L}_{\mathrm{int}}$ due to the levelling process.

The effect of the bunch population on the parameters of interest is shown in the rest of the plots in Fig. 5.4 for both nominal and ultimate operation. Plots in the second and forth columns show the fractional variation of the corresponding parameter in the plot to its left with respect to the HL-LHC with full (unchanged) baseline parameters

---

[2] From this point, any reference to the HL-LHC baseline corresponds to the baseline with the *standard* filling scheme, unless stated otherwise

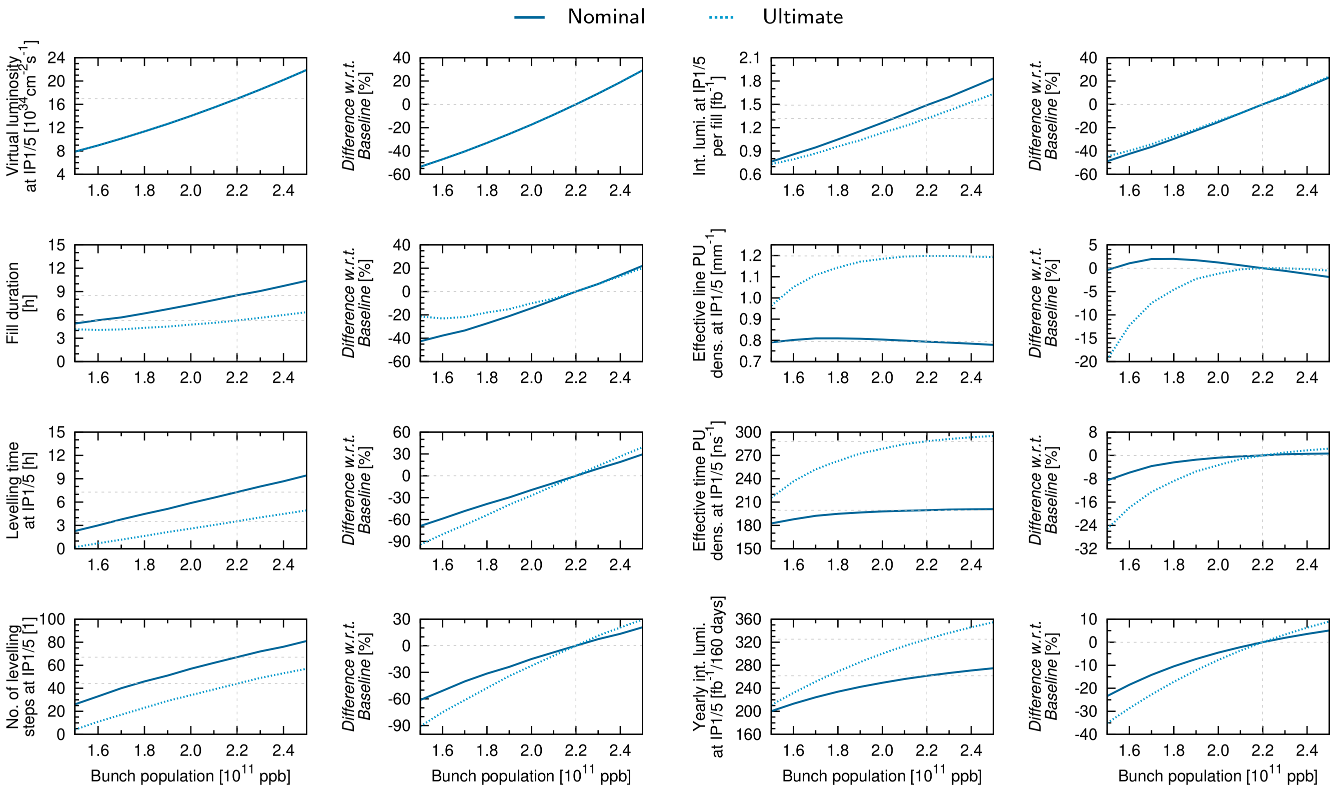

Figure 5.4. Virtual luminosity and performance parameters at IP1/5 as a function of the bunch population for the HL-LHC baseline at nominal and ultimate levelling (and their difference w.r.t the corresponding levelling operation with the baseline bunch population of 2.2×10^{11} ppb).

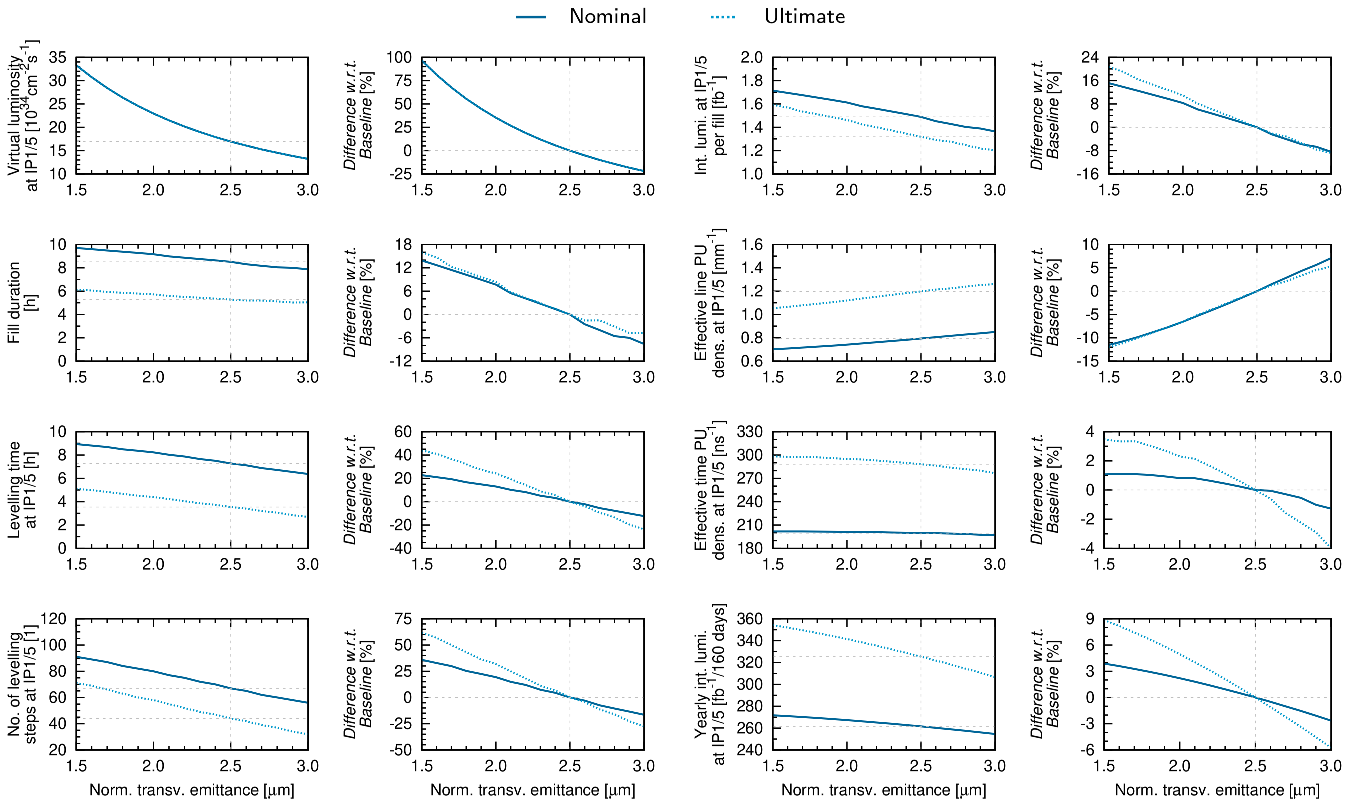

Figure 5.5. Virtual luminosity and performance parameters at IP1/5 as a function of the normalised transverse emittance for the HL-LHC baseline at nominal and ultimate levelling (and their difference w.r.t the corresponding levelling operation with the baseline normalised transverse emittance of 2.5 µm).

(nominal or ultimate, as it corresponds). Both fill duration and levelling time at IP1/5 increase with the bunch intensity, this effect being more prominent –in net terms– for the nominal. It has to be noted, nevertheless, that the levelling time is close to zero for 1.5×10^{11} ppb, that is, most of the fill duration corresponds to luminosity decay. Running the machine with the largest studied bunch population (2.5×10^{11} ppb) would demand 80 (60) levelling steps for nominal (ultimate) which poses a technical challenge. The effective line and time PU densities remain almost constant at values similar to those found at 2.2×10^{11} ppb, except for small bunch population for which they quickly decrease (specially at ultimate operation) mainly due to the significant reduction of levelling time. In terms of yearly integrated luminosity, a non-linear behaviour as a function of the bunch population is observed. As in the case on effective PU densities, the ultimate operation is more sensitive to the variation of the bunch population. While for 1.5×10^{11} ppb, both nominal and ultimate performance drops to around 200-210 fb^{-1} (representing a loss of 23 %-35 % with respect to the corresponding values of the baseline at 2.2×10^{11} ppb), pushing the bunch population to 2.5×10^{11} ppb increases $\mathcal{L}_{\mathrm{int}}$ by 5 %-9 % (that is, 275 fb^{-1}-355 fb^{-1}).

5.3.1.2 Emittance

Contrary to the bunch population, the relation of $\mathcal{L}_{\mathrm{virt}}$ at IP1/5 with the initial emittance (assumed to be the same for both transverse coordinates) is inverse: while an increased normalised emittance of 3.0 µm yields to a reduction of the virtual luminosity by around 20 %, its reduction to 1.5 µm results in an increase of almost 100 %, see Fig. 5.5. The discrete nature of the simulation is more evident in the evolution of some of the parameters with the normalised emittance.

While the relation of $\mathcal{L}_{\mathrm{virt}}$ and the transverse emittance is clearly not linear, it is reasonably linear for the fill duration, levelling time at IP1/5, and number of levelling steps. A difference of 2 h (1 h) on the fill duration is found for nominal (ultimate) levelling when increasing the normalised emittance from 1.5 µm to 3.0 µm. The effective line PU density experiences a greater variation as a function of the transverse emittance than its time counterpart: for nominal (ultimate) operation, $\bar{\rho}_s$ goes from 0.70 mm^{-1} (1.05 mm^{-1}) to 0.85 mm^{-1} (1.26 mm^{-1}), while $\bar{\rho}_t$ remains almost constant at 200 ns^{-1} (280 ns^{-1}-300 ns^{-1}) in the studied emittance range. While a larger emittance of 3.0 µm results in a performance loss of almost 3 % and 4 % for nominal and ultimate, respectively, its reduction to half of this value yields to gains of 4 % and 9 % with respect to the baseline values at 2.5 µm.

5.3.1.3 Bunch length

As seen in the first plot of Fig. 5.6, $\mathcal{L}_{\mathrm{virt}}$ shows an almost linear dependency with the q-Gaussian RMS bunch length. A reduction from the baseline 7.6 cm to 6.0 cm yields, in particular, to an increase of $\mathcal{L}_{\mathrm{virt}}$ by 14 %; contrarily, a longer bunch length of 12.5 cm decreases it by around 40 %.

While the effect on fill duration is relatively small, the reduction of the levelling times with larger bunch lengths is more pronounced. Both effective line and time PU densities significantly drop from their maximum value for the lowest RMS bunch length to a value slightly smaller than that found for 7.6 cm, after which they continue decaying but more slowly. Thus, reduction of the bunch length beyond the current baseline value quickly yields to a more challenging environment for the reconstruction

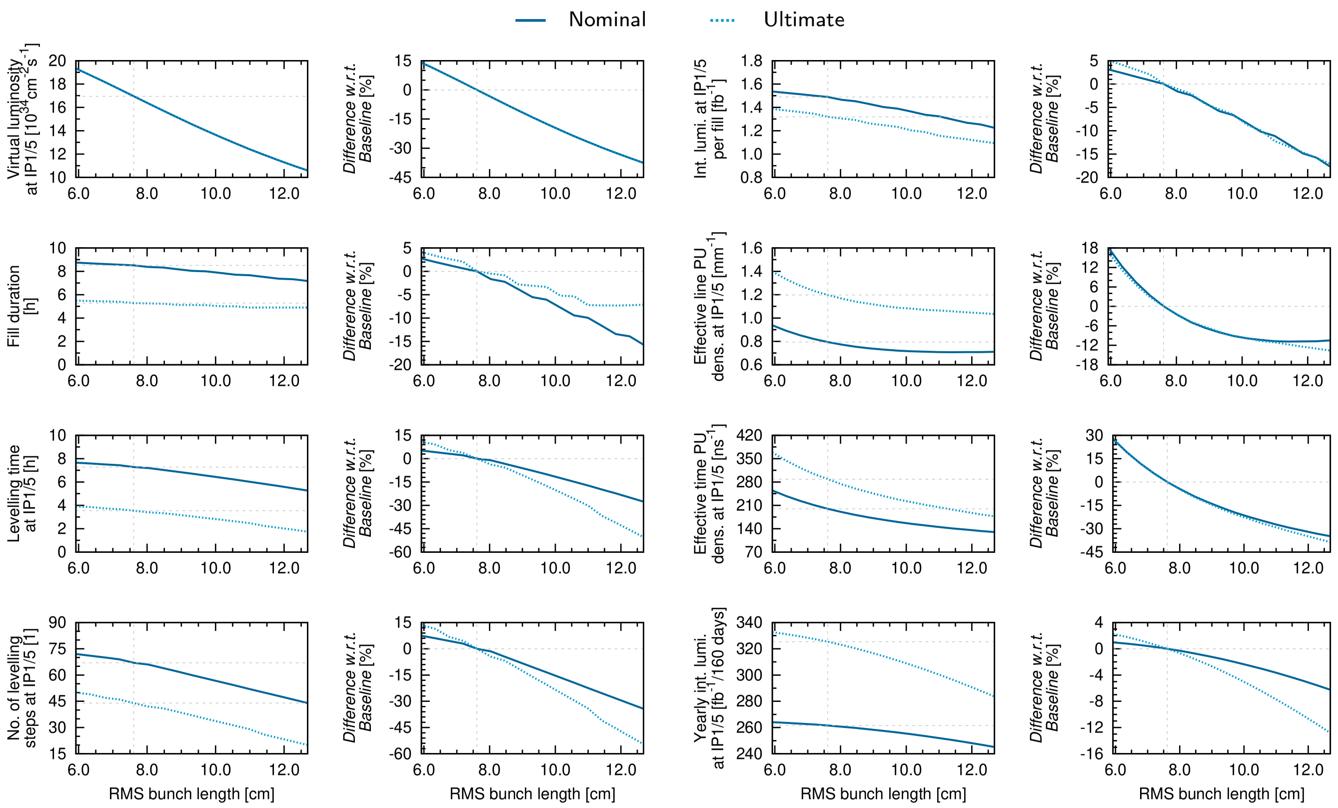

Figure 5.6. Virtual luminosity and performance parameters at IP1/5 as a function of the RMS bunch length for the HL-LHC baseline at nominal and ultimate levelling (and their difference w.r.t the corresponding levelling operation with the baseline RMS bunch length of 7.6 cm).

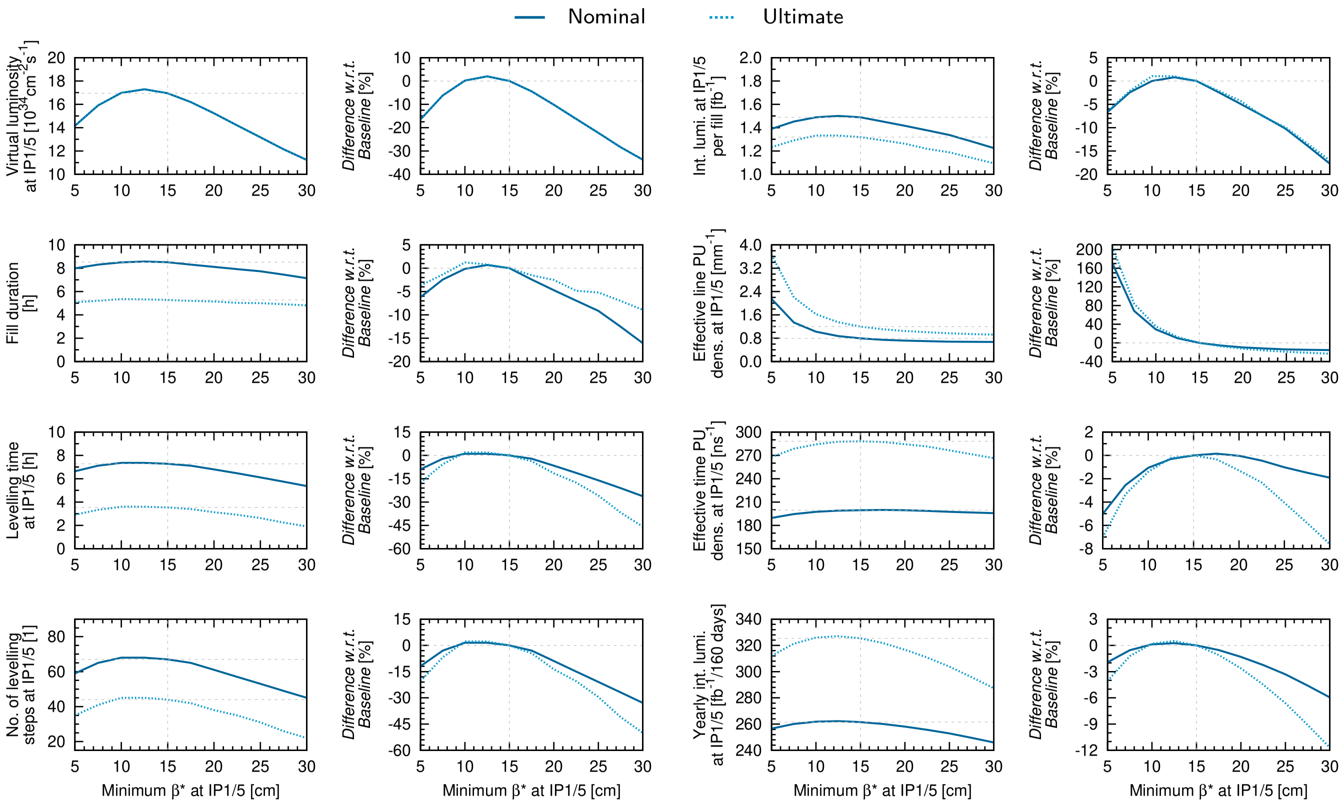

Figure 5.7. Virtual luminosity and performance parameters at IP1/5 as a function of the β^* at IP1/5 for the HL-LHC baseline at nominal and ultimate levelling (and their difference w.r.t the corresponding levelling operation with the baseline β^* at IP1/5 of 15 cm).

of events in the main IPs by the detectors. Regarding $\mathcal{L}_{\text{int}}$, stronger dependency with the bunch length is found for ultimate operation: while gains are limited to less than 2 % for the smallest studied bunch length for both levelling operations, losses rapidly grow (both in absolute and relative terms) as the bunch lengthens, reaching 6 % and 12 % at 12.5 cm for nominal and ultimate operation, respectively.

5.3.1.4 Betatron function at IP1/5

As usual, the first plot of Fig. 5.7 shows $\mathcal{L}_{\text{virt}}$ at IP1/5, in this case, as a function of the minimum betatron function at the main IPs assuming round beams. While $\mathcal{L}_{\text{virt}}$ decreases almost linearly for $\beta^* > 15\,\text{cm}$, it reaches a maximum with gain of 2 % at around $\beta^* \approx 12.5\,\text{cm}$ with respect to the baseline virtual luminosity; then it decreases again for smaller β^*. As the normalised long-range beam-beam separation is assumed to remain constant at 10.5σ, this implies a full crossing angle of 860 µrad at $\beta^* = 5\,\text{cm}$, and 350 µrad at $\beta^* = 30\,\text{cm}$. The crabbing angle is, however, limited to a maximum of 380 µrad due to the available number of CCs and their maximum voltage [102]. In consequence, the fraction of crabbing angle with respect to crossing angle is not constant; moreover, full crabbing is possible for the smaller crossing angles.

The fill duration, levelling time at IP1/5, and the number of levelling steps peak for the case with the maximum $\mathcal{L}_{\text{virt}}$, decreasing all for β^* both below and above the baseline (the latter in a steeper fashion). While the line PU density was found to remain relatively constant for β^* above its baseline magnitude, it rapidly grows for smaller β^* to levels that might pose a serious problem for the detectors, even at nominal operation. The time PU density, on the other hand, remains between $190\,\text{ns}^{-1}$-$200\,\text{ns}^{-1}$ ($270\,\text{ns}^{-1}$-$290\,\text{ns}^{-1}$) for the nominal (ultimate), reaching also its maximum at the peak of $\mathcal{L}_{\text{virt}}$. Similar behaviour is followed by $\mathcal{L}_{\text{int}}$, although less pronounced: a small gain of $0.7\,\text{fb}^{-1}$ ($1.7\,\text{fb}^{-1}$) for the nominal (ultimate) is obtained at $\beta^* \approx 12.5\,\text{cm}$. For large β^*, however, $\mathcal{L}_{\text{int}}$ quickly decays; for example, for nominal levelling it drops by 2 % and 6 % for 5 cm and 30 cm, respectively, doubling these figures at ultimate operation.

5.3.1.5 Crossing angle at IP1/5

While the reduction of the $\mathcal{L}_{\text{virt}}$ with a full crossing angle larger than 380 µrad is almost linear, below this threshold its reduction is limited thanks to the possibility of fully crabbing the bunches with the available CC voltage. As in the case of the betatron function at the main IPs, this behaviour is followed by the fill duration, the levelling time, and number of levelling steps at IP1/5, although at different decreasing rates. As the full crossing angle increases, the effective line PU density worsens: at 300 µrad (the lower limit of the considered range), $\bar{\rho}_s = 0.70\,\text{mm}^{-1}$ ($1.03\,\text{mm}^{-1}$), and remains around this value for angles up to slightly above the maximum crabbing angle of 380 µrad, after which it begins to grow rapidly reaching $0.95\,\text{mm}^{-1}$ ($1.46\,\text{mm}^{-1}$) by the end of the studied range, as seen in Fig, 5.8. The effective time PU density remains almost constant for all crossing angles for nominal levelling (around $200\,\text{ns}^{-1}$), with a slightly larger variation at ultimate (between $275\,\text{ns}^{-1}$-$290\,\text{ns}^{-1}$). When the crossing angle is reduced as low as 300 µrad, $\mathcal{L}_{\text{int}}$ can be pushed to $267\,\text{fb}^{-1}$ ($338\,\text{fb}^{-1}$), which represents an increase of around 2 % (4 %) for nominal (ultimate) operation. In contrast, losses of around 3 % (6 %), corresponding to $\mathcal{L}_{\text{int}} = 254\,\text{fb}^{-1}$ ($305\,\text{fb}^{-1}$), are expected for a crossing angle as large as 600 µrad.

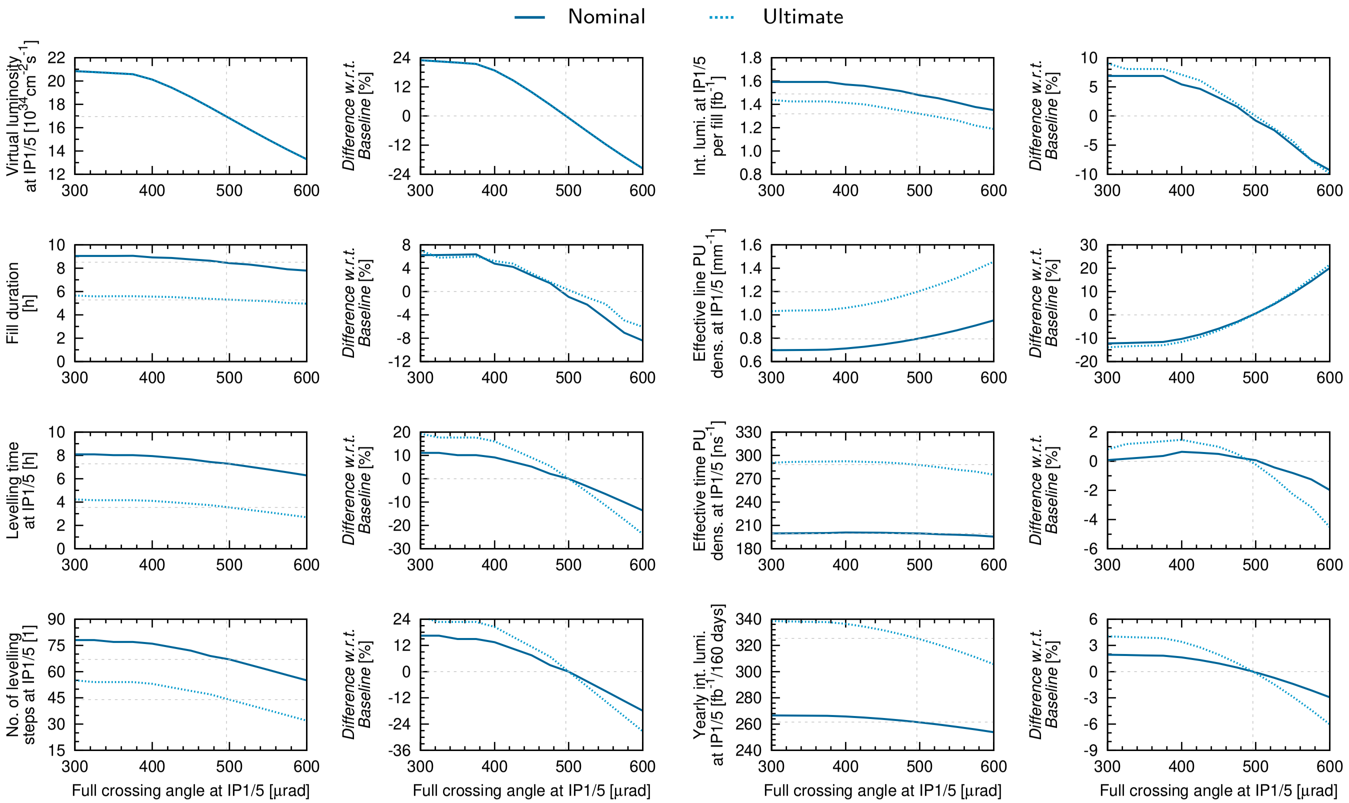

Figure 5.8. Virtual luminosity and performance parameters at IP1/5 as a function of the crossing angle at IP1/5 for the HL-LHC baseline at nominal and ultimate levelling (and their difference w.r.t the corresponding levelling operation with the baseline crossing angle at IP1/5 of 500 μrad).

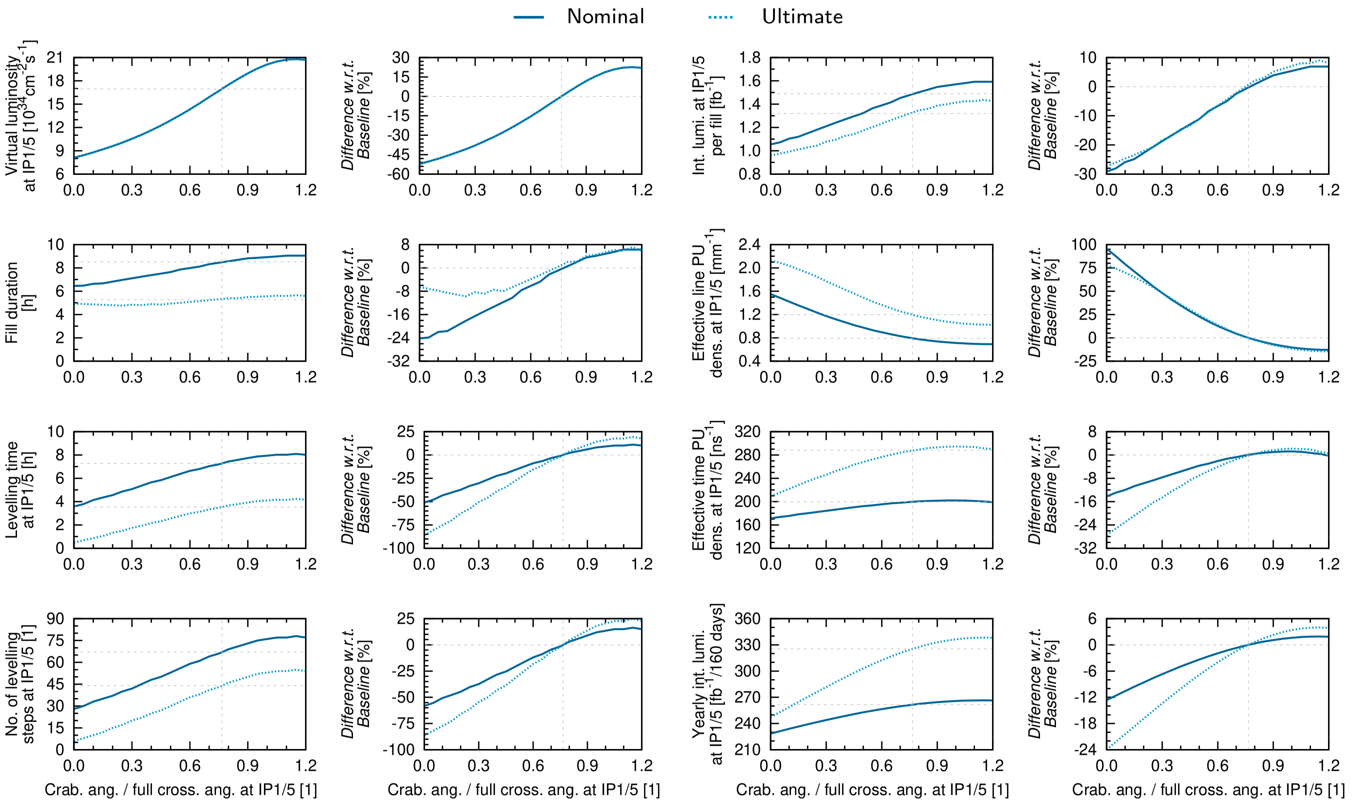

Figure 5.9. Virtual luminosity and performance parameters at IP1/5 as a function of the crab crossing ratio at IP1/5 for the HL-LHC baseline at nominal and ultimate levelling (and their difference w.r.t the corresponding levelling operation with the baseline crab crossing ratio at IP1/5 of $\theta_{\text{CC}}/\theta = 0.76$).

5.3.1.6 Crab crossing ratio at IP1/5

Exploring the potential performance of the HL-LHC with additional CC voltage is of interest as a possible machine upgrade. For the baseline, four CCs per beam per main IP side can deliver the 9.0 MV necessary to fully crab the beam (that is, $\theta_{\mathrm{CC}} = \theta$), yielding to a 19 %-gain on $\mathcal{L}_{\mathrm{virt}}$. The virtual luminosity does not peak at $\theta_{\mathrm{CC}}/\theta = 1$, though, but slightly above it ($\theta_{\mathrm{CC}}/\theta \approx 1.15$), a result in line with that found in other works [57]; at this point, the $\mathcal{L}_{\mathrm{virt}}$ increases by an additional 4 % with respect to its value at the baseline $\theta_{\mathrm{CC}}/\theta = 0.77$. In the opposite scenario, that is, the absence of CCs ($\theta_{\mathrm{CC}}/\theta = 0$), a 52 %-loss on $\mathcal{L}_{\mathrm{virt}}$ can be expected, as seen in Fig. 5.9.

At full crabbing, the fill duration and levelling time increase by 0.3 h and 0.6 h for nominal and ultimate operation, respectively, while the number of levelling steps increases, in both cases, by 10. In the absence of crabbing, the fill duration of the HL-LHC baseline nominal (ultimate) extends for only 6.5 h (3.6 h), with the levelling process –consisting of 28 (6) steps– ending after 4.9 h (0.5 h). Even though the gain on $\mathcal{L}_{\mathrm{int}}$ at full crabbing is limited, around 2 % (3 %) for nominal (ultimate), its reduction as a result of the absence of crabbing is substantial: 13 % (24 %), proving the CCs to be a crucial component to meet the project's goals. The use of additional CC voltage to reach $\theta_{\mathrm{CC}}/\theta = 1.15$, on the other hand, does not result in a significant increase of $\mathcal{L}_{\mathrm{int}}$. Despite the gain on $\mathcal{L}_{\mathrm{int}}$ with full crabbing with respect to the case with the baseline 6.4 MV being small, the effective PU density does experience a moderate improvement: 0.71 mm^{-1} (1.06 mm^{-1}) for nominal (ultimate) levelling, positively impacting on the detector efficiency. Without CCs, $\bar{\rho}_s$ increases to 1.55 mm^{-1} (2.13 mm^{-1}) for nominal (ultimate).

5.3.2 Performance parameters

The variation of the turn-around time, the luminosity step, the magnitude of the cross-section for burn-off, or the addition of penalty steps without luminosity, does no have any effect on $\mathcal{L}_{\mathrm{virt}}$; they do, nevertheless, have an impact of the machine performance. In the following, the sensitivity of the HL-LHC baseline to the aforementioned parameters, as well as to CC noise, is studied with emphasis on the impact on the usual figures-of-merit.

5.3.2.1 Turn-around time

The variation of the turn-around time was found to have little effect on the fill duration – a difference of around 0.5 h for both levelling operations between the minimum and maximum values considered. Due to the discrete nature of the simulations of the levelling process, the variation of the turn-around time has a null effect on the levelling time at IP1/5 or the corresponding number of levelling steps. As a result, the effective line and time PU density are almost unaffected, remaining around their baseline values, although showing a slight decrease as the turn-around time shortens. As seen in Fig. 5.10, $\mathcal{L}_{\mathrm{int}}$ exhibits an approximate linear relation with the parameter of interest. The two vertical lines represent the baseline turn-around times for nominal (145 min) and ultimate (150 min) operation. The fractional difference with respect to the corresponding baseline is shown, as usual, in the right-hand side plot. The upper limit of the studied range, 180 min, coincides with the turn-around time assumed in previous studies on the HL-LHC performance [34]; thus, with the current baseline assumptions, a gain of 5 %-6 % on $\mathcal{L}_{\mathrm{int}}$ has been achieved with respect to the estimates

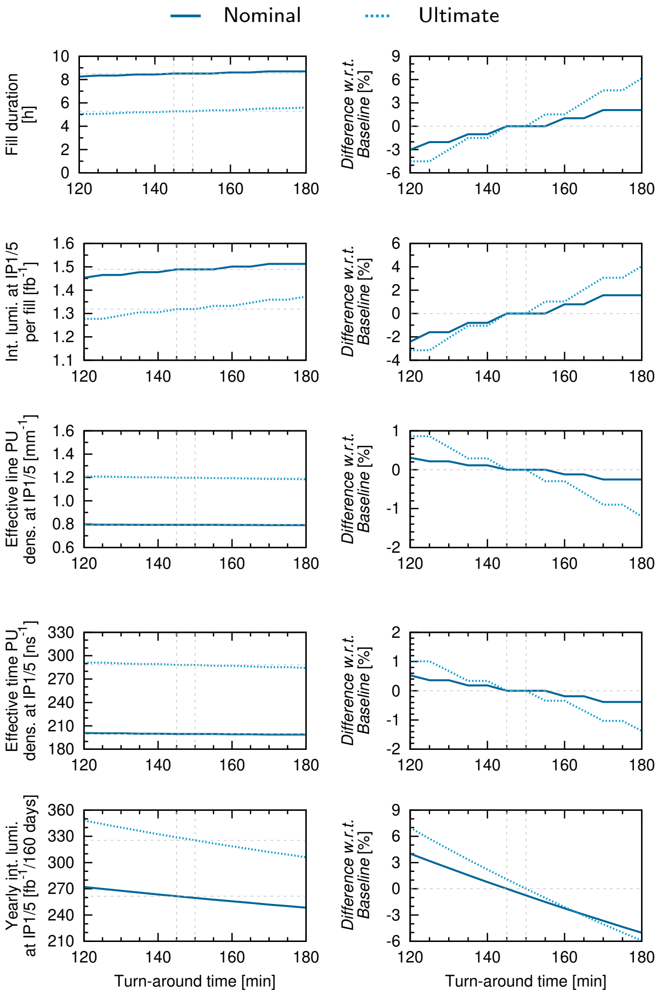

Figure 5.10. Selected performance parameters at IP1/5 as a function of the turn-around time for the HL-LHC baseline at nominal and ultimate levelling (and their difference w.r.t the corresponding levelling operation with the baseline turn-around time of 145 min and 150 min, respectively).

with the original parameters. The cases with a turn-around time reduced by 15 min are of special interest, in particular, since this is the expected improvement resulting from a potential upgrade of the triplet power converters at IP2 and IP8 [99]. In such scenario, that is, 130 min and and 135 min for nominal and ultimate, respectively, the corresponding performances can be further pushed by 2.4 % and 3.3 %, respectively.

5.3.2.2 Luminosity step

For all cases presented in this work, a luminosity step of 2 % is assumed, that is, β^* is squeezed every time the instantaneous luminosity has dropped to $p = 98\,\%$ of its

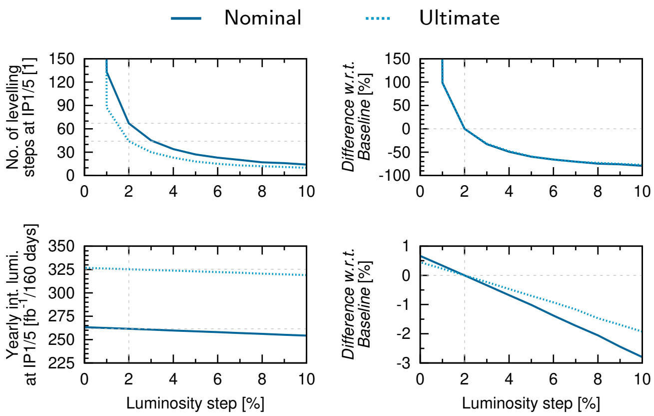

Figure 5.11. Selected performance parameters at IP1/5 as a function of the luminosity step for the HL-LHC baseline at nominal and ultimate levelling (and their difference w.r.t the corresponding levelling operation with the baseline luminosity step of 2 %).

levelled value (nominal or ultimate, as it corresponds). The effect of the variation of this parameter is studied for luminosity steps from near zero (0.01 %) to up to 10 %, see Fig. 5.11. Naturally, the case with a luminosity step of zero diverges since it would require an infinite number of infinitely-small steps (each of them representing an optics to commission) to keep $\mathcal{L}_{\text{virt}}$ equal to its levelled value. The variation of the luminosity step also has an impact on the optimum fill duration and the levelling time; however, this effect is limited, and it is partially due to the discrete nature of the levelling simulation, and the loss of resolution to precisely find the optimum fill duration as the luminosity steps grows larger. The integrated luminosity follows a linear trend for small luminosity steps, and the theoretical case with zero-length steps can thus be extrapolated easily (gain below 1 % for both levelling operations). Operation with an increased luminosity step of 10 %, on the other hand, reduces the performance by 2 % (3 %) for nominal (ultimate) operation. A luminosity step between 2 % and 5 % therefore represents a good trade-off between a reasonable number of optics, and a limited performance loss. In particular, operation with a levelling step of 5 % ($p = 0.95$) sees a loss of performance below 1 %, and makes use of 27 (18) levelling steps for the nominal (ultimate) levelling; the latter can be compared with the 67 (44) steps for the HL-LHC baseline with a levelling step of 2 %, or with the commissioning of LHC, in which only one (in 2015) or two (in 2017 and 2018) optics for physics were required [111].

5.3.2.3 Penalty steps

In all simulations, an *instantaneous* levelling process has been adopted, that is, it is assumed that the change of optics from one levelling step to the next (with smaller β^*, for example) is performed *instantaneously*. In operation, however, switching between consecutive optics takes some time, during which the beams might get misaligned. The necessary time to perform the change of optics and optimise collisions is modelled in the present work as an extra *penalty* step (with a short length), during which the luminosity drops to zero (the worst scenario).

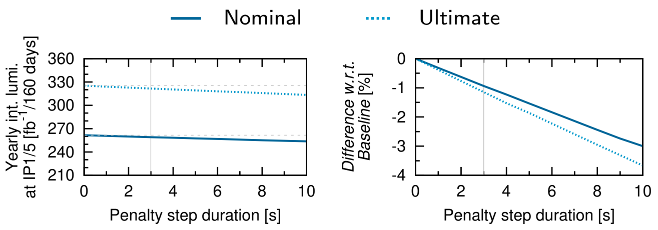

Figure 5.12. Selected performance parameters at IP1/5 as a function of the penalty step for the HL-LHC baseline at nominal and ultimate levelling (and their difference w.r.t the corresponding levelling operation without penalty steps (0 s).

Initial studies took a naïve approach and assumed 30 s for the length of such penalty step. A 5 %-10 % loss during 30 s is, nonetheless, more realistic [112]; which is equivalent to a 3 s lapse with no luminosity. By conducting a variation of the the penalty step duration, it was found that the fill duration, levelling time, and number of levelling steps, remain around 8.6 h (5.3 h), 7.3 h (3.5 h), and 66 (44) steps, respectively, for all the studied range at nominal (ultimate) operation. Similarly, the effective line and time PU densities do not experience significant changes, remaining around 0.79 mm^{-1} (1.19 mm^{-1}) and 199 ns^{-1} (286 ns^{-1}) for penalty steps lasting from 0 s to 10 s. Figure 5.12 shows the linear decrease –valid in the studied range– on the yearly integrated luminosity for both levelling modes. The grey vertical dotted line indicates penalty steps of 3 s for which the reduction of $\mathcal{L}_{\text{int}}$ is limited to around 1 % at both levelling operations. Posterior results [7], however, hinted at this assumption on the duration of the penalty steps at zero luminosity also to be too pessimistic.

5.3.2.4 Crab cavity noise

Crab cavity noise is an important concern since it generates emittance blow-up [72, 73]. Preliminary simulations have been conducted to assess the effect of the emittance growth from CCs, approximated by

$$\frac{\mathrm{d}\epsilon_{u_{\mathrm{CC}}}}{\mathrm{d}t} \approx 0.115\,\mu\mathrm{m/h} \cdot \frac{V_{\mathrm{CC}}^2}{(6.8\,\mathrm{MV})^2}\,\frac{15\,\mathrm{cm}}{\beta_u^*}\,, \qquad u = x, y\,, \tag{5.3}$$

as introduced in Section 2.2. The additive growth rate of 0.115 µm/h is taken from the sum of the phase noise (0.94 %/h) and amplitude noise (3.7 %/h) of the CC voltage, according to present estimates of the achievable minimum noise level, taking into account the effect of the transverse feedback [113]. Moreover, this growth rate has been estimated for a transverse emittance of 2.5 µm, $\beta^* = 15\,\mathrm{cm}$, and a 3.4 MV-deflecting voltage for each of the two CCs per beam and per IP side (or, equivalently, $\theta_{\mathrm{CC}} = 380\,\mu\mathrm{rad}$), so it has to be scaled accordingly at each levelling step.

Figure 5.13 illustrates the influence of the CC noise given by Eq. 5.3 on the evolution of the horizontal and vertical emittances along the fill for the HL-LHC nominal baseline (the effects of IBS and synchrotron radiation are also present). At the beginning of the fill, the CCs around the main IPs induce emittance blow-up in both planes –horizontal (vertical) crossing is assumed in IP1 (IP5)– at a reduced rate of 0.027 µm/h (after scaling) due to the larger initial β^*. With the CC noise rate in Eq. 5.3, the fill duration is found to decrease by 0.6 h (0.4 h) for the nominal (ultimate) operation

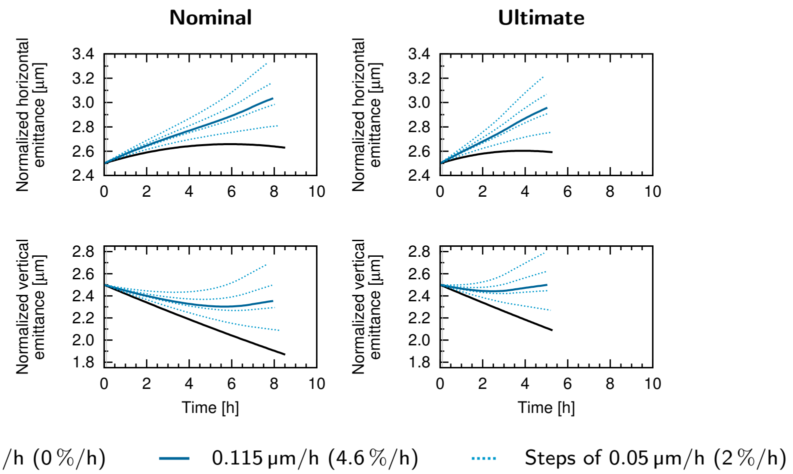

Figure 5.13. Evolution of the normalised transverse emittances at IP1/5 along the fill in the HL-LHC baseline with and without crab cavity noise (virtual noise estimates for $\beta^* = 15\,\mathrm{cm}$ and 6.8 MV in µm/h and %/h relative to 2.5 µm).

with respect to the its baseline value in the absence of noise. Similarly, the levelling time experiences a reduction of 0.8 h (0.4 h), while the number of levelling steps is lowered by 9 (6). The effective PU densities are found to remain almost constant, independently of the CC noise level.

As seen in Fig. 5.14, the decrease on performance is linear behaviour for small emittance growth rates. At nominal (ultimate) operation and the growth rate in Eq. 5.3, in particular, the reduction of $\mathcal{L}_{\mathrm{int}}$ with respect to the case without noise is around 1.5 % (2.3 %). A 1 % reduction of performance can be limited if a CC noise of 0.08 µm/h (0.05 µm/h) at nominal (ultimate) levelling is maintained. Both the fill duration of the optimum fill, as well as the levelling time, shorten slightly for larger CC noise rates, while $\bar{\rho}$ is found to remain almost constant. These preliminary results have triggered efforts to mitigate the sources of CC noise by introducing a feedback system acting on CC voltage and phase based on the measurement of the head-tail motion at a dedicated pick-up [114]. Despite the performance not being seriously compromised, it must be noted the large emittance spread in both transverse coordinates found at the end of the nominal fill between the cases without CC noise and with a growth rate of 0.115 µm/h:

$$\frac{\Delta\epsilon_{x_\mathrm{n}}}{\epsilon_{x_\mathrm{n}}} = \frac{3.04\,\mu\mathrm{m} - 2.63\,\mu\mathrm{m}}{2.63\,\mu\mathrm{m}} \approx 15\,\% \qquad \text{and} \qquad \frac{\Delta\epsilon_{y_\mathrm{n}}}{\epsilon_{y_\mathrm{n}}} = \frac{2.35\,\mu\mathrm{m} - 1.87\,\mu\mathrm{m}}{1.87\,\mu\mathrm{m}} \approx 26\,\%\,. \tag{5.4}$$

The corresponding figures for ultimate operation are 14 % and 20 %, respectively. Such large induced emittance growth by the CC noise might pose further problems in operation, strengthening the need for its control and reduction in the HL-LHC.

5.3.2.5 Time offset

In operation, the bunches could be longitudinally displaced by a time offset with respect to their ideal positions; e.g. a bunch of B1 can be travelling with a given delay

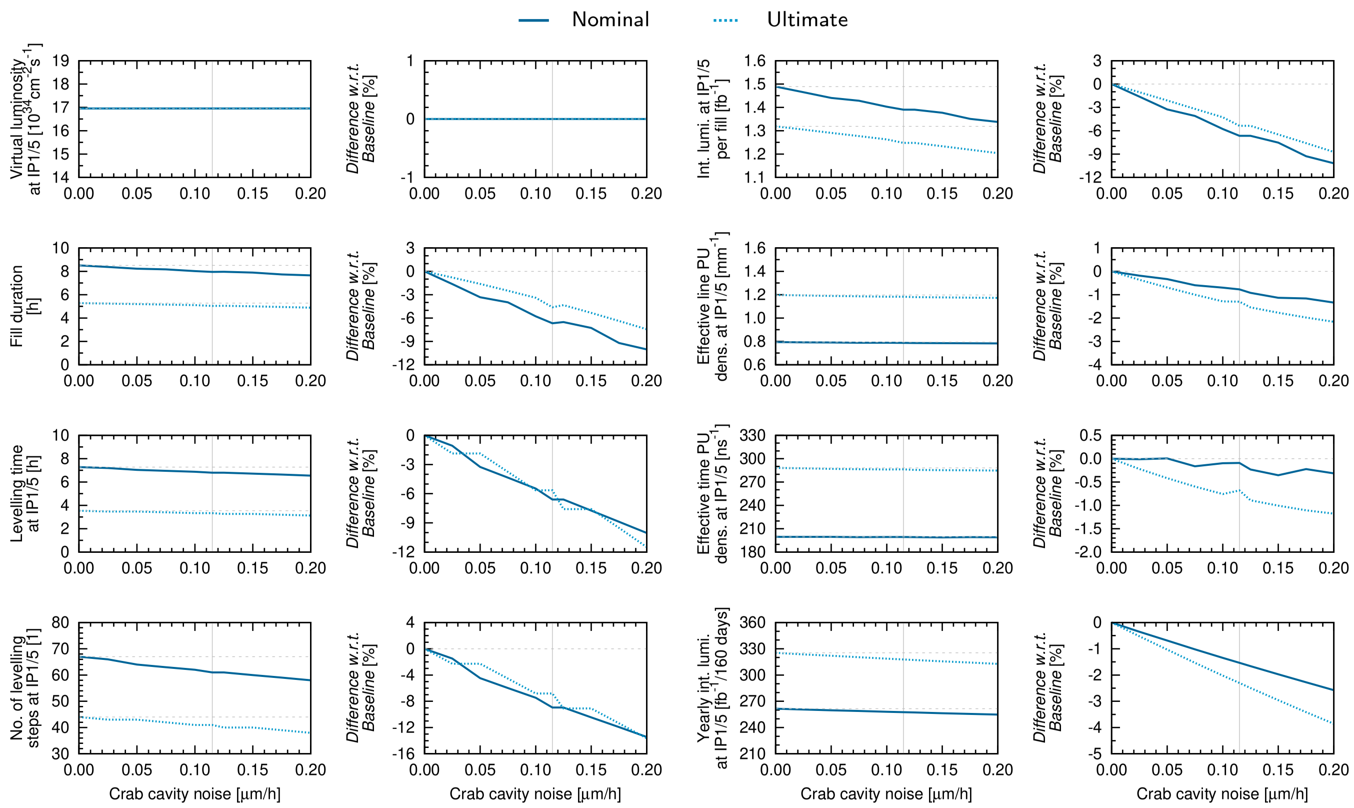

Figure 5.14. Virtual luminosity and performance parameters at IP1/5 as a function of the crab cavity noise at IP1/5 for the HL-LHC baseline at nominal and ultimate levelling (and their difference w.r.t the corresponding levelling operation with the baseline crossing angle at IP1/5 of 0 µm/h).

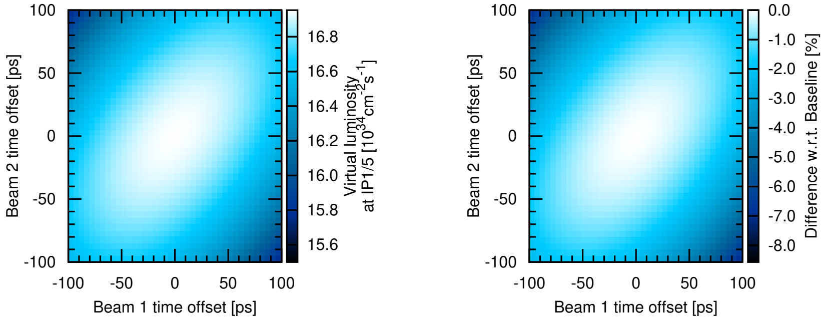

Baseline Standard Nominal

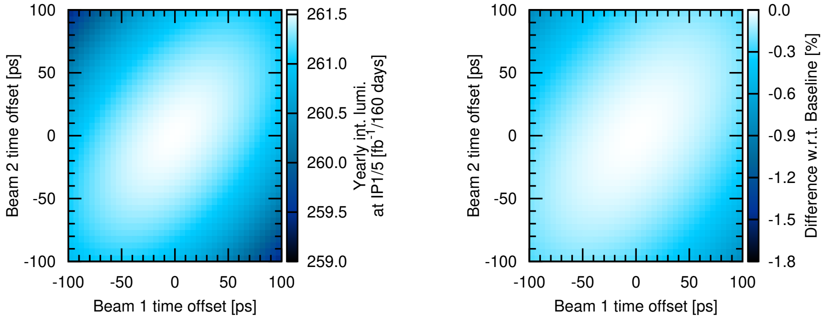

Baseline Standard Ultimate

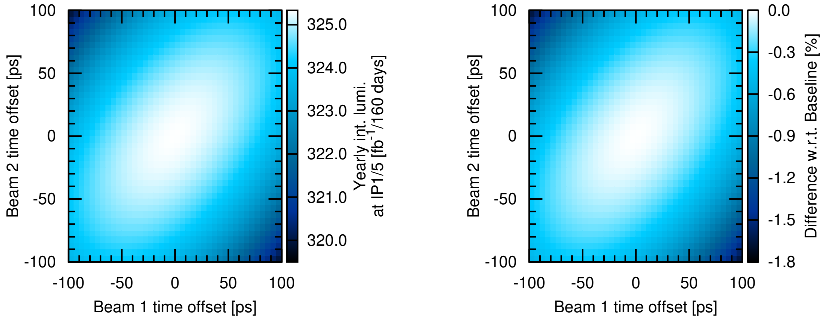

Figure 5.15. Virtual luminosity (*top*) and integrated luminosity at IP1/5 as a function of the bunch time offsets for the HL-LHC baseline at nominal and ultimate levelling (and their difference w.r.t the corresponding levelling operation with the baseline time offsets of 0 s).

t_{0_1}, while the corresponding bunch of B2 –with which it collides– can be travelling with delay t_{0_2}. This yields to the physical collision point to be shifted from its ideal position (the IP defined by the optics where β is minimum). Additionally, when the bunches cross their corresponding CCs, they will experience a reduced voltage due, precisely, to their delay. This results in a lower crabbing angle, which in turn yields to a lower overlap of the bunches and therefore a reduced virtual luminosity. Simulations of the effect of time offsets on luminosity are performed for the HL-baseline (q-Gaussian) following the model given by Eqs. (2.39) and (2.40).

The plots in the upper row of Fig. 5.15 show $\mathcal{L}_{\mathrm{virt}}$ in absolute terms (*left*) and relative to the case with absence of delays (*right*) for different time offsets ranging from −100 ps to 100 ps for both beams. This range has been chosen as 30 ps is believed to be a likely magnitude to be observed in the HL-LHC [113]. In order to study the worst-case scenario, a systematic (equal) time delay is assumed for all the bunches of the same beam. In reality, the magnitude of these time offsets would present variation, partially cancelling the average effect. As expected, the cases with $t_{0_1} = -t_{0_2}$ yield to the lowest $\mathcal{L}_{\mathrm{virt}}$ (losses of more than 8 %) due to the difference on the crabbing angle between the two bunches being maximum for this configuration, resulting in turn in the compensation of the crossing angle being the minimum. The shift of the position of the collision point (to the left or right of the IP, depending on the signs of $t_{0_{1,2}}$) is also the maximum for these cases. For the cases with $t_{0_1} = t_{0_2}$, conversely, the $\mathcal{L}_{\mathrm{virt}}$ decreases at a lower rate and the collision point, in fact, does not shift.

The effect of time offsets on $\mathcal{L}_{\mathrm{int}}$ at nominal and ultimate levelling is shown in the rest of plots of Fig. 5.15; the relative loss, in each case, is computed with respect to the corresponding levelling operation of the HL-LHC baseline with no time offsets. Reductions of around 1 % (2 %) are found at nominal (ultimate) for time offsets of 100 ps (with opposite signs), and therefore negligible reduction is expected below 30 ps.

5.3.2.6 Cross-section for burn-off and summary

The 111 mb cross-section for burn-off assumed in this work is an empirical estimate based on LHC observations (at lower bunch charge) at the beginning of the fill, taking into account the contributions of both elastic and inelastic proton-proton processes. This value has been assumed as a pessimistic scenario, since observations also show that $\sigma_{\mathrm{b.o}}$ tends to 81 mb (the inelastic cross-section exclusively) as the fill progresses [78].

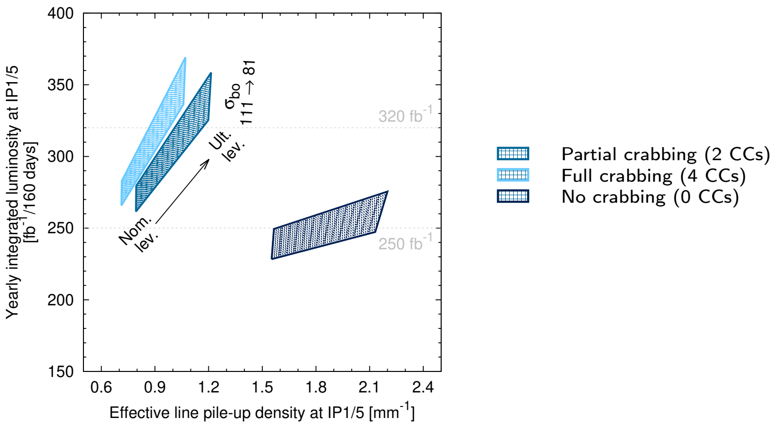

Figure 5.16. Extent of the yearly integrated luminosity and effective line PU density at IP1/5 of the HL-LHC baseline at nominal and ultimate levelling assuming $\sigma_{\mathrm{b.o.}} = 111$ mb and 81 mb. The corresponding cases with full crabbing and zero-crabbing are shown for comparison.

Table 5.6. Optics and virtual parameters at IP1/5 of the scenarios for the potential improvement of the HL-LHC baseline: with wires at IP1/5, with adaptive crossing at IP1/5, and at ultimate energy.

Parameter	Unit	Wires	Adaptive	7.5 TeV
Number of colliding bunches	1	2748	2748	2748
Minimum $\beta^*_{\times,\parallel}$	cm	13.0	15.0	15.0
Full crossing angle	µrad	430	310	500
Minimum norm. BBLR sep.	σ	8.5	6.5	10.9
Piwinski parameter	1	2.49	1.65	2.76
Virtual luminosity	$10^{34}\,\mathrm{cm}^{-2}\,\mathrm{s}^{-1}$	21.51	20.82	17.00
Virtual pile-up	1	564	546	446
Virtual loss factor	1	0.787	0.879	0.670
Virtual beam-beam	10^{-2}	1.01	1.07	0.79

To obtain estimates on the performance extent with the two extreme values of $\sigma_{\mathrm{b.o.}}$, simulations with 81 mb are performed for the HL-LHC (as well as its main potential improvements, and main alternative scenarios); the results on the two main figures-of-merit ($\mathcal{L}_{\mathrm{int}}$ and $\bar{\rho}$) are summarised in the typical plot shown in Fig. 5.16, which commonly includes the corresponding cases with full or null crabbing for comparison.

Regarding the HL-LHC baseline, a proportional increment of 7 % (11 %) on $\mathcal{L}_{\mathrm{int}}$ is expected for nominal (ultimate) operation assuming a more optimistic $\sigma_{\mathrm{b.o}}$. Combined full crabbing voltage and reduced cross-section for burn-off can boost the current estimate on integrated luminosity by up to 8 % (14 %) for nominal (ultimate) operation. In terms of the effective line PU density, the more optimistic value of $\sigma_{\mathrm{b.o.}}$ has negligible impact for the cases with partial (the baseline) and full crabbing, while a small effect is observed at ultimate operation for the case with absent CCs.

5.4 Potential improvements to the baseline

As exemplified in the previous section, different parameters can be pushed to improve the baseline performance of the HL-LHC. Improvements can also aim at providing additional benefits in other aspects (such as improving the beam stability, for example), while keeping the baseline performance. In particular, two scenarios have been developed to operate with a smaller crossing angle, and they are described in the following. While in the first case the reduced crossing angle is kept constant, which in turn demands the implementation of a compensation technique of the increased long-range beam-beam forces (such as the use of current-carrying wires [46–49]), the second scenario consists on reducing the crossing angle as a function of the bunch intensity.

5.4.1 Baseline with wires

To study the improved baseline scenario with wires [115] the general parameters of HL-LHC with standard filling scheme were assumed to remain unchanged (Table 5.1), while the optics parameters are listed in Table 5.6 (together with other scenarios). In particular, operation with wires features a minimum β^* of 13 cm and a normalised BBLR separation of $d_{\mathrm{BBLR}} = 8.5\sigma$ for a total crossing angle of $\theta = 430\,\mu\mathrm{rad}$. This configuration leads to an increase of 27 % on $\mathcal{L}_{\mathrm{virt}}$, see Fig. 5.17. As a result, β^* is larger

Table 5.7. Performance at IP1/5 of the scenarios in Table 5.6.

Parameter	Unit	Wires		Adaptive		7.5 TeV	
		Nom.	Ult.	Nom.	Ult.	Nom.	Ult.
Levelled luminosity	$10^{34}\,\mathrm{cm}^{-2}\,\mathrm{s}^{-1}$	5.0	7.5	5.0	7.5	5.0	7.5
Levelled pile-up	1	131	197	131	197	131	197
At the start of the fill							
$\beta^*_{\times,\parallel}$	cm	68.0	44.2	70.0	46.2	67.4	42.3
Norm. BBLR sep.	σ	19.4	15.7	14.1	11.4	23.0	18.3
RMS luminous region	mm	51.5	50.4	53.1	52.5	48.0	45.5
RMS luminous time	ns	0.179	0.178	0.179	0.179	0.180	0.180
Peak line PU density	mm^{-1}	0.98	1.50	0.95	1.44	1.05	1.68
Peak time PU density	ns^{-1}	281	423	280	421	280	421
At the end of the levelling							
$\beta^*_{\times,\parallel}$	cm	13.0	13.0	15.0	15.0	15.0	15.0
Norm. BBLR sep.	σ	8.3	8.3	9.5	9.2	10.9	10.8
RMS luminous region	mm	44.4	44.4	43.4	44.4	38.2	38.2
RMS luminous time	ns	0.178	0.178	0.178	0.178	0.179	0.179
Peak line PU density	mm^{-1}	1.18	1.76	1.21	1.74	1.39	2.08
Peak time PU density	ns^{-1}	283	425	284	425	283	424
Fill duration	h	9.2	5.7	8.8	5.4	8.7	5.5
Levelling time	h	8.2	4.3	7.6	3.9	7.5	3.7
Number of levelling steps	1	80	56	71	49	70	46
Integrated luminosity per fill	fb^{-1}	1.61	1.45	1.55	1.36	1.52	1.36
Yearly integrated luminosity	fb^{-1}/160 days	267	340	264	330	261	324
Diff. w.r.t. baseline nominal	%	+2.2	–	+1.0	–	−0.2	–
Diff. w.r.t. baseline ultimate	%	–	+4.6	–	+1.5	–	−0.3
Effective line PU density	mm^{-1}	0.74	1.11	0.73	1.07	0.83	1.26
Diff. w.r.t. baseline nominal	%	−7.0	–	−7.9	–	+4.6	–
Diff. w.r.t. baseline ultimate	%	–	−7.2	–	−10.5	–	+5.2
Effective time PU density	ns^{-1}	201	294	200	290	199	286
Diff. w.r.t. baseline nominal	%	+0.8	–	+0.3	–	−0.3	–
Diff. w.r.t. baseline ultimate	%	–	+2.1	–	+0.7	–	−0.6

Table 5.8. Parameters of the Gaussian fits of the line and time PU densities at IP1/5 of the scenarios in Table 5.7.

Parameter	Unit	Wires		Adaptive		7.5 TeV	
		Nom.	Ult.	Nom.	Ult.	Nom.	Ult.
At the start of the fill							
σ_s	mm	53.7	52.4	55.3	54.7	49.7	46.8
σ_t	ns	0.186	0.185	0.186	0.186	0.187	0.186
$\hat{\rho}_s$	mm^{-1}	0.98	1.51	0.96	1.45	1.06	1.69
$\hat{\rho}_t$	ns^{-1}	284	427	283	425	283	425
At the end of the levelling							
σ_s	mm	44.7	44.6	43.7	44.9	37.8	37.9
σ_t	ns	0.185	0.185	0.184	0.184	0.185	0.185
$\hat{\rho}_s$	mm^{-1}	1.15	1.76	1.18	1.74	1.37	2.03
$\hat{\rho}_t$	ns^{-1}	281	428	283	428	282	421

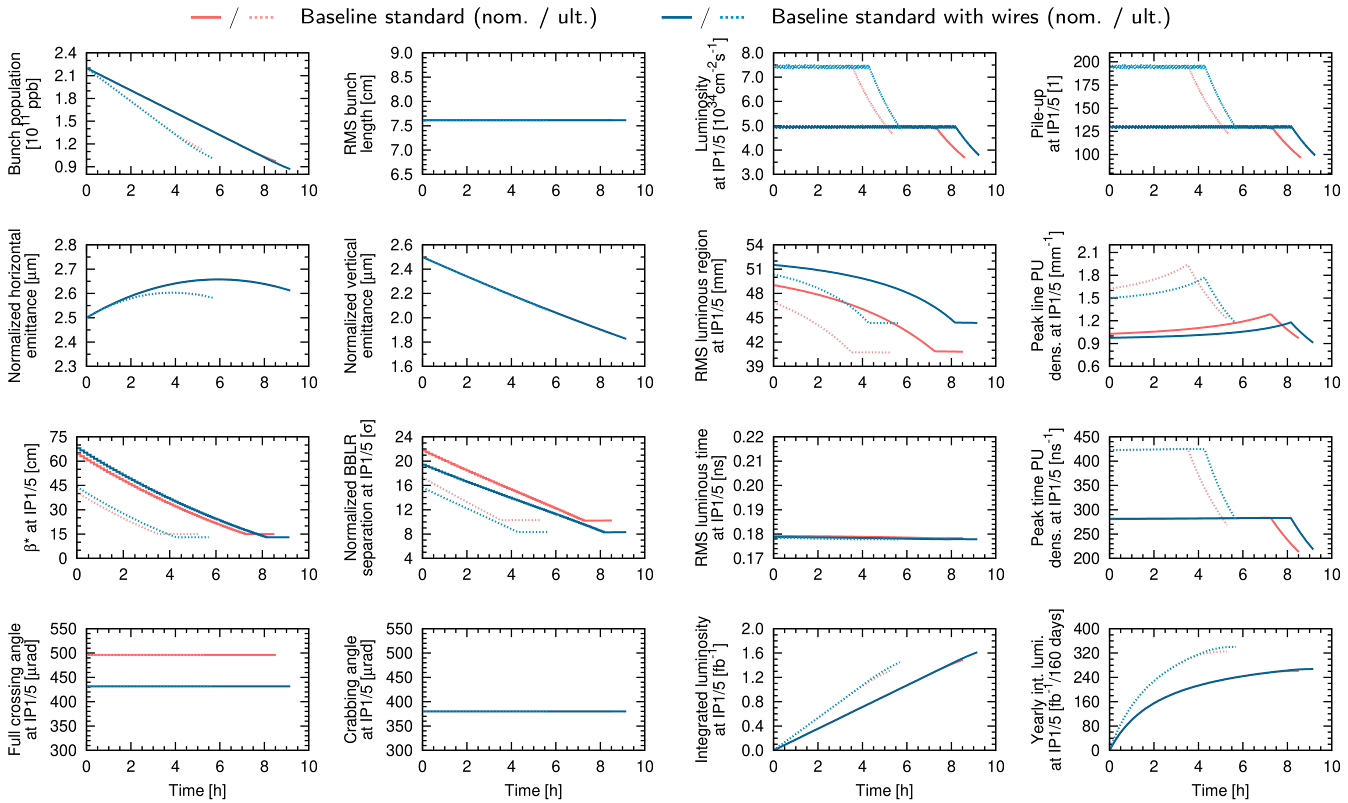

Figure 5.17. Evolution at IP1/5 of the optimum fill in the HL-LHC baseline standard with wires at nominal and ultimate levelling. The HL-LHC baseline is included for comparison.

at the start of the levelling (68 cm for nominal, 44 cm for ultimate). The evolution of the transverse emittance at nominal and ultimate operation does not show a significant deviation from their baseline counterparts.

While the peak line PU density increases by around $0.10\,\mathrm{mm}^{-1}$ ($0.20\,\mathrm{mm}^{-1}$) for nominal (ultimate) levelling due to the reduction of the RMS luminous region, the peak time PU density does not experience significant change. Another consequence of the reduction of the minimum θ is the lengthening of the fill duration by 0.7 h (0.4 h) for nominal (ultimate) operation, with respect to its baseline counterpart. Naturally, this comes with an increase of the number of necessary optics for the levelling stage, reaching almost 80 (56) steps. A moderate improvement on $\bar{\rho}_s$ is also observed, reducing by around 7 %; $\bar{\rho}_t$, on the other hand, experiences a small increase of 1 % (2 %). In terms of $\mathcal{L}_{\mathrm{int}}$, this scenario with wires improves the performance by around 2 % (5 %) for nominal (ultimate) operation with respect to the baseline. The results above are summarised in Table 5.7. Gaussian fits have been conducted for the line and time PU densities and the resulting parameters are listed in Table 5.8.

The effect of variable crabbing and the assumption of a reduced $\sigma_{\mathrm{b.o.}}$ (as described in Section 5.3.2.6) has been assessed for the present scenario. The relative impact on $\mathcal{L}_{\mathrm{int}}$ from the complete absence of CCs in the case with wires is lower than that on the baseline: it decreases to $241\,\mathrm{fb}^{-1}$ ($275\,\mathrm{fb}^{-1}$) for nominal (ultimate) levelling, that is, a reduction of 8 % (16 %) with respect to its counterpart with partial crabbing (2 CCs). As expected, $\bar{\rho}_s$ rises due to the absence of crabbing, with its magnitude increasing by almost 80 % for both nominal and ultimate operation, with respect to partial crabbing. Conversely, running the present case with full crabbing reduces $\bar{\rho}_s$ by more than 10 % for both levelling operation, and pushes $\mathcal{L}_{\mathrm{int}}$ by 2.7 % at nominal (and more than double for ultimate), corresponding to $269\,\mathrm{fb}^{-1}$ ($344\,\mathrm{fb}^{-1}$),. respectively. Reduction of the $\sigma_{\mathrm{b.o}}$ also increases the performance by 9 %-15 % depending on the levelled luminosity. The performance extent of this scenario is shown in Fig. 5.18.

Finally, the individual impact on the performance from two additional parameters is studied for the scenario with wires. Reduction of the turn-around time by 15 min yields to more than $270\,\mathrm{fb}^{-1}$ ($350\,\mathrm{fb}^{-1}$), that is, an increase of 5 % (8 %) on $\mathcal{L}_{\mathrm{int}}$ with respect to the baseline nominal (ultimate), with no significantly effect on $\bar{\rho}_s$. Crab cavity noise, as given by Eq. (5.3) does have a small negative impact on the performance: it decreases $\mathcal{L}_{\mathrm{int}}$ by around with respect to the case without CC noise, and leads to a small reduction of $\bar{\rho}_s$ of $0.01\,\mathrm{mm}^{-1}$ for both levelling operations.

A novel compensation technique of the beam-beam forces using local magnets in the IR is proposed in Chapter 7.

5.4.2 Adaptive crossing angle

Unlike the baseline, the total crossing angle does not remain constant in this scenario, but it varies over the course of the fill [96, 97]. At the initial bunch population of 2.2×10^{11} ppb, θ is set to 308 µrad; then, it is increased progressively until reaching 366 µrad when the intensity has shrank to 1.9×10^{11} ppb. The crossing angle continues to be increased linearly until reaching a maximum of 470 µrad when the bunch population has reduced to just below 1.2×10^{11} ppb. Lastly, as the beams continue to burn-off, θ is now reduced to compensate the loss of luminosity: at 1.1×10^{11} ppb, $\theta = 464$ µrad, and by 0.9×10^{11} ppb, it is further reduced by 32 µrad. After this point, $\theta = 418$ µrad is kept constant, even if the intensity continues to decrease. This adaptive crossing program has been developed to improve the beam stability and keep

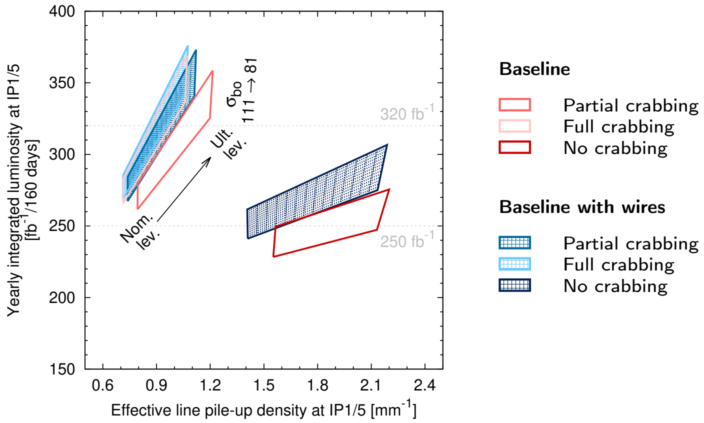

Figure 5.18. Extent of the yearly integrated luminosity and effective line PU density at IP1/5 of the HL-LHC baseline with wires at nominal and ultimate levelling assuming $\sigma_{\mathrm{b.o.}} = 111\,\mathrm{mb}$ and 81 mb.

acceptable dynamic aperture, and can be observed in the first plot of Fig. 5.19. Since the available CC voltage allows for a maximum crabbing angle of 380 µrad, it is clear that the crossing angle is fully compensated at the start of the fill; when θ grows beyond 380 µrad, however, the fractional compensation $\theta_{\mathrm{CC}}/\theta$ goes below the 1 (around 82 %-85 % by the end of the fill, a point that coincides with the maximum crossing angle). The present scenario with adaptive crossing accomplishes a 23 %-gain on $\mathcal{L}_{\mathrm{virt}}$.

A significant increment of the RMS luminous region is observed throughout the fill (with respect to the baseline) for both nominal and ultimate operations, reaching 53 mm for both levelling modes, as seen in Fig. 5.19. Unlike the baseline, however, the RMS luminous region increases again after reaching its minimum at the end of the levelling, instead of remaining constant. As a result of the increase of the luminous region, $\bar{\rho}_s$ decreases accordingly throughout the fill and its peak is lowered to $1.21\,\mathrm{mm}^{-1}$ ($1.74\,\mathrm{mm}^{-1}$) for the nominal (ultimate). The RMS luminous time and time PU density remain almost unchanged. Around four additional steps are needed to cover the slight increase of the levelling duration. Although the gain on $\mathcal{L}_{\mathrm{int}}$ is found to be limited, namely 1 % (2 %) for nominal (ultimate) with respect to the baseline, a significant improvement is observed in $\bar{\rho}_s$ which decreases by 8 % (11 %), corresponding to $0.73\,\mathrm{mm}^{-1}$ ($1.07\,\mathrm{mm}^{-1}$) for nominal (ultimate). The performance parameters for this scenario have been included in Table 5.7 alongside the scenario discussed in the previous section. Additionally, the parameters of the Gaussian fits for the corresponding 1D PU densities are also listed in Table 5.8.

Similarly to the scenario with wires, the impact on the performance due to a reduced $\sigma_{\mathrm{b.o}}$ and increased turn-around, as well as CC noise, is assessed. Performance estimates with 81 mb show a gain of 8 % (12 %) with respect to the HL-LHC baseline nominal (ultimate). While $\bar{\rho}_s$ does not experience a significant variation as a result of the reduction of $\sigma_{\mathrm{b.o}}$ at nominal operation, its resulting magnitude at ultimate levelling corresponds to a reduction of 9 % with respect to the baseline at the same operation. The reduction of the turn-around time by 15 min pushes the performance by 3 % (5 %) for the nominal (ultimate), with negligible impact on $\bar{\rho}_s$. The addition of CC noise,

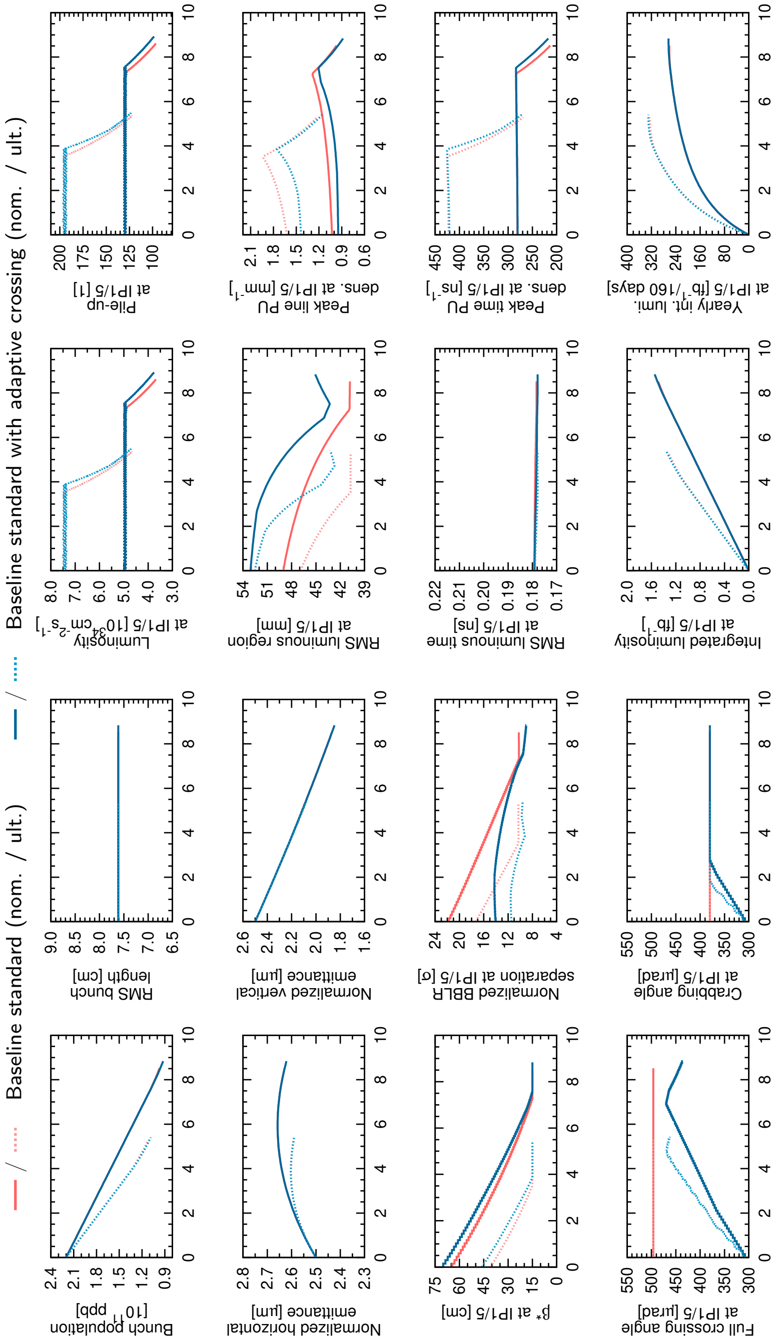

Figure 5.19. Evolution at IP1/5 of the optimum fill in the HL-LHC baseline standard with adaptive crossing at nominal and ultimate levelling. The HL-LHC baseline is included for comparison.

on the other hand, has a negative repercussion on $\mathcal{L}_{\mathrm{int}}$ (intensified by the smaller β^* of 13 cm): at ultimate operation, the performance gain is completely outweighed by the noise and, for nominal levelling, the situation even worsens as $\mathcal{L}_{\mathrm{int}}$ experiences a 1 %-loss.

5.5 Ultimate energy

In order to fully exploit the capabilities of the LHC, studies on possible collisions at a centre-of-mass energy of 15 TeV are ongoing. According to the timeline, however, this scenario falls in the high-luminosity era [37–39]. Operation at an *ultimate* beam energy of 7.5 TeV corresponds to a magnetic field of 8.93 T in the main arc dipoles and a current of 12 748 A; this provides an operational margin with respect to maximum dipole field and current of 9.0 T and 12 850 A, respectively, for a beam energy of 7.56 TeV defined in the LHC Technical Design Report [53] (the original definition of *ultimate* beam energy). In the present section, an estimation of the performance of the HL-LHC baseline at *ultimate* beam energy is studied and compared with the case at *nominal* energy (7.0 TeV).[3] As in all scenarios, levelling at both 5.0 and $7.5 \times 10^{34}\,\mathrm{cm}^{-2}\,\mathrm{s}^{-1}$ is studied. For the performance estimations, the same number of days of operation and efficiency than those for the current baseline are assumed. Nevertheless, as a result of the longer time required to ramp both up and down the magnets during the physics fills at 7.5 TeV, the turn-around times are expected to increase by 5 min. Additionally, as the variation of the inelastic and total cross-sections at the ultimate energy are at the percent level, they are assumed for practical-purposes identical to those at 7 TeV.

With the exception of the beam energy (and a relative energy spread of 1.038×10^{-4}), identical general beam parameters[4] to those found in Table 5.1 are assumed for the simulations. Regarding optics, a slightly larger minimum d_{BBLR} of 10.9σ is required to keep the same full crossing angle of 500 µrad due to the increased energy (and the scaling of the beam size), see Table 5.6. Since the BBLR effects depend on the normalised BBLR separation (moreover, the BBLR kicks also scale inversely with energy), a scheme with the same d_{BBLR} could be implemented at ultimate energy instead, gaining operational margins. This optimised scenario profits from the smaller physical beam emittance at higher energy, which allows the reduction of the crossing angle and the minimum β^*, as well as the aperture of the collimators (in mm) [38]. However, the performance of this scenario is expected to be limited due to the operation in levelling mode, and further studies are needed.

For the present scenario, simulations show that the potential increment of $\mathcal{L}_{\mathrm{int}}$ due to operation at higher energy is fully outweighed by the simultaneous increase of the turn-around times (in fact, the performance decreases, although the reduction is almost negligible). Other conservative and relaxed scenarios of machine availability yield to a reduction of $\mathcal{L}_{\mathrm{int}}$ by up to 25 %, or its increase by around 13 %, respectively [108]. The levelling time and fill duration at 7.5 TeV for the present configuration are longer than at nominal energy thanks to the smaller emittances at higher energy (Table 5.7). The RMS luminous region shrinks by 1 mm for both levelling operations as a result

---

[3] Not to confuse with *nominal* and *ultimate* used in context of levelled luminosity/PU.

[4] The total number of bunches for operation at ultimate energy has yet to be confirmed due to a possible increase of the rise time of the MKD extraction kicker, as found from first estimates.

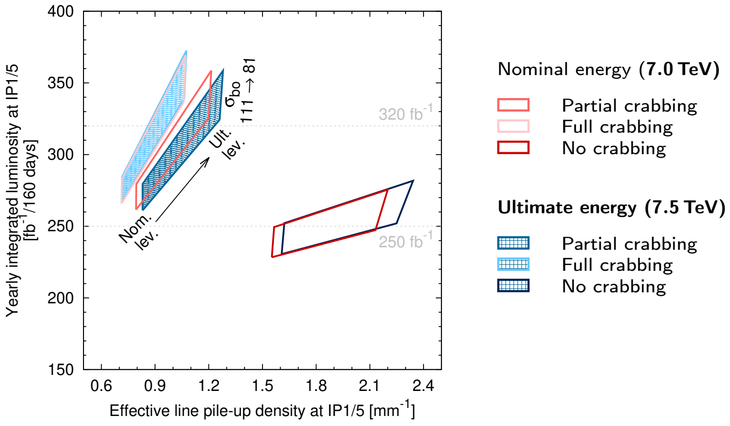

Figure 5.20. Extent of the yearly integrated luminosity and effective line PU density at IP1/5 of the HL-LHC baseline at ultimate energy (7.5 TeV) at nominal and ultimate levelling assuming $\sigma_{\mathrm{b.o.}} = 111\,\mathrm{mb}$ and 81 mb.

of the reduction of the crabbing angle ($\theta_{\mathrm{CC}} \approx 354\,\mu\mathrm{rad}$ instead of 380 µrad) provided by the CCs at a higher energy. This leads to an increase of the peak line PU density reaching around $1.4\,\mathrm{mm}^{-1}$ ($2.1\,\mathrm{mm}^{-1}$) at the end of the nominal (ultimate) levelling and to the rise of $\bar{\rho}_s$ by about 5 % for both levelling operations. Such increments could be mitigated in the optimised scenario where a lower geometrical crossing angle is considered, as previously discussed. The parameters of the Gaussian fits for the line and time PU densities of the scenario at ultimate energy for both nominal and ultimate levelling are listed in Table 5.8.

Performance estimates assuming the potential reduction of 15 min of the turn-around times, the reduced cross-section for burn-off (81 mb), or the presence of CC noise, do not show significant variations with respect to the corresponding HL-LHC baseline cases at the beam nominal energy of 7.0 TeV. On the other hand, $\mathcal{L}_{\mathrm{int}}$ does decrease by 12 % (23 %) for nominal (ultimate) levelling in the absence of CCs at 7.5 TeV, while $\bar{\rho}_s$ goes from $1.55\,\mathrm{mm}^{-1}$ ($2.13\,\mathrm{mm}^{-1}$) to $1.61\,\mathrm{mm}^{-1}$ ($2.25\,\mathrm{mm}^{-1}$). The latter figures represent a more challenging environment for the detectors, but do not necessarily constitute a serious impact. Conversely, a gain of 2 % (4 %) on $\mathcal{L}_{\mathrm{int}}$ and a reduction of 10 %-11 % on $\bar{\rho}_s$ are expected if full crabbing is available, figures that are similar than those for the baseline with nominal energy. The full extent of the performance of the HL-LHC at ultimate energy under the considerations above is shown in Fig. 5.20.

Lastly, assuming the same baseline turn-around times at nominal energy for the scenario at 7.5 TeV, a gain of 1 % on $\mathcal{L}_{\mathrm{int}}$ is observed for both nominal and ultimate levelling. A further reduction of the turn-around time by 10 min (for a total reduction of 15 min with respect to its original values) yields to an extra 1 % (2 %) gain at nominal (ultimate) levelling. In both cases the effective PU density increases slightly, but the changes remain almost negligible.

5.6 High-luminosity LHCb

The simulations of all the different HL-LHC operational scenarios included in this work are performed assuming a baseline optics configuration at IP8 and a levelled luminosity of $2.0 \times 10^{33}\,\mathrm{cm}^{-2}\,\mathrm{s}^{-1}$, as described below. Although the instantaneous luminosity at IP8 (LHCb) is much lower than at IP1/5 (ATLAS/CMS), it has a non-negligible impact on the burn-off (even if small), and therefore it plays a role at the estimation of the integrated performance at the main IPs. The presence of collisions at IP2 (ALICE) is negligible since it operates at an even lower luminosity and therefore can be ignored for the present work. Lastly, prompted by a recent interest on the operation of LHCb at high-luminosity ($\sim 10^{34}\,\mathrm{cm}^{-2}\,\mathrm{s}^{-1}$), studies to find sets of optics optics at IP8 that meet this goal have been conducted for different levelling configurations [40, 116]. In the following subsection, the latest scenarios are described in detail, discussing, in particular, the corresponding cost on the performance at the two main experiments with nominal levelling.

5.6.1 Baseline optics and levelling at IP8

The baseline operation at IP8 assumes the use of round optics with $\beta^* = 3\,\mathrm{m}$ and 2572 colliding bunches (an increase from 2524, the value in previous studies) [99]. Unlike IP1/5, levelling for LHCb is performed with parallel separation in the vertical plane, thus keeping β^* and the crossing angle in the horizontal plane constant along the fill. The beam crossing geometry at IP8 is different than that at the main IPs; in this case, the crossing angle is defined by an external and an internal crossing angle which, depending on their polarity, can take two different values. For the HL-LHC baseline, the external and internal half crossing angles are 250 µrad and 135 µrad, respectively, and thus the full crossing angle is [117]

$$\theta = 2(250 \mp 135) = \begin{cases} 230\,\mu\mathrm{rad}, & \text{for opposite polarities } (\textit{negative}) \\ 770\,\mu\mathrm{rad}, & \text{for equal polarities } (\textit{positive}). \end{cases} \tag{5.5}$$

All fill simulations in this work (for any scenario) have been conducted assuming the *negative* configuration at IP8; as shown later, this choice does not yield to any difference on the expected performance at IP1/5. The use of the positive crossing reduces $\mathcal{L}_{\mathrm{virt}}$ by around 24 % with respect to the negative option (which reaches $10.7 \times 10^{33}\,\mathrm{cm}^{-2}\,\mathrm{s}^{-1}$); the corresponding virtual PU are 23 and 30 events per bunch

Table 5.9. Optics and virtual parameters at IP8 of the HL-LHC baseline with horizontal crossing at $\mathcal{L}_{\mathrm{lev}} = 2.0 \times 10^{33}\,\mathrm{cm}^{-2}\,\mathrm{s}^{-1}$. Nominal levelling in IP1/5 is assumed.

Parameter	Unit	Negative	Positive
Number of colliding bunches	1	2572	2572
Minimum $\beta^*_{\times,\parallel}$	cm	300	300
Full crossing angle	µrad	230	770
Virtual luminosity	$10^{33}\,\mathrm{cm}^{-2}\,\mathrm{s}^{-1}$	10.68	8.07
Virtual pile-up	1	29.9	22.6
Virtual loss factor	1	0.963	0.728
Virtual beam-beam	10^{-2}	1.02	0.73

Table 5.10. Performance at IP8 of the cases in Table 5.9.

Parameter	Unit	Negative	Positive
Levelled luminosity	$10^{33}\,\mathrm{cm}^{-2}\,\mathrm{s}^{-1}$	2.0	2.0
Levelled pile-up	1	5.6	5.6
At the start of the fill			
Full parallel sep.	µm	82.1	74.9
RMS luminous region	mm	52.2	40.4
RMS luminous time	ns	0.181	0.187
Peak line PU density	mm^{-1}	0.041	0.055
Peak time PU density	ns^{-1}	11.9	11.3
At the end of the fill			
Full parallel sep.	µm	22.0	0.0
RMS luminous region	mm	52.2	40.8
RMS luminous time	ns	0.181	0.187
Peak line PU density	mm^{-1}	0.041	0.049
Peak time PU density	ns^{-1}	11.9	10.1
Levelling time	h	8.5	8.1
Integrated luminosity per fill	fb^{-1}	0.06	0.06
Yearly integrated luminosity	fb^{-1}/160 days	10.7	10.6
Diff. w.r.t. baseline negative	%	–	−0.3
Effective line PU density	mm^{-1}	0.030	0.038
Diff. w.r.t. baseline negative	%	–	+29.0
Effective time PU density	ns^{-1}	8.6	8.2
Diff. w.r.t. baseline negative	%	–	−4.0
Impact on IP1/5 (nominal)			
Yearly integrated luminosity	fb^{-1}/160 days	262	262
Diff. w.r.t. baseline negative	%	–	+0.0
Effective line PU density	mm^{-1}	0.79	0.79
Diff. w.r.t. baseline negative	%	–	−0.0
Effective time PU density	ns^{-1}	200	200
Diff. w.r.t. baseline negative	%	–	−0.0

crossing, respectively (Table 5.9). At $\mathcal{L}_{\mathrm{lev}} = 2.0 \times 10^{34}\,\mathrm{cm}^{-2}\,\mathrm{s}^{-1}$, the levelled PU remains just below 6 events per bunch crossing, a reduction by a factor of five (six) for the negative (positive) crossing with respect to its virtual value.

Figure 5.21 shows the evolution of the beam, optics, and performance parameters for the optimum fills of the two angle configurations at IP8. Naturally, the bunch population, bunch length, and transverse emittance are identical to those presented for IP1/5 as they are properties of the common beams. At the beginning of the levelling, the full parallel separation at IP8 is around 82 µm (75 µrad) for the 230 µrad (770 µrad) case. As explained before, the fill duration (8.5 h for the HL-LHC baseline nominal) is fixed by the optimum fill (in terms of integrated luminosity) at the main IPs. The parallel separation collapses to zero shortly before the fill ends for the configuration with positive crossing, while, for the case with negative crossing, a zero-parallel separation is not reached. The RMS luminous region and RMS luminous time do not change significantly from the beginning to the end of the fill. Moreover, since levelling is still enacted by the end of the fill for the 230 µrad case, they do not change (the same applies to the peak line and time PU densities). For the case with positive crossing, only the peak line and time PU densities drop at the end of the levelling,

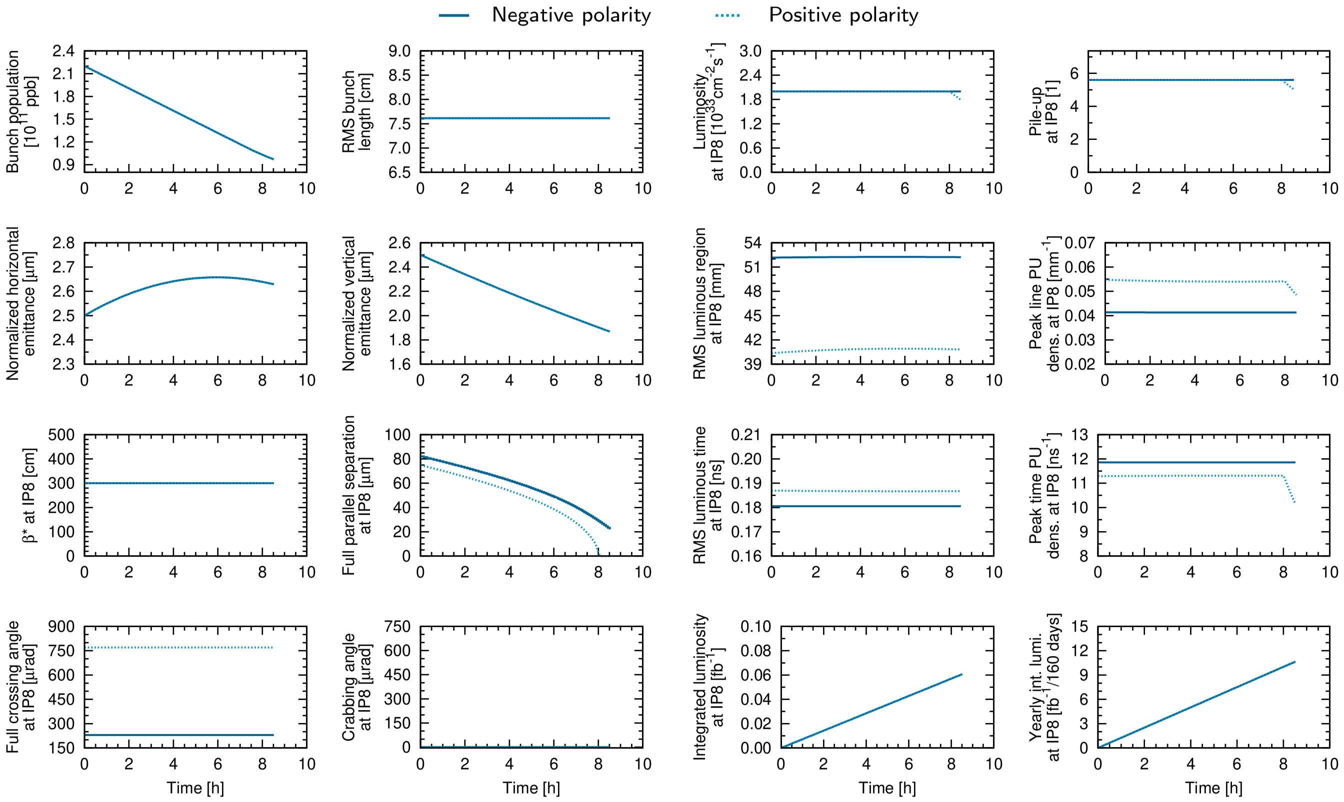

Figure 5.21. Evolution at IP8 of the optimum fill in the HL-LHC baseline with horizontal crossing at $\mathcal{L}_{\text{lev}} = 2.0 \times 10^{33}\,\text{cm}^{-2}\,\text{s}^{-1}$.

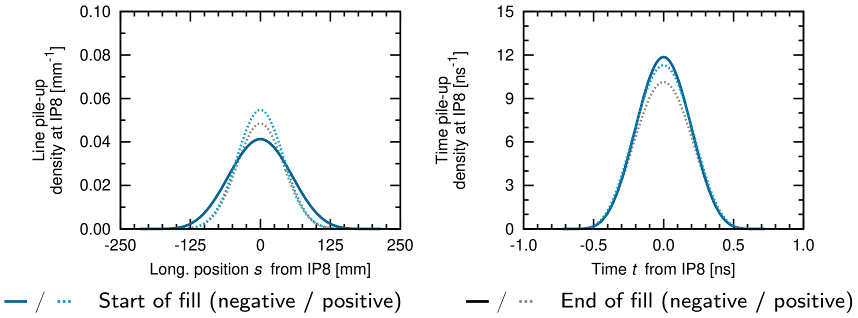

Figure 5.22. Line and time PU densities at IP8 at the start and at the end of the fill in the HL-LHC baseline nominal with horizontal crossing at $\mathcal{L}_{\text{lev}} = 2.0 \times 10^{33}\,\text{cm}^{-2}\,\text{s}^{-1}$.

soon before the fill ends. As seen from Figure 5.22, both the line and PU densities are well-described, as usual, by Gaussian distributions.

In terms of integrated luminosity for LHCb, both operational options deliver effectively the same performance ($0.06\,\text{fb}^{-1}$ per fill), accounting for almost $11\,\text{fb}^{-1}$ per year under the baseline assumptions of efficiency and turn-around time. Characterisation in terms of $\bar{\rho}_s$ ($\bar{\rho}_t$) finds $0.03\,\text{mm}^{-1}$ ($8.6\,\text{ns}^{-1}$) and $0.04\,\text{mm}^{-1}$ ($8.2\,\text{ns}^{-1}$) for negative and positive internal crossing angle, respectively. Assuming nominal levelling at the main IPs, the performance at IP1/5 is not found to be compromised by the choice of the polarity of the crossing angles at IP8 both in terms of $\mathcal{L}_{\text{int}}$ or $\bar{\rho}_{s,t}$, see Table 5.10.

5.6.2 New optics at IP8

In order to increase the luminosity at IP8, several optics configuration with different reduced β^* and crossing angles, were explored. By reducing β^* to 2.0 m, and then as low as 1.4 m, it was possible to reach the virtual luminosities necessary for the different levelling thresholds, namely $1.0 \times 10^{34}\,\text{cm}^{-2}\,\text{s}^{-1}$, $1.5 \times 10^{34}\,\text{cm}^{-2}\,\text{s}^{-1}$, and $2.0 \times 10^{34}\,\text{cm}^{-2}\,\text{s}^{-1}$. First studies on a high-luminosity LHCb were performed assuming external/internal crossing angles of 250 µrad/135 µrad which yielded to full crossing angles of 230 µrad and 770 µrad for negative and positive polarities, respectively [118]. Since then, new and optimised optics were developed assuming not only a horizontal crossing at IP8, but for a vertical crossing too [40].

5.6.2.1 Horizontal crossing

Operated with negative polarity, the new optics at IP8 features an external and internal crossing angle of 200 µrad and 135 µrad, respectively, resulting in a full crossing angle of 130 µrad. For positive polarity, the former can be reduced to 150 µrad, while the latter remains the same, and thus the full crossing angle is 570 µrad [119]. Thanks to these pushed sets of optics, $\mathcal{L}_{\text{virt}}$ reaches around $2.2 \times 10^{34}\,\text{cm}^{-2}\,\text{s}^{-1}$ ($1.6 \times 10^{34}\,\text{cm}^{-2}\,\text{s}^{-1}$) for negative (positive) polarity. This allows to level the case with negative polarity at several possible thresholds, in particular $(1.0, 1.5, 2.0) \times 10^{34}\,\text{cm}^{-2}\,\text{s}^{-1}$, while only

Table 5.11. Newly proposed levelling options at IP8 for a high-luminosity LHCb in the HL-LHC baseline ($\beta^* = 1.50\,\mathrm{m}$ for all cases). Nominal levelling in IP1/5 is assumed.

Levelled luminosity	Horizontal		Vertical
	130 µrad	570 µrad	419 µrad
$1.0 \times 10^{34}\,\mathrm{cm^{-2}\,s^{-1}}$	(a)	(A)	(d)
$1.5 \times 10^{34}\,\mathrm{cm^{-2}\,s^{-1}}$	(b)	(B)	(e)
$2.0 \times 10^{34}\,\mathrm{cm^{-2}\,s^{-1}}$	(c)	–	

Table 5.12. Optics and virtual parameters at IP8 for the cases in Table 5.11.

Parameter	Unit	(a) (b) (c)	(A) (B)	(d) (e)
Number of colliding bunches	1	2572	2572	2572
Minimum $\beta^*_{\times,\parallel}$	cm	150	150	150
Full crossing angle	µrad	130	570	420
Virtual luminosity	$10^{33}\,\mathrm{cm^{-2}\,s^{-1}}$	21.62	15.77	17.98
Virtual pile-up	1	60.5	44.2	50.3
Virtual loss factor	1	0.975	0.712	0.811
Virtual beam-beam	10^{-2}	1.04	0.71	0.82

the first two are possible for positive. These scenarios[5] are labelled (a), (b), (c), and (A) and (B), respectively in Table 5.11. Just as in the baseline operation of IP8 at low luminosity, the use of CCs is not forseen for the high-luminosity LHCb; also, the number of colliding bunches at IP8 remains unchanged, see Table 5.12. The corresponding virtual PU for the cases with a full crossing angle of 130 µrad (570 µrad) is 60 (44) events per bunch crossing, thus doubling the baseline figures at IP8.

As seen in Fig. 5.23, operation of LHCb at high luminosity has a sizeable impact on the evolution of the beam parameters, even for the two cases at the lowest levelled luminosity ($1.0 \times 10^{34}\,\mathrm{cm^{-2}\,s^{-1}}$). In particular, the decrease of bunch population throughout the fill is slightly more pronounced (the decay, nevertheless, continues to be driven mainly by the burn-off at the two main IPs). In the case of the emittance, the impact is visible in the horizontal plane, but negligible in the vertical. These effects are stronger at higher $\mathcal{L}_{\mathrm{lev}}$ (cases (b)/(B) and (c)). The smaller β^* and θ are also evident in the same plot.

Depending on the chosen $\mathcal{L}_{\mathrm{lev}}$, PU increase to $\mu = 30$–60 events per bunch crossing, which correspond to an increase of 5–10 times the estimated number at the baseline LHCb. For the same levelling, the initial full parallel separation is smaller for positive polarity than for negative. Unlike the baseline levelling at IP8, a null parallel separation is reached before the fill ending for both polarities for all cases, and the luminosity starts its natural decay. For negative polarity, the duration of the levelling stage reduces from 4.7 h for the case levelled $1.0 \times 10^{34}\,\mathrm{cm^{-2}\,s^{-1}}$ to only 0.6 h for the case with doubled $\mathcal{L}_{\mathrm{lev}}$. The switch to positive polarities reduces this numbers to 3.1 h at $1.0 \times 10^{34}\,\mathrm{cm^{-2}\,s^{-1}}$ and only 0.4 h at $1.5 \times 10^{34}\,\mathrm{cm^{-2}\,s^{-1}}$.

Unlike the behaviour at IP1/5, the line PU density does not peak at the end of

---

[5] Although (a), (b), and (c) ((A) and (B)) all correspond to a crossing with negative (positive) polarity, any reference from this point to the *negative* (*positive*) case alludes to the baseline levelling scenario at $2.0 \times 10^{33}\,\mathrm{cm^{-2}\,s^{-1}}$ with negative (positive) polarity and a full crossing angle of 230 µrad (770 µrad).

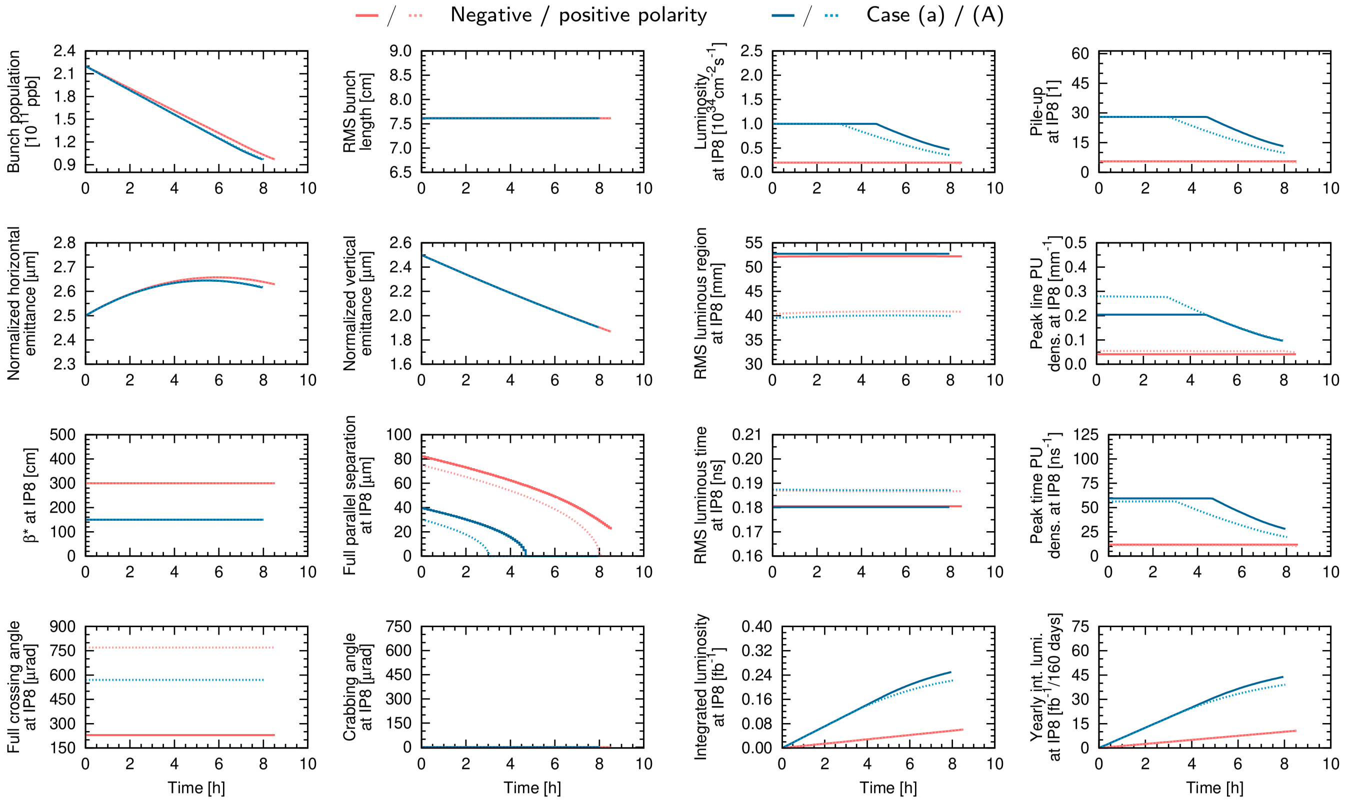

Figure 5.23. Evolution at IP8 of the optimum fill in cases (a) and (A).

Table 5.13. Performance at IP8 of the cases in Table 5.12.

Parameter	Unit	(a)	(b)	(c)	(A)	(B)	(d)	(e)
Levelled luminosity	$10^{33}\,\mathrm{cm^{-2}\,s^{-1}}$	10.0	15.0	20.0	10.0	15.0	10.0	15.0
Levelled pile-up	1	28.0	42.0	56.0	28.0	42.0	28.0	42.0
At the start of the fill								
Full parallel separation	µm	39.4	27.1	12.5	30.3	10.0	34.3	19.1
RMS luminous region	mm	52.7	52.7	52.7	39.5	39.5	44.7	44.7
RMS luminous time	ns	0.180	0.180	0.180	0.187	0.187	0.185	0.185
Peak line PU density	$\mathrm{mm^{-1}}$	0.204	0.307	0.409	0.280	0.420	0.246	0.369
Peak time PU density	$\mathrm{ns^{-1}}$	59.5	89.2	118.9	56.3	84.4	57.4	86.1
At the end of the fill								
Full parallel separation	µm	0.0	0.0	0.0	0.0	0.0	0.0	0.0
RMS luminous region	mm	52.7	52.7	52.7	39.9	39.9	42.6	42.6
RMS luminous time	ns	0.180	0.180	0.180	0.187	0.187	0.186	0.186
Peak line PU density	$\mathrm{mm^{-1}}$	0.096	0.096	0.096	0.096	0.096	0.096	0.096
Peak time PU density	$\mathrm{ns^{-1}}$	28.0	28.0	28.0	19.6	19.6	21.2	21.2
Levelling time	h	4.7	2.4	0.6	3.1	0.4	3.6	1.3
Integrated luminosity per fill	$\mathrm{fb^{-1}}$	0.25	0.30	0.33	0.22	0.25	0.23	0.27
Yearly integrated luminosity	$\mathrm{fb^{-1}}$/160 days	46.3	57.3	61.7	40.9	46.1	42.5	49.9
Diff. w.r.t. baseline negative	%	+334	+438	+479	–	–	+299	+368
Diff. w.r.t. baseline positive	%	–	–	–	+285	+334	–	–
Effective line PU density	$\mathrm{mm^{-1}}$	0.134	0.179	0.203	0.166	0.202	0.154	0.196
Diff. w.r.t. baseline negative	%	+352	+501	+582	–	–	+419	+558
Diff. w.r.t. baseline positive	%	–	–	–	+333	+425	–	–
Effective time PU density	$\mathrm{ns^{-1}}$	39.2	52.2	59.2	34.7	42.0	36.1	46.9
Diff. w.r.t. baseline negative	%	+358	+509	+590	–	–	+321	+435
Diff. w.r.t. baseline positive	%	–	–	–	+322	+411	–	–
Impact on IP1/5 (nominal)								
Yearly integrated luminosity	$\mathrm{fb^{-1}}$/160 days	257	256	255	258	257	258	257
Diff. w.r.t. baseline negative	%	−1.7	−2.3	−2.5	–	–	−1.5	−1.9
Diff. w.r.t. baseline positive	%	–	–	–	−1.5	−1.7	–	–
Effective line PU density	$\mathrm{mm^{-1}}$	0.79	0.79	0.80	0.79	0.80	0.79	0.80
Diff. w.r.t. baseline negative	%	+0.0	+0.1	+0.2	–	–	+0.1	+0.2
Diff. w.r.t. baseline positive	%	–	–	–	+0.1	+0.2	–	–
Effective time PU density	$\mathrm{ns^{-1}}$	199	199	199	199	199	199	199
Diff. w.r.t. baseline negative	%	−0.1	−0.2	−0.2	–	–	−0.1	−0.2
Diff. w.r.t. baseline positive	%	–	–	–	+0.1	+0.2	–	–

the levelling process for the levelling with parallel separation implemented in IP8, but remains constant at the same level than at the beginning of the fill for the entire duration of the levelling stage. For this reason, the values at the end of the fill are reported for IP8 in Table 5.13 (aside the usual values at the beginning of the fill) instead of the end of levelling, as done for the main IPs in the previous sections. The peak line PU density at $1.0 \times 10^{34}\,\mathrm{cm^{-2}\,s^{-1}}$ is found to be around $0.20\,\mathrm{mm^{-1}}$ and increasing proportionally to around $0.41\,\mathrm{mm^{-1}}$ for the case with doubled $\mathcal{L}_{\mathrm{lev}}$. The use of positive crossing at IP8 increases the peak line PU density of cases (A) and (B) by 40 % with respect to (a) and (b), respectively. At the end of the fill, the peak line PU density has decreased to approximately $0.10\,\mathrm{mm^{-1}}$ for all cases. A similar behaviour is followed by the peak time PU density. Regarding the RMS luminous region (time), it remains constant for the entire fill duration, independently of the levelling case: 53 mm (0.18 ns) and 40 mm (0.19 ns) for the cases with 130 µrad and 570 µrad, respectively.

The first row in Figure 5.24 shows the typical shape of the line and time PU densities at IP8, exemplified for case (a) at the start of the fill; these shapes remains

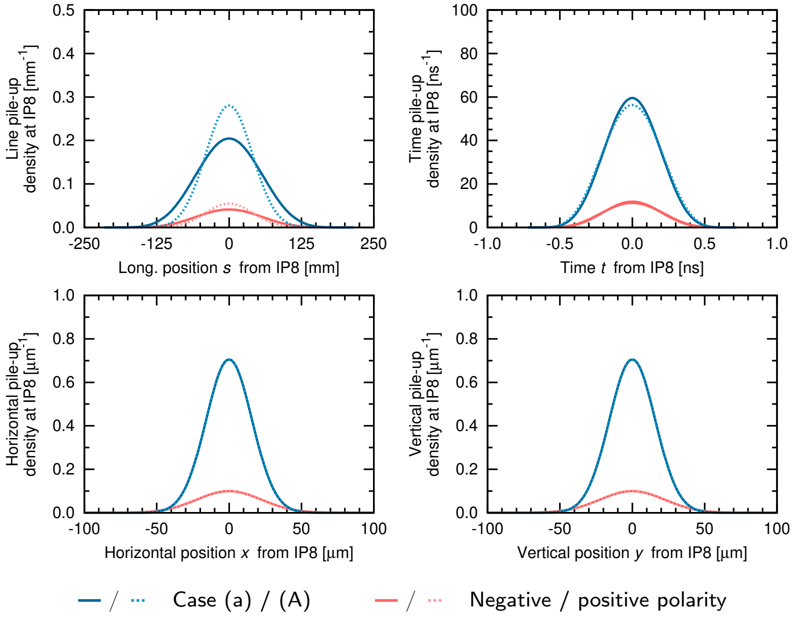

Figure 5.24. Line, time, horizontal, and vertical PU densities at IP8 at the start of the fill in the cases with horizontal crossing at $\mathcal{L}_{\text{lev}} = 1.0 \times 10^{34}\,\text{cm}^{-2}\,\text{s}^{-1}$. The HL-LHC baseline nominal with horizontal crossing at $\mathcal{L}_{\text{lev}} = 2.0 \times 10^{33}\,\text{cm}^{-2}\,\text{s}^{-1}$ is included for comparison.

almost constant until the end of the levelling, when the peak value of the corresponding variable starts decreasing while the RMS of the distribution remains almost constant. Of special interest for LHCb are the projections of the PU density along the transverse coordinates; for this reason, they have been computed for all the scenarios for a high-luminosity IP8 under study. The second row of Fig. 5.24 illustrates the horizontal and vertical PU densities at the start of the fill for case (a), and its comparison with respect to the baseline scenario with negative polarity crossing.

The RMS of the horizontal and vertical projection of the 4D PU density is the same for all cases at the start of the fill: around 22 µm for the baseline IP8, and 16 µm for the high-luminosity cases. Also at the start of the fill, the peak of the density depends on $\mathcal{L}_{\text{lev}}$: $0.1\,\mu\text{m}^{-1}$ for the baseline, and from $0.7\,\mu\text{m}^{-1}$ to $1.5\,\mu\text{m}^{-1}$ the high-luminosity cases (note the order of magnitude or units for the parameters of the transverse projections). By the end of the fill, the horizontal (vertical) RMS have grown (reduced) slightly; the peak of the distribution, on the other hand, remains almost unchanged for the case of the baseline IP8, but drops to around $0.3\,\mu\text{m}^{-1}$–$0.4\,\mu\text{m}^{-1}$ ($0.2\,\mu\text{m}^{-1}$–$0.3\,\mu\text{m}^{-1}$) for the cases with negative (positive) polarity, independently of the $\mathcal{L}_{\text{lev}}$. The parameters of the corresponding Gaussian fits for all the different 1-dimensional projections of the PU density for all the operational scenarios for IP8 (baseline and high-luminosity) are listed in Table 5.14.

The substantial increase of $\mathcal{L}_{\text{lev}}$ at IP8 comes with an increased cost on the performance at IP1/5 due to the extra burn-off: assuming nominal levelling at the main IPs, the corresponding $\mathcal{L}_{\text{int}}$ decreases by 1.5 %, 2.3 %, and up to 2.5 % from their baseline value of $262\,\text{fb}^{-1}$ when IP8 is operated at the high-luminosity level of 1.0,

Table 5.14. Parameters of the Gaussian fits of the line, time, and transverse PU densities of the cases in Tables 5.10 and Table 5.13.

Parameter	Unit	Negative	(a)	(b)	(c)	Positive	(A)	(B)	(d)	(e)
At the start of the fill										
σ_s	mm	54.1	54.7	54.7	54.7	40.8	39.9	39.9	45.5	45.5
σ_t	ns	0.188	0.188	0.188	0.188	0.197	0.198	0.198	0.194	0.194
σ_x	µm	22.4	15.9	15.9	15.9	22.4	15.9	15.9	15.9	15.9
σ_y	µm	22.4	15.9	15.9	15.9	22.4	15.9	15.9	15.9	15.9
$\hat{\rho}_s$	mm^{-1}	0.042	0.206	0.392	0.412	0.055	0.281	0.421	0.247	0.370
$\hat{\rho}_t$	ns^{-1}	12.0	60.1	90.2	120.2	11.5	57.3	85.9	58.3	87.4
$\hat{\rho}_x$	mm^{-1}	0.100	0.705	1.057	1.409	0.100	0.705	1.057	0.705	1.057
$\hat{\rho}_y$	ns^{-1}	0.100	0.705	1.057	1.409	0.100	0.705	1.057	0.705	1.057
At the end of the fill										
σ_s	mm	54.1	54.7	54.7	54.7	41.3	40.3	40.3	43.2	43.2
σ_t	ns	0.188	0.188	0.188	0.188	0.197	0.198	0.198	0.196	0.196
σ_x	µm	23.0	16.2	16.2	16.2	23.0	16.2	16.2	13.8	13.9
σ_y	µm	19.4	13.8	13.9	13.9	19.4	13.8	13.8	16.2	16.2
$\hat{\rho}_s$	mm^{-1}	0.042	0.097	0.097	0.097	0.049	0.097	0.097	0.097	0.097
$\hat{\rho}_t$	ns^{-1}	12.0	28.3	28.3	28.3	10.3	20.0	19.9	21.5	21.5
$\hat{\rho}_x$	mm^{-1}	0.097	0.325	0.325	0.325	0.087	0.240	0.240	0.301	0.300
$\hat{\rho}_y$	ns^{-1}	0.115	0.381	0.380	0.380	0.103	0.281	0.281	0.256	0.257

1.5, and $2.0 \times 10^{34}\,\mathrm{cm}^{-2}\,\mathrm{s}^{-1}$, respectively, assuming a negative internal crossing for $\theta = 130\,\mu\mathrm{rad}$. On the other hand, operation of IP8 with an internal crossing angle with a positive positive polarity, resulting in $\theta = 570\,\mu\mathrm{rad}$, reduces $\mathcal{L}_{\mathrm{int}}$ at the two main IPs by 1.5 %-1.7 % for the same set of levelled luminosities. In terms of the effective PU density at IP1/5, negligible impact is expected from operation of LHCb at high-luminosity, regardless of the polarity of its crossing angle.

The implementation of reduced β and θ (negative polarity) pushes $\mathcal{L}_{\mathrm{int}}$ to $46\,\mathrm{fb}^{-1}$ per year for LHCb, that is, an increment of around 330 % with respect to the current baseline optics and levelling at IP8 with the same internal crossing angle. For an increased $\mathcal{L}_{\mathrm{lev}}$ of $1.5 \times 10^{34}\,\mathrm{cm}^{-2}\,\mathrm{s}^{-1}$, or as high as $2.0 \times 10^{34}\,\mathrm{cm}^{-2}\,\mathrm{s}^{-1}$, $\mathcal{L}_{\mathrm{int}}$ can be pushed by 24 % ($57\,\mathrm{fb}^{-1}$) and 33 % ($62\,\mathrm{fb}^{-1}$), respectively, with respect to the estimate for $1.0 \times 10^{34}\,\mathrm{cm}^{-2}\,\mathrm{s}^{-1}$; the former corresponding to an increase of around 440 % and the later to 480 % with respect to the baseline IP8. In the case of positive polarity, $\mathcal{L}_{\mathrm{int}}$ still features a gain (by a factor three) with respect to the current baseline with positive internal angle: $41\,\mathrm{fb}^{-1}$ ($46\,\mathrm{fb}^{-1}$) for the case levelled at 1.0 (1.5) $\times 10^{34}\,\mathrm{cm}^{-2}\,\mathrm{s}^{-1}$. Regarding $\bar{\rho}_s$, it increases by 350 %–580 % for the cases with negative polarity: in particular, $\bar{\rho}_s$ reaches $0.13\,\mathrm{mm}^{-1}$ for case (a), $0.18\,\mathrm{mm}^{-1}$ for case (b), and $0.20\,\mathrm{mm}^{-1}$ for case (c). For the cases with positive polarity, on the other hand, $\bar{\rho}_s = 0.17\,\mathrm{mm}^{-1}$ for case (A), and $0.20\,\mathrm{mm}^{-1}$ for case (B), that is, it increases by around 320 % and 410 %, respectively.

5.6.2.2 Vertical crossing

A scheme with vertical crossing can also be implemented, keeping the same β^* and number of colliding bunches. In such scenario, the external crossing angle is $160\,\mu\mathrm{rad}$, while the internal crossing angle remains at $135\,\mu\mathrm{rad}$. This leads to a full vertical

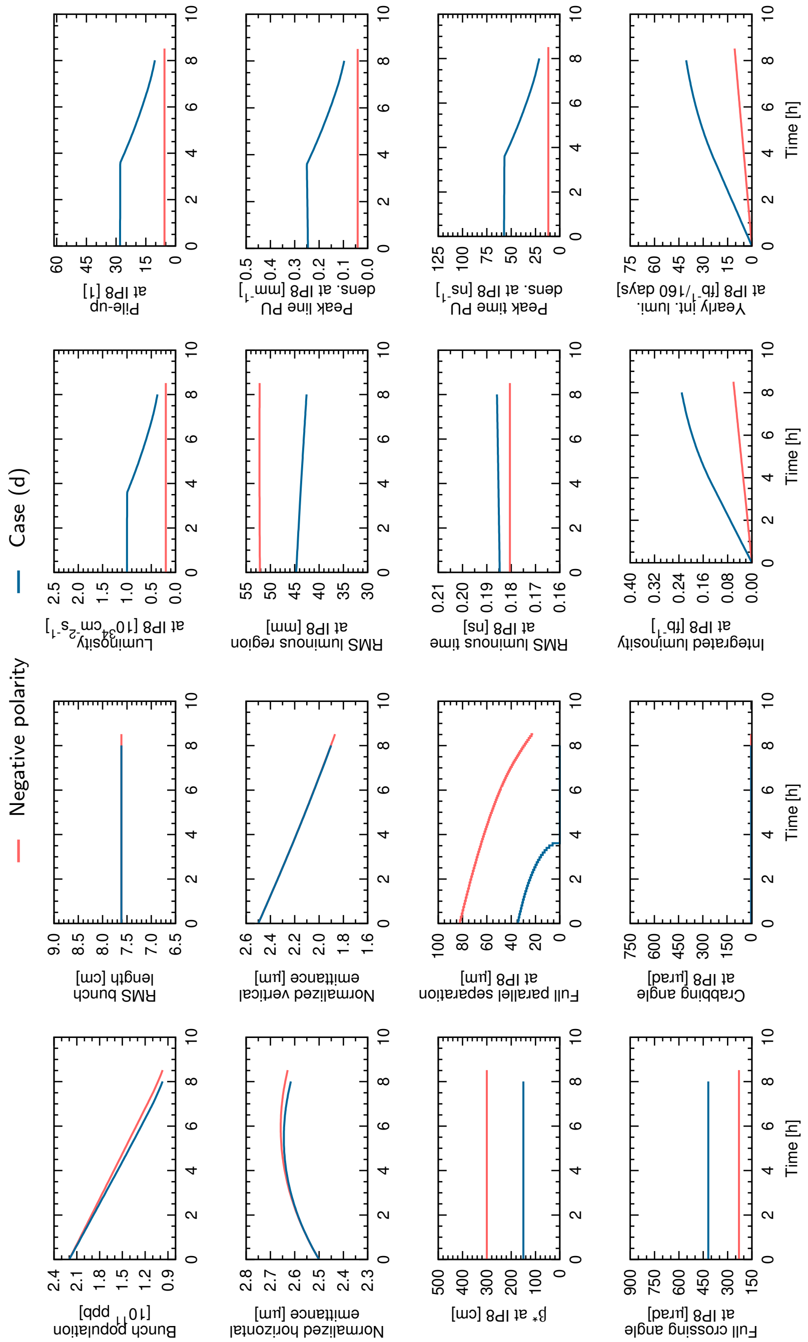

Figure 5.25. Evolution at IP8 of the optimum fill in case (d).

crossing angle of [119, 120]

$$\theta = 2\sqrt{160^2 + 135^2} \approx 419\,\mu\mathrm{rad}\,. \tag{5.6}$$

As listed in Table 5.12, the virtual luminosity under this optics can be pushed to almost $1.8 \times 10^{34}\,\mathrm{cm^{-2}\,s^{-1}}$, corresponding to a virtual PU of just above 50 events per bunch crossing. Therefore, two cases are studied: (e) at levelled luminosity of $1.0 \times 10^{34}\,\mathrm{cm^{-2}\,s^{-1}}$, and (d) at $1.5 \times 10^{34}\,\mathrm{cm^{-2}\,s^{-1}}$, see Table 5.11.

Similar to the cases of high-luminosity LHCb with horizontal crossing, the full parallel separation at IP8 (in this case in the horizontal plane) collapses to zero prior the fill ending, from an initial magnitude of $34\,\mu\mathrm{m}$ and $19\,\mu\mathrm{m}$ for cases (d) and (e), respectively, at the start of the fill, as seen in Fig. 5.25). This occurs after 3.6 h for the case levelled at $1.0 \times 10^{34}\,\mathrm{cm^{-2}\,s^{-1}}$, and reduces to only $1.3\,\mathrm{cm^{-2}\,s^{-1}}$ for the case at $1.5 \times 10^{34}\,\mathrm{cm^{-2}\,s^{-1}}$. The evolution of the bunch population and transverse emittances under the vertical crossing scheme is similar to that found for the cases horizontal crossing.

The integrated luminosity resulting from the extrapolation to one year of operation (under the usual assumptions) is around $43\,\mathrm{fb^{-1}}$–$50\,\mathrm{fb^{-1}}$. The effective line PU density reaches $0.15\,\mathrm{mm^{-1}}$–$0.20\,\mathrm{mm^{-1}}$, a more challenging environment for the LHCb detector with respect to the baseline $0.03\,\mathrm{mm^{-1}}$–$0.04\,\mathrm{mm^{-1}}$. The expected impact on $\mathcal{L}_{\mathrm{int}}$ at IP1/5 is at the same level than the cases with horizontal crossing and positive polarity, namely 1.5 %–1.9 %, without noticeable effect on the time densities. These results are summarised in Table 5.13.

Unlike the cases with horizontal crossing, the RMS luminous region does change throughout the fill, (although in almost a linear fashion): it decreases by 3 mm at the end of the fill from 42.6 mm at the start of the levelling, independently of the implemented levelled luminosity. The peak PU density remains constant at $0.25\,\mathrm{mm^{-1}}$ for case (d) and $0.37\,\mathrm{mm^{-1}}$ for case (e) during the levelling stage, dropping by the end of it. The RMS luminous time, on the other hand, remains fairly constant for the entire fill duration. The parameters of the corresponding Gaussian fits are listed in Table 5.14. In particular, as in the case with horizontal crossing, the transverse distributions are identical at the start of the fill (with RMS and peak also similar to those with horizontal crossing at the corresponding $\mathcal{L}_{\mathrm{lev}}$, but diverge by the end of the fill; however, the magnitude of the horizontal and vertical parameters are interchanged, as the crossing occurs, precisely, in the opposite plane.

Chapter 6

Performance of HL-LHC alternative scenarios

As the HL-LHC baseline was revised, the parameters of the alternative operational scenarios were updated accordingly. These scenarios, known as 8b+4e, Flat, No CCs and CK, aim at either improving the baseline performance or providing alternative operation schemes to overcome possible limitations. Simulations for each of these scenarios have been performed with both nominal and ultimate levelling to estimate, in the same way than in the previous chapter, the corresponding performance in terms of the expected yearly integrated luminosity and effective PU density. The impact on the performance of the full or null availability of crabbing and the presence of CC noise (when applicable), as well as the reduction of the assumed turn-around times and cross-section for burn off, are also addressed for every case.

6.1 Flat

As the parameters of the HL-LHC baseline were revised and updated [121], a study was conducted to update the corresponding alternative operational scenario with flat optics [122]. The normalised BBLR separation was computed from the linear interpolation of the previous baseline and Flat scenarios ($\beta^* = 20\,\text{cm}$ with $d_{\text{BBLR}} = 10.5\sigma$, and $\beta^*_{\times}/\beta^*_{\parallel} = 40\,\text{cm}/15\,\text{cm}$ with $d_{\text{BBLR}} = 12.5\sigma$, respectively [90]). The chosen configuration, namely $\beta^*_{\times} = 18\,\text{cm}$ and $\beta^*_{\parallel} = 7.5\,\text{cm}$ at IP1/5 with $d_{\text{BBLR}} = 11.4\sigma$, maximises the virtual luminosity, as seen in Fig. 6.1, reaching around $21.1 \times 10^{34}\,\text{cm}^{-2}\,\text{s}^{-1}$. It has to be noted, nevertheless, that this normalised BBLR separation is optimistic, and has yet to be fully demonstrated in operation with flat optics [123]; moreover, it might require the implementation of BBLR compensation techniques [46–49, 124–127].

Table 6.1. General parameters of the HL-LHC main alternative scenarios: Flat, 8b+4e, 200 MHz, and No CCs.

Parameter	Unit	Flat	8b+4e	200 MHz	No CCs
Beam energy	TeV	7.0	7.0	7.0	7.0
Tot. no. bunches per beam	1	2760	1972	2760	2760
Bunch population (ppb)	10^{11}	2.2	2.2	2.2	2.2
Total beam current	A	1.10	0.79	1.10	1.10
Longitudinal profile	–	q-Gaussian	q-Gaussian	Gaussian	q-Gaussian
RMS bunch length	cm	7.6	7.6	15.0	7.6
Full width at half maximum	cm	21.2	21.2	35.3	21.2
Relative energy spread	10^{-4}	1.07	1.07	1.00	1.07
Norm. transv. emittance	µm	2.5	2.2	2.5	2.5

Table 6.2. Optics and virtual parameters at IP1/5 of the scenarios in Table 6.1.

Parameter	Unit	Flat	8b+4e	200 MHz	No CCs
Number of colliding bunches	1	2748	1967	2748	2748
Minimum $\beta^*_\times$, $\beta^*_\parallel$	cm	18.0, 7.5	15.0	18.0, 7.5	31.5, 7.5
Full crossing angle	µrad	490	470	490	410
Minimum norm. BBLR sep.	σ	11.4	10.5	11.4	12.6
Piwinski parameter	1	2.42	2.66	4.76	1.53
Virtual luminosity	$10^{34}\,\mathrm{cm}^{-2}\,\mathrm{s}^{-1}$	21.09	14.44	11.54	11.69
Virtual pile-up	1	553	529	303	306
Virtual loss factor	1	0.690	0.749	0.378	0.506
Virtual beam-beam	10^{-2}	0.87	1.06	0.67	0.41

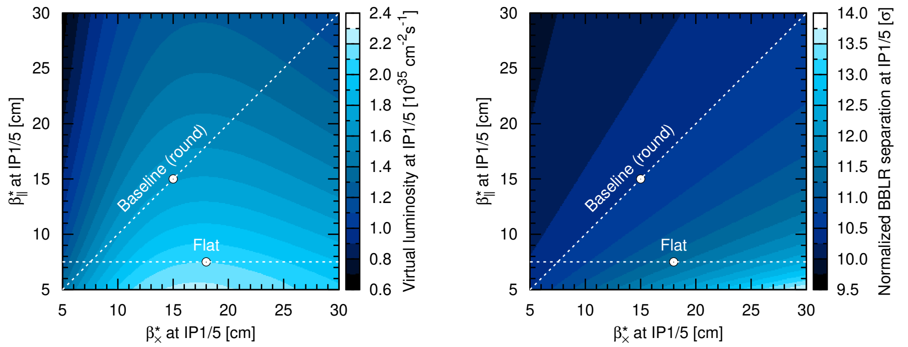

(a) Virtual luminosity at IP/5 **(b)** Norm. BBLR separation at IP1/5

Figure 6.1. Optics for the Flat alternative scenario: **(a)** virtual luminosity at IP1/5 as a function of $\beta^*_{x,y}$, and **(a)** normalised BBLR separation as a function of $\beta^*_{x,y}$. The selected alternative scenario with flat optics ($\beta^*_\times/\beta^*_\parallel = 18.0\,\mathrm{cm}/7.5\,\mathrm{cm}$ with $d_{\mathrm{BBLR}} = 11.5\sigma$) is highlighted, together with the HL-LHC baseline for comparison.

Table 6.3. Performance at IP1/5 of the scenarios in Table 6.2.

Parameter	Unit	Flat		8b+4e		200 MHz		No CCs	
		Nominal	Ultimate	Nominal	Ultimate	Nominal	Ultimate	Nominal	Ultimate
Levelled luminosity	$10^{34}\,\mathrm{cm}^{-2}\,\mathrm{s}^{-1}$	5.0	7.5	3.8	5.5	5.0	7.5	5.0	7.5
Levelled pile-up	1	131	197	140	200	131	197	131	197
At the start of the fill									
$\beta^*_\times$	cm	103.0	66.0	70.3	47.6	66.0	36.7	110.8	63.6
$\beta^*_\parallel$	cm	42.9	27.5	70.3	47.6	27.5	15.3	26.4	15.2
Norm. BBLR sep.	σ	27.3	21.9	22.7	18.7	21.9	16.3	23.7	18.0
RMS luminous region	mm	50.5	48.8	50.1	48.7	63.0	54.3	42.1	36.6
RMS luminous time	ns	0.179	0.179	0.179	0.179	0.301	0.294	0.186	0.189
Peak line PU density	mm^{-1}	1.00	1.56	1.07	1.58	0.82	1.48	1.23	2.13
Peak time PU density	ns^{-1}	280	420	301	431	178	276	266	391
At the end of the levelling									
$\beta^*_\times$	cm	18.0	18.0	15.0	15.0	18.0	18.0	31.5	31.5
$\beta^*_\parallel$	cm	7.5	7.5	15.0	15.0	7.5	7.5	7.5	7.5
Norm. BBLR sep.	σ	11.4	11.4	10.5	10.5	11.4	11.4	12.6	12.6
RMS luminous region	mm	39.6	39.6	42.8	42.6	43.2	43.9	29.3	29.1
RMS luminous time	ns	0.180	0.180	0.178	0.178	0.258	0.276	0.192	0.192
Peak line PU density	mm^{-1}	1.34	2.02	1.30	1.87	1.30	1.93	1.81	2.72
Peak time PU density	ns^{-1}	279	419	304	434	207	294	256	383
Fill duration	h	9.1	5.6	8.2	5.4	8.1	5.2	7.4	4.9
Levelling time	h	8.2	4.3	7.1	3.9	6.5	2.4	5.7	2.2
Number of levelling steps	1	79	56	71	51	57	28	48	25
Int. luminosity per fill	fb^{-1}	1.60	1.44	1.09	1.00	1.40	1.22	1.27	1.13
Yearly int. luminosity	fb^{-1}/160 days	267	339	198	242	256	304	249	293
Diff. w.r.t. baseline nominal	%	+2.1	–	−24.1	–	−2.1	–	−4.9	–
Diff. w.r.t. baseline ultimate	%	–	+4.3	–	−25.6	–	−6.7	–	−10.0
Effective line PU density	mm^{-1}	0.78	1.20	0.82	1.17	0.70	1.08	1.02	1.58
Diff. w.r.t. baseline nominal	%	−1.4	–	+2.9	–	−11.7	–	+29.1	–
Diff. w.r.t. baseline ultimate	%	–	+0.2	–	−2.3	–	−9.7	–	+31.7
Effective time PU density	ns^{-1}	199	291	214	297	133	182	184	250
Diff. w.r.t. baseline nominal	%	−0.1	–	+7.3	–	−33.4	–	−7.7	–
Diff. w.r.t. baseline ultimate	%	–	+1.0	–	+3.1	–	−36.9	–	−13.2

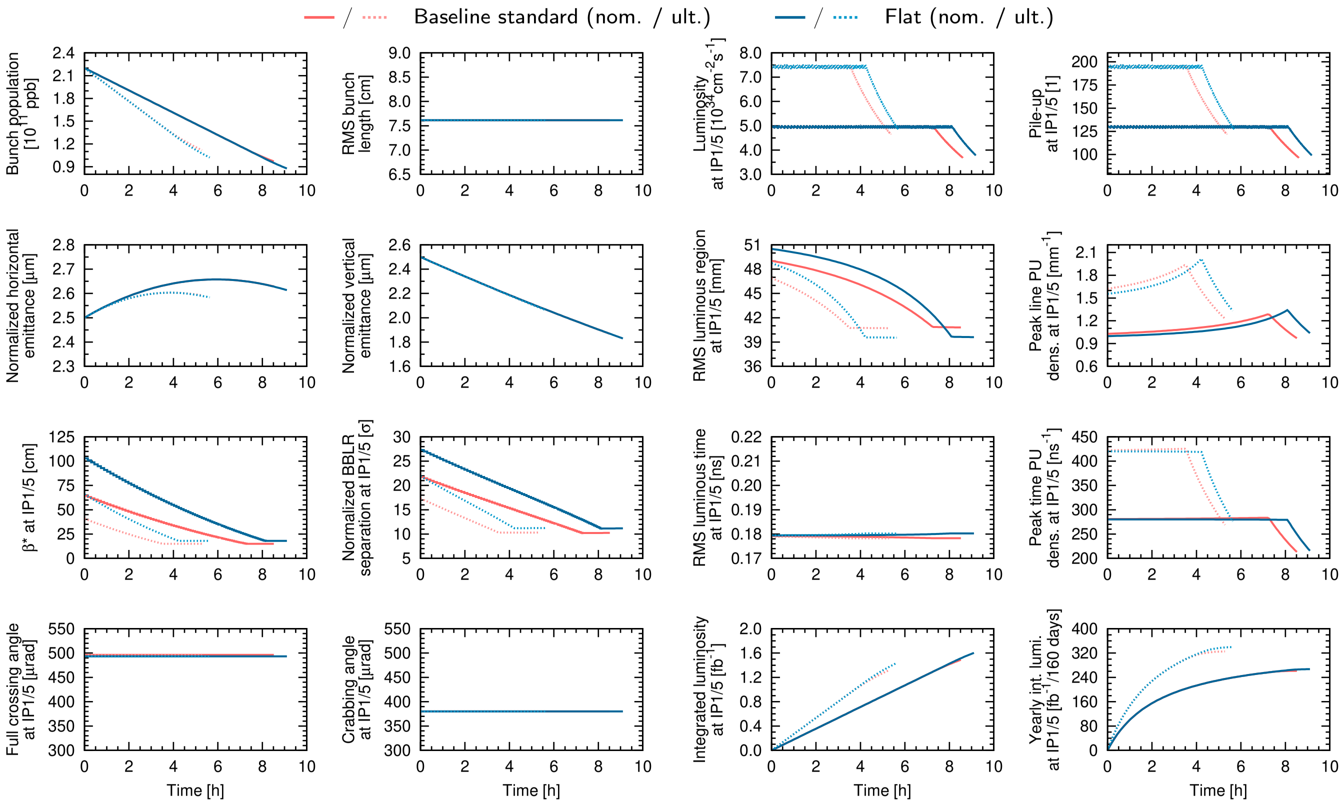

Figure 6.2. Evolution at IP1/5 of the optimum fill in the Flat alternative scenario at nominal and ultimate levelling. The HL-LHC baseline is included for comparison.

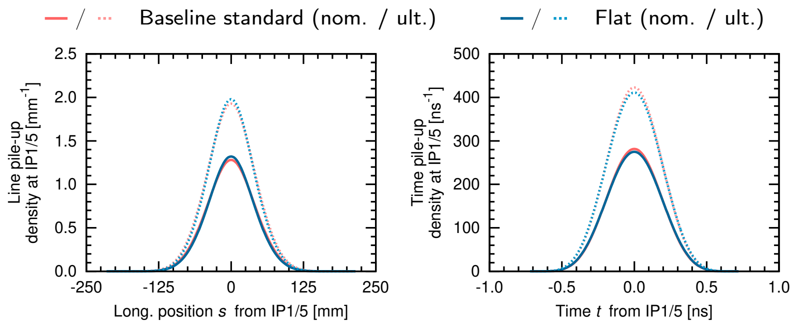

Figure 6.3. Line and time PU densities at IP1/5 at the end of the levelling in the Flat alternative scenario. The HL-LHC baseline is included for comparison.

Thus, for the current Flat scenario, the full crossing angle is $\theta = 490\,\mu\text{rad}$ (before: $360\,\mu\text{rad}$). Similarly to the HL-LHC baseline, the Flat alternative makes use of two CCs per beam per IP side which deliver up to $380\,\mu\text{rad}$ of crabbing angle, and a q-Gaussian distribution is used to describe the longitudinal profile, with a constant RMS bunch length of 7.61 cm. Following the latest update of the beam baseline parameters, the total number of bunches per beam and the number of colliding pairs at the main IPs are increased accordingly for the Flat scenario. As for the baseline, the high virtual PU (around 550 events per bunch crossing) is controlled via β^*-levelling at two different $\mathcal{L}_{\text{lev}}$, which in turn define the nominal ($5.0 \times 10^{34}\,\text{cm}^{-2}\,\text{s}^{-1}$) and ultimate ($7.5 \times 10^{34}\,\text{cm}^{-2}\,\text{s}^{-1}$) operation. In scenarios with flat optics, the process of levelling is implemented in such a way that the ratio between the betatron functions in the crossing and parallel planes remains constant. All the parameters above are listed in Tables 6.1 and 6.2 alongside the rest of the alternative scenarios, for reference.

Figure 6.2 shows the evolution of the parameters of interest for an optimum fill of the Flat alternative scenario. The evolution of the bunch population, as well as the transverse emittances remains similar to the baseline, although the fill duration is lengthened by 0.6 h (0.3 h) for the nominal (ultimate) operation, with respect to their baseline counterparts. In the Flat scenario, the levelling stage is slightly longer, and requires the implementation of almost 80 (56) optics for nominal (ultimate) operation, an increase of around a dozen with respect to the baseline The difference in the optics between the Flat and baseline scenarios is evident in plots of β^* and the d_{BBLR}; for Flat, only the betatron function in the crossing plane is plotted, since the ratio $\beta^*_\times/\beta^*_\parallel$ is constant (for the baseline, $\beta^*_\times = \beta^*_\parallel$ due to round optics).

The RMS luminous region is the at its largest at the beginning of the fill (around 2.0 mm larger than the baseline); by the end of the levelling, the situation reverses, with the RMS luminous region shirking below the baseline by around the same margin, see Fig. 6.2. As a result, the peak PU density remains slightly lower for most of the levelling stage, only growing slightly above the baseline at the end of this stage. Regarding the RMS luminous time and peak time PU density, their behaviour remains almost identical to the baseline for both levelling operations, with the difference of extending over a slightly longer levelling time. Similarly to the baseline, the line and time PU densities of the Flat scenario are well described by Gaussian distributions (Fig. 6.3), with the parameters associated to their corresponding fits listed in Table 6.4 for both nominal and ultimate operation.

Table 6.4. Parameters of the Gaussian fits of the line and time PU densities at IP1/5 of the scenarios in Table 6.3.

Parameter	Unit	Flat		8b+4e		200 MHz		No CCs	
		Nom.	Ult.	Nom.	Ult.	Nom.	Ult.	Nom.	Ult.
At the start of the fill									
σ_s	mm	52.5	50.5	52.2	50.5	64.4	54.1	42.7	36.8
σ_t	ns	0.187	0.187	0.186	0.185	0.293	0.283	0.196	0.200
$\hat{\rho}_s$	mm^{-1}	1.01	1.57	1.08	1.59	0.82	1.45	1.23	2.13
$\hat{\rho}_t$	ns^{-1}	283	424	304	435	177	275	270	398
At the end of the levelling									
σ_s	mm	39.2	39.2	43.1	42.9	40.9	41.1	28.9	28.7
σ_t	ns	0.187	0.187	0.184	0.184	0.251	0.265	0.204	0.204
$\hat{\rho}_s$	mm^{-1}	1.31	1.96	1.27	1.85	1.24	1.87	1.77	2.70
$\hat{\rho}_t$	ns^{-1}	277	415	302	435	205	292	256	386

The integrated luminosity of the current Flat scenario is found to exceed the baseline by 2 % (4 %) at nominal (ultimate) operation. Moreover, while $\bar{\rho}_s$ remains almost identical to the baseline for ultimate operation, a slight reduction is indeed found for nominal levelling, translating into a better detector performance. It has to be stressed again, nevertheless, that the Flat alternative has yet to be further validated, in particular, in terms of beam-beam effects. Lastly, the choice of flat optics can be pushed further by reducing β^* and θ; this, however, is likely to demand the implementation of a BBLR compensation scheme –such as the wires assumed for the baseline in Section 5.4.1 or the novel technique in Chapter 7– to preserve (or possibly improve) performance.

6.2 8b+4e

The 8b+4e filling scheme[1] [41, 42], aiming at addressing potential *electron-cloud* [128, 129] limitations in the machine, makes use of fewer bunches (1972) which yields to a reduced beam current (the number of colliding bunches in IP1/5, is reduced accordingly) [35, 36, 101, 110]. Operation with the baseline round β^* and normalised BBLR separation of 15 cm and 10.5σ, respectively, yields to slightly-reduced total crossing angle (470 µrad) with respect to the baseline due to the use of a smaller transverse emittance (2.2 µm). As a result, the virtual luminosity of the 8b+4e scenario decreases by around 15 % with respect to the baseline. However, luminosity is also levelled at lower thresholds, namely, $3.8 \times 10^{34}\,\mathrm{cm}^{-2}\,\mathrm{s}^{-1}$ for the nominal and $5.5 \times 10^{34}\,\mathrm{cm}^{-2}\,\mathrm{s}^{-1}$ for the ultimate operation. Compared to the baseline, these levelled luminosities correspond nonetheless to slightly higher PU levels, namely 140 and 200 events per bunch crossing, respectively, but they remain consistent with the maximum PU tolerable by the experiments. These figures were, in fact, the original targets for the two levelling operations of the HL-LHC with levelling [34], and they are still commonly found in the detector studies from the experimental side [17, 20]

Figure 6.4 shows the evolution of the 8b+4e beam and machine parameters at

---

[1] The name derives from the bunch train structure: eight bunches spaced by 25 ns followed by four empty 25 ns RF buckets [101].

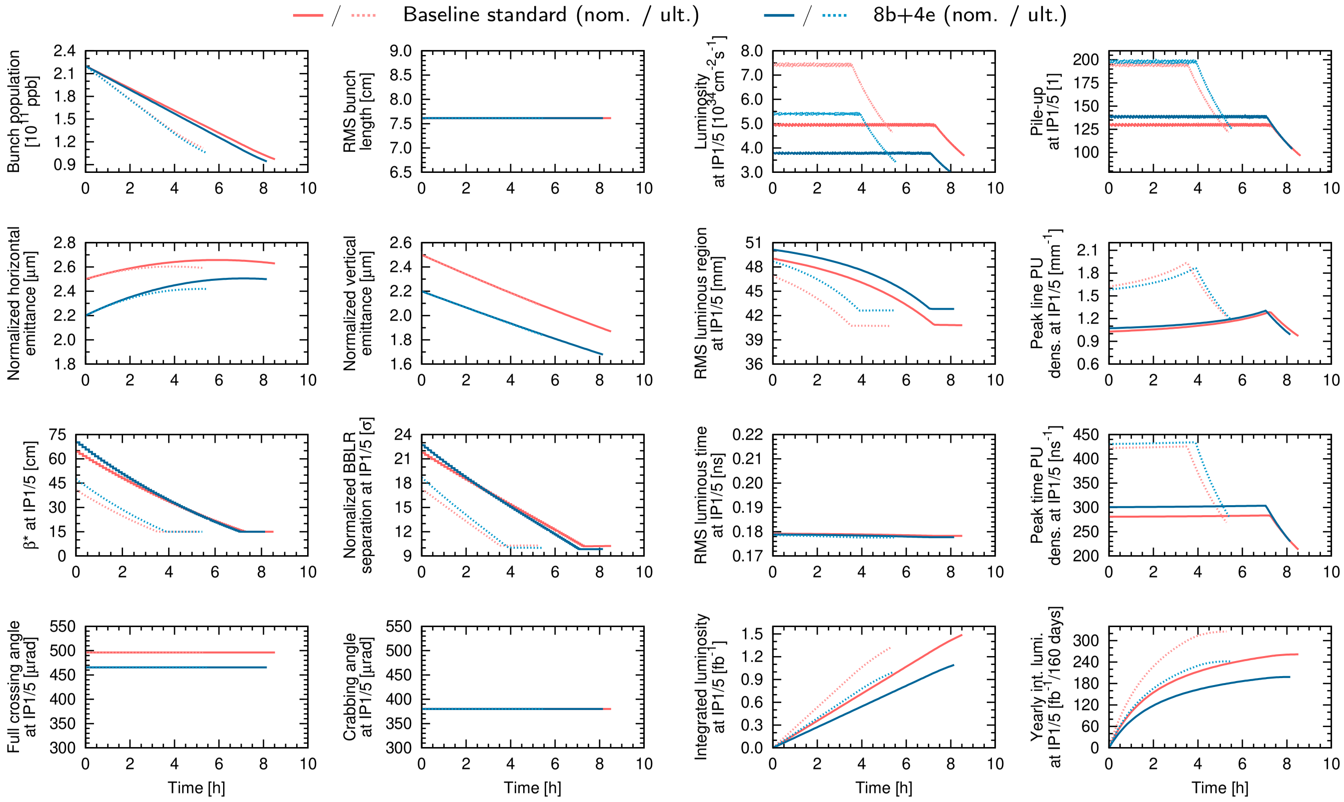

Figure 6.4. Evolution at IP1/5 of the optimum fill in the 8b+4e alternative scenario at nominal and ultimate levelling. The HL-LHC baseline is included for comparison.

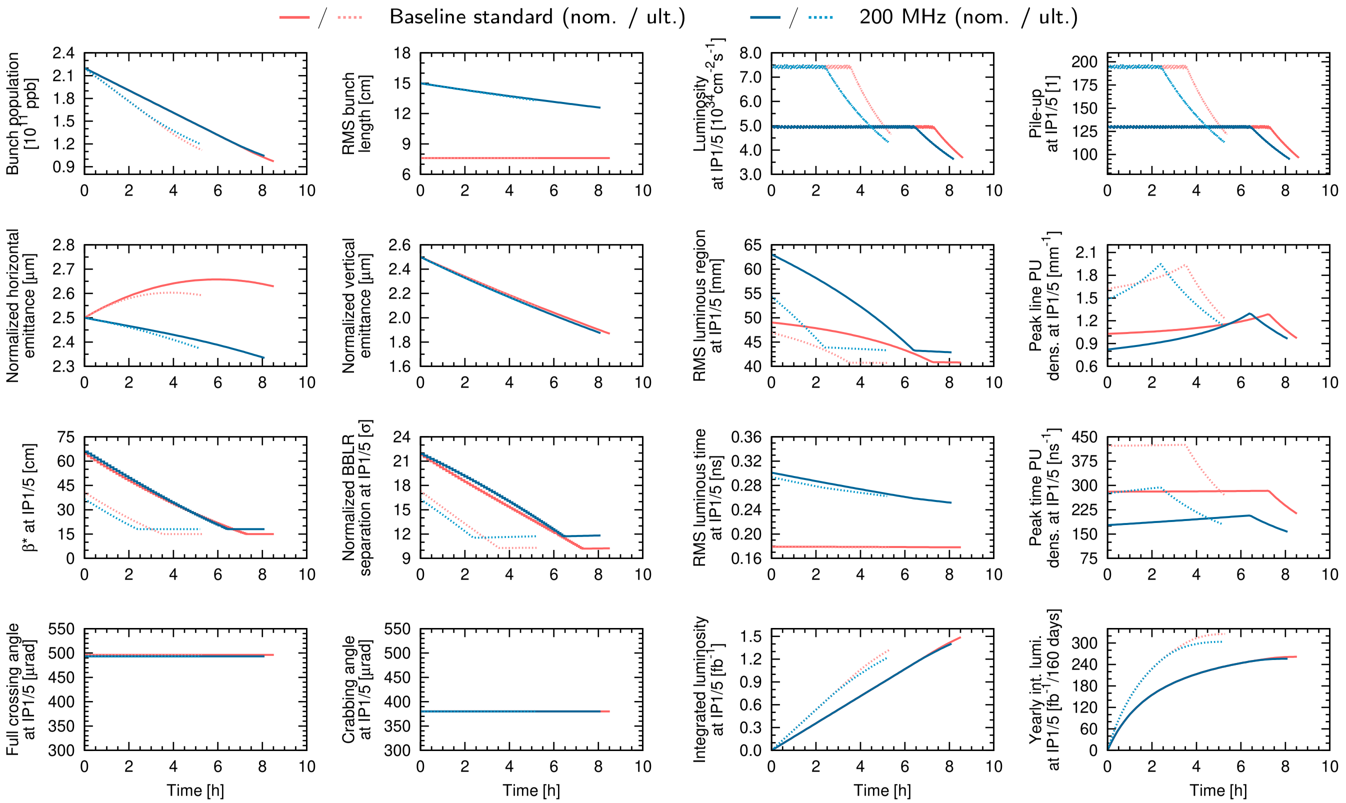

Figure 6.5. Evolution at IP1/5 of the optimum fill in the 200 MHz alternative scenario at nominal and ultimate levelling. The HL-LHC baseline is included for comparison.

the main IPs. Both the q-Gaussian RMS bunch length and the crabbing angle are kept constant at 7.6 µm and 380 µrad, respectively, throughout the fill. While the bunch population follows a similar behaviour than the baseline, β^* at IP1/5 experiences a slightly more pronounced reduction, resulting in a shorter levelling stage. The growth of the horizontal emittance is found to be more marked for the 8b+4e alternative than the baseline; on the other hand, the vertical emittance drops at a slightly reduced rate. Despite the shorter fill duration, the levelling process that keeps the instantaneous luminosity within a 2 %-margin requires a larger number of steps for the 8b+4 alternative (71 for nominal and 51 for ultimate), thus proving to be more challenging from the operational point-of-view, as a larger number of optics have to be commissioned [9, 10, 106, 107].

The difference between the levelled luminosities (and corresponding PU levels, for which the differences are smaller) of the 8b+4e and the baseline scenarios at nominal and ultimate operation is evident in the third and fourth plots of the first row of Fig. 6.4. Although the RMS luminous region of the 8b+4e case remains slightly higher than the baseline for most of the fill, the peak line PU density remains almost unchanged (within 3 %). Both the RMS luminous time and peak time PU density remain almost completely unchanged. As in the previous cases, the longitudinal and temporal projects of the time density are well-described by Gaussian distributions, with their parameters listed in Table 6.4.

Operating the machine with the 8b+4e alternative comes with a loss of around 25 % of the baseline $\mathcal{L}_{\text{int}}$. In terms of the effective line PU density, simulations show that an increase of 3 % is expected for nominal operation, while at ultimate the opposite is true, that is, a reduction of 2 % on $\bar{\rho}_s$ is found. Therefore, from the experimental point of view, detector efficiency is not expected to be significantly affected in the nominal 8b+4e operation and, on the contrary, it is expected to improve at ultimate by a few percent. Means to increase the performance while still providing suppression of the electron cloud effect remain to be explored.

6.3 200 MHz

Constituting a second alternative scenario for the mitigation of the electron-cloud effects, the 200 MHz scheme [130, 131] is characterised by the use of a secondary RF system with a total voltage of 6 MV and frequency of 200 MHz, in which longer bunches are accelerated. No additional space is expected to be required for the new low-harmonic system as it would replace two of the existing modules of the main LHC RF system. For the present study, bunches with a Gaussian longitudinal profile with an RMS bunch length of 15 cm are assumed for the 200 MHz alternative scenario, as these have shown mitigation of the heat load for a secondary emission yield of 1.4 in simulations [132]. Unlike the baseline, the bunch length is not kept constant during the fill, but it is allowed to decrease due to the cooling caused by synchrotron radiation damping. The longitudinal stability of 200 MHz scenario is guaranteed by the main 400 MHz RF system, which can be used for re-capture in a double RF harmonic operation (with total voltages of $V_{200} = 6\,\text{MV}$ and $V_{400} = 3\,\text{MV}$ per beam for both bunch-shortening or bunch-lengthening modes) [133]. Additionally, simulations at zero chromaticity have shown a reduction of the threshold of the transverse mode couple instability at 2.6×10^{11} ppb [134], that is, above the foreseen operational bunch intensity; it is possible, however, that multi-bunch effects decrease the threshold slightly,

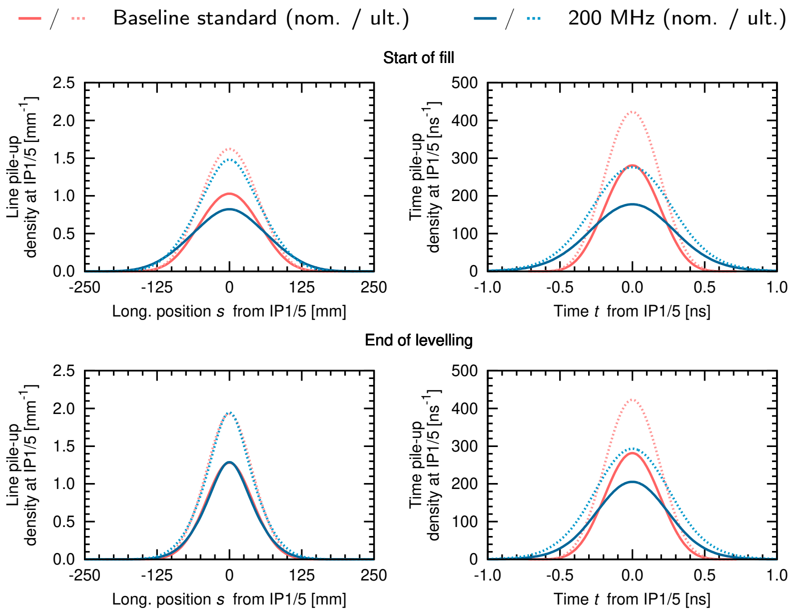

Figure 6.6. Line and time PU densities at IP1/5 at the start of the fill and at the end of the levelling in the 200 MHz alternative scenario. The HL-LHC baseline is included for comparison.

approaching the operational bunch charge [3]. Longer bunches could also be used in the 200 MHz scheme if limitations in the SPS are overcome.

As listed in Table 6.1, the beam energy, number of bunches, bunch population, and transverse emittances remain identical to the baseline. Following the increase of the bunch length, the relative energy spread is reduced to around 1.00×10^{-4}. In order to maximise the performance, the same Flat optics has been adopted for the 200 MHz scenario, yielding to $\mathcal{L}_{\mathrm{virt}} = 11.5 \times 10^{34}\,\mathrm{cm}^{-2}\,\mathrm{s}^{-1}$ (with a corresponding virtual PU of 300 events per bunch crossing).

Although the intensity burn-off is slightly slower compared to the baseline (specially at ultimate levelling), the duration of the optimum fill is shorter than the baseline. While the evolution of the normalised vertical emittance follows a similar behaviour than the baseline, its horizontal counterpart exhibits a much more drastic change, decreasing continuously along the fill and reaching 2.3 µrad–2.4 µrad by the end of the fill, as observed in Fig. 6.5. The absence of controlled longitudinal emittance (assumed in all other operational scenarios), is evident from the reduction of the bunch length with time. As for the baseline, both θ and θ_{CC} are kept constant throughout the fill, while β^* and d_{BBLR} evolve in a slightly different way. It is worth to highlight that $\beta^*_{\parallel}$ is as low as 15 cm at the beginning of the fill for ultimate operation (that is, the same as the minimum baseline β^*), which constitutes an operational challenge.

At a levelling of $5.0 \times 10^{34}\,\mathrm{cm}^{-2}\,\mathrm{s}^{-1}$ ($7.5 \times 10^{34}\,\mathrm{cm}^{-2}\,\mathrm{s}^{-1}$), the 200 MHz alternative delivers some of the largest luminous regions among the alternative scenarios: 63 mm (54 mm), while the peak line PU density is kept lower than the baseline for most of the fill duration). This leads to a significant reduction of the effective line

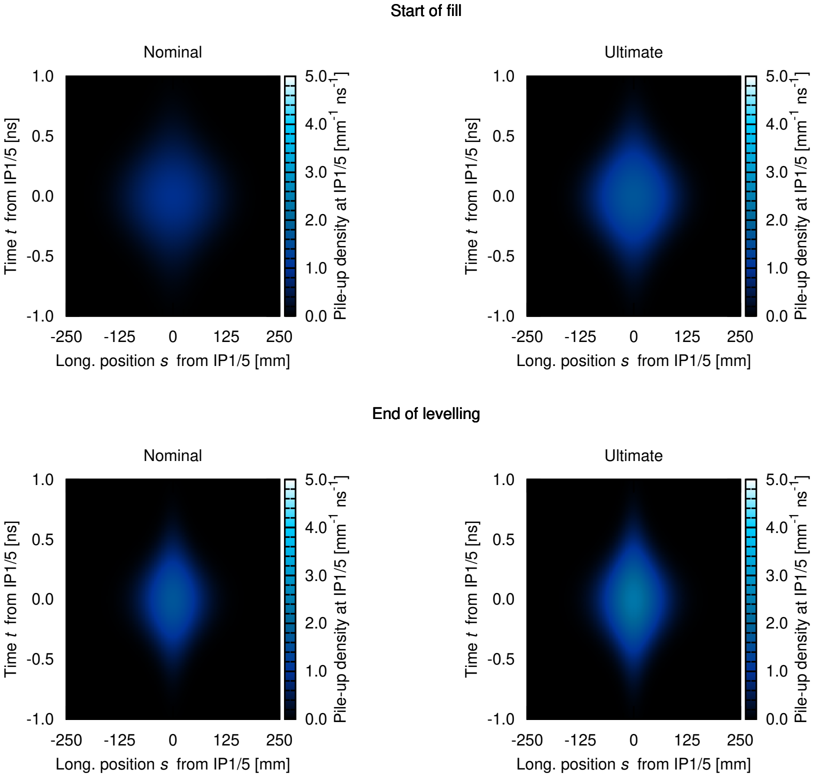

Figure 6.7. Line-time PU densities at IP1/5 at the start of the fill and at the end of the levelling in the 200 MHz alternative scenario.

PU density to $0.70\,\mathrm{mm}^{-1}$ ($1.08\,\mathrm{mm}^{-1}$) for nominal (ultimate), which represents a reduction by around 12 % (10 %). A similar behaviour is found in the corresponding time counterparts of these parameters: the RMS luminous time increases as large as 0.300 ns (at the beginning of the fill) and the peak time PU density remains almost constant at $180\,\mathrm{ns}^{-1}$ ($280\,\mathrm{ns}^{-1}$) for the nominal (ultimate) operation. The line and time PU densities of the 200 MHz scenario are shown in Fig. 6.6. While the former tends to the baseline distribution by the end of the levelling –independently of the levelling operation–, the latter remains almost constant. The usual parameters of the Gaussian fits describing each of the different 1D-distributions are listed in Table 6.4. The effect of the longer bunch length on the event distribution around the IP is specially evident in Fig. 6.7, where the shape of the 2D line-time projection of the PU density significantly differs from the baseline in Fig. 5.3.

Lastly, in terms of luminosity performance, little to moderate loss is observed for the 200 MHz operational scheme with respect to the baseline, specially at nominal levelling for which a reduction of only 2 % is expected; at ultimate levelling, the loss increases to almost 7 %. Despite the lower $\mathcal{L}_{\mathrm{int}}$, first studies from the experimental side have found improved detector efficiency in the 200 MHz scenario with respect to the baseline, as suggested by the lower effective line PU densities, although these

Table 6.5. Impact of the absence of crab cavities on the performance at IP1/5 of selected HL-LHC operational scenarios. The baseline and 8b+4e scenarios feature a round optics at the IP with $\beta^*_{\times,\parallel} = 15.0\,\text{cm}, 15.0\,\text{cm}$, while the Flat and 200 MHz alternatives feature a flat optics at the IP with $\beta^*_{\times,\parallel} = 18.0\,\text{cm}, 7.5\,\text{cm}$.

Parameter	Unit	Baseline		Flat		8b+4e		200 MHz
		Nom.	Ult.	Nom.	Ult.	Nom.	Ult.	Nom.
Fill duration	h	6.4	5.1	7.2	4.8	6.2	4.8	6.5
Levelling time	h	3.6	0.5	5.4	1.9	3.7	1.0	2.1
Number of levelling steps	1	28	6	45	22	31	12	16
At the start of the fill								
Peak pile-up density	mm^{-1}	1.94	3.85	1.53	2.88	1.99	3.61	2.02
RMS luminous region	mm	27	21	34	27	28	22	26
At the end of the levelling								
Peak pile-up density	mm^{-1}	2.66	4.07	2.51	3.79	2.80	4.12	2.48
RMS luminous region	mm	20	20	21	21	20	20	22
Effective pile-up density	mm^{-1}	1.57	2.13	1.38	2.17	1.63	2.25	1.46
Diff. w.r.t. baseline nominal	%	–	+36	−12	+39	+4	+44	−7
Yearly integrated luminosity	fb^{-1}/160 days	229	248	247	288	174	190	214
Diff. w.r.t. baseline nominal	%	–	+8	+8	+26	−24	−17	−7

differences narrow at ultimate operation. Research to fully exploit the potential of the 200 MHz scheme remains to be done.

6.4 Absence of crab cavities

Despite recent successful results in SPS tests [135], crab cavities could be absent in the HL-LHC due to several reasons such as machine protection issues, CC impedance,

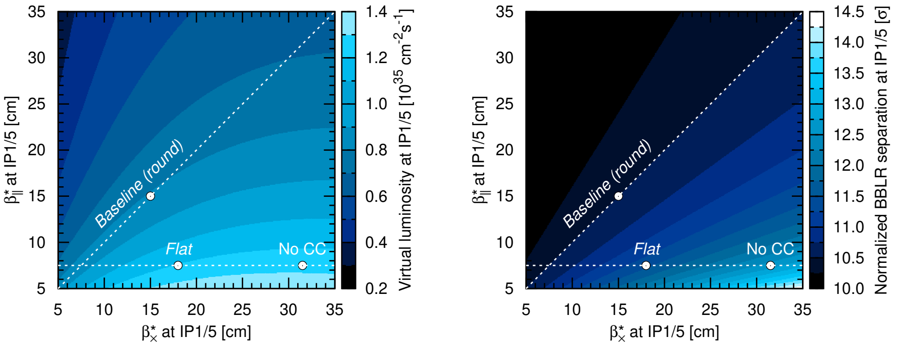

(a) Virtual luminosity at IP/5 **(b)** Norm. BBLR separation at IP1/5

Figure 6.8. Optics for the No CCs alternative scenario: **(a)** virtual luminosity at IP1/5 as a function of $\beta^*_{x,y}$, and **(a)** normalised BBLR separation as a function of $\beta^*_{x,y}$. The selected alternative scenario in the absence of CCs has flat optics ($\beta^*_{\times}/\beta^*_{\parallel} = 31.5\,\text{cm}/7.5\,\text{cm}$ with $d_{\text{BBLR}} = 12.6\sigma$) has been highlighted, together with the HL-LHC baseline and Flat scenario (both with CCs) for comparison.

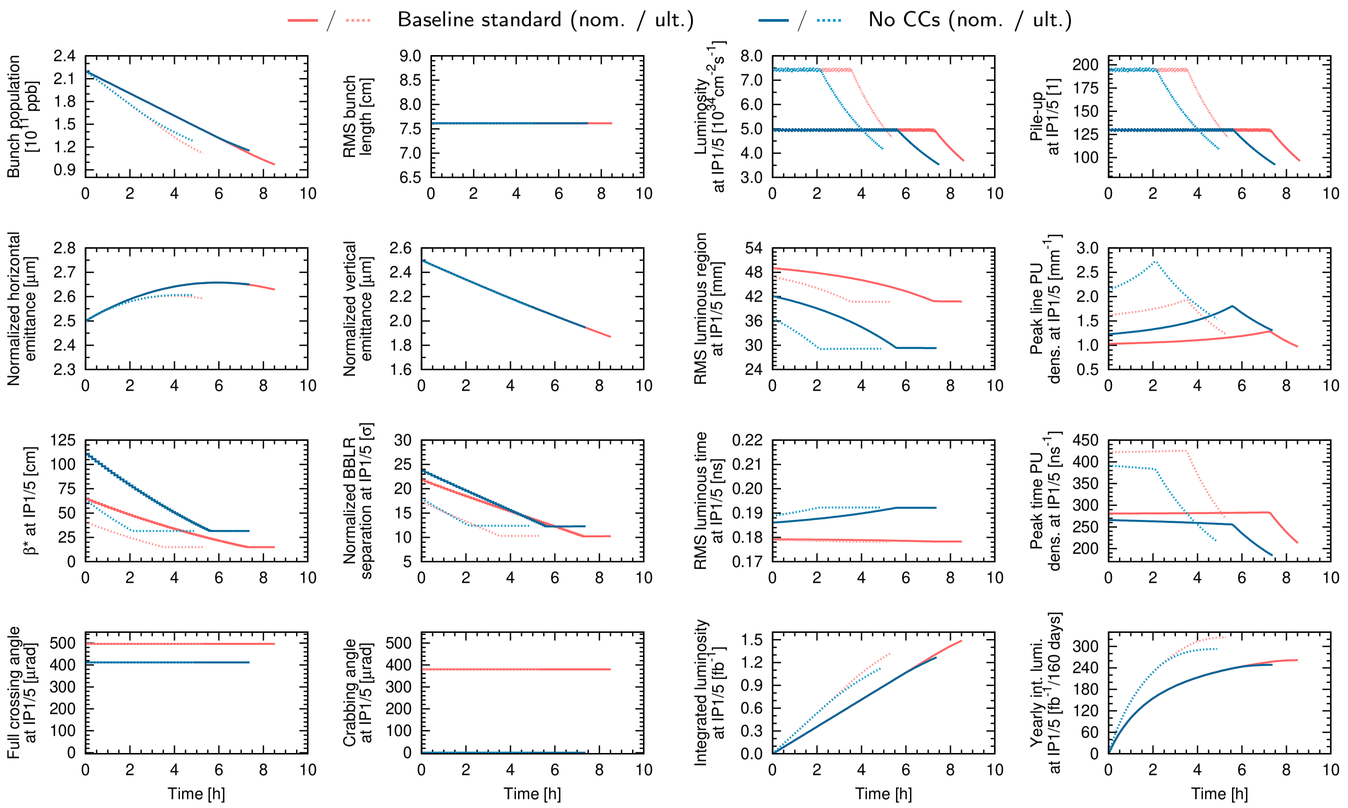

Figure 6.9. Evolution at IP1/5 of the optimum fill in the alternative scenario in the absence of CCs at nominal and ultimate levelling. The HL-LHC baseline is included for comparison.

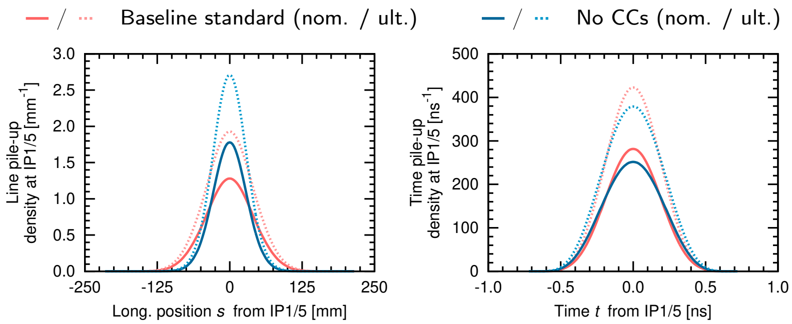

Figure 6.10. Line and time PU densities at IP1/5 at the end of the levelling in the alternative scenario in the absence of CCs. The HL-LHC baseline is included for comparison.

emittance growth induced by RF phase noise, or due to installation delays [136, 137]. At nominal levelling, the $\mathcal{L}_{\text{int}}$ of the baseline is found to decrease to $229\,\text{fb}^{-1}$, that is, by more than $12\,\%$. Similarly, the Flat, 8b+4e, and 200 MHz alternative scenarios (nominal levelling) experience performance losses of $8\,\%$, $12\,\%$, and $17\,\%$, respectively when CCs are not present. The lack of crabbing also has an effect on their corresponding effective line PU density, with the scenarios featuring flat optics delivering the lowest $\bar{\rho}_s$: $1.38\,\text{mm}^{-1}$ in Flat and $1.46\,\text{mm}^{-1}$ in 200 MHz, compared with $1.57\,\text{mm}^{-1}$ in the baseline, and $1.63\,\text{mm}^{-1}$ in 8b+4e. It must be noted that these values even surpass those found at ultimate levelling with CCs. The corresponding impact on the RMS luminous region, fill duration and levelling time, are listed in Table 6.5. The situation considerably worsens at ultimate operation, where the absence of CCs doubles the fractional reduction of $\mathcal{L}_{\text{int}}$ and rises $\bar{\rho}_s$ beyond $2\,\text{mm}^{-1}$ in all scenarios (except the 200 MHz scenario, for which ultimate levelling is not reachable without CCs with the present optics).

Hence, in the absence of CCs, the current baseline and Flat scenarios are no longer optimum and the use of flat optics at the main IPs is mandatory (see Fig. 6.8). In particular, $\beta^*_\times/\beta^*_\parallel = 31.5\,\text{cm}/7.5\,\text{cm}$ and 12.6σ-normalised BBLR separation ($410\,\mu\text{rad}$ full crossing angle) were found to maximise $\mathcal{L}_{\text{virt}}$. As in Section 6.1, this optics (referred from now on as the No CCs scenario) was derived from the extrapolation of the parameters of the previous baseline and Flat schemes, and has yet to be fully validated. Assuming the baseline number of colliding bunches in the main IPs, $\mathcal{L}_{\text{virt}} \approx 11.7 \times 10^{34}\,\text{cm}^{-2}\,\text{s}^{-1}$ (i.e. a virtual PU of 306 events).

As seen in Fig. 6.9, the normalised transverse emittances follow a similar behaviour in the No CCs alternative than in the baseline for both levelling operations (the RMS bunch length is also kept constant), although the fill duration is shortened. The bunch intensity decreases also in a similar rate than the baseline due to burn-off, although it slows down by the end of the levelling stage, thus deviating from the baseline (specially at ultimate levelling). The full crabbing angle is kept constant throughout the fill.

Due to the absence of crabbing, the extent of the RMS luminous region decreases significantly along the entire fill duration, while the RMS luminous time experiences the opposite effect. This leads to a large peak line PU density, which reaches a maximum of $1.8\,\text{mm}^{-1}$ ($2.7\,\text{mm}^{-1}$) at the end of the levelling stage for the nominal (ultimate) operation. These figures, although high when compared to the baseline with partial crabbing, are significantly lower than those found for the baseline with $\theta_{\text{CC}} = 0$,

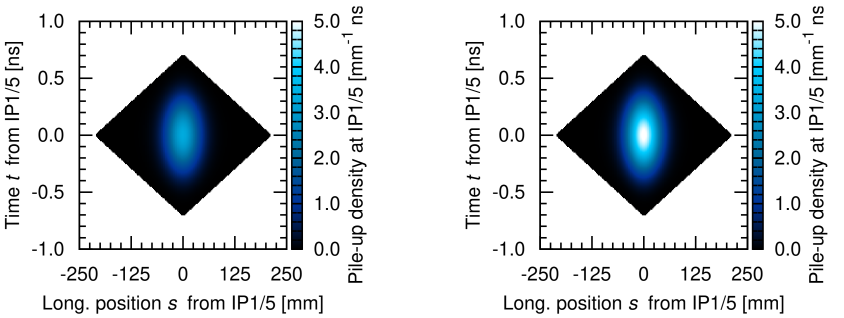

Figure 6.11. Line-time PU densities at IP1/5 at the end of the levelling in the alternative scenario in the absence of crab cavities.

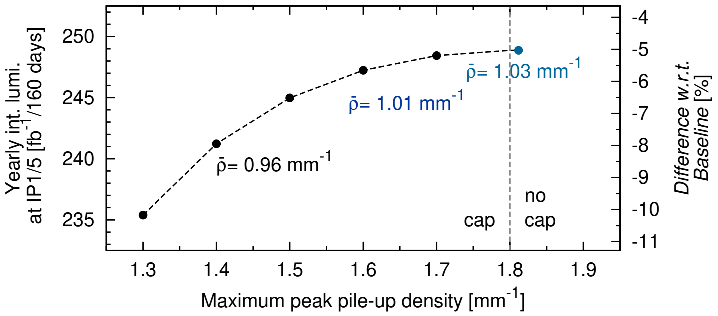

Figure 6.12. Integrated luminosity as a function of the applied cap on the maximum peak PU density in the scenario in the absence of CCs. Only the case with the largest peak PU density is unconstrained. The effective PU densities are shown for selected points.

thus limiting the negative impact of the absence of CCs. The 1D PU densities at the end of the levelling are shown in Fig. 6.10, and the parameters of their Gaussian fits listed in Table 6.4. For completeness, the 2D s–t PU density is plotted in Fig. 6.11; the sharp increase of the event density around the origin is evident for the ultimate.

The results for the No CC scenario are summarised in Table 6.3. The loss on $\mathcal{L}_{\text{int}}$ is notoriously limited to 5 % (10 %) at nominal (ultimate) operation, but it comes with a larger $\bar{\rho}_s$ of around $1.0\,\text{mm}^{-1}$ ($1.6\,\text{mm}^{-1}$). A limit on the maximum peak line PU density can be implemented as part of the levelling to improve the performance in terms of $\bar{\rho}_s$. This is accomplished by slowing down the rate of the reduction of β^*, but it comes at a greater cost on $\mathcal{L}_{\text{int}}$, as seen in Fig. 6.12. The balance between these two parameters is currently being evaluated by the experiments. Implementation of current-bearing wires or electron beams for BBLR compensation could allow to further reduce the crossing angle, resulting into an increased RMS luminous region, and improving the overall performance of the No CC scenario, a possibility that has yet to be studied.

Table 6.6. General parameters of the crab kissing scenarios.

Parameter	Unit	Original Baseline	Original Crab kissing	New crab kissing
Beam energy	TeV	7.0	7.0	7.0
Total no. bunches per beam	1	2808	2808	2760
Bunch population (ppb)	10^{11}	2.2	2.2	2.2
Total beam current	A	1.12	1.12	1.10
Longitudinal profile	–	Gaussian	super-Gaussian	super-Gaussian
RMS bunch length	cm	7.5	10.0	10.0
Full width at half maximum	cm	17.7	31.4	31.4
Relative energy spread	10^{-4}	1.20	1.20	1.07
Norm. transv. emittance	µm	2.5	2.5	2.5

Table 6.7. Optics and virtual parameters at IP1/5 of the scenarios in Table 6.6.

Parameter	Unit	Original Baseline	Original Crab kissing	New crab kissing
Number of colliding bunches	1	2808	2808	2748
Minimum $\beta^*_\times$, $\beta^*_\parallel$	cm	15.0, 15.0	30.0, 10.0	18.0, 7.5
Full crossing angle	µrad	590	500	490
Minimum norm. BBLR sep.	σ	12.5	15.0	11.4
Piwinski parameter	1	3.12	2.50	3.17
Virtual luminosity	$10^{34}\,\mathrm{cm}^{-2}\,\mathrm{s}^{-1}$	20.12	14.63	19.04
Virtual pile-up	1	542	394	499
Virtual loss factor	1	0.831	0.698	0.623
Virtual beam-beam	10^{-2}	1.07	1.02	1.02

6.5 Crab kissing

In the original crab kissing concept [86], the process of levelling not only kept the luminosity under control, but a maximum peak line PU density is also enforced (similarly to the limit discussed at the end of the previous section). In the operation with CK, however, this is accomplished by the use of two knobs, the crab crossing angle (in the crossing plane) and the crab kissing angle (in the parallel separation plane), while β^* is kept at its minimum for the entire fill. There are three clearly differentiated stages along the fill. The CK angle is first adjusted to achieve the desired peak line PU density; this, in turn, reduces the luminosity, which is then levelled by adjusting the crab crossing angle. Lastly, once $\theta_{\mathrm{CC}} = \theta$ and the θ_{CK} has reduced to zero, the luminosity is left to decay naturally. Operation with CK thus requires the use of four CCs per beam and per IP side to deflect the bunches in both transverse planes, making it incompatible with the current HL-LHC baseline. Despite this, the CK scheme remains an operational scenario of interest as it delivers the lowest effective PU density –which translates into the largest detector efficiency–, with a limited reduction of integrated luminosity with respect to the baseline (under certain conditions).

The CK scheme has been identically reproduced with the *original* parameters in Ref. [86] (Tables 6.6 and 6.7) with the aim to characterise it in terms of both the integrated performance and the expected detector efficiency, in a similar way to rest of

Table 6.8. Parameters for the estimation of yearly integrated luminosity at IP1/5 of the scenarios in Table 6.7.

Parameter	Unit	Original Baseline	Original Crab kissing	New crab kissing
Cross-section for burn-off	mb	100	100	111
Cross-section for pile-up	mb	85	85	81
Days in physics (within a year)	days	160	160	160
Efficiency	%	50	50	50
Turn-around time	min	145	145	145

alternative scenarios. This is motivated by the absence of an estimation of $\mathcal{L}_{\text{int}}$ for an optimum fill with CK in the said work (characterisation in terms of $\bar{\rho}$ is obviously not presented), where the very important role of turn-around time was omitted; Table 6.8 lists the parameters assumed for the performance assessment in the present work.

The CK scheme makes use, in particular, of bunches with a longitudinal density described by a super-Gaussian function of order 4 [138],

$$\varrho_s^{\text{SG}}(s) = \frac{2^{3/5}}{\Gamma\left(^1\!/_4\right)\sigma_{\text{SG}}} \exp\left(-\frac{s^4}{2\sigma_{\text{SG}}^4}\right) , \tag{6.1}$$

with RMS

$$\sigma_{s_{\text{SG}}} \equiv \sigma_{\text{SG}} \left(\sqrt{2}\,\frac{\Gamma\left(^3\!/_4\right)}{\Gamma\left(^1\!/_4\right)}\right)^{1/2} = 10\,\text{cm}\,, \tag{6.2}$$

see Appendix A. Figure 6.13 shows the evolution of the optimum fills of both the original baseline and CK scenarios at nominal operation. The latter scheme is found to deliver an effective line PU density of $0.50\,\text{mm}^{-1}$ for a constant peak PU density of $0.61\,\text{mm}^{-1}$ with a yearly integrated luminosity of $245\,\text{fb}^{-1}/160$ days, that is, a reduction of 9 % with respect to the original HL-LHC baseline (four CCs per beam per IP side) under the same performance assumptions.

Operation with CK has been re-evaluated with the same flat optics from Section 6.1 and revised CC voltage. As in the original CK scheme, the longitudinal density is described by Eq. (6.1). In this scenario (also shown in Fig.6.13), bunches are crabbed with $\theta_{\text{CC}}/\theta = 90\,\%$ at the beginning of the fill, and after 4 h, the 490 µrad crossing angle is fully compensated. In parallel, θ_{CK} (of a magnitude similar than θ) lowers the peak line PU density to $0.61\,\text{mm}^{-1}$, that is, less than half of the baseline nominal, a value that is kept constant over the entire the fill. During this first stage of levelling, a constant PU of 131 events per bunch crossing and an RMS luminous region of around 68 mm are maintained.

For this updated CK scenario with the current flat optics, the fill duration is found to be 8.9 h, but $\theta_{\text{CK}} = 0$ is not reached at the end of fill. During the second stage of levelling, the luminosity and PU drop almost linearly, reaching $3.6 \times 10^{34}\,\text{cm}^{-2}\,\text{s}^{-1}$ and 95 events per bunch crossing, respectively. The new CK scheme delivers a $\mathcal{L}_{\text{int}} = 249\,\text{fb}^{-1}$, representing only a 5 %-reduction with respect to the current HL-LHC baseline nominal. The effective line PU density, on the other hand, is the lowest among the analysed scenarios, namely $0.51\,\text{mm}^{-1}$. It has to be highlighted again, nevertheless, the need of doubling the number of CCs to run the machine with this alternative operation.

Figure 6.14 shows the 1D PU densities of the new CK scheme. The remarkable reduction of the peak line PU density (and $\bar{\rho}_s$ in consequence), is due to the flatter

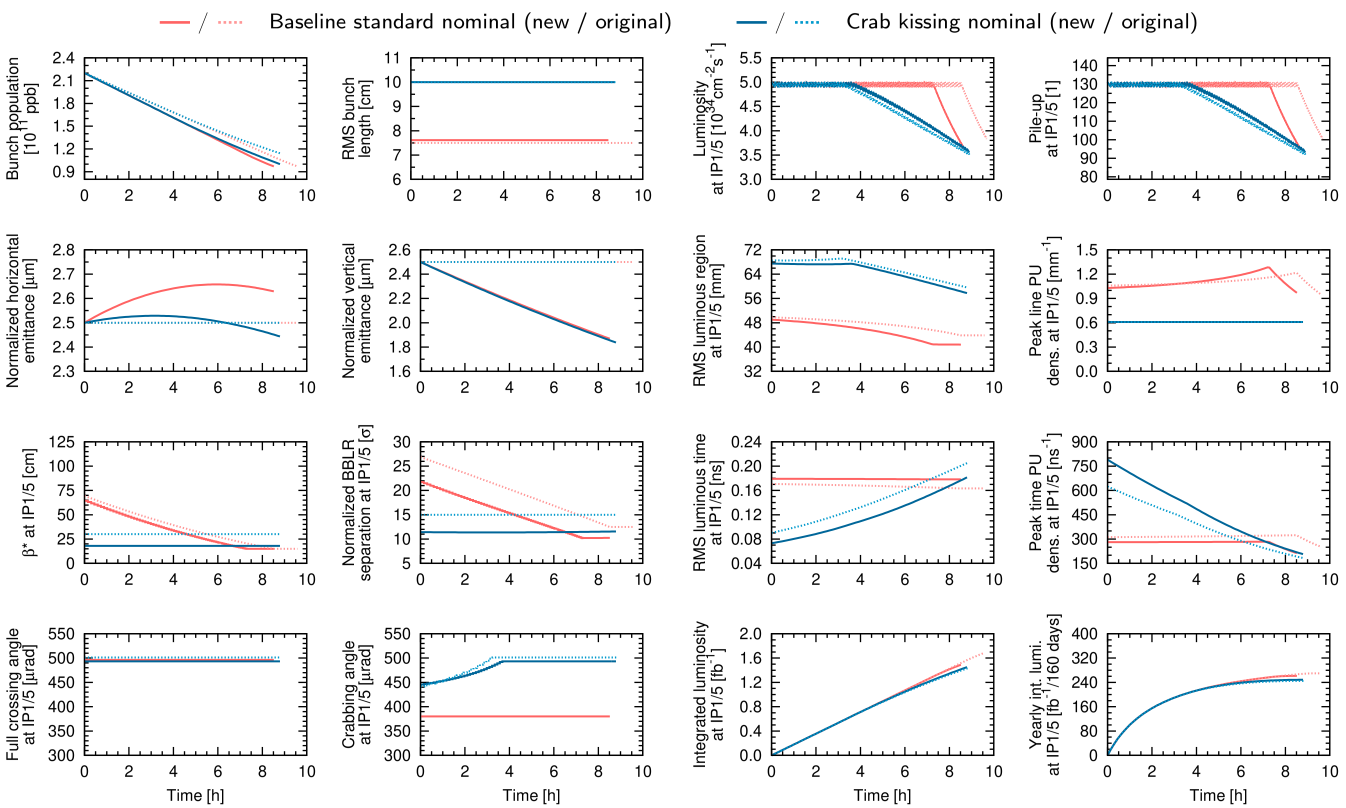

Figure 6.13. Evolution at IP1/5 of the optimum fill in the original and new crab kissing alternative scenarios at nominal and ultimate levelling. The original and current ("new") HL-LHC baseline nominal are included for the corresponding comparison.

Table 6.9. Performance at IP1/5 of the scenarios in Table 6.7.

Parameter	Unit	Original Baseline	Original Crab kissing	New crab kissing
Levelled luminosity	$10^{34}\,\mathrm{cm}^{-2}\,\mathrm{s}^{-1}$	5.0	5.0	5.0
Levelled pile-up	1	135	135	131
At the start of the fill				
$\beta^*_\times$	cm	69.4	30.0	18.0
$\beta^*_\parallel$	cm	69.4	10.0	7.5
Norm. BBLR sep.	σ	26.9	15.0	11.4
Crabbing angle	µrad	591	442	446
Kissing angle	µrad	–	396	484
RMS luminous region	mm	49.8	68.5	67.5
RMS luminous time	ns	0.171	0.090	0.073
Peak line PU density	mm^{-1}	1.06	0.61	0.61
Peak time PU density	ns^{-1}	312	625	790
End of the levelling				
$\beta^*_\times$	cm	15.0	30.0	18.0
$\beta^*_\parallel$	cm	15.0	10.0	7.5
Norm. BBLR sep.	σ	12.5	15.0	11.4
Crabbing angle	µrad	591	501	493
Kissing angle	µrad	–	95	103
RMS luminous region	mm	43.8	59.6	57.8
RMS luminous time	ns	0.163	0.205	0.182
Peak line PU density	mm^{-1}	1.21	0.61	0.61
Peak time PU density	ns^{-1}	323	186	211
Fill duration	h	9.6	8.8	8.8
Levelling time	h	8.5	8.8	8.8
Number of levelling steps	1	70	66	79
Int. luminosity per fill	fb^{-1}	1.69	1.43	1.60
Yearly int. luminosity	fb^{-1}/160 days	270	245	249
Diff. w.r.t. baseline*	%	–	-9.3	-5.0
Effective line PU density	mm^{-1}	0.79	0.50	0.51
Diff. w.r.t. baseline*	%	–	-35.9	-35.9
Effective time PU density	ns^{-1}	224	277	335
Diff. w.r.t. baseline*	%	–	$+24.0$	$+67.7$

event distribution around the IP in comparison to the baseline (such distribution, although clearly not Gaussian, does tend to Gaussian as the fill evolves). The wider RMS luminous region and, in consequence, shorter RMS luminous time, are evident in the *st*-projection of the event density in Fig. 6.15.

The effective line PU density can be indirectly pushed to even smaller values by reducing the limit on the maximum peak line PU density during the levelling process. Doing this, however, can lead to an important performance loss. Contrary to this, by relaxing the constraint on the peak line PU density, it is possible to almost fully recover the integrated luminosity of the baseline nominal, but lower detector efficiency should be expected, see Fig. 6.16. As in the case of the absence of CCs, the limits are set by the experiments.

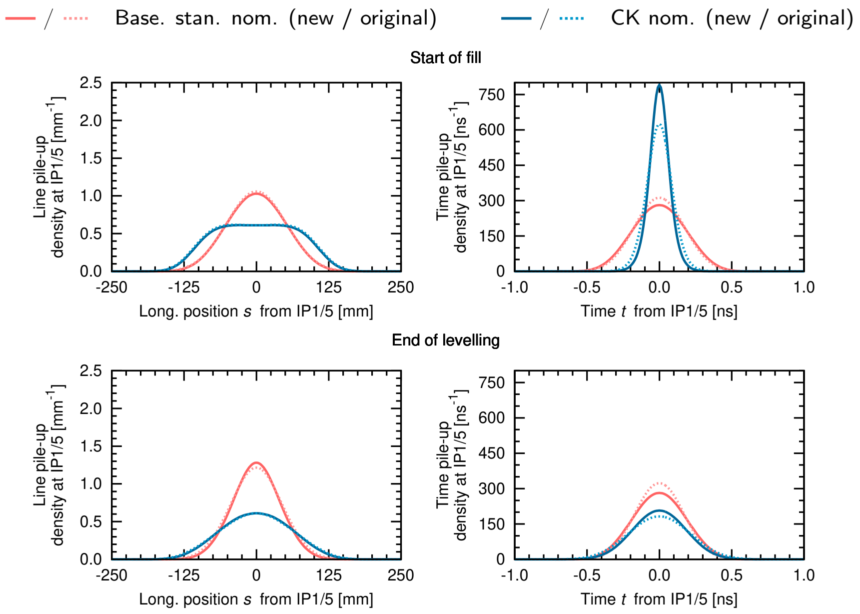

Figure 6.14. Line and time PU densities at IP1/5 at the start of the fill and at the end of the levelling in the original and new crab kissing alternative scenarios at nominal levelling. The original and current ("new") HL-LHC baseline nominal are included for the corresponding comparison.

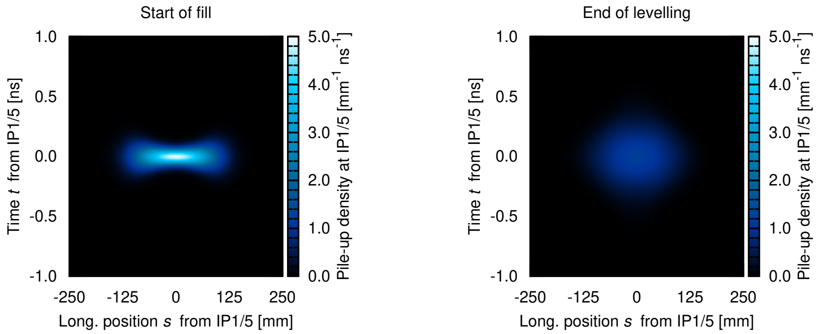

Figure 6.15. Line-time PU densities at IP1/5 of the new crab kissing alternative scenario at nominal levelling.

6.6 Sensitivity studies

The impact of the variation of a set of parameters of interest on the performance is reviewed for the alternative scenarios, similarly to the studies performed in Section 5.3. These parameters are the crabbing ratio and CC noise, as well as the turn-around time and the cross-section for burn-off.

6.6.1 Crab cavity noise

Similarly to the baseline, CC noise is simulated by assuming an emittance growth rate of 0.115 µm/h scaled at every levelling step with θ_{CC} and β^*, Eq. (5.3). Results show that the effect of the CC noise on the Flat performance is small and, in fact, $\mathcal{L}_{\mathrm{int}}$ remains above the baseline for both levelling operations (by around 1 %–3 %), with negligible impact on $\bar{\rho}_s$. On the other had, CC noise reduces the integrated performance of the 8b+4e alternative by an additional 1 %–2 % with respect to the baseline, although the effect on $\bar{\rho}_s$ remains minimum. Lastly, for the 200 MHz scenario, the emittance growth in Eq. (5.3) yields to a loss on $\mathcal{L}_{\mathrm{int}}$ at nominal (ultimate) operation of 1.6 % (2.7 %), corresponding to $\mathcal{L}_{\mathrm{int}} = 252\,\mathrm{fb}^{-1}$ ($295\,\mathrm{fb}^{-1}$). As a consequence of the reduced fill duration, $\bar{\rho}_s$ also decreases to $0.69\,\mathrm{mm}^{-1}$ ($1.06\,\mathrm{mm}^{-1}$) at nominal levelling, and therefore, a slightly better detector performance is expected in this scenario in comparison to the other alternatives.

6.6.2 Turn-around time

Reduction of the turn-around times by 15 min from the current estimates for nominal and ultimate operation, yields to an increase of $\mathcal{L}_{\mathrm{int}}$ by 2 %–3 % for both the Flat and 8b+4e scenarios, a similar gain than the baseline under the same assumption. For the 8b+4e alternative, this means that the loss on $\mathcal{L}_{\mathrm{int}}$ with respect to the baseline is limited to 22 %–23 %. In the case of the 200 MHz scheme, $\mathcal{L}_{\mathrm{int}}$ also profits from the reduction of the turn-around time, which allows to reach the baseline performance at nominal levelling (at ultimate, the loss is reduced by half). Lastly, in the alternative scenario without CCs, the $\mathcal{L}_{\mathrm{int}}$ improves by 3 %–4 %, with minimum impact on the effective line or time PU densities.

6.6.3 Crabbing ratio

As in the baseline case, the impact on the performance of each of the main alternative scenarios from both the absence and the full availability of crabbing voltage is studied as extreme cases. Full crabbing is less crucial for the Flat scenario than for the baseline due to its slightly smaller crossing angle; that is, the relative performance gain with

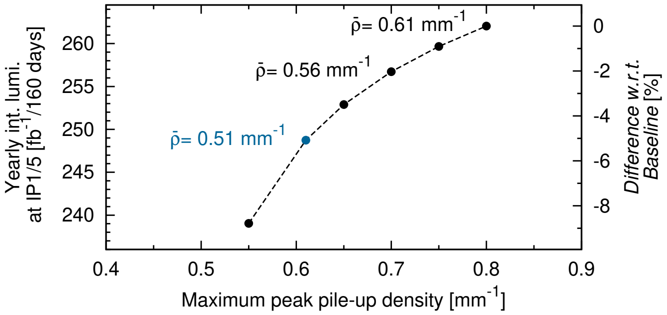

Figure 6.16. Integrated luminosity as a function of the applied cap on the maximum peak PU density for the new CK alternative scenario. The effective PU densities are shown for selected points.

respect to operation with only partial crabbing is limited. Moreover, the effective line PU density for the Flat scenario remains almost unchanged with respect to the baseline. The advantage of operating the machine with flat optics is evident when CCs are absent, as $\mathcal{L}_{\text{int}}$ drops by only 6 % (12 %) with respect to the Flat scenario with partial crabbing, that is, the loss is limited with respect to that experienced by the baseline itself in the absence of crabbing. With no crabbing, the effective line PU density of the Flat scenario is also slightly smaller than the baseline, specially at nominal operation.

The use of CCs, on the other hand, for the 8b+4e filling scheme as their absence shrinks the integrated performance by 33 % (42 %) at nominal (ultimate) operation with respect to the baseline with the current partial crabbing, thus falling below the HL-LHC objectives. Similarly, the impact on $\bar{\rho}_s$ is negative (an increase of more than 100 % (86 %)), although its magnitude remains only slightly larger than that of the baseline without CCs. Contrarily, implementation of full crabbing does not significantly compensate the innate reduction of performance in the 8b+4e scenario, with $\mathcal{L}_{\text{int}}$ increasing by only 1 %–2 %. The effective line PU density does, however, profit from $\theta_{\text{CC}}/\theta = 1$, decreasing to $0.76\,\text{mm}^{-1}$ ($1.08\,\text{mm}^{-1}$) for nominal (ultimate) levelling.

Thanks to full crabbing voltage, $\mathcal{L}_{\text{int}}$ can be pushed by 2.5 % and almost 6 % for nominal and ultimate operation, respectively, in the 200 MHz scenario. These increments allow to recover the baseline performance with partial crossing within ±1 %. Full crabbing also has a significant effect on $\bar{\rho}_s$, which decreases by 26 %–27 % with respect to the baseline with partial crabbing, or by 16 %–18 % with respect to the baseline with full crabbing. In the absence of CCs, the 200 MHz scenario can only operate, however, at nominal levelling since the virtual luminosity is limited to $6.13 \times 10^{34}\,\text{cm}^{-2}\,\text{s}^{-1}$. In this situation, the integrated performance drops by 6.5 % with respect to the baseline without CCs and $\bar{\rho}_s = 1.46\,\text{mm}^{-1}$, an effective line PU density slightly smaller than the baseline under the same conditions.

6.6.4 Cross-section for burn-off and summary

The extent of the performance of each of the main alternative scenarios (with full, partial, and no crabbing) is estimated under the assumption of a potentially reduced cross-section for burn-off and the results are summarised in Fig. 6.17; the corresponding baseline cases have been outlined for comparison. Similar fractional changes between the corresponding Flat and baseline cases are found when each of them is evaluated with $\sigma_{\text{b.o}} = 81\,\text{mb}$ and 111 mb. In the case of the 8b+4e alternative, the performance of the nominal (ultimate) levelling is pushed to $212\,\text{fb}^{-1}$ ($266\,\text{fb}^{-1}$), equivalent to a 7 % (10 %)-gain, thus reducing the difference of $\mathcal{L}_{\text{int}}$ with respect to the corresponding baseline operation. These figures, however, still do not meet the project's corresponding goals on performance. With baseline partial crabbing, the reduced cross-section yields to a performance increase of 8 % (12 %) for the 200 MHz scheme at nominal (ultimate) operation with respect to 111 mb, although these figures decrease by 1 % with full crabbing. Lastly, reduction of the cross-section for burn-off to 81 mb results in an increase of performance of 8 % (14 %) for the scenario in the absence of CCs at a levelling of $5.0 \times 10^{34}\,\text{cm}^{-2}\,\text{s}^{-1}$ ($7.5 \times 10^{34}\,\text{cm}^{-2}\,\text{s}^{-1}$). While the effective line PU density remains practically unaltered for nominal operation, a slight increase is observed at ultimate.

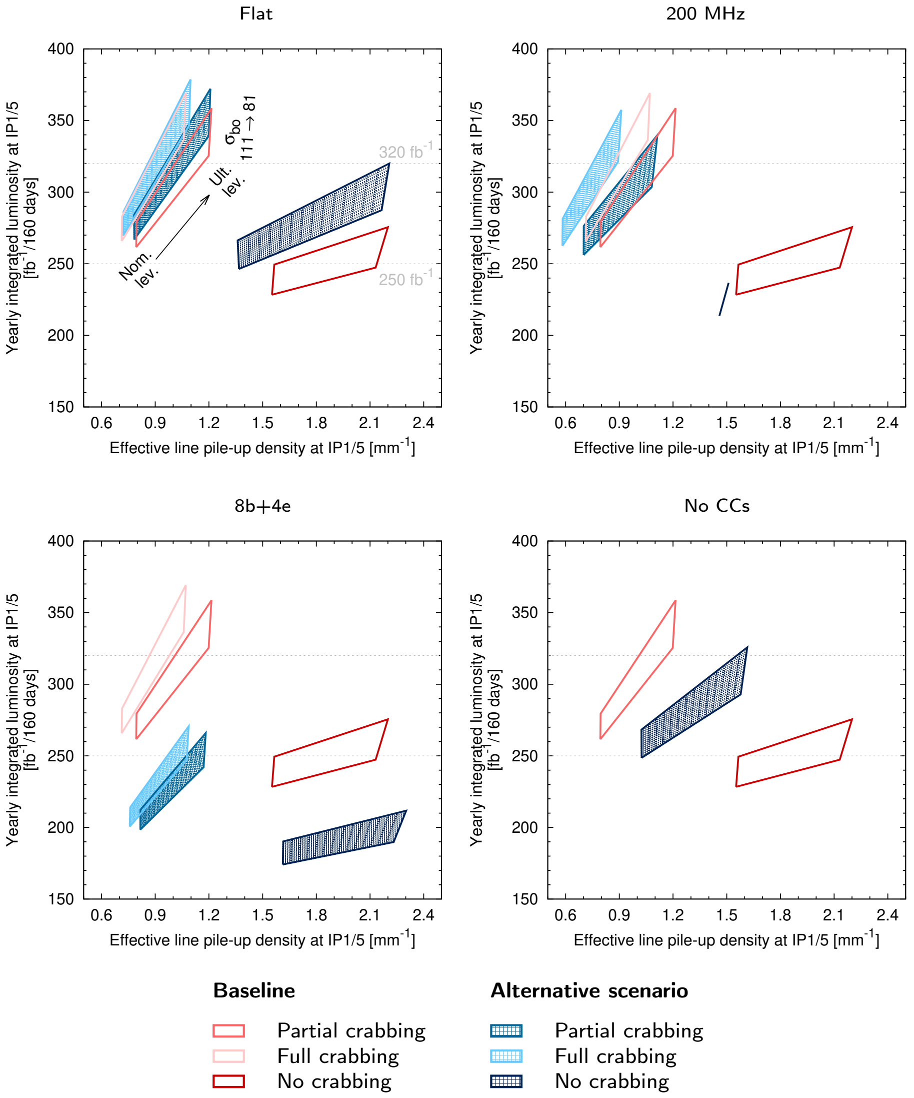

Figure 6.17. Extent of the yearly integrated luminosity and effective line PU density at IP1/5 of the main HL-LHC alternative scenarios at nominal and ultimate levelling assuming $\sigma_{\mathrm{b.o.}} = 111\,\mathrm{mb}$ and 81 mb.

Chapter 7

Compensation of beam-beam effects with local multipoles

In this Chapter, studies on the compensation of the beam-beam effects in the HL-LHC are presented. Correction of the linear head-on beam-beam is briefly discussed in the first section. Then, a method for the correction of the effect of long-range beam-beam interactions is proposed in the subsequent section. This scheme aims at the term-by-term compensation of the different orders of the Taylor multipolar expansion of the BBLR transverse kicks, using the kicks from local corrector magnets in the IR with an offset with respect to the design orbit. Profiting from the polarity of the corrector magnets seen by particles travelling in opposite directions, the proposed correction scheme can be applied to both beams simultaneously. In the last section, the principle of this formalism is applied to the correction of a specific order of the multipolar expansion of a beam-beam compensation wire (BBCW). Successful experimental operation of the BBCWs in the LHC validates the proposed compensation scheme [139].

Measurements of beam-beam effects, such as tune-shift and β-beating $\Delta\beta_u/\beta_{u_0}$, have been conducted in the LHC in view of its upgrade [140–142]. Stronger forces are expected in the HL-LHC mainly due to the larger bunch population and, depending on the operational scenario, to the reduced beam-beam separation. Figure 7.1 shows the β-beating at zero amplitude in beam 1 of the baseline scenario at the beginning of the fill (that is, at full intensity) due to head-on (BBHO) and long-range beam-beam (BBLR) interactions at the four IPs. The expected peak and RMS β-beating are around 15 % and 5 %–8 %, respectively, for both transverse coordinates. Amplitude-dependant β-beating –originated from the non-linear terms of the beam-beam kicks– has also been evaluated, with preliminary results discussed in Ref. [127]. Likewise, a detailed study on beam-beam amplitude detuning is presented in Ref. [143].

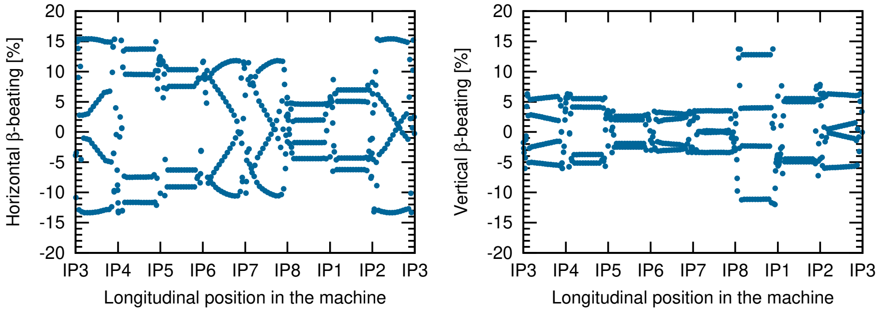

Figure 7.1. β-beating at zero amplitude of the HL-LHC baseline at the start of the fill due to BBHO and BBLR interactions in the four IPs.

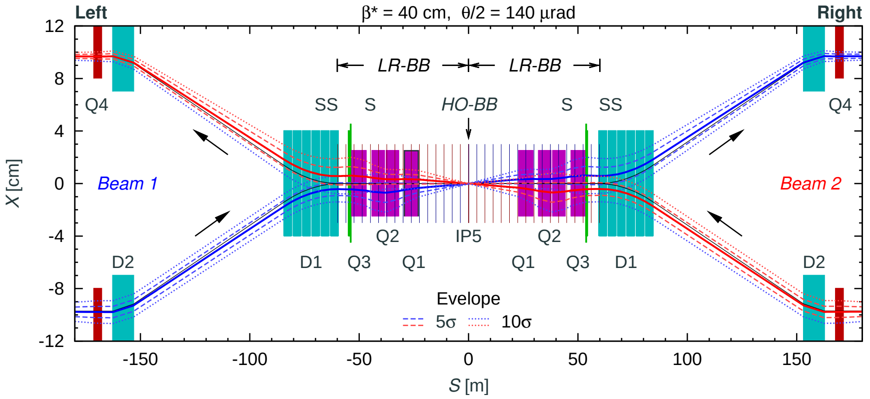

Figure 7.2. Interaction region around IP5 of the LHC and location of the BBHO and BBLR interactions (vertical blue and red bars) and selected final-focus magnets. D1 and D2 (in teal) are the separation/recombination dipoles, respectively. Quadrupoles Q1, Q2, and Q3 (in purple) constitute the inner triplet. The matching quadrupoles Q4 (in red) to Q7 (downstream, not shown) are used in the correction of the linear BBHO. The *normal* (S) and *skew* (SS) sextupoles (in green), and decapoles (available in the HL-LHC, not shown), are used in the simultaneous correction of the BBLR. The design orbits of B1 (solid blue line) and B2 (solid red line) for $\beta = 40\,\mathrm{cm}$ and a half-crossing angle of $140\,\mu\mathrm{rad}$ are also shown, as well as the corresponding beam envelopes at 5σ (dashed) and 10σ (dotted) assuming $\epsilon_{\mathrm{n}} = 2.5\,\mu\mathrm{m}$. A similar lattice is present around IP1. The magnet's width is not to scale.

Several techniques for the compensation of the beam-beam effects have been proposed in the past for different machines, for example, the use of electron beam lenses [43–45] and current-carrying wires [47, 48]. These approaches rely, however, on new hardware in the IR (Fig. 7.2). Correction schemes with magnets have also been explored [124, 125, 144] but, unlike those, the scheme presented in this work performs a simultaneous local correction for both beams using magnets in the shared beam pipe. The original idea was introduced in Ref. [63] and was further expanded in Refs. [126, 127].

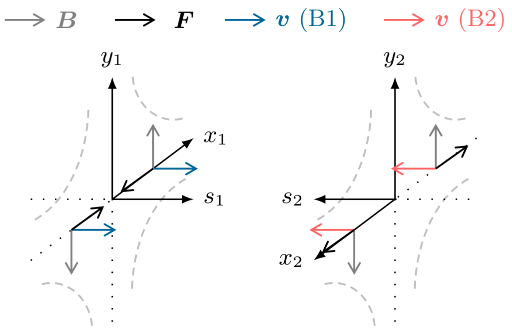

Beam 1 in a QF Beam 2 sees a QD

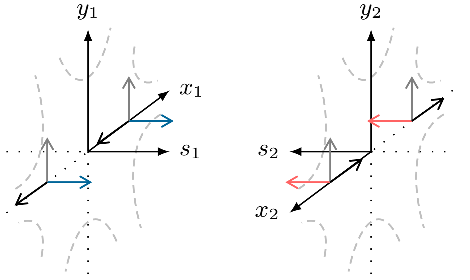

Beam 1 in a SF Beam 2 sees a SF too

Figure 7.3. Polarity of common magnets, as seen by same-charge particles in B1 and B2 travelling in opposite directions: a focusing/defocusing quadrupole (QF/QD) and a focusing sextupole (SF).

7.1 Compensation of head-on beam-beam

As discussed in Section 2.1.3, the linearised BBHO force for small amplitudes is equivalent to a quadrupole error in the lattice and thus it can be corrected locally and close to the source (ideally) by means of, for example, a quadrupole corrector with the opposite focusing effect. However, due to its cylindrical symmetry, the BBHO kick is defocusing in both transverse planes for same-charge bunches.

When travelling in opposite directions through the axis of a quadrupole, particles of the same charge see an opposite polarity for the same magnet in their corresponding reference system (rotated 180° around the y axis with respect to each other, see Fig. 7.3). In the case of the LHC and HL-LHC, the inner triplet constitutes the last magnets of the focusing system before the IP, as shown in Fig. 7.2. Since a focusing force with the same sign is needed for both beams to compensate the beam-beam kick, quadrupoles that are common for beam 1 (B1) and beam 2 (B2) –such as those in the inner triplet– cannot be considered for the simultaneous correction of the BBHO for both beams. The same situation applies for octupoles, dodecapoles, etc., due to their field symmetry. Contrarily, same-charge particles travelling in opposite directions through dipoles, sextupoles, etc. see the same polarity in their corresponding reference system for the same magnet. In general, the polarity of the $2(n+1)$-pole

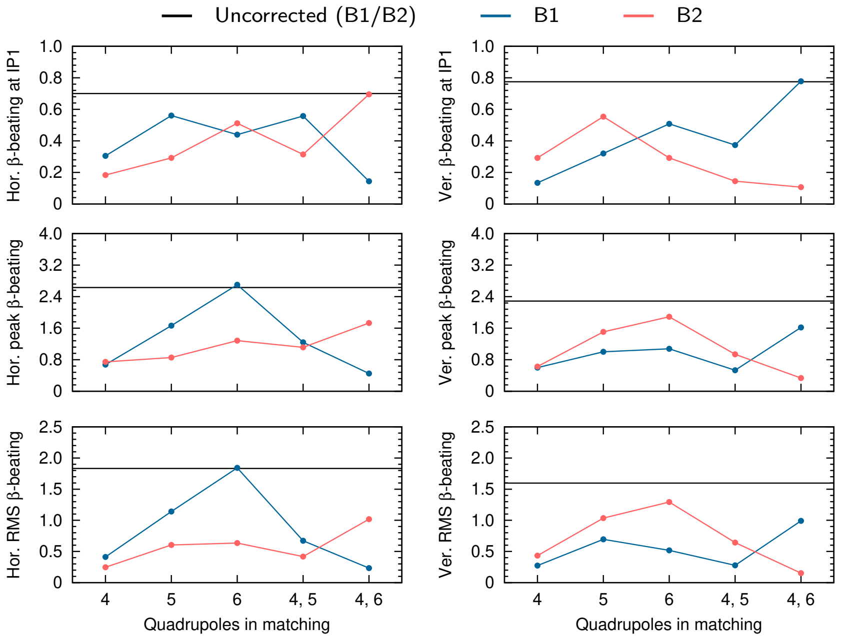

Figure 7.4. Correction in B1 and B2 of the β-beating at IP1, peak β-beating, and RMS β-beating, due to BBHO at IP1 [63].

magnet strength $\mathtt{K}_n$ seen by particles of the same charge in beams travelling in opposite directions changes according to

$$\mathtt{K}_n^{\mathrm{B2}} = (-1)^n \mathtt{K}_n^{\mathrm{B1}} \,, \tag{7.1}$$

with $n = 0$ for dipoles, 1 for quadrupoles, 2 for sextupoles, etc. By convention, a magnet with positive (negative) polarity strength has a focusing (defocusing) effect on the particles of B1. Therefore, in order to compensate the linear component of the BBHO at small amplitude, adjustment of the quadrupolar strength of dedicated correctors in the matching sections (the sections connecting the IR with the ring arcs, and where the magnets act separately on each beam) has to be implemented instead.

A preliminary study was conducted for the two beams (separately) of the LHC, assuming a beam energy of 7 TeV, a bunch population of 1.3×10^{11} ppb, a normalised transverse emittance of 2.5 µm, and $\beta^* = 0.6$ µm at IP1/5 [63, 126]. The optics at each of the two main IPs (where the BBHO effect originates), and at the start and at the end of the IR, was re-matched using different configurations involving the quadrupole strengths of Q4 to Q7. As seen in Fig. 7.4, adjustment of a single quadrupole, such as Q4 or Q5, proved to be the most efficient strategy, achieving a reduction of both the peak and RMS β-beating by a factor of 4 for both planes, and the reduction of the β-beating at the IP by a factor of 2.5 or more (depending on the transverse plane and beam under consideration). The correction achieved by the pair Q4-Q5 is also noteworthy, specially in terms of its minimum tune-shift. Corrections involving Q6 do not perform satisfactorily due to its strength being very close to its limit. It must be noted, nevertheless, that BBHO compensation by this method might deteriorate β for particles at large amplitudes, raising in turn concerns over the collimator system [127, 145]. Refined linear- and higher-order BBHO corrections, as well as studies as a function of the bunch population and β^* remain to be performed in view of the HL-LHC.

7.2 Compensation of long-range beam-beam

Multi-bunch beams circulating in opposite directions interact not only at the IP, but also in its vicinity, with the number of parasitic (or long-range) interactions at each side of the IP being defined by the distance between consecutive bunches and the length of the IR section where the beams share the same pipe (Fig. 7.2).

As in the head-on case, it is possible, in principle, to counteract the effects on the optics due to the long-range force by compensating the different terms (orders) of the Taylor expansion of the BBLR kick using the magnetic field of local corrector magnets in the IR. Assuming a horizontal crossing plane (see the reference systems in Fig. 2.4) and a beam-beam separation[1] d, the Taylor expansions of the beam-beam kicks on the transverse momenta (or, equivalently, the transverse angles) in Eq. (2.11) around the point $(x_2, y_2) = (d, 0)$ are

$$\left\{ \begin{array}{c} \Delta x_2' \\ \Delta y_2' \end{array} \right\} = \sum_{n=0}^{\infty} \sum_{m=0}^{n} \frac{1}{n!} \left\{ \begin{array}{c} C_{n,m} \\ D_{n,m} \end{array} \right\} (x_2 - d)^{n-m} y_2^m \, , \tag{7.2}$$

where

$$\left\{ \begin{array}{c} C_{n,m} \\ D_{n,m} \end{array} \right\} = \left. \frac{\partial^n \left\{ \begin{array}{c} \Delta x_2' \\ \Delta y_2' \end{array} \right\}}{\partial x^{n-m} \partial y^m} \right|_{(d,0)} \, . \tag{7.3}$$

Upon expansion of the Taylor series and evaluation of its coefficients, and assuming round beams (beam size σ) and a large beam separation ($d \gg \sigma$), Eq. (7.2) can be rewritten as

$$\begin{aligned} \left\{ \begin{array}{c} \Delta x_2' \\ \Delta y_2' \end{array} \right\} =& \frac{1}{0!} K_0 \left\{ \begin{array}{c} 1 \\ 0 \end{array} \right\} + \frac{1}{1!} K_1 \left\{ \begin{array}{c} (x_2 - d) \\ -y_2 \end{array} \right\} + \frac{1}{2!} K_2 \left\{ \begin{array}{c} (x_2 - d)^2 - y_2^2 \\ -2(x_2 - d) y_2 \end{array} \right\} \\ &+ \frac{1}{3!} K_3 \left\{ \begin{array}{c} (x_2 - d)^3 - 3(x_2 - d) y_2^2 \\ -3(x_2 - d)^2 y_2 + y_2^3 \end{array} \right\} + \cdots \\ =& \sum_{n=0}^{\infty} \frac{K_n}{n!} \left\{ \begin{array}{c} \mathrm{Re}\left[((x_2 - d) - i y_2)^n\right] \\ \mathrm{Im}\left[((x_2 - d) - i y_2)^n\right] \end{array} \right\} \, , \end{aligned} \tag{7.4}$$

where the coefficients K_n of the BBLR kicks are given by

$$K_n \equiv (-1)^n \cdot \frac{2 N r_p}{\gamma_r} \left(\frac{n!}{d^{n+1}} - \sum_{l=0}^{\lfloor n/2 \rfloor} \frac{n!}{(2l)!!} \frac{E_d}{\sigma^{2l} \, d^{(n+1)-2l}} \right) \, , \tag{7.5}$$

and

$$E_d \equiv \exp\left(-\frac{d^2}{2\sigma^2} \right) \, . \tag{7.6}$$

---

[1] To simplify notation, the normalised beam-beam separation is denoted by d in this Chapter, instead of d_{BBLR} as used in the rest of this work.

Table 7.1. K_n coefficients of the n-th order BBLR kick ($n = 0, \ldots, 4$).

K_n
$K_0 = +\frac{2Nr_p}{\gamma_r}\left(\frac{1}{d} - \sum_{l=0}^{0}\frac{1}{(2l)!!}\frac{E_d}{\sigma^{2l}\,d^{1-2l}}\right) = +\frac{2Nr_p}{\gamma_r}\left[\frac{1}{d} - \left(\frac{1}{d}\right)E_d\right]$
$K_1 = -\frac{2Nr_p}{\gamma_r}\left(\frac{1}{d^2} - \sum_{l=0}^{0}\frac{1}{(2l)!!}\frac{E_d}{\sigma^{2l}\,d^{2-2l}}\right) = -\frac{2Nr_p}{\gamma_r}\left[\frac{1}{d^2} - \left(\frac{1}{d^2}\right)E_d\right]$
$K_2 = +\frac{2Nr_p}{\gamma_r}\left(\frac{2!}{d^3} - \sum_{l=0}^{1}\frac{2}{(2l)!!}\frac{E_d}{\sigma^{2l}\,d^{3-2l}}\right) = +\frac{2Nr_p}{\gamma_r}\left[\frac{2}{d^3} - \left(\frac{1}{d^3} + \frac{1}{\sigma^2\,d}\right)E_d\right]$
$K_3 = -\frac{2Nr_p}{\gamma_r}\left(\frac{3!}{d^4} - \sum_{l=0}^{1}\frac{3!}{(2l)!!}\frac{E_d}{\sigma^{2l}\,d^{4-2l}}\right) = -\frac{2Nr_p}{\gamma_r}\left[\frac{6}{d^4} - \left(\frac{1}{d^4} + \frac{3}{\sigma^2\,d^2}\right)E_d\right]$
$K_4 = +\frac{2Nr_p}{\gamma_r}\left(\frac{4!}{d^5} - \sum_{l=0}^{2}\frac{4!}{(2l)!!}\frac{E_d}{\sigma^{2l}\,d^{5-2l}}\right) = +\frac{2Nr_p}{\gamma_r}\left[\frac{24}{d^5} - \left(\frac{1}{d^5} + \frac{12}{\sigma^2\,d^3} + \frac{3}{\sigma^4\,d}\right)E_d\right]$

The coefficients K_n are common for both the horizontal and vertical coordinates due to the symmetries between the transverse BBLR forces. Explicit forms of the first K_n coefficients are included in Table 7.1.

The transformation between the coordinate systems of B1 and B2 is

$$x_2 = d - x_1\,, \qquad y_2 = y_1\,, \qquad \text{and} \qquad s_2 = -s_1\,, \tag{7.7}$$

which yields the following relations for the transverse kicks:

$$x_1' \equiv \frac{\mathrm{d}x_1}{\mathrm{d}s_1} = x_2' \qquad \text{and} \qquad y_1' \equiv \frac{\mathrm{d}y_1}{\mathrm{d}s_1} = -y_2'\,. \tag{7.8}$$

Thus, the BBLR kick experienced by a proton in a bunch of B1 is described in its corresponding reference system by

$$\left\{\begin{array}{c}\Delta x_1' \\ \Delta y_1'\end{array}\right\} = \sum_{n=0}^{\infty}\frac{K_n}{n!}\left\{\begin{array}{c}(-1)^n\,\mathrm{Re}\left[(x_1+iy_1)^n\right] \\ (-1)^n\,\mathrm{Im}\left[(x_1+iy_1)^n\right]\end{array}\right\}. \tag{7.9}$$

Each order of the BBLR force can be corrected, in principle, either with a corrector magnet of the same order or exploiting the feed-down field coming from the offset between the centre of a magnet and the beam orbit. Using the MAD-X convention for the multipolar expansion of the magnetic field in the reference system x–y with origin at the centre of the magnet, the kicks on the transverse angles of particles in a relativistic beam are, in complex notation, [70]

$$\Delta x' - i\Delta y' = -\sum_{n=0}^{\infty}(\mathtt{KN}_n L + i\mathtt{KS}_n L)\frac{(x+iy)^n}{n!}\,, \tag{7.10}$$

where $\mathtt{KN}_n$ and $\mathtt{KS}_n$ are the normal and skew multipole coefficients at order n, and L is the length of the magnet. The products $\mathtt{KN}_n L$ and $\mathtt{KS}_n L$ are the integrated magnetic strengths. For explanation purposes, only normal magnets ($\mathtt{KS}_n = 0$) will be considered as all corrections used in the following examples are performed for IP5, where collisions take place in the horizontal plane. In the case of collisions in the vertical plane –such as those in IP1–, pure skew magnets must be used instead.

Beams 1 and 2 travel typically at a distance $\pm d_x$ from the centre of the magnets $(x, y) = (0, 0)$ located in the region where parasitic encounters occur, as shown in Fig. 2.4. Thus, B1 and B2 see a magnet with an offset d_x in their corresponding reference system and, in consequence, lower-order fields resulting from a process of feed-down are encountered by their particles. The transformation between the reference frame of the magnet's field and the coordinate system of B1 is

$$x = x_1 + d_x\,, \qquad y = y_1\,, \qquad \text{and} \qquad s = s_1\,. \tag{7.11}$$

Similarly to Eq. (7.8), this transformation leads to the following relations between the transverse kicks in both systems:

$$x' = x'_1 \qquad \text{and} \qquad y' = y'_1\,. \tag{7.12}$$

Therefore, the kick exerted by a normal magnet of order n and length L_n with an offset d_x in the reference system x_1–y_1 can be written as

$$\left\{\begin{array}{c}\Delta x'_1\\ \Delta y'_1\end{array}\right\} = -\sum_{m=0}^{n-1}\frac{\mathtt{KN}_m^{(n)}L_n}{m!}\left\{\begin{array}{c}\mathrm{Re}\left[(x_1+iy_1)^m\right]\\ \mathrm{Im}\left[(x_1+iy_1)^m\right]\end{array}\right\} - \frac{\mathtt{KN}_n L_n}{n!}\left\{\begin{array}{c}\mathrm{Re}\left[(x_1+iy_1)^n\right]\\ \mathrm{Im}\left[(x_1+iy_1)^n\right]\end{array}\right\}, \tag{7.13}$$

where

$$\frac{\mathtt{KN}_m^{(n)}}{m!} \equiv (-1)^{n-m}\frac{\mathtt{KN}_n}{n!}\binom{n}{m} d_x^{n-m}\,, \tag{7.14}$$

with $m = 0, 1, 2, \ldots, n-1$. The $\mathtt{KN}_m^{(n)} L_n/m!$ terms represents the strengths of the kicks of order m (equivalent to the kicks of $2(m+1)$-pole magnets) coming from the feed-down of the $2(n+1)$-pole magnet, and can be used to compensate lower-order components of the BBLR kick. The second term in Eq. (7.13) represent the n-th order kick of the $2(n+1)$-pole magnet, and can be used to directly compensate the n-th order of the BBLR expansion.

General formulae for the correction scheme in the two situations above is derived in the following sections, applying it in each case to the correction of a particular order of the BBLR kick in the HL-LHC baseline as proof-of-principle. For simplicity, corrections are illustrated for one beam only (B1), assuming BBLR interactions in one IP only (namely, IP5, where collisions take place in the horizontal plane). Studies are conducted using the HLLHCV1.3 optics [35] with a beam energy of 7 TeV, 2.2×10^{11} protons per bunch, a normalised emittance of 2.5 µrad, and a bunch spacing of 25 ns. Under this configuration, 16 parasitic collisions are expected in the regions between the IP and the left/right separation dipoles D1. A constant BBLR separation at each parasitic encounter ($d_i = 12\sigma$) is also assumed for all cases. The impact on the beam stability of the different corrector settings found by means of this technique is accounted by the reduction or improvement of the dynamic aperture (DA) [96] of the resulting lattice, estimated by single-particle tracking (10^6 turns and 10 seeds) using SixTrack [146] and SixDesk [147].

7.2.1 Direct compensation with corrector magnets

7.2.1.1 General case

Equating with opposite sign (for compensation) the terms of order n in Eq. (7.9) –the BBLR kick– and Eq. (7.13) –the magnet– yields to

$$-\frac{\mathtt{KN}_n L_n}{n!}\left\{\begin{array}{c}\mathrm{Re}\left[(x_1+iy_1)^n\right]\\ \mathrm{Im}\left[(x_1+iy_1)^n\right]\end{array}\right\} = -\left((-1)^n\frac{K_n}{n!}\left\{\begin{array}{c}\mathrm{Re}\left[(x_1+iy_1)^n\right]\\ \mathrm{Im}\left[(x_1+iy_1)^n\right]\end{array}\right\}\right). \tag{7.15}$$

Thus, a $2(n+1)$-pole corrector magnet with strength

$$\mathtt{KN}_n = \frac{(-1)^n}{L_n}K_n\,, \tag{7.16}$$

directly compensates the n-th order of a single BBLR kick for both transverse coordinates.

Since multiple parasitic encounters occur at both the left and right of the IP, the correction above has to be performed separately for the beam-beam contributions on each side of the IP. Moreover, as the interactions in one side of the IP and the magnet to compensate them are all located in different points in the machine, an additional factor has to be taken into account. This scaling factor is a function of the square-root of the ratios of the transverse betatron functions ($u = x, y$) at the location of each of the BBLR sources (β_{u_i}) and at the corrector magnet (β_{u_c}). The strength of the corrector magnet of order n that compensates the effect of a BBLR kick i of order n at a given side of the IP is

$$\mathtt{KN}_{n\,i} = \frac{(-1)^n}{L_n}K_{n\,i}\cdot\frac{1}{2}\left[\left(\frac{\beta_{x_i}}{\beta_{x_c}}\right)^{\frac{n+1}{2}} + \left(\frac{\beta_{y_i}}{\beta_{y_c}}\right)^{\frac{n+1}{2}}\right], \tag{7.17}$$

where $K_{n\,i} = K_{n\,i}(d_i, \sigma_i)$ is the coefficients of the Taylor expansion given by Eq. (7.5) for the BBLR kick i (a function of the normalised separation d_i and beam size σ_i at the parasitic encounter). The scaling factor holds when the phase advance between the locations of the corrector magnet and the beam-beam interaction is small. The power of the square-root of the ratios of the betatron functions corresponds the order (increased by one unit) of the BBLR component to be corrected (in this case, the same order of the magnet). The ratios of the horizontal and vertical betatron functions are averaged to minimise the beam-beam effects in both transverse coordinates simultaneously, and the correction scheme performs optimally when $\beta_{x_c} \approx \beta_{y_c}$, as it is the case in the following examples. The total strength of a corrector magnet that compensates a series of BBLR kicks is then the sum of the necessary individual corrections for all parasitic interactions, i.e.

$$\mathtt{KN}_n = \sum_i \mathtt{KN}_{n\,i}\,. \tag{7.18}$$

7.2.2 Compensation with the feed-down of corrector magnets

7.2.2.1 General case

Unlike the previous case where compensation of the n-order term of the BBLR kick is directly achieved with a corrector magnet of the same order, in the following we derive a scheme where the BBLR kick is compensated with the feed-down field of a magnet displaced with respect to the beam. Equating with opposite sign (for compensation) the terms of order m in Eq. (7.9) –the BBLR component of order m– and Eq. (7.13) –which represent a $2(m+1)$-pole magnet resulting from the feed-down of a corrector magnet of order n with a transverse (horizontal) offset d_x of its axis with respect to the beam– yields to

$$-\frac{\mathtt{KN}_m^{(n)} L_n}{m!}\left\{\begin{array}{l}\mathrm{Re}\left[(x_1+iy_1)^m\right]\\ \mathrm{Im}\left[(x_1+iy_1)^m\right]\end{array}\right\} = -\left((-1)^m\frac{K_m}{m!}\left\{\begin{array}{l}\mathrm{Re}\left[(x_1+iy_1)^m\right]\\ \mathrm{Im}\left[(x_1+iy_1)^m\right]\end{array}\right\}\right) . \quad (7.19)$$

Following a similar procedure than in Section 7.2.1.1, but using in addition Eq. (7.14) for the strength of the feed-down fields, the necessary strength of the normal corrector magnet can be easily found. After the inclusion of the sum over all the BBLR interactions and taking into account the average scaling factor discussed before, it is found for a given side of the IP:

$$\mathtt{KN}_n = \frac{(-1)^{n-m}\, n!}{\binom{n}{m} {d_{xn}}^{n-m} L_n}\left\{(-1)^m \sum_i \frac{K_{m\,i}}{m!}\cdot\frac{1}{2}\left[\left(\frac{\beta_{x\,i}}{\beta_{x\,c}}\right)^{\frac{m+1}{2}} + \left(\frac{\beta_{y\,i}}{\beta_{y\,c}}\right)^{\frac{m+1}{2}}\right]\right\} , \quad (7.20)$$

where $K_{m\,i} = K_{m\,i}(d_i, \sigma_i)$ are the coefficient of the BBLR Taylor expansion given by Eq. (7.5) for each BBLR encounter i.

The strength of the corrector magnet in Eq. (7.20) can be further adjusted to also include the compensation of the undesired fields (of the same order than the BBLR) coming from the feed-down of other corrector magnets of higher order with their own offsets. Thus, the necessary field strength for the $2(n+1)$-pole corrector of order n with offset d_{xn} to locally compensate the component of order m of a series of BBLR kicks i, as well as the kicks of order m from a series of corrector magnets of order p ($p = n+2, n+4, \dots$) with offsets d_{xp} at a given side of the IP is

$$\mathtt{KN}_n = \frac{(-1)^{n-m}\, n!}{\binom{n}{m} {d_{xn}}^{n-m} L_n}\left\{(-1)^m \sum_i \frac{K_{m\,i}}{m!}\cdot\frac{1}{2}\left[\left(\frac{\beta_{x\,i}}{\beta_{x\,c}}\right)^{\frac{m+1}{2}} + \left(\frac{\beta_{y\,i}}{\beta_{y\,c}}\right)^{\frac{m+1}{2}}\right] - \sum_p (-1)^{p-m}\frac{\mathtt{KN}_p}{p!}\binom{p}{m} {d_{xp}}^{p-m} L_p\right\} . \quad (7.21)$$

7.2.2.2 Compensation of the BBLR quadrupolar component with the feed-down of a sextupole corrector

To illustrate the proposed correction scheme, compensation of the linear components of the BBLR interactions at each side of the IP using the quadrupolar fields resulting from the offset of a sextupole corrector at each side of the IP is presented in the following. The sextupole correctors, located between the second separation dipole (D2) and the crab cavities of the corresponding left/right side, are assumed to be 1 m in length (thin-lens approximation). For simplicity, the horizontal offset of the corrector magnet with respect the orbit is assumed as $d_x = \frac{1}{2}\bar{d} = \frac{1}{2}(\frac{1}{16}\sum_i d_i)$, as it is normally the case due to the symmetry of the beam crossing. Similarly to the normalised separation d, the sign of d_x inverts on the other side of the IP in the corresponding reference system of

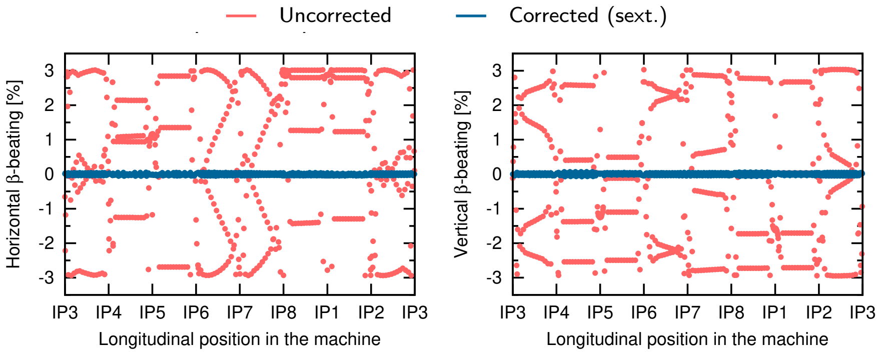

Figure 7.5. β-beating at zero amplitude of the HL-LHC baseline at the start of the fill before and after correction of the quadrupolar components of the left and right BBLR encounters using the feed-down of a sextupole with offset at each side of the IP. In both lattices, only the BBLR interactions around IP5 are present.

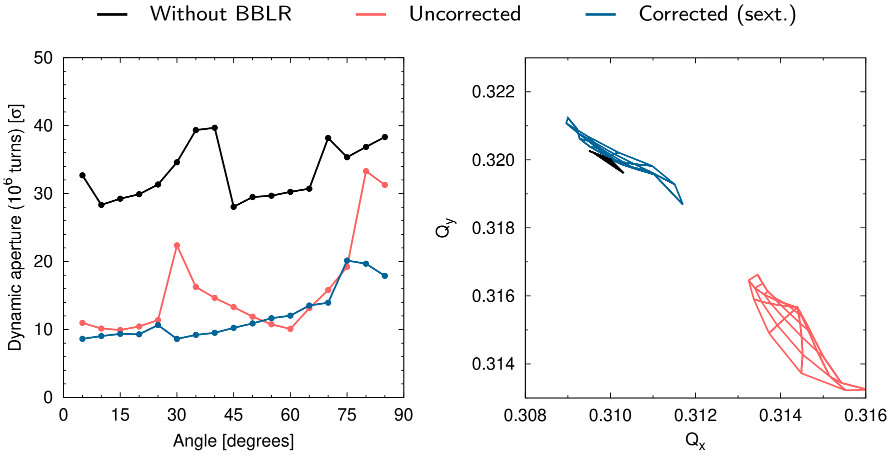

Figure 7.6. Minimum dynamic aperture (*left*) and footprint (*right*) of the lattices in Fig. 7.5.

each beam (see Fig. 2.4). The strength of the sextupolar kicks that compensates the quadrupolar effects of the BBLR encounters at a each side of the IP are then given by Eq. (7.20) for $n = 2$ and $m = 1$.

Minimisation of the β-beating to almost zero along the entire machine is achieved in the corrected lattice, as observed in Fig. 7.5. The impact on the beam stability of the (non-linear) sextupolar fields used for the correction is assessed by their effect on the minimum DA.[2] To perform comparisons, the tunes of the corrected and uncorrected lattices are first re-matched to the design tunes without beam-beam, namely $(Q_x, Q_y) = (62.31, 62.32)$, using the trim quadrupoles (MQT) before tracking. The left-hand-side plot of Fig. 7.6 shows the minimum DA as a function of the initial angle of the tracked particles in the physical space. As observed, the smallest minimum DA

---

[2] The *minimum* DA of all particles at a given angle, and among all seeds.

is reduced from around 28σ for the lattice without beam-beam to around 10σ once the BBLR effects are taken into account. Implementation of the proposed correction, however, does not further degrade the smallest minimum DA significantly. The peak minimum DA –which takes place for angles close to 90°– is, however, slightly lower. The right-hand-side plot in Fig. 7.6 shows the footprint of the corrected and uncorrected lattices, as well as the lattice where the parasitic interactions have been neglected. As expected, the design tunes are recovered once the correction is applied, with residual horizontal and vertical tune shifts of $(\Delta Q_x, \Delta Q_y) = (-6.5 \times 10^{-5}, +6.5 \times 10^{-5})$.

7.2.2.3 Compensation of the BBLR octupolar component with the feed-down of a decapole corrector

Contrary to the LHC, the HL-LHC is equipped with decapoles in the triplet region. Such magnets can then be used to compensate the octupolar component of the BBLR by profiting of their offset position with respect to the beam orbit. The same technique than for the previous example is applied on the same uncorrected lattice with BBLR interactions in both side of one of the main IPs with horizontal crossing. The necessary strength of the decapole magnets for the correction of the parasitic encounters at each side of the IP are given by Eq. (7.20) for $n = 4$ and $m = 3$. Furthermore, simultaneous compensation of both the octupolar and quadrupolar components of the BBLR can be achieved using first a decapole corrector with an offset for the former, and then a sextupole corrector with an offset (of different magnitude, in general) for the latter. Due to the offset of the decapolar magnet with respect to the orbit, however, an additional linear magnetic kick is created. The correction scheme given in Eq. (7.21) allows for this additional quadrupolar ($m = 1$) contribution created by the decapole ($p = 4$) magnet to be included in the compensation of the linear BBLR kick provided by the sextupolar ($n = 2$) corrector.

To illustrate this joint compensation of the BBLR encounters at both sides of the IP, each pair of corrector magnets is assumed, for simplicity, to be positioned at the same locations in the corresponding left/right side and thus, to have the same offset with respect to the beam orbit. Figure 7.7 shows the results achieved by this simultaneous correction: first, the β-beating is slightly reduced by the use of the decapole magnets for the octupolar term of the BBLR; then the inclusion of the sextupolar magnets for the linear order of the BBLR further reduces the β-beating, reaching almost zero, in both transverse coordinates along the entire machine.

As expected, the addition of the sextupole correctors also improves the tune-shift, reducing it to $(-6.6 \times 10^{-5}, 7.1 \times 10^{-5})$ and thus bringing it closer to the design tunes. This tune-shift can be compared with $(3.8 \times 10^{-3}, -3.7 \times 10^{-3})$, which are the corresponding figures found in the lattice with only decapole correctors. A substantial reduction of the tune spread (footprint) is also observed, as seen in Fig. 7.8. The right-hand-side plot of Fig. 7.8 shows the reduction of minimum DA in the two corrected lattices using non-linear magnetic elements. As in the previous examples, the tunes were first re-matched, in both cases, to the design tunes $(62.61, 62.32)$ to perform the computation of the DA. The minimum DA is not found to be compromised by the inclusion of decapolar fields; moreover, in the case of the joint use of decapoles and sextupoles, the smallest minimum DA remains almost unchanged for most angles, with only a slight decrease being observed for particles at a large angle. Compensation of the additional sextupolar field added for the correction on the linear BBLR effects is necessary to further increase the DA.

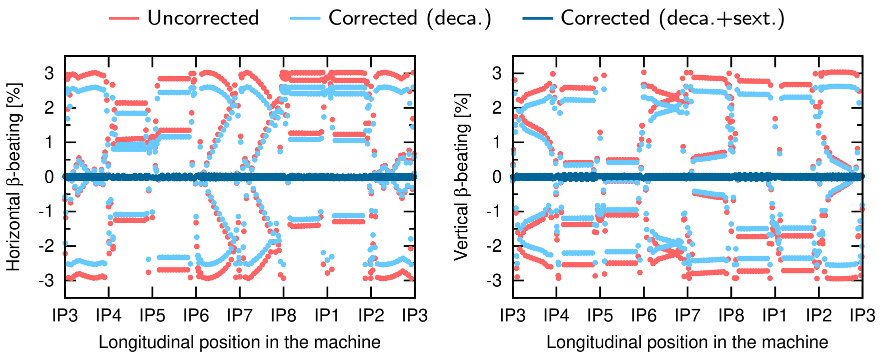

Figure 7.7. β-beating at zero amplitude of the HL-LHC baseline at the start of the fill before and after correction of the octupolar components of the left and right BBLR encounters using the feed-down of a decapole with offset at each side of the IP. The quadrupolar components of both the left and right BBLR encounters and the decapole feed-down are also compensated using the feed-down of a sextupole with offset at each side of the IP. In the three lattices, only the BBLR interactions around IP5 are present.

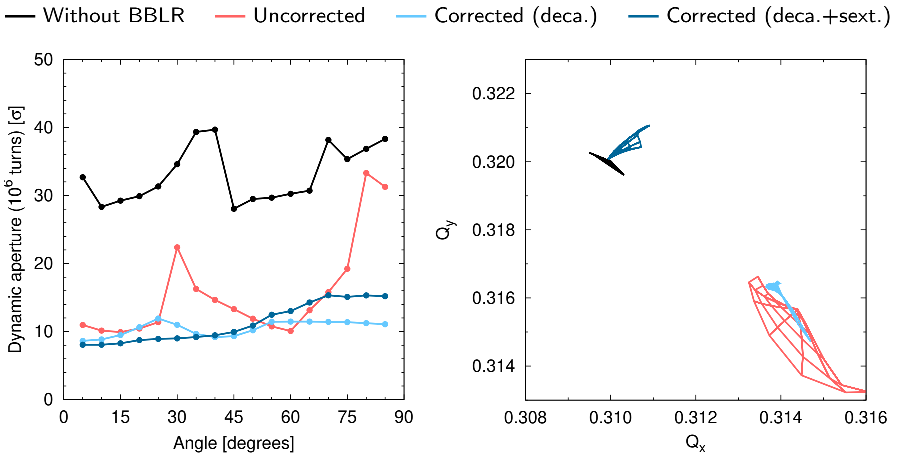

Figure 7.8. Minimum dynamic aperture (*left*) and footprint (*right*) of the lattices in Fig. 7.7.

7.3 Application to the compensation of multipolar components of a beam-beam compensation wire

Tested with the ATS optics [11, 12] of the LHC in a series of experiments in 2017 and 2018 at top energy [139, 148, 149], each of the beam-beam compensation wires (BBCWs) consist of a copper wire (around 1 m in length) capable of carrying up to 350 A DC across its round cross-section diameter of 2.48 µm. Each BBCW is powered by an independent power converter, and it is embedded in the jaws of a tertiary collimator. The BBCWs run in parallel to the beam that they aim to correct (lying

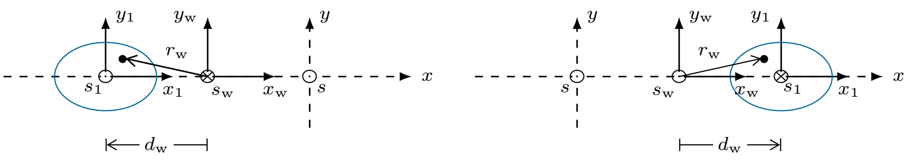

(a) Before (left of) the IP **(b)** After (right of) the IP

Figure 7.9. Reference system for the beam-beam compensation wires acting on B1.

in the same crossing plane used at the IP, between the two beams), and the electrical current flows in the same direction than the beam.

Let us consider the reference systems x_w–y_w and x_1–y_1 centred at the wire and B1, respectively (see Fig. 7.9). The transverse kicks exerted at a point $(x_\mathrm{w}, y_\mathrm{w})$ by the magnetic field generated by an electric current I_w flowing in a wire of length L_w are [49]

$$\left\{ \begin{array}{c} \Delta x'_\mathrm{w} \\ \Delta y'_\mathrm{w} \end{array} \right\} = + \frac{qc\mu_0 I_\mathrm{w} L_\mathrm{w}}{2\pi m c^2} \frac{1}{r_\mathrm{w}^2} \left\{ \begin{array}{c} x_\mathrm{w} \\ y_\mathrm{w} \end{array} \right\} . \tag{7.22}$$

Note the similarity of this expression with Eq. (2.11). Assuming a small round beam, the equation above can be expanded around a point at a distance $d_\mathrm{w} \gg \sigma$ in the same horizontal plane. This point coincides with the origin of the coordinate system x_1–y_1 and thus, the kick exerted by a BBCW on a proton of B1 can be expressed in its own reference system in the following way:

$$\left\{ \begin{array}{c} \Delta x'_1 \\ \Delta y'_1 \end{array} \right\} = \sum_{n=0}^{\infty} \frac{K_n^\mathrm{w}}{n!} \left\{ \begin{array}{c} (-1)^n \operatorname{Re}\left[(x_1 + iy_1)^n\right] \\ (-1)^n \operatorname{Im}\left[(x_1 + iy_1)^n\right] \end{array} \right\} , \tag{7.23}$$

where

$$K_n^\mathrm{w} \equiv (-1)^n \cdot \frac{qc\mu_0 I_\mathrm{w} L_\mathrm{w}}{2\pi m c^2} \left(\frac{n!}{d_\mathrm{w}^{n+1}} \right) . \tag{7.24}$$

Note also the similarity of these coefficients K_n^w with those in Eq. (7.5), the coefficients of the BBLR kick expansion. Then, applying the reasoning used in the formalism for the compensation of the parasitic encounters, the term of a given order of the multipolar expansion of the wire kick can be compensated directly by the kick of corrector magnet, or by the kick of a magnetic field generated from the relative offset of the corrector with the beam.

During wire experiments performed in Machine Development studies in 2018 [150], the orbit feed-forward was implemented to compensate the dipolar effect of the wire. Additionally, two quadrupole correctors (Q4 and Q5) close to the corresponding left and right BBCWs were used to compensate the quadrupolar effects of the wires, with the necessary magnet strengths being obtained by applying the compensation scheme described before for the desire order. This correction allowed to reduce the β-beating and tune shift, and improved the performance of the BBCWs. Measurements were conducted with a low- and high-intensity beam (B2). By setting up the machine in a BBLR-dominated regime (the conditions for this are given by the number of bunches/trains of bunches present in both beams, as detailed in Ref. [139]), the effect of the BBCWs is directly observed in the variation of the effective cross-section

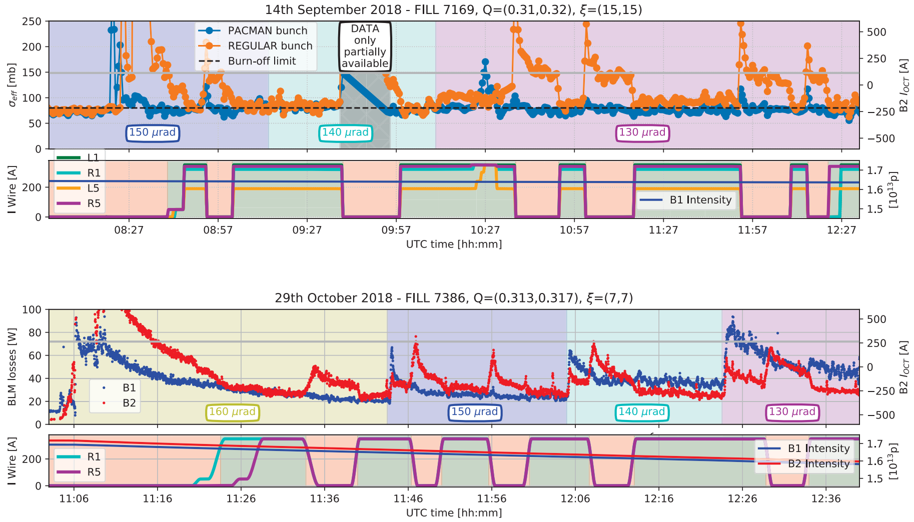

Figure 7.10. Reduction of the effective cross-section (*top*) and beam losses (*bottom*) with the current of the BBCWs in the low- and high-intensity experiments, respectively. *Courtesy of: G. Sterbini* [139].

$\sigma_{\mathrm{eff}} = -(\sum_i \mathcal{L}_i)^{-1}\,\mathrm{d}N\,/\,\mathrm{d}t$. In an ideal situation, σ_{eff} corresponds approximately to the proton-proton inelastic cross-section (80 mb at 6.5 TeV); this is found indeed to be closely the case when the BBCWs are acting on the beam, as seen in the results in Fig. 7.10.

Further numerical studies on the optimisation of the wire compensation for the HL-LHC are presented in Ref. [151].

Chapter 8

Conclusions

In view of the unprecedented levels of pile-up and pile-up density that the experiments will face in the HL-LHC upgrade, a detailed characterisation of these parameters for the different operational scenarios is extremely important. For this work, continuous studies on the performance of the different HL-LHC scenarios have been conducted via realistic simulations of their optimum fills, as their corresponding parameters have evolved. Such simulations are possible thanks to the implementation of a step-based luminosity levelling at 2 %, and the addition of possible penalty steps to account for the partial loss of instantaneous luminosity during its use in operation.

A new figure-of-merit, the effective pile-up density $\bar{\rho}_s$, has been proposed as a means to evaluate the HL-LHC operational scenarios in terms of the expected detector performance. The concept of effective line pile-up density is based on the event density defined in Ref. [86], extending it to an integrated average over the fill duration. The introduction of this parameter is motivated by detector simulations [30, 31] showing a linear relation of the detector efficiency in the reconstruction of primary vertices with the local density (and not with the peak pile-up density, as commonly considered in the past). The computation of an average pile-up density over a fill mirrors the integrated luminosity as a more interesting figure for the experiments than the peak instantaneous luminosity at all times. Thus, the effective pile-up density –the main theoretical contribution of this work– provides a complementary figure-of-merit to the integrated luminosity to characterise the performance of a given operational scenario: while the integrated luminosity accounts for the expected amount of data arising from the bunch collisions, the effective pile-up density provides an insight on the expected data quality of such collisions.

In order to simulate the optimum physics fill of each of HL-LHC operational scenarios and assess their corresponding performance in terms of both figures-of-merit, a numerical tool –the LEVELLING program– has been developed. A step-based luminosity (or peak pile-up density) levelling has been adopted to ensure this parameter remains within a threshold during the process. The possibility of including penalty steps with reduced luminosity to account for the necessary time to change between consecutive optics and beam realignment has also been added. The effects of luminosity burn-off, synchrotron radiation, quantum excitation, intrabeam scattering (estimated via an accurate model, as provided by MAD-X), and crab cavity noise (not studied in the past), are all taken into account on the evolution of the beam intensity and emittance. Theoretical derivations for the computation of the luminosity and pile-up-related quantities arising from the collision of bunches with a q-Gaussian longitudinal profile –the latest description based on observations in the LHC– were also conducted and included in LEVELLING for the more accurate assessment of the figures-of-merit. Theoretical formulae for the case of bunch collisions with longitudinal time offsets were also derived and implemented in the code. Together, all the aforementioned considerations allow for a more realistic simulation of a physics fill. Additionally, studies on the effect of different turn-around time, cross-section for burn-off, partial crabbing, crab kissing, adaptive crossing, and bunch length gymnastics can also be performed by Levelling. Lastly, this new software has recently been adapted and used on independent fill simulations for the High-Energy LHC (HE-LHC), another possible upgrade of the LHC [152].

The HL-LHC baseline, the main operational scenario, has been thoroughly studied with the latest set of parameters which include, in particular, nominal beam energy of 7 TeV, round optics with $\beta^* = 15\,\mathrm{cm}$ and a full crossing angle of 500 µrad at the main IPs, partially compensated by two RF crab cavities per beam and per main IP side, and bunches with a longer bunch length (q-Gaussian RMS bunch length of 7.6 cm, equivalent to a Gaussian RMS bunch length of 9 cm) to ensure single-bunch stability [100]. Implementation of a q-Gaussian description for the longitudinal bunch profile allows for a more accurate computation of the virtual luminosity with respect to previous works, which in turn affects the estimation of the integrated performance (as well as luminous region and pile-up densities, as the beam evolves in a slightly different way). In terms of data quantity, it was found that the current baseline delivers around $262\,\mathrm{fb}^{-1}$ and $325\,\mathrm{fb}^{-1}$ per year for nominal ($5.0 \times 10^{34}\,\mathrm{cm}^{-2}\,\mathrm{s}^{-1}$) and ultimate ($7.5 \times 10^{34}\,\mathrm{cm}^{-2}\,\mathrm{s}^{-1}$) operation, respectively, assuming the current machine efficiency estimate of 50 % (160 days in physics a year, 145 min and 150 min turn-around time for nominal and ultimate, respectively). These estimates on the yearly integrated performance not only meet but surpass the current HL-LHC goals at each corresponding operation, namely $250\,\mathrm{fb}^{-1}$ and $320\,\mathrm{fb}^{-1}$, necessary to meet $3000\,\mathrm{fb}^{-1}$ and $4000\,\mathrm{fb}^{-1}$ over a period of twelve years. While the pile-up levels at nominal and ultimate operation of 131 and 200 events per bunch crossing, respectively, are challenging, they fall within the expected detector capabilities of ATLAS and CMS. Characterisation of the HL-LHC baseline in terms of data quality finds effective pile-up densities of $0.80\,\mathrm{mm}^{-1}$ and $1.20\,\mathrm{mm}^{-1}$ for nominal and ultimate levelling; these figures provide the reference for comparisons with the alternative scenarios.

From simulations, it has been realised that the process of β^*-levelling will require a large number of optics for the HL-LHC. For the baseline, luminosity steps at 5 % seem to find a compromise between an affordable number of optics to commission and operate, and a limited reduction of the delivered integrated luminosity. Sensitivity studies for the baseline allow to estimate the expected performance with reduced or increased bunch population, transverse emittance, bunch length, betatron functions, crossing angle, crabbing ratio at the main IPs, etc. The latest update of the HL-LHC baseline parameters was driven, in part, by the continuous studies performed in this work, with the results providing insights on the possible areas for optimisation. The impact of crab cavity noise on performance, assessed for the first time in this work, is found to be limited to a loss of around 2 % for the current estimate of the induced emittance growth rate of 0.115 µm/h; this comes, however, with a considerable deviation of the transverse emittance by the end of the fill with respect to the case without crab cavity noise. Systematic time offsets of ±30 ps –the typical magnitude expected from RF control estimates– were not found to pose a problem in terms of integrated performance, as its reduction is found to be negligible up to ±100 ps.

Two possible improvements to the HL-LHC baseline using BBCWs and an adaptive crossing angle program were also analysed. While the former delivers a 2 % (4 %) gain on yearly integrated luminosity at nominal (ultimate) operation with a reduced average local event density by 2 % (5 %), the integrated luminosity sees a more modest increase of 1 % (2 %), but with a better expected detector efficiency as accounted by the considerably smaller –by 7 % (11 %)– effective pile-up density. Additionally to the improved performance, these scenarios aim at mitigating the negative induced beam-beam effects (with current-carrying wires) or at ensuring beam stability with a minimum dynamic aperture of 6σ (with adaptive crossing angle). Lastly, as the LHC machine is envisioned to operate at an ultimate centre-of-mass collision energy of 15 TeV at a later stage in the HL-LHC era, its performance has also been studied. With the current optics and foreseen longer turn-around times at both levelling operations (by 5 min, necessary for the extended energy ramp), simulations found that the impact on performance in terms of both figures-of-merit is not significantly changed with respect to operation at the nominal energy of 7 TeV, mainly due to the reduced fraction of compensated crossing angle. By profiting from the reduced normalised emittance at a higher beam energy, the optics at the main IPs can be further optimised, delivering, in this case, a slightly increased integrated luminosity and reduced effective pile-up density. Studies on the feasibility of operation of machine components at 7.5 TeV and their possible required upgrades are ongoing.

Regarding the alternative scenarios, the use of flat optics, as implemented in the Flat and 200 MHz scenarios, was found not only to preserve the integrated performance, but also to reduce the effective pile-up densities, from which detector efficiency can profit. The yearly integrated luminosity of the optimum fills of the proposed Flat scenario ($\beta^* = 18\,\text{cm}/7.5\,\text{cm}$, 490 µrad full crossing angle), in fact, surpasses the baseline by 2 % and 4 % for the nominal and ultimate operation, respectively. It has been noted, however, that the use of flat optics has yet to be fully tested in operation, and that the full implications of this operational mode should be thoroughly assessed [123]. While the 200 MHz scenario has a slight loss on integrated luminosity, it constitutes an attractive operational mode as it minimises the electron cloud effects that could limit the machine performance [129] while delivering a remarkable 10 % lower effective pile-up density (due to the large RMS luminous regions coming from longer bunches). In the case of the 8b+4e filling scheme, another alternative scenario to mitigate possible electron-cloud effects, the same baseline detector performance can be expected but it comes with a much larger impact on the yearly integrated luminosity. Finally, in the event of absent RF crab cavities, the use of flat optics is mandatory to mitigate the performance loss. The proposed No CCs scenario features $\beta^* = 31.5\,\text{cm}/7.5\,\text{cm}$ and a full crossing angle of 410 µrad, and provides a backup operational mode for the HL-LHC in such event. In this scheme, a reduction of 5 % and 10 % for nominal and ultimate levelling, respectively, is foreseen, provided a 30 %-higher local pile-up density can be afforded by the experiments. Despite the performance loss with respect to the current estimate for the baseline, the goal on integrated luminosity at nominal levelling is still met even without crab cavities thanks to the new optics and lower turn-around times. Due to its reduced crossing angle, however, the implementation of compensation techniques of BBLR effects might be necessary, with studies on several approaches (such as the BBCWs) currently ongoing.

First estimates of the impact of emittance blow-up induced by crab cavity noise show reductions by 1 % to 3 % on the integrated luminosity for all scenarios: the Flat alternative proves to be the least sensitive scenario, while performance loss for the baseline is expected in the middle of this range at nominal operation, and at the maximum of it with ultimate levelling. Therefore mitigation techniques for the effect of crab cavity noise should be investigated and implemented in operation. Lack of crabbing in IP1 and IP5, on the other hand, was found to yield a performance loss of 12 % for the baseline; while the Flat alternative mitigates this figure by half, the 8b+4e and 200 MHz schemes experience a similar or worse impact than the baseline when crab cavities are absent. Conversely, full availability of crabbing voltage to fully restore head-on collisions at the main IPs yields to increased integrated luminosities by a few percent in all scenarios, at the same time that it lowers their corresponding effective pile-up densities, which translates, in turn, into improved data quality. From sensitivity studies on the turn-around times, it has been realised that these play a prominent role on the machine performance: reduction of the turn-around time by 15 min can increase the integrated luminosity by up to 4 %, depending on the operational scenario. Lastly, studies assuming an 81 mb cross-section for burn-off (that is, corresponding to the inelastic cross-section exclusively) have provided an overview of the expected performance of the baseline and alternative scenarios under more optimistic conditions –as observed in the LHC– with respect to the more conservative approach at 111 mb implemented in all simulations.

Although incompatible with the current HL-LHC due to the use of four crab cavities per beam and per main IP side, the crab kissing scheme remains an interesting study case due to its remarkable low pile-up densities. This scenario has been reproduced as originally proposed [86], and further studied by means of the simulation of its optimum fill for its performance assessment. It has been found that the yearly integrated luminosity is reduced by 9 % with respect to the original baseline and, in terms of the new figure-of-merit, the average local event density is $0.51\,\mathrm{mm}^{-1}$, a value explained by the flatter distribution of the pile-up density at the beginning of the fill. An updated version adopting the crab kissing scheme (with the rest of the parameters corresponding to those for the Flat scenario) was also analysed. In this configuration, the loss on integrated luminosity with respect to the current baseline is reduced to only 5 %, while delivering the lowest effective pile-up up density among the alternative scenarios. From these studies, it seems that to achieve a sizeable reduction of the effective pile-up density, a major hardware component has to be involved, such as a new 200 MHz RF system or additional crab cavities for crab kissing. Nevertheless, due to the doubled number of crab cavities in the latter, the effects of cavity noise are expected to be more serious, possibly compromising the performance.

Studies on several optics and levelling configurations (ranging from $1 \times 10^{34}\,\mathrm{cm}^{-2}\,\mathrm{s}^{-1}$ to $2 \times 10^{34}\,\mathrm{cm}^{-2}\,\mathrm{s}^{-1}$) for IP8 have also been conducted, proving that operation of LHCb at high luminosity is feasible. In this work, the cases with $\beta^* = 1.5\,\mathrm{m}$ and total crossing angles of 130 µrad and 570 µrad with horizontal crossing (for external and internal crossing angles with opposite or same polarities, respectively), and 419 µrad (vertical crossing), have been summarised, although more options have been explored [118]. Depending on the case, yearly integrated luminosities between $41\,\mathrm{fb}^{-1}$ and $62\,\mathrm{fb}^{-1}$ are achievable, with limited loss on the integrated performance of the two main IPs (1 %–2 %) and negligible impact on the effective pile-up density. These figures for the integrated performance at IP8 have to be compared with the current estimate of $11\,\mathrm{fb}^{-1}$ for the baseline operation of the same IP (namely, $\beta^* = 3\,\mathrm{m}$ with a full crossing angle of $230\,\mu\mathrm{rad}$ or $770\,\mu\mathrm{rad}$ in the horizontal plane for external and internal crossing angles with opposite or same polarities, respectively, and levelled at a constant luminosity of $2 \times 10^{33}\,\mathrm{cm}^{-2}\,\mathrm{s}^{-1}$). Gaussian fits for the pile-up densities around the IP1, IP5, and IP8 in each operational scenario were obtained by the method of least squares. Results have provided a detailed characterisation of the luminous region associated to the collisions at the IPs, which the ATLAS, CMS, and LHCb experiments in turn have taken as input for the simulation of the performance of their corresponding detectors under different (and possibly) extreme configurations, with the aim of optimising and improving them.

The extensive studies in this work [153] deliver a detailed and updated picture of the foreseen performance of the HL-LHC under a wide range of operational scenarios in terms of integrated luminosity and expected data quality from the collisions.

In order to mitigate the possible limitations on the HL-LHC performance or its protection system, compensation of beam-beam effects by means of local multipolar magnets have been explored. Studies have centred around the long-range parasitic interactions, as this correction method can be applied for two beams simultaneously using the common magnets in the area where they originate. The proposed general technique aims at the term-by-term compensation of the different orders of the beam-beam force using kicks of similar order exerted by corrector magnets near the source. This method profits from the feed-down fields originated due to the offsets between the axes of the corrector magnets and the beam orbits, and exploits the fact that $2(n+1)$-pole magnets ($n = 2, 4, \dots$) have the same effect over same-charge particles travelling through them in opposite directions. The proposed technique was applied to the compensation of linear and octupolar components of the beam-beam long-range (BBLR) force in the HL-LHC baseline using sextupoles and decapoles with offsets, respectively, as a proof-of-principle. Unlike other compensation methods, this has the advantage of not relying on additional hardware in the interaction region. Results showed a successful reduction of the induced β-beating, correction of the tunes (reduction of the tune shifts), and decrease of the footprint, with a negligible impact on the minimum dynamic aperture. Further optimisation of the correction of high-order components of the BBLR force can yield to the improvement of the transverse beam stability and the increase of dynamic aperture. A modified version of this technique has been used to derive a compensation for the linear components of the beam-beam compensation wires, which were then successfully tested in the LHC.

Appendix A

Longitudinal bunch profiles

In this Appendix, the three density distributions used to describe the longitudinal bunch profile, namely Gaussian, q-Gaussian, and super-Gaussian, are presented. The general parameters used to characterise the distributions are defined first, and they are then applied to each of the particular distributions.

Let us consider a general density distribution $f(s;\sigma)$ function of the variable s and characterised for some parameter σ. The corresponding normalised distribution $F(s;\sigma)$ is

$$F(s;\sigma) = Af(s;\sigma)\,, \tag{A.1}$$

where

$$A \equiv \left(\int_{-\infty}^{\infty} f(s;\sigma)\,\mathrm{d}s\right)^{-1}\,, \tag{A.2}$$

is the normalisation factor, that is, $\int_{-\infty}^{\infty} F(s;\sigma)\,\mathrm{d}s = 1$.

A series of useful parameters are commonly used to characterise the density distribution. The *root mean square* (RMS) value of the variable s over the normalised distribution (σ_s) is defined as

$$\sigma_s \equiv \sqrt{\int_{-\infty}^{\infty} s^2 F(s;\sigma)\,\mathrm{d}s}\,. \tag{A.3}$$

The original distribution can then be written as $F(s;\sigma)$, that is, in terms of σ_s instead of the parameter σ.

Although the RMS value σ_s is commonly used to describe the bunch length, in operation, however, the *full width at half maximum* (FWHM) of the distribution is used instead due to its relation with the stability threshold for different distributions:

$$\mathrm{FWHM} \equiv s^{+} - s^{-}\,, \tag{A.4}$$

with $s^{\pm}$ are the right and left extremes of the distribution at half of its height, that is $s^{\pm} \equiv F^{-1}\left(\frac{1}{2}\max[F]\right)$, and where F^{-1} the inverse function of F. For the distributions of interest, in particular, $F(s)$ is symmetric and centred around $s = 0$, where it has its maximum: $\max\left[F(s;\sigma_s)\right] = F(0;\sigma_s) = A$.

A.1 Gaussian distribution

A bunch with a longitudinal Gaussian profile is described by the well-known normalised Gaussian distribution

$$\varrho_s^{\mathrm{G}}(s) = \frac{1}{\sqrt{2\pi}\sigma_{s_{\mathrm{G}}}} \exp\left(-\frac{s^2}{2\sigma_{s_{\mathrm{G}}}^2}\right), \qquad \text{(A.5)}$$

where $\sigma_{s_{\mathrm{G}}}$, the standard deviation of the particle distribution, defines the *Gaussian* RMS bunch length. The FWHM of the bunch profile in Eq. (A.5) is

$$\mathrm{FWHM}_{\mathrm{G}} = 2\sigma_{s_{\mathrm{G}}}\sqrt{2\ln 2}\,. \qquad \text{(A.6)}$$

A.2 q-Gaussian distribution

The q-Gaussian distribution of interest for the present work is given by

$$\varrho_s^{\mathrm{qG}}(s) = \frac{1}{\mu\sigma_{\mathrm{qG}}}\left(1 - \frac{4s^2}{\sigma_{\mathrm{qG}}^2}\right)^n, \qquad \text{with} \quad n = \frac{5}{2}, \qquad \text{(A.7)}$$

for a parameter σ_{qG}, and

$$\mu \equiv \frac{5\pi}{32}\,. \qquad \text{(A.8)}$$

In particular, the case $\sigma_{\mathrm{qG}} = \lambda\sigma_{s_{\mathrm{G}}}$ where

$$\lambda \equiv 2\left(\frac{2\ln 2}{1 - 2^{-2/5}}\right)^{1/2}, \qquad \text{(A.9)}$$

ensures that the FWHM of the q-Gaussian distribution is identical to the Gaussian FWHM:

$$\mathrm{FWHM}_{\mathrm{qG}} = \mathrm{FWHM}_{\mathrm{G}}\,. \qquad \text{(A.10)}$$

This yields to the following relation between their corresponding RMS values:

$$\sigma_{s_{\mathrm{qG}}} = \frac{1}{\sqrt{32}}\lambda\sigma_{s_{\mathrm{G}}}, \qquad \text{(A.11)}$$

in terms of which the distribution in Eq. (A.7) can be rewritten as follows:

$$\varrho_s^{\mathrm{qG}}(s) = \frac{\sqrt{32}}{5\pi\sigma_{s_{\mathrm{qG}}}}\left(1 - \frac{s^2}{8\sigma_{s_{\mathrm{qG}}}^2}\right)^{5/2}. \qquad \text{(A.12)}$$

A Gaussian density with an RMS bunch length[1] of $\sigma_{s_{\mathrm{G}}} = 9\,\mathrm{cm}$ (the HL-LHC baseline) and a q-Gaussian density with RMS bunch length of $\sigma_{s_{\mathrm{qG}}} = 7.6\,\mathrm{cm}$ are said

---

[1] Another common convention is to express the bunch length as 4σ in units of time, that is, $\tau_{4\sigma}\,[\mathrm{s}] = 4\sigma\,[\mathrm{m}]/c$; e.g. for a Gaussian RMS bunch length of 9 cm, $\tau_{4\sigma} = 1.2\,\mathrm{ns}$.

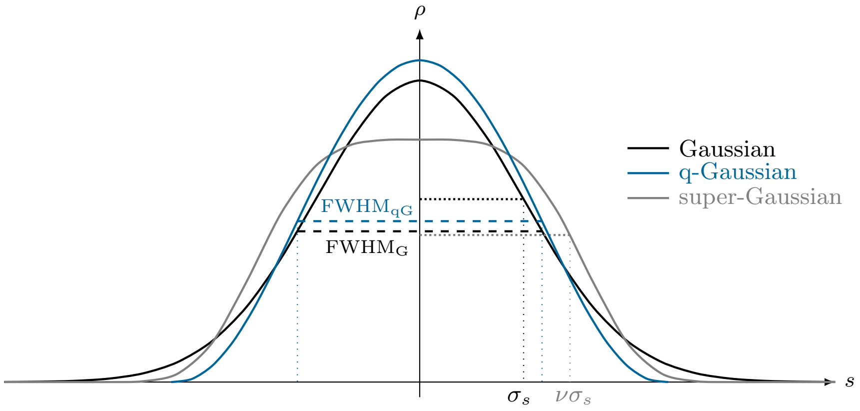

Figure A.1. Longitudinal bunch profiles.

to be *equivalent* in the sense that the FWHM of both distribution is the same, namely, 21.2 cm. From observations, the q-Gaussian distribution (Fig. A.1) better describes the longitudinal bunch profiles in the LHC, as the particle population concentrates mostly in the centre of the bunch rather than in the tails (depending on n).

The distribution in Eq. (A.7) is a particular case of the general Tsallis q-Gaussian distribution [154]

$$f(s) = \frac{\sqrt{\beta_q}}{C_q} \mathrm{e}_q[-\beta_q (s-\mu_q)^2]\,, \tag{A.13}$$

where the mean μ_q, deformation parameter q_q, and scale parameter β_q take the following values:

$$\mu_q = 0\,, \quad q = \frac{3}{5}\,, \quad \text{and} \quad \beta_q = \frac{10}{{\sigma_{\mathrm{qG}}}^2}\,; \tag{A.14}$$

the q-exponential function $\mathrm{e}_q(s)$ and the normalisation factor C_q are given, in general, by

$$\mathrm{e}_q(s) = \begin{cases} \exp(x) & \text{if} \quad q = 1 \\ [\,1+(1-q)\,s\,]^{\frac{1}{1-q}} & \text{if} \quad q \neq 1 \quad \text{and} \quad 1+(1-q)\,s > 0 \\ 0^{\frac{1}{1-q}} & \text{if} \quad q \neq 1 \quad \text{and} \quad 1+(1-q)\,s \leq 0 \end{cases}\,, \tag{A.15}$$

and

$$C_q = \begin{cases} \frac{2\sqrt{\pi}\,\Gamma\left(\frac{1}{1-q}\right)}{(3-q)\sqrt{1-q}\,\Gamma\left(\frac{3-q}{2(1-q)}\right)} & \text{for } -\infty < q < 1 \\ \sqrt{\pi} & \text{for } q = 1 \\ \frac{\sqrt{\pi}\,\Gamma\left(\frac{3-q}{2(q-1)}\right)}{\sqrt{q-1}\,\Gamma\left(\frac{1}{q-1}\right)} & \text{for } 1 < q < 3 \end{cases}\,, \tag{A.16}$$

respectively.

Table A.1. Gaussian, super-Gaussian, and q-Gaussian distributions.

Parameter	**Gaussian**	**super-Gaussian**	**q-Gaussian**
Norm. distribution $F(s)$	$\varrho_s^{\mathrm{G}}(s) = A_{\mathrm{G}}\ \exp\left(-\frac{s^2}{2\sigma_{\mathrm{G}}^2}\right)$	$\varrho_s^{\mathrm{SG}}(s) = A_{\mathrm{SG}} \exp\left(-\frac{s^4}{2\sigma_{\mathrm{SG}}^4}\right)$	$\varrho_s^{\mathrm{qG}}(s) = A_{\mathrm{qG}} \left(1 - \frac{4s^2}{\sigma_{\mathrm{qG}}^2}\right)^{5/2}$
Norm. amplitude A	$A_{\mathrm{G}} = \frac{1}{\sqrt{2\pi}\sigma_{\mathrm{G}}}$	$A_{\mathrm{SG}} = \frac{1}{\nu\sigma_{\mathrm{SG}}}$	$A_{\mathrm{qG}} = \frac{1}{\mu\sigma_{\mathrm{qG}}}$
RMS σ_s	$\sigma_{s_{\mathrm{G}}} = \sigma_{\mathrm{G}}$	$\sigma_{s_{\mathrm{SG}}} = \frac{1}{\kappa}\sigma_{\mathrm{SG}} \approx 0.691\,\sigma_{\mathrm{SG}}$	$\sigma_{s_{\mathrm{qG}}} = \frac{1}{\sqrt{32}}\,\sigma_{\mathrm{qG}} \approx 0.177\,\sigma_{\mathrm{qG}}$
i.e.	$\sigma_{\mathrm{G}} = \sigma_{s_{\mathrm{G}}}$	$\sigma_{\mathrm{SG}} = \kappa\sigma_{s_{\mathrm{SG}}} \approx 1.446\,\sigma_{s_{\mathrm{SG}}}$	$\sigma_{\mathrm{qG}} = \sqrt{32}\,\sigma_{s_{\mathrm{qG}}} \approx 5.657\,\sigma_{s_{\mathrm{qG}}}$
$F(s)$ and A in terms of RMS σ_s	$\varrho_s^{\mathrm{G}}(s) = A_{\mathrm{G}}\ \exp\left(-\frac{s^2}{2\sigma_{s_{\mathrm{G}}}^2}\right)$ $A_{\mathrm{G}} = \frac{1}{\sqrt{2\pi}\sigma_{s_{\mathrm{G}}}}$	$\varrho_s^{\mathrm{SG}}(s) = A_{\mathrm{SG}} \exp\left(-\frac{s^4}{2(\kappa\sigma_{s_{\mathrm{SG}}})^4}\right)$ $A_{\mathrm{SG}} = \frac{1}{\nu(\kappa\sigma_{s_{\mathrm{SG}}})}$	$\varrho_s^{\mathrm{qG}}(s) = A_{\mathrm{qG}} \left(1 - \frac{s^2}{8\sigma_{s_{\mathrm{qG}}}^2}\right)^{5/2}$ $A_{\mathrm{qG}} = \frac{\sqrt{32}}{5\pi\sigma_{s_{\mathrm{qG}}}}$
Full width at half maximum FWHM	$\mathrm{FWHM}_{\mathrm{G}} = 2\,(2\ln 2)^{1/2}\,\sigma_{\mathrm{G}}$ $\approx 2.355\,\sigma_{\mathrm{G}}$	$\mathrm{FWHM}_{\mathrm{SG}} = 2\,(2\ln 2)^{1/4}\,\sigma_{\mathrm{SG}}$ $\approx 2.170\,\sigma_{\mathrm{SG}}$	$\mathrm{FWHM}_{\mathrm{qG}} = \left(1 - 2^{-2/5}\right)^{1/2}\sigma_{\mathrm{qG}}$ $\approx 0.492\,\sigma_{\mathrm{qG}}$
i.e. in terms of RMS σ_s	$\mathrm{FWHM}_{\mathrm{G}} = 2\,(2\ln 2)^{1/2}\,\sigma_{s_{\mathrm{G}}}$ $\approx 2.355\,\sigma_{s_{\mathrm{G}}}$	$\mathrm{FWHM}_{\mathrm{SG}} = 2\,(2\ln 2)^{1/4}\,\kappa\sigma_{s_{\mathrm{SG}}}$ $\approx 3.140\,\sigma_{s_{\mathrm{SG}}}$	$\mathrm{FWHM}_{\mathrm{qG}} = \sqrt{32}\left(1 - 2^{-2/5}\right)^{1/2}\sigma_{s_{\mathrm{qG}}}$ $\approx 2.784\,\sigma_{s_{\mathrm{qG}}}$
Relation of RMS σ_s (or FWHM) with Gaussian		$\sigma_{s_{\mathrm{SG}}} \equiv \sigma_{s_{\mathrm{G}}}$	$\mathrm{FWHM}_{\mathrm{qG}} \equiv \mathrm{FWHM}_{\mathrm{G}}$
σ in terms of $\sigma_{s_{\mathrm{G}}}$		$\sigma_{\mathrm{SG}} = \kappa\sigma_{s_{\mathrm{G}}} \approx 1.446\,\sigma_{s_{\mathrm{G}}}$	$\sigma_{\mathrm{qG}} = \lambda\sigma_{s_{\mathrm{G}}} \approx 4.785\,\sigma_{s_{\mathrm{G}}}$
FWHM (or RMS σ_s) in terms of $\sigma_{s_{\mathrm{G}}}$		$\mathrm{FWHM}_{\mathrm{SG}} = 2\,(2\ln 2)^{1/4}\,\kappa\sigma_{s_{\mathrm{G}}} \approx 3.139\,\sigma_{s_{\mathrm{G}}}$	$\sigma_{s_{\mathrm{qG}}} = \frac{1}{\sqrt{32}}\,\lambda\sigma_{s_{\mathrm{G}}} \approx 0.846\,\sigma_{s_{\mathrm{G}}}$
$F(s)$ and A in terms of $\sigma_{s_{\mathrm{G}}}$	$\varrho_s^{\mathrm{G}}(s) = A_{\mathrm{G}}\ \exp\left(-\frac{s^2}{2\sigma_{s_{\mathrm{G}}}^2}\right)$ $A_{\mathrm{G}} = \frac{1}{\sqrt{2\pi}\sigma_{s_{\mathrm{G}}}}$	$\varrho_s^{\mathrm{SG}}(s) = A_{\mathrm{SG}} \exp\left(-\frac{s^4}{2(\kappa\sigma_{s_{\mathrm{G}}})^4}\right)$ $A_{\mathrm{SG}} = \frac{1}{\nu(\kappa\sigma_{s_{\mathrm{G}}})}$	$\varrho_s^{\mathrm{qG}}(s) = A_{\mathrm{qG}} \left(1 - \frac{4s^2}{(\lambda\sigma_{s_{\mathrm{G}}})^2}\right)^{5/2}$ $A_{\mathrm{qG}} = \frac{1}{\mu(\lambda\sigma_{s_{\mathrm{G}}})}$

where $\mu \equiv \frac{5\pi}{32}$, $\lambda \equiv 2\left(\frac{2\ln 2}{1 - 2^{-2/5}}\right)^{1/2}$, $\nu \equiv 2^{-3/4}\Gamma\left(\frac{1}{4}\right) = 2^{5/4}\Gamma\left(\frac{5}{4}\right)$, and $\kappa \equiv \left(\frac{1}{\sqrt{2}}\frac{\Gamma\left(\frac{1}{4}\right)}{\Gamma\left(\frac{3}{4}\right)}\right)^{1/2}$.

A.3 Super-Gaussian distribution

There are several common definitions for the super-Gaussian function of order n, for example [138]:

$$f(s) = f_0 \exp\left[-\left(\frac{s^2}{2\sigma_0^2}\right)^n\right] , \qquad \text{and} \qquad f(s) = f_0 \exp\left[-2\left(\frac{s}{\sigma_0}\right)^n\right] , \tag{A.17}$$

for a given parameter σ_0. In this work, the general super-Gaussian distribution of order n is defined by

$$f(s) = f_0 \exp\left(-\frac{s^n}{2\sigma_0^n}\right) , \tag{A.18}$$

for a given parameter σ_0 and where f_0 is the normalisation factor. In particular, the case with $n = 4$ is of special interest, i.e.

$$\varrho_s^{\mathrm{SG}}(s) = \frac{1}{\nu\sigma_{\mathrm{SG}}} \exp\left(-\frac{s^4}{2\sigma_{\mathrm{SG}}^4}\right) , \tag{A.19}$$

for a given parameter σ_{SG} and where

$$\nu \equiv 2^{-3/4}\Gamma\left(\tfrac{1}{4}\right) = 2^{5/4}\Gamma\left(\tfrac{5}{4}\right) , \tag{A.20}$$

as this distribution optimises the peak pile-up line density for operation with crab kissing (Section 6.5). Unlike the Gaussian and q-Gaussian densities, the particle population in a bunch with super-Gaussian longitudinal profile is more evenly distributed around the centre (Fig. A.1). The relation between the super-Gaussian and the Gaussian distributions is, by construction, via equal RMS bunch lengths,

$$\sigma_{s_{\mathrm{SG}}} = \sigma_{s_{\mathrm{G}}} . \tag{A.21}$$

This relation is ensured when $\sigma_{\mathrm{SG}} = \kappa\sigma_{s_{\mathrm{G}}}$, where

$$\kappa \equiv \left(\frac{1}{\sqrt{2}}\frac{\Gamma\left(\frac{1}{4}\right)}{\Gamma\left(\frac{3}{4}\right)}\right)^{1/2} , \tag{A.22}$$

and thus Eq. (A.19) can then be rewritten as

$$\varrho_s^{\mathrm{SG}}(s) = \frac{1}{\nu(\kappa\sigma_{s_{\mathrm{SG}}})} \exp\left(-\frac{s^4}{2(\kappa\sigma_{s_{\mathrm{SG}}})^4}\right) . \tag{A.23}$$

The FWHM of the super-Gaussian profile differs, in this case, from the Gaussian. The full characterisation of the three distributions of interest is summarised in Table A.1.

Bibliography

[1] European Organization for Nuclear Research (CERN), Aug. 2019. URL: `https://home.cern/`.

[2] The HL-LHC Project, Apr. 2019. URL: `http://hilumilhc.web.cern.ch/`.

[3] G. Apollinari et al. *High-Luminosity Large Hadron Collider (HL-LHC): Technical Design Report V.0.1*. CERN Yellow Reports: Monographs. CERN, Geneva, Switzerland, 2017. URL: `http://cds.cern.ch/record/2284929`.

[4] O. Brüning and L. Rossi. *The High Luminosity Large Hadron Collider: The New Machine for Illuminating the Mysteries of the Universe*. Advanced Series on Directions in High Energy Physics. World Scientific, Singapore, 2015. `doi:10.1142/9581`.

[5] G. Arduini et al. How to maximize the HL-LHC performance. In B. Goddard and F. Zimmermann, editors, *Proc. of RLIUP: Review of LHC and Injector Upgrade Plans, Archamps, France, October 29–31, 2013*, CERN Yellow Reports: Conference Proceedings, pages 81–94, Geneva, Switzerland, 2014. CERN. CERN-2014-006. `doi:10.5170/CERN-2014-006.81`.

[6] G. Arduini et al. High Luminosity LHC: challenges and plans. *JINST*, 11(12):C12081–C12081, Dec. 2016. `doi:10.1088/1748-0221/11/12/c12081`.

[7] A. Gorzawski, D. Mirarchi, B.M. Salvachua Ferrando, and J. Wenninger. MD 239 on collide and squeeze (part 2). Technical Report CERN-ACC-NOTE-2016-0018, CERN, Geneva, Switzerland, Jan. 2016. URL: `https://cds.cern.ch/record/2124690`.

[8] A. Gorzawski. *Luminosity control and beam orbit stability with beta star leveling at LHC and HL-LHC*. PhD thesis, École Polytechnique Fédérale de Lausanne (EPFL), Lausanne, Switzerland, 2016. Presented 30 Nov. 2016. `doi:10.5075/epfl-thesis-7338`.

[9] J. Wenninger et al. β^* leveling with telescopic ATS squeeze (MD 2410). Technical Report CERN-ACC-NOTE-2017-0052, CERN, Geneva, Switzerland, Sep. 2017. URL: `https://cds.cern.ch/record/2285184`.

[10] M. Hostettler et al. β^* levelling using the LHC Lumi Server (MD 2427). Technical Report CERN-ACC-NOTE-2018-0001, CERN, Geneva, Switzerland, Jan. 2018. URL: `https://cds.cern.ch/record/2300212`.

[11] S. Fartoukh. An achromatic telescopic squeezing (ATS) scheme for LHC upgrade. In *Proc. of 2nd International Particle Accelerator Conference (IPAC'11), San Sebastián, Spain, 4–9 September 2011*, pages 2288–2290. JACoW Publishing, Jun. 2011. URL: `http://accelconf.web.cern.ch/AccelConf/IPAC2011/papers/wepc037.pdf`.

[12] S. Fartoukh. Achromatic telescopic squeezing scheme and application to the LHC and its luminosity upgrade. *Phys. Rev. ST Accel. Beams*, 16:111002, Nov. 2013. `doi:10.1103/PhysRevSTAB.16.111002`.

[13] H. Damerau et al. LHC Injectors Upgrade, Technical Design Report, Vol. I: Protons. Technical Report CERN-ACC-2014-0337, CERN, Geneva, Switzerland, Dec. 2014. URL: `https://cds.cern.ch/record/1976692`.

[14] High-Luminosity LHC, CERN, Apr. 2019. URL: `https://home.cern/science/accelerators/high-luminosity-lhc`.

[15] P. Vankov and the ATLAS Collaboration. ATLAS future upgrade. Technical Report ATL-UPGRADE-PROC-2016-003, CERN, Geneva, Switzerland, Jun. 2016. `doi:10.22323/1.273.0061`.

[16] W. Walkowiak and the ATLAS Collaboration. ATLAS plans for the High-Luminosity LHC. Technical Report ATL-PHYS-PROC-2018-048, CERN, Geneva, Switzerland, Jun. 2018. `doi:10.22323/1.326.0055`.

[17] ATLAS Collaboration. Expected performance of the ATLAS detector at the High-Luminosity LHC. Technical Report ATL-PHYS-PUB-2019-005, CERN, Geneva, Switzerland, Jan. 2019. URL: `https://cds.cern.ch/record/2655304`.

[18] S. Zenz and the CMS Collaboration. Prospects for Higgs physics with an upgraded CMS detector at the High-Luminosity LHC. *Nucl. Part. Phys. Proc.*, 273–275:890–895, 2016. `doi:10.1016/j.nuclphysbps.2015.09.137`.

[19] B. Bendavid. CMS detector performance for HL-LHC. Workshop on the physics of HL-LHC and perspectives at HE-LHC, CERN, October 30, 2017, Oct. 2017. URL: `https://indico.cern.ch/event/647676/contributions/2721136/attachments/1549024/2432814/cmsphase2-Oct30-2017.pdf`.

[20] CMS Collaboration. Expected performance of the physics objects with the upgraded CMS detector at the HL-LHC. Technical Report CMS-NOTE-2018-006, CERN-CMS-NOTE-2018-006, CERN, Geneva, Switzerland, Dec. 2018. URL: `http://cds.cern.ch/record/2650976`.

[21] G. Passaleva. LHCb in the HL-LHC era, Oct. 2017. LHCb-TALK-2017-339. URL: `https://cds.cern.ch/record/2291497`.

[22] LHCb Collaboration. Physics case for an LHCb Upgrade II - Opportunities in flavour physics, and beyond, in the HL-LHC era. Technical Report LHCB-PUB-2018-009, LHCC-G-171, CERN-LHCC-2018-027, CERN, Geneva, Switzerland, Aug. 2018. URL: `https://cds.cern.ch/record/2636441`, `arXiv:1808.08865`.

[23] ALICE Collaboration. ALICE upgrade physics performance studies for 2018 Report on HL/HE-LHC physics. Technical Report ALICE-PUBLIC-2019-001, CERN, Geneva, Switzerland, Feb. 2019. URL: `https://cds.cern.ch/record/2661798`.

[24] P. Campana, M. Klute, and P. Wells. Physics goals and experimental challenges of the proton-proton High-Luminosity Operation of the LHC. *Ann. Rev. Nucl. Part. Sci.*, 66:273–295, 2016. `arXiv:1603.09549`, `doi:10.1146/annurev-nucl-102115-044812`.

[25] S. Burkhard. The High-Luminosity upgrade of the LHC: Physics and Technology Challenges for the Accelerator and the Experiments. *JPCS*, 706:022002, Apr. 2016. `doi:10.1088/1742-6596/706/2/022002`.

[26] M. Mangano. The physics landscape of the High Luminosity LHC. In O. Brüning and L. Rossi, editors, *The High Luminosity Large Hadron Collider: The New Machine for Illuminating the Mysteries of the Universe*, Advanced Series on Directions in High Energy Physics, chapter 2, pages 19–30. World Scientific, 2015. `doi:10.1142/9789814675475_0002`.

[27] S. Jezequel. Prospects for the high-luminosity LHC. *Nuclear Physics B*, 245:145–148, 2013. `doi:10.1016/j.nuclphysbps.2013.10.027`.

[28] F. Ruggiero, W. Scandale, and F. Zimmermann. Scenarios for the LHC Luminosity Upgrade (LHC-LUMI-05). In *Proc. of 2nd CARE-HHH-APD Workshop on Scenarios for the LHC Luminosity Upgrade, Arcidosso, Italy, August 31–September 3, 2005*, Geneva, Switzerland, 2006. CERN. CERN-2006-008, CARE-CONF-06-014-HHH, CARE-CONF-2006-014-HHH. `doi:10.5170/CERN-2006-008`.

[29] G. Apollinari, I. Béjar Alonso, O. Brüning, M. Lamont, and L. Rossi. *HL-LHC Preliminary Design Report: Deliverable: D1.5*. CERN, Geneva, Switzerland, Nov. 2014. CERN-ACC-2014-0300. URL: `http://cds.cern.ch/record/1972604`.

[30] P. Azzi. CMS performance: Dependence on scenario for luminous region. ECFA High Luminosity LHC Experiments Workshop 2016, Aix-Les-Bains, France, Oct. 2016. URL: `https://indico.cern.ch/event/524795/contributions/2235253/attachments/1347082/2031647/EDQCMS_ECFA_Azzi.pdf`.

[31] B. Petersen. ATLAS performance for different luminous region scenarios. ECFA High Luminosity LHC Experiments Workshop 2016, Aix-Les-Bains, France, Oct. 2016. URL: `https://indico.cern.ch/event/524795/contributions/2235251/attachments/1347098/2031687/LumiStudies.pdf`.

[32] E. Shaposhnikova and J. Esteban Müller. Bunch length and particle distribution for (HL-)LHC. 82nd HL-LHC WP2 Meeting, CERN, Geneva, Jan. 2017. URL: `https://indico.cern.ch/event/572439/contributions/2423329/attachments/1394442/2125205/HL-LHC_WP2_Jan17.pdf`.

[33] S. Papadopoulou et al. Modelling and measurements of bunch profiles at the LHC. In *Proc. of 8th International Particle Accelerator Conference (IPAC'17), Copenhagen, Denmark, May 14–19, 2017*, pages 2167–2170. JACoW Publishing, May 2017. `doi:10.18429/JACoW-IPAC2017-TUPVA044`.

[34] L. Medina and R. Tomás. Performance and operational aspects of HL-LHC scenarios. In *Proc. of 7th International Particle Accelerator Conference (IPAC'16), Busan, Korea, May 8–13, 2016*, pages 1516–1519. JACoW Publishing, Jun. 2016. `doi:10.18429/JACoW-IPAC2016-TUPMW035`.

[35] HiLumi Optics and Layout, Jun. 2018. URL: `https://espace.cern.ch/HiLumi/WP2/task2/SitePages/Home.aspx`.

[36] G. Iadarola. HL-LHC filling schemes: possible optimization. 140th HL-LHC WP2 Meeting, CERN, Geneva, Jan. 2019. URL: `https://indico.cern.ch/event/788818/contributions/3277254/attachments/1786584/2909004/002_filling_schemes.pdf`.

[37] L. Rossi. HL-LHC: baseline and operational scenario. LHC Performance Workshop Chamonix, Jan. 2018. URL: `https://indico.cern.ch/event/676124/contributions/2768608/attachments/1591920/2520437/1_-_HL-LHC_Baseline_and_recap_options_-_Rossi.pdf`.

[38] O. Brüning et al. LHC Full Energy Exploitation Study: Operation at ultimate energy of 7.5 TeV. Technical Report CERN-ACC-2019-0015, CERN, Geneva, Switzerland, Jan. 2019. URL: `https://cds.cern.ch/record/2655017`.

[39] L. Medina et al. New High-Luminosity LHC baseline and performance at ultimate energy. In *Proc. of 9th International Particle Accelerator Conference (IPAC'18), Vancouver, BC, Canada, April 29–May 4, 2018*, pages 408–411. JACoW Publishing, Jun. 2018. `doi:10.18429/JACoW-IPAC2018-MOPML009`.

[40] I. Efthymiopoulos et al. LHCb upgrades and operation at $10^{34}\,\mathrm{cm}^{-2}\,\mathrm{s}^{-1}$ luminosity - A first study. Technical Report CERN-ACC-NOTE-2018-0038, CERN, Geneva, Switzerland, May 2018. URL: `https://cds.cern.ch/record/2319258`.

[41] R. Tomás, O. Dominguez, and S. White. HL-LHC alternatives. In B. Goddard and F. Zimmermann, editors, *Proc. of RLIUP: Review of LHC and Injector Upgrade Plans, Archamps, France, October 29–31, 2013*, CERN Yellow Reports: Conference Proceedings, pages 119–126, Geneva, Switzerland, 2014. CERN. CERN-2014-006. `doi:10.5170/CERN-2014-006.119`.

[42] R. Tomás et al. HL-LHC alternative scenarios. In M. Draper, editor, *Proc. of Chamonix 2014 Workshop on LHC Performance, Chamonix, France, September 22–25, 2014*, CERN Yellow Reports: Conference Proceedings, pages 217–224, Geneva, Switzerland, 2015. CERN. CERN-2015-002, CERN-ATS-2015-002. `doi:10.5170/CERN-2015-002`.

[43] J.-P. Koutchouk. Principle of a correction of the long-range beam-beam effect in LHC using electromagnetic lenses. Technical Report LHC-PROJECT-NOTE-223, CERN, Geneva, Switzerland, Mar. 2000. URL: `https://cds.cern.ch/record/692058`.

[44] A. Valishev and V. Shiltsev. Electron lens for beam-beam compensation at LHC. In *Proc. of 23rd Particle Accelerator Conference (PAC'09), Vancouver, Canada, May 4–8, 2009*, May 2010. FERMILAB-CONF-09-171-AD-APC. URL: `http://accelconf.web.cern.ch/AccelConf/PAC2009/papers/we6pfp034.pdf.pl?conf-09-171`.

[45] X. Gu et al. Electron lenses for head-on beam-beam compensation in RHIC. *Phys. Rev. Accel. Beams*, 20:023501, Feb. 2017. `doi:10.1103/PhysRevAccelBeams.20.023501`.

[46] U. Dorda, F. Zimmermann, W. Fischer, and V. Shiltsev. LHC beam-beam compensation using wires and electron lenses. In *2007 IEEE Particle Accelerator Conference (PAC)*, pages 1589–1591, Jun. 2007. `doi:10.1109/PAC.2007.4440832`.

[47] S. Fartoukh, A. Valishev, Y. Papaphilippou, and D. Shatilov. Compensation of the long-range beam-beam interactions as a path towards new configurations for the high luminosity LHC. *Phys. Rev. ST Accel. Beams*, 18:121001, Dec. 2015. `doi:10.1103/PhysRevSTAB.18.121001`.

[48] F. Zimmermann and H. Schmickler. Long-range beam-beam compensation using wires. In O. Brüning and L. Rossi, editors, *The High Luminosity Large Hadron Collider: The New Machine for Illuminating the Mysteries of the Universe*, Advanced Series on Directions in High Energy Physics, chapter 14, pages 243–267. World Scientific, 2015. `doi:10.1142/9789814675475_0014`.

[49] A. Poyet. Compensation of the long-range beam-beam interaction in the LHC. Master's thesis, Institut polytechnique de Grenoble (INP), Grenoble, France, Sep. 2017. Presented 07 Sep. 2017. URL: `https://cds.cern.ch/record/2320490`.

[50] A.W. Chao, K.H. Mess, M. Tigner, and F. Zimmermann. *Handbook of Accelerator Physics and Engineering*. World Scientific, Singapore, 2nd edition, 2013. `doi:10.1142/8543`.

[51] H. Wiedemann. *Particle Accelerator Physics*. Springer, Berlin, 4th edition, 2015. `doi:10.1007/978-3-319-18317-6`.

[52] W. Herr. Introduction to Landau damping. In *CAS - CERN Accelerator School: Advanced Course on Accelerator Physics, Trondheim, Norway, November 19–29, 2013*, Geneva, Switzerland, 2014. CERN. CERN-2014-009. `arXiv:1601.05227`, `doi:10.5170/CERN-2014-009.377`.

[53] O. Brüning et al. *LHC Design Report*. CERN Yellow Reports: Monographs. CERN, Geneva, Switzerland, 2004. `doi:10.5170/CERN-2004-003-V-1`.

[54] W. Herr and B. Muratori. Concept of luminosity. In *CAS - CERN Accelerator School: Intermediate Course on Accelerator Physics, Zeuthen, Germany, September 15–26, 2003*, Geneva, Switzerland, 2006. CERN. CERN-2006-002. `doi:10.5170/CERN-2006-002.361`.

[55] R.B. Palmer. Energy scaling, crab crossing and the pair problem. Technical Report SLAC-PUB-4707, SLAC, Stanford, CA, Dec. 1988. URL: `https://pdfs.semanticscholar.org/c5ee/9ebe9562b2c175169bcb1787fc3d64a21bbe.pdf`.

[56] K. Oide and K. Yokoya. The crab crossing scheme for storage ring colliders. *Phys. Rev.*, A40:315–316, 1989. `doi:10.1103/PhysRevA.40.315`.

[57] Y.-P. Sun et al. Beam dynamics aspects of crab cavities in the CERN Large Hadron Collider. *Phys. Rev. ST Accel. Beams*, 12:101002, Oct. 2009. `doi:10.1103/PhysRevSTAB.12.101002`.

[58] W. Herr. Beam-beam interactions. In *CAS - CERN Accelerator School: Intermediate Course on Accelerator Physics, Zeuthen, Germany, September 15–26, 2003*, Geneva, Switzerland, 2006. CERN. CERN-2006-002. `doi:10.5170/CERN-2006-002.379`.

[59] W. Herr and T. Pieloni. Beam-beam effects. In *CAS - CERN Accelerator School: Advanced Accelerator Physics Course: Trondheim, Norway, August, 18–29, 2013*, Geneva, Switzerland, 2014. CERN. `arXiv:1601.05235`, `doi:10.5170/CERN-2014-009.431`.

[60] M. Crouch et al. MD385: Long range beam-beam interaction and the effect on the beam and luminosity lifetimes. Technical Report CERN-ACC-NOTE-2016-0019, CERN, Geneva, Switzerland, Jan. 2016. URL: `https://cds.cern.ch/record/2124748`.

[61] A. Gorzawski, K. Fuchsberger, M. Hostettler, T. Pieloni, and J. Wenninger. Long-range beam-beam orbit effects in LHC, simulations and observations from machine operation in 2016. In *Proc. of 8th International Particle Accelerator Conference (IPAC'17), Copenhagen, Denmark, 14–19 May, 2017*, pages 3799–3802. JACoW Publishing, May 2017. `doi:https://doi.org/10.18429/JACoW-IPAC2017-THPAB042`.

[62] A. Piwinski. Computer simulation of the beam-beam interaction at a crossing angle. *IEEE Trans. Nucl. Sci.*, 32(5):2240–2242, Oct. 1985. `doi:10.1109/TNS.1985.4333872`.

[63] T. Pieloni et al. Dynamic beta and beta-beating effects in the presence of the beam-beam interactions. In *Proc. of ICFA Advanced Beam Dynamics Workshop on High-Intensity and High-Brightness Hadron Beams (HB'16), Malmö, Sweden, July 3–8, 2016*, pages 136–139. JACoW Publishing, Aug. 2016. `doi:10.18429/JACoW-HB2016-MOPR027`.

[64] M. Conte and W. MacKay. *An Introduction to the Physics of Particle Accelerators.* World Scientific, Singapore, 2nd edition, 2008. `doi:10.1142/6683`.

[65] S.Y. Lee. *Accelerator Physics.* World Scientific, Singapore, 4th edition, 2019. `doi:10.1142/11111`.

[66] A. Wolski. *Beam Dynamics in High Energy Particle Accelerators.* Imperial College Press, Singapore, 2014. `doi:10.1142/p899`.

[67] M. Martini. Intrabeam scattering. In *CAS - CERN Accelerator School: Intensity Limitations in Particle Beams, Geneva, Switzerland, November 2–11, 2015*, Geneva, Switzerland, 2017. CERN. CERN-2017-006-SP. `doi:10.23730/CYRSP-2017-003.291`.

[68] A. Piwinski. Intra-beam scattering. In *Proc. of 9th Int. Conference on High Energy Accelerators, Stanford, CA, 1974*, page 405. SLAC, 1974. `doi:10.5170/CERN-1992-001.226`.

[69] J.D. Bjorken and S.K. Mtingwa. *Part. Accel.* 13 (1983) 115.

[70] MAD. Methodical Accelerator Design program, Aug. 2019. URL: `http://mad.web.cern.ch/mad/`.

[71] F. Antoniou and F. Zimmermann. Revision of intrabeam scattering with non-ultrarelativistic corrections and vertical dispersion for MAD-X. Technical Report CERN-ATS-2012-066, CERN, Geneva, Switzerland, May 2012. URL: `http://cds.cern.ch/record/1445924`.

[72] K. Ohmi et al. Response of colliding beam-beam system to harmonic excitation due to crab-cavity rf phase modulation. *Phys. Rev. ST Accel. Beams*, 14:111003, Nov. 2011. `doi:10.1103/PhysRevSTAB.14.111003`.

[73] P. Baudrenghien and T. Mastoridis. Transverse emittance growth due to rf noise in the High-Luminosity LHC crab cavities. *Phys. Rev. ST Accel. Beams*, 18:101001, Oct. 2015. `doi:10.1103/PhysRevSTAB.18.101001`.

[74] C. Møller and K. Danske. *Vidensk. Selsk. Mat.-Fys. Medd.* 23 (1995) 1.

[75] L. Medina. Luminosity integrals, 2017. unpublished.

[76] E. McCrory, V. Shiltsev, A.J. Slaughter, and A. Xiao. Fitting the luminosity decay in the Tevatron. In *Proc. of Particle Accelerator Conference (PAC'05), Knoxville, TN, USA, May 16–20, 2005*, May 2005. URL: `http://accelconf.web.cern.ch/AccelConf/p05/PAPERS/TPAP036.PDF`.

[77] M. Benedikt, D. Schulte, and F. Zimmermann. Optimizing integrated luminosity of future hadron colliders. *Phys. Rev. ST Accel. Beams*, 18:101002, Oct. 2015. `doi:10.1103/PhysRevSTAB.18.101002`.

[78] ATLAS and CMS Collaborations. Expected pileup values at the HL-LHC. Technical Report ATL-UPGRADE-PUB-2013-014, CERN, Geneva, Switzerland, Sep. 2013. URL: `https://cds.cern.ch/record/1604492`.

[79] V. Shiltsev and E. McCrory. Characterizing luminosity evolution in the Tevatron. In *Proc. of Particle Accelerator Conference (PAC'05), Knoxville, TN, USA, May 16–20, 2005*, May 2005. URL: `http://accelconf.web.cern.ch/AccelConf/p05/PAPERS/TPAP038.PDF`.

[80] M. Giovannozzi. Simple models describing the time-evolution of luminosity in hadron colliders. Technical Report CERN-ACC-2014-0086, CERN, Geneva, Switzerland, Jun. 2014. URL: `https://cds.cern.ch/record/1742039`.

[81] S. Paret. Measurement and simulation of luminosity levelling in LHC via beam separation. In *Proc. of ICFA Advanced Beam Dynamics Workshop on High-Intensity and High-Brightness Hadron Beams (HB'12), Beijing, China, September 17–21, 2012*, pages 451–4559. JACoW Publishing, Sep. 2012. URL: `http://accelconf.web.cern.ch/AccelConf/HB2012/papers/weo1c06.pdf`.

[82] A. Niemi, A. Apollonio, J. Gutleber, P. Sollander, J.-P. Penttinen, and S. Virtanen. Availability modeling approach for future circular colliders based on the LHC operation experience. *Phys. Rev. Accel. Beams*, 19:121003, Dec. 2016. `doi:10.1103/PhysRevAccelBeams.19.121003`.

[83] A. Apollonio. *Machine Protection: Availability for Particle Accelerators.* PhD thesis, Technische Universität Wien (TU Wien), Vienna, Austria, Mar. 2015. Presented 16 Mar. 2015. URL: `http://cds.cern.ch/record/2002820`.

[84] R. Bartoldus. Online determination of the LHC luminous region with the ATLAS high-level trigger. *Phys. Procedia*, 37:2080–2088, 2012. Proc. of 2nd International Conference on Technology and Instrumentation in Particle Physics (TIPP 2011). `doi:https://doi.org/10.1016/j.phpro.2012.04.109`.

[85] J. Esteban Müller. *Longitudinal intensity effects in the CERN Large Hadron Collider*. PhD thesis, École Polytechnique Fédérale de Lausanne (EPFL), Lausanne, Switzerland, Apr. 2016. Presented 28 Jun. 2016. `doi:10.5075/epfl-thesis-7077`.

[86] S. Fartoukh. Pile up management at the high-luminosity LHC and introduction to the crab-kissing concept. *Phys. Rev. ST Accel. Beams*, 17:111001, Nov. 2014. `doi:10.1103/PhysRevSTAB.17.111001`.

[87] ATLAS Collaboration. Technical Design Report for the ATLAS Inner Tracker Strip Detector. Technical Report CERN-LHCC-2017-005, ATLAS-TDR-025, CERN, Geneva, Switzerland, Apr. 2017. URL: `http://cds.cern.ch/record/2257755`.

[88] B. Petersen. ATLAS pile-up studies. 9th Experimental Data Quality Meeting, CERN, Geneva, Apr. 2017. URL: `https://indico.cern.ch/event/626264/contributions/2529218/attachments/1442395/2221239/AtlasStudies.pdf`.

[89] B. Petersen. Private communication, Oct. 2017.

[90] R. Tomás. Updated optics layout and machine performance. 6th HL-LHC Collaboration Meeting, Paris, France, Nov. 2016. URL: `https://indico.cern.ch/event/549979/contributions/2257122/attachments/1370681/2079634/SLIDESBeamer.pdf`.

[91] LEVELLING program, Aug. 2019. URL: `https://github.com/lmedinam/Levelling.git`.

[92] PYTHON. Interpreted, high-level, general-purpose programming language, Aug. 2019. URL: `https://www.python.org/`.

[93] NUMPY. Library for scientific and technical computing with Python, Aug. 2019. URL: `https://www.numpy.org/`.

[94] SCIPY. Library for scientific computing with Python, Aug. 2019. URL: `https://www.scipy.org/`.

[95] MAPCLASS2. Code to aid particle accelerator lattice design and optimization, Aug. 2019. URL: `https://github.com/pylhc/MapClass2`.

[96] D. Pellegrini, S. Fartoukh, N. Karastathis, and Y. Papaphilippou. Multiparametric response of the HL-LHC dynamic aperture in presence of beam-beam effects. In *Proc. of 8th International Particle Accelerator Conference (IPAC'17), Copenhagen, Denmark, May 14–19, 2017*, pages 2055–2058. JACoW Publishing, May 2017. `doi:10.18429/JACoW-IPAC2017-TUPVA010`.

[97] N. Karastathis, R. De Maria, S. Fartoukh, Y. Papaphilippou, and D. Pellegrini. Refining the HL-LHC operational settings with inputs from dynamic aperture simulations: A progress report. In *Proc. of 9th International Particle Accelerator Conference (IPAC'18), Vancouver, BC, Canada, April 29–May 4, 2018*, pages 188–191. JACoW Publishing, Jun. 2018. `doi:10.18429/JACoW-IPAC2018-MOPMF041`.

[98] AFS Service. Andrew File System Service for CERN users, Aug. 2019. URL: `http://information-technology.web.cern.ch/services/afs-service`.

[99] E. Metral et al. Update of the HL-LHC operational scenarios for proton operation. Technical Report CERN-ACC-NOTE-2018-0002, CERN, Geneva, Switzerland, Jan. 2018. URL: `http://cds.cern.ch/record/2301292`.

[100] E. Shaposhnikova and J. Esteban Müller. Longitudinal stability limits and bunch length specifications. 78th HL-LHC WP2 Meeting, CERN, Geneva, Sep. 2016. URL: `https://indico.cern.ch/event/563288/contributions/2308739/attachments/1342048/2021482/HLLHC_WP2_v1.pdf`.

[101] G. Arduini et al. Beam parameters at LHC injection. Technical Report CERN-ACC-2014-0006, CERN, Geneva, Switzerland, Jan. 2014. URL: `https://cds.cern.ch/record/1644771`.

[102] R. Calaga. Crab cavities for the High-Luminosity LHC. In *Proc. of International Conference on RF Superconductivity (SRF'17), Lanzhou, China, July 17-21, 2017*, pages 695–699. JACoW Publishing, Jan. 2018. `doi:https://doi.org/10.18429/JACoW-SRF2017-THXA03`.

[103] G. Arduini et al. LIU-HL-LHC: PICs: what do we gain in beam performances? In S. Myers and F. Zimmermann, editors, *Review of LHC and injector upgrade plans - Summary*. CERN, Oct. 2013. CERN-ACC-NOTE-2014-0071. URL: `https://cds.cern.ch/record/1953694`.

[104] L. Medina, G. Arduini, and R. Tomás. Studies on luminous region, pile-up and performance for HL-LHC scenarios. In *Proc. of 8th International Particle Accelerator Conference (IPAC'17), Copenhagen, Denmark, May 14–19, 2017*, pages 1908–1911. JACoW Publishing, May 2017. URL: `http://jacow.org/ipac2017/papers/tupik089.pdf`.

[105] L. Medina. Table on HL-LHC operation scenarios. 6th Experimental Data Quality Meeting, CERN, Geneva, Oct. 2016. URL: `https://indico.cern.ch/event/571576/contributions/2312584/attachments/1358576/2055141/2016-10-20_HLLHC-EDQ.pdf`.

[106] F.S. Carlier et al. Optics measurements and correction challenges for the HL-LHC. Technical Report CERN-ACC-2017-0088, CERN, Geneva, Switzerland, Oct. 2017. URL: `https://cds.cern.ch/record/2290899`.

[107] R. Tomás et al. CERN Large Hadron Collider optics model, measurements, and corrections. *Phys. Rev. ST Accel. Beams*, 13:121004, Dec. 2010. `doi:10.1103/PhysRevSTAB.13.121004`.

[108] A. Apollonio. Machine efficiency and performance reach for operation at ultimate beam energy. LHC Performance Workshop Chamonix, Jan. 2018. URL: `https://indico.cern.ch/event/676124/contributions/2768608/attachments/1591920/2520437/1_-_HL-LHC_Baseline_and_recap_options_-_Rossi.pdf`.

[109] A. Apollonio et al. Reliability and availability of particle accelerators: Concepts, lessons, strategy. In *Proc. of 9th International Particle Accelerator Conference (IPAC'18), Vancouver, BC, Canada, April 29–May 4, 2018*, pages 5014–5018. JACoW Publishing, Jun. 2018. URL: `http://jacow.org/ipac2018/papers/frxgbd1.pdf`.

[110] H. Damerau, S. Hancock, A. Lasheen, and D. Perrelet. RF manipulations for special LHC-type beams in the CERN PS. In *Proc. 9th International Particle Accelerator Conference (IPAC'18), Vancouver, BC, Canada, April 29–May 4, 2018*, pages 1971–1974. JACoW Publishing, Jun. 2018. `doi:10.18429/JACoW-IPAC2018-WEPAF063`.

[111] E.H. Maclean et al. New approach to LHC optics commissioning for the nonlinear era. *Phys. Rev. Accel. Beams*, 22:061004, Jun. 2019. `doi:10.1103/PhysRevAccelBeams.22.061004`.

[112] J. Wenninger. Private communication, Oct. 2015.

[113] P. Baudrenghien, R. Calaga, T. Mastoridis, and E. Yamakawa. Crab cavities, RF noise and operational aspects (counter-phasing, full detuning). An update. 96th HL-LHC WP2 Meeting, CERN, Geneva, Jun. 2017. URL: `https://indico.cern.ch/event/645814/contributions/2622537/attachments/1475139/2291024/Meeting_13_06_2017.pdf`.

[114] T. Mastoridis, P. Baudrenghien, S. Hansen, B. Miller, and J. Wachter. Crab cavity RF noise mitigation. 101st HL-LHC WP2 Meeting, CERN, Geneva, Aug. 2017. URL: `https://indico.cern.ch/event/659970/contributions/2692112/attachments/1510812/2355979/ABPtalk_Aug2017.pdf`.

[115] A. Rossi et al. Progress with long-range beam-beam compensation studies for High Luminosity LHC. In *Proc. of 8th International Particle Accelerator Conference (IPAC'17), Copenhagen, Denmark, May 14–19, 2017*, pages 2358–2361. JACoW Publishing, May 2017. `doi:https://doi.org/10.18429/JACoW-IPAC2017-TUPVA115`.

[116] J. Albrecht et al. Luminosity scenarios for LHCb Upgrade II. Technical Report LHCb-PUB-2019-001, CERN-LHCb-PUB-2019-001, CERN, Geneva, Switzerland, Jan. 2019. URL: `https://cds.cern.ch/record/2653011`.

[117] W. Herr and Y. Papaphilippou. Alternative running scenarios for the LHCb experiment. Technical Report LHC-PROJECT-Report-1009, CERN-LHC-PROJECT-Report-1009, CERN, Geneva, Switzerland, Jan. 2007. URL: `https://cds.cern.ch/record/1038089`.

[118] L. Medina. Update on beam parameters and operation schemes and operation of IP8 at high luminosity. 12th Experimental Data Quality Meeting, CERN, Geneva, Nov. 2017. URL: `https://indico.cern.ch/event/676473/contributions/2768892/attachments/1552804/2445658/2017-11-06_HLLHC-EDQ.pdf`.

[119] R. De Maria. Private communication, Mar. 2018.

[120] B. Holzer, R. Versteegen, and R. Alemany. Vertical crossing angle in IR8. Technical Report CERN-ATS-Note-2013-024 PERF, CERN, Geneva, Switzerland, Apr. 2013. URL: `https://cds.cern.ch/record/1541986`.

[121] R. Tomás. HL-LHC operational scenarii and machine performance. 7th HL-LHC Collaboration Meeting, Paris, France, Nov. 2017. URL: `https://indico.cern.ch/event/647714/contributions/2632846/attachments/1556811/2450371/SLIDESlogo.pdf`.

[122] L. Medina and R. Tomás. Performance of the new baseline and other operational scenarios. 108th HL-LHC WP2 Meeting, CERN, Geneva, Oct. 2017. URL: `https://indico.cern.ch/event/668033/contributions/2759488/attachments/1546097/2570075/2017-10-24_HLLHC-WP2.pdf`.

[123] S. Fartoukh, N. Karastathis, L. Ponce, M. Solfaroli Camillocci, and R. Tomás. About flat telescopic optics for the future operation of the LHC. Technical Report CERN-ACC-2018-0018, CERN, Geneva, Switzerland, Mar 2018. URL: `https://cds.cern.ch/record/2622595`.

[124] J. Shi, L. Jin, and O. Kheawpum. Multipole compensation of long-range beam-beam interactions with minimization of nonlinearities in Poincaré maps of a storage-ring collider. *Phys. Rev. E*, 69:036502, Mar. 2004. `doi:10.1103/PhysRevE.69.036502`.

[125] J. Barranco and T. Pieloni. Global compensation of long-range beam-beam effects with octupole magnets: dynamic aperture simulations for the HL-LHC case and possible usage in LHC and FCC. Technical Report CERN-ACC-NOTE-2017-0036, CERN, Geneva, Switzerland, May 2017. URL: `https://cds.cern.ch/record/2263347`.

[126] L. Medina, J. Barranco, X. Buffat, Y. Papaphilippou, T. Pieloni, and R. Tomás. Correction of beta-beating due to beam-beam for the LHC and its impact on dynamic aperture. In *Proc. of 8th International Particle Accelerator Conference (IPAC'17), Copenhagen, Denmark, May 14–19, 2017*, pages 2512–2515. JACoW Publishing, May 2017. `doi:https://doi.org/10.18429/JACoW-IPAC2017-WEOAB2`.

[127] L. Medina, J. Barranco, X. Buffat, T. Pieloni, and R. Tomás. Assessment of linear and non-linear optics errors due to beam-beam with multipoles for the High-Luminosity LHC. In *Proc. of 9th International Particle Accelerator Conference (IPAC'18), Vancouver, BC, Canada, April 29–May 4, 2018*, pages 3557–3560. JACoW Publishing, Jun. 2018. `doi:10.18429/JACoW-IPAC2018-THPAK135`.

[128] G. Rumolo and G. Iadarola. Electron clouds. In *CAS - CERN Accelerator School: Intensity Limitations in Particle Beams, Geneva, Switzerland, November 2–11, 2015*, Geneva, Switzerland, 2017. CERN. CERN-2017-006-SP. `doi:10.23730/CYRSP-2017-003`.

[129] G. Rumolo, A. Axford, G. Iadarola, and A. Romano. Progress on electron cloud studies for HL-LHC. 48th HL-LHC WP2 Meeting, CERN, Geneva, Apr. 2015. URL: `https://indico.cern.ch/event/376196/contributions/1798658/attachments/749822/1028685/HL-LHCTaskLeader-GR-240415.pdf`.

[130] R. Tomás, C.O. Domínguez, and S. White. HL-LHC performance with a 200 MHz RF system. In *Proc. of 5th International Particle Accelerator Conference (IPAC'14), Dresden, Germany, June 15–20, 2014*, pages 1043–1045. JACoW Publishing, Jul. 2014. `doi:https://doi.org/10.18429/JACoW-IPAC2014-TUPRO017`.

[131] R. Calaga and R. Tomás. A 200 MHz SC-RF system for the HL-LHC. In *Proc. of 7th International Particle Accelerator Conference (IPAC'16), Busan, Korea, May 8–13, 2016*, pages 1513–1515. JACoW Publishing, Jun. 2016. `doi:10.18429/JACoW-IPAC2016-TUPMW034`.

[132] G. Iadarola and G. Rumolo. 200 MHz option for HL-LHC: e-cloud considerations (heat load aspects). 68th HL-LHC WP2 Meeting, CERN, Geneva, May 2016. URL: `https://indico.cern.ch/event/523881/contributions/2154409/attachments/1267275/1876504/006_ecloud_200Mhz.pdf`.

[133] E. Shaposhnikova and J. Esteban Müller. Possible beam parameters in double RF operation of the CERN LHC. In *Proc. of 7th International Particle Accelerator Conference (IPAC'16), Busan, Korea, May 8–13, 2016*, pages 2430–2433. JACoW Publishing, Jun. 2016. `doi:10.18429/JACoW-IPAC2016-WEPMW008`.

[134] K. Li and E. Métral. 200 MHz option for HL-LHC and intensity limitations. 68th HL-LHC WP2 Meeting, CERN, Geneva, May 2016. URL: `https://indico.cern.ch/event/523881/contributions/2154410/attachments/1267263/1876558/001b_200_MHZ_option.pdf`.

[135] R. Calaga, O. Capatina, and G. Vandoni. The SPS tests of the HL-LHC crab cavities. In *Proc. of 9th International Particle Accelerator Conference (IPAC'18), Vancouver, BC, Canada, April 29–May 4, 2018*, pages 846–849. JACoW Publishing, Jun. 2018. `doi:10.18429/JACoW-IPAC2018-TUPAF057`.

[136] Y. Sun, R. Tomás, and F. Zimmermann. Crab-cavity beam dynamics issued for an LHC upgrade. Technical Report CERN-AB-Note-2008-033, CERN, Geneva, Switzerland, Jul. 2008. URL: `https://cds.cern.ch/record/1117049`.

[137] B. Yee-Rendon et al. Simulations of fast crab cavity failures in the high luminosity Large Hadron Collider. *Phys. Rev. ST Accel. Beams*, 17:051001, May 2014. `doi:10.1103/PhysRevSTAB.17.051001`.

[138] F.-J. Decker. Beam distributions beyond RMS. Technical Report SLAC-PUB-6684, SLAC, Stanford, CA, Sep. 1994. URL: `http://www.slac.stanford.edu/pubs/slacpubs/6500/slac-pub-6684.pdf`.

[139] G. Sterbini et al. First results of the compensation of the beam-beam effect with DC wires in the LHC. In *Proc. of 10th International Particle Accelerator Conference (IPAC'19), Melbourne, Australia, 19–24 May 2019*, pages 2262–2265. JACoW Publishing, Jun. 2019. `doi:10.18429/JACoW-IPAC2019-WEYYPLM3`.

[140] P. Gonçalves Jorge et al. Measurement of beta-beating due to strong head-on beam-beam interactions in the LHC. In *Proc. of 8th International Particle Accelerator Conference (IPAC'17), Copenhagen, Denmark, 14–19 May, 2017*, pages 2121–2124. JACoW Publishing, May 2017. `doi:10.18429/JACoW-IPAC2017-TUPVA030`.

[141] P. Gonçalves Jorge et al. MD 979: Beta-beating measurements on colliding beams. Technical Report CERN-ACC-NOTE-2017-0060, CERN, Geneva, Switzerland, Nov. 2017. URL: `http://cds.cern.ch/record/2292102`.

[142] P. Gonçcalves Jorge and J. Barranco. Observations and measurements of dynamic effects due to beam-beam interactions in the LHC and extrapolation to the FCC-hh. Master's thesis, École Polytechnique Fédérale de Lausanne (EPFL), Lausanne, Switzerland, Aug. 2017. Presented 06 Aug. 2017. URL: `http://cds.cern.ch/record/2286079`.

[143] R. Tomás, X. Buffat, S. White, J. Barranco, P. Gonçalves Jorge, and T. Pieloni. Beam-beam amplitude detuning with forced oscillations. *Phys. Rev. Accel. Beams*, 20:101002, Oct. 2017. `doi:10.1103/PhysRevAccelBeams.20.101002`.

[144] J. Shi, O. Kheawpum, and L. Jin. Global compensation of long-range beam-beam interactions with multipole correctors. In *Proc. of European Particle Accelerator Conference (EPAC'02), Paris, France, 3–7 Jun 2002*, pages 1296–1298. JACoW Publishing, Jun. 2002. URL: `http://accelconf.web.cern.ch/accelconf/e02/PAPERS/WEPRI097.pdf`.

[145] R. Bruce et al. Parameters for HL-LHC aperture calculations and comparison with aperture measurements. Technical Report CERN-ACC-2014-0044, CERN, Geneva, Switzerland, Mar. 2014. URL: `https://cds.cern.ch/record/1697805`.

[146] SixTrack. 6D tracking code, Aug. 2019. URL: `http://sixtrack.web.cern.ch/SixTrack/`.

[147] SixDesk. SixTrack running environment, Aug. 2019. URL: `https://github.com/SixTrack/SixDesk/`.

[148] D. Pellegrini and G. Sterbini. Experimental results and studies on the (HL-)LHC LRBB compensation. 102nd HL-LHC WP2 Meeting, CERN, Geneva, Sep. 2017. URL: `https://indico.cern.ch/event/662031/contributions/2703190/attachments/1517302/2368464/2016_09_01_BBLR.pdf`.

[149] A. Poyet, S. Fartoukh, N. Karastathis, Y. Papaphilippou, K. Skoufaris, and G. Sterbini. Numerical simulations of the DC wire prototypes in LHC for enhancing the HL-LHC performances. In *Proc. of 10th International Particle Accelerator Conference (IPAC'19), Melbourne, Australia, 19–24 May 2019*, pages 566–569. JACoW Publishing, Jun. 2019. `doi:10.18429/JACoW-IPAC2019-MOPMP052`.

[150] G. Sterbini. Experimental tests for BBLR compensation with wires in the LHC. 133rd HL-LHC WP2 Meeting, CERN, Geneva, Oct. 2018. URL: `https://indico.cern.ch/event/760612/contributions/3155276/attachments/1730316/2796258/2018_10_07_GS.pdf`.

[151] K. Skoufaris et al. Numerical optimization of DC wire compensation in HL-LHC. In *Proc. of 10th International Particle Accelerator Conference (IPAC'19), Melbourne, Australia, 19–24 May 2019*, pages 570–573. JACoW Publishing, Jun. 2019. `doi:10.18429/JACoW-IPAC2019-MOPMP053`.

[152] J. Keintzel. Optics design and performance aspects of the HE-LHC. Master's thesis, Technische Universität Wien (TU Wien), Vienna, Austria, Aug. 2018. Presented Aug. 2018. URL: `https://cds.cern.ch/record/2640684`.

[153] L. Medina, R. Tomás, G. Arduini, and M. Napsuciale. Assessment of the performance of High-Luminosity LHC operational scenarios: integrated luminosity and effective pile-up density. *Can. J. Phys.*, 97(5):498–508, 2019. `doi:10.1139/cjp-2018-0291`.

[154] S. Umarov, C. Tsallis, and S. Steinberg. On a q-central limit theorem consistent with nonextensive statistical mechanics. *Milan J. Math.*, 76(1):307–328, 2008. `doi:10.1007/s00032-008-0087-y`.

Members of the Jury

Dr. Ramón Castañeda Priego (UG-DCI)
President

Dr. Georfrey Humberto Israel Maury Cuna (UG-DCI)
Secretary

Dr. Rogelio Tomás García (CERN)

Dr. Gerardo Herrera Corral (CINVESTAV)

Dr. Alejandro Castilla Loeza (Lancaster University and CERN)

Dr. Mauro Napsuciale Mendívil (UG-DCI)
Alternate

UNIVERSIDAD
DE GUANAJUATO
Campus León
División de Ciencias e Ingenierías

October 14th, 2019

Dr. David Yves Ghislain Delepine
Director, Sciencies and Engineering Division
University of Guanajuato

Dear Dr. Delepine,

I am pleased to inform you that I have read and reviewed the content of the PhD thesis titled **“Performance and Operational Aspects of High Luminosity LHC Operational Scenarios”** written by **Luis Eduardo Medina Medrano** and advised by Dr. Rogelio Tomás García and co-advised by Dr. Mauro Napsuciale Mendivil. Luis Eduardo has reported about the simulation study to improve the performance of the HL-LHC. After discussing fundamental aspects of the thesis with Luis Eduardo and given the significance of the results, as well as the original scientific contribution of Luis Eduardo to the research, it is my opinion that the thesis meets the criteria for a doctoral degree. Thus, I recommend this work for presentation to the PhD committee with subsequent dissertation defense.

Sincerely,

Dr. Ramón Castañeda-Priego
Full Professor (Titular Professor C)

UNIVERSIDAD DE
GUANAJUATO

León, Gto. a 28 de octubre de 2019
Asunto: Visto bueno para defensa de tesis

DR. DAVID YVES GHISLAIN DELEPINE
DIRECTOR
DIVISIÓN DE CIENCIAS E INGENIERÍAS
CAMPUS LEÓN
PRESENTE

Por este medio, le informo que he leído la tesis titulada "***Performance and Operational Aspects of High-Luminosity LHC Operational Scenarios*"** que para obtener el grado de **Doctor en Física** ha formulado el **M. F. Luis Eduardo Medina Medrano.** En mi opinión, **este trabajo reúne las características de calidad y forma para el grado al que se aspira**, por lo tanto, no tengo inconveniente en que se realice la defensa correspondiente.

Sin más por el momento reciba un cordial saludo.

Atentamente
"La Verdad Os Hará Libres"

Dr. Georfrey Humberto Israel Maury Cuna
Sinodal
Profesor Asociado C
Departamento de Física

ORGANISATION EUROPÉENNE POUR LA RECHERCHE NUCLÉAIRE
EUROPEAN ORGANIZATION FOR NUCLEAR RESEARCH
Laboratoire Européen pour la Physique des Particules
European Laboratory for Particle Physics

GENÈVE, SUISSE
GENEVA, SWITZERLAND

Adresse postale / Postal address *:

Rogelio Tomás
CERN
CH - 1211 GENÈVE 23

Téléphone / Telephone : +41 75 411 0996
Electronic mail : rogelio.tomas@cern.ch

28 October 2019

Letter of support for Luis Eduardo Medina Medrano thesis' defense

Dear Dr. Delpine,

I had the pleasure to co-supervise, read and review Luis Medina's PhD thesis titled "Performance and Operational Aspects of High Luminosity LHC Operational Scenarios", co-advised by Dr. Mauro Napsuciale Mendivil. The thesis contains original scientific results that have been fundamental to shape the HL-LHC upgrade program. This thesis meets the criteria for a doctoral degree. Thus, I recommend this work for presentation to the PhD committee with subsequent dissertation defense.

Dr. R. Tomás (CERN BE-ABP)

*Adresse pour le courrier posté en France: CERN: Site de Prévessin F-01631 CERN CEDEX

Cinvestav

29 de octubre de 2019.

Dr. David Y. Delepine
Director
División de Ciencias e Ingenierías,
CLE,
Presente.

Por este medio comunico a usted que he leído la tesis: **"Performance and Operational Aspects of High Luminosity LHC Operational Scenarios"**, que presenta el M.F. **Luis Eduardo Medina Medrano** para obtener el grado de Doctor en Física.

Después de discutir con el alumno expreso mi conformidad con su contenido. La tesis desarrolla un trabajo destacado de investigación y por lo que no tengo inconveniente en que sea defendido por el interesado cuando a el convenga.

Sin otro particular, aprovecho para extenderle mis saludos cordiales.

Atentamente,

Dr. Gerardo Antonio Herrera Corral
Departamento de Física

ORGANISATION EUROPÉENNE POUR LA RECHERCHE NUCLÉAIRE
EUROPEAN ORGANIZATION FOR NUCLEAR RESEARCH

Laboratoire Européen pour la Physique des Particules
European Laboratory for Particle Physics

Dr Alejandro Castilla Loeza
Physicist
Lancaster University, UK.
BE-RF-LRF
Bat 18 2-026, CERN
CH - 1211 GENEVA 23, Switzerland.

Mobile (+41-75) 411 7977
e-mail: a.castilla@cern.ch

CERN, 21 Octubre 2019

Dr David Y. Delepine
Director
División de Ciencias e Ingenierías, CLE
PRESENTE

Por este conducto me permito comunicarle que, en relación a la tesis: "**Performance and Operational Aspects of High Luminosity LHC Operational Scenarios**", que presenta el M. F. **Luis Eduardo Medina Medrano** para obtener el grado de Doctor en Física, he leído detenidamente el documento, aportando sugerencias, correcciones, y discutido ampliamente su contenido con el alumno.

Después de lo anterior, expreso mi conformidad con su contenido, considerando el trabajo de un nivel destacado como trabajo de doctorado, no teniendo inconveniente en que el mencionado trabajo sea defendido por el interesado cuando a él convenga.

Sin otro particular, aprovecho la presente para extenderle mis saludos cordiales.

ATENTAMENTE

Dr Alejandro Castilla Loeza

Universidad de Guanajuato

León, Guanajuato, 25 de Octubre de 2019

Dr. David Delepine

Director DCI

Presente

Por este conducto le informo que he leído la tesis titulada *“Performance and Operational Aspects of High Luminosity LHC Operational Scenarios ”* que para obtener el grado de Doctor en Física ha formulado el M.F. Luis Eduardo Medina Medrano.

En mi opinión, este trabajo reúne las características de calidad y forma para el grado al que se aspira, por lo cual, no tengo inconveniente en que se realice la defensa de tesis correspondiente.

Sin otro particular, reciba un cordial saludo.

Atentamente

Dr. Mauro Napsuciale Mendivil

Profesor Titular C

Sinodal Suplente

c.c.p. archivo

DEPARTAMENTO DE FISICA, DIVISION DE CIENCIAS E INGENIERÍAS, CAMPUS LEÓN
Loma del Bosque 103, Fracc. Lomas del Campestre C.P. 37150 León, Gto., Ap. Postal E-143 C.P. 37000 Tel. (477) 788-5100, Fax: (477) 788-5100 ext. 8410, http://www.fisica.ugto.mx